Polymer Micro- and Nanofabrication for On-Chip Immune Cell Handling

Hobæk, Thor Christian

Publication date:
2014

Document Version
Publisher's PDF, also known as Version of record

Polymer Micro- and Nanofabrication for On-Chip Immune Cell Handling

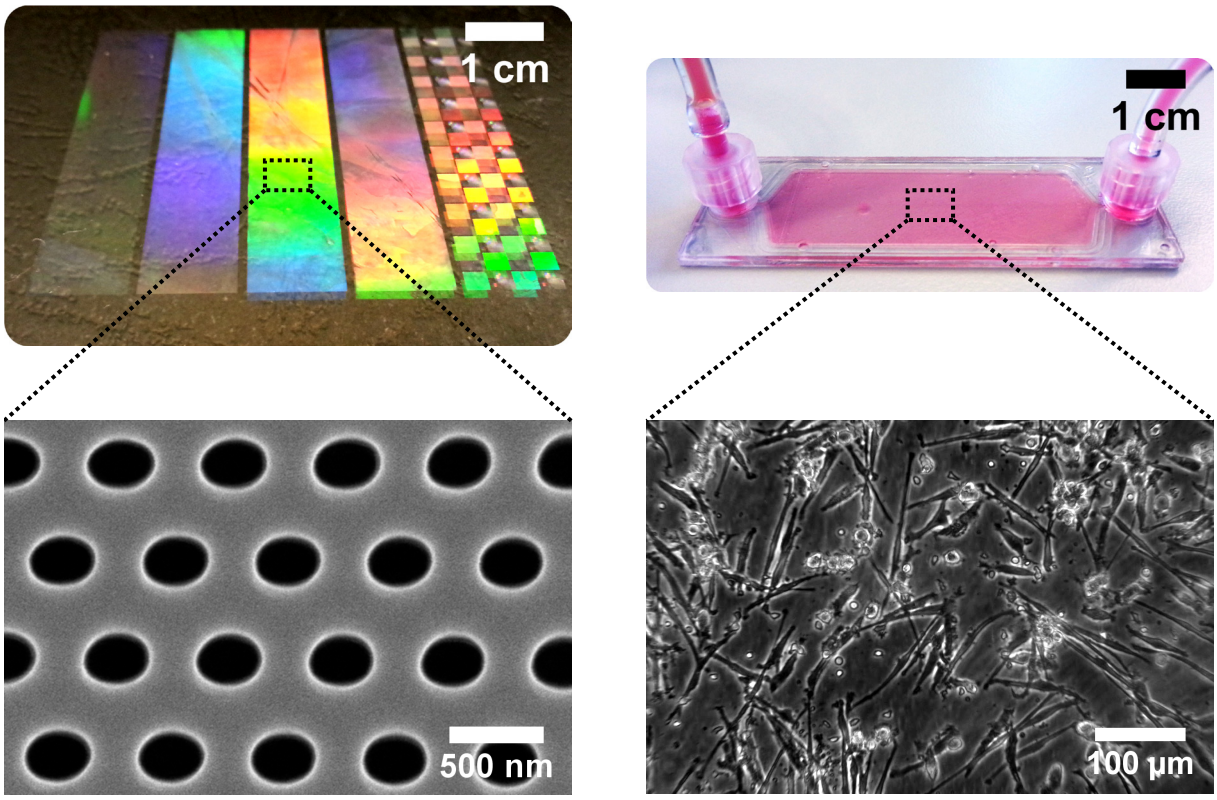

Thor Christian Hobæk

Ph.D. Thesis

August 2014

DTU Nanotech
Department of Micro- and Nanotechnology

Polymer Micro- and Nanofabrication for On-Chip Immune Cell Handling

Submitted by

Thor Christian Hobæk

PhD Thesis

Department of Micro- and Nanotechnology
at the Technical University of Denmark

Supervisor: Professor Niels Bent Larsen

August 2014

Abstract

There is an increasing interest in combining micro- and nanotechnology with mass-fabrication techniques for clinical applications such as diagnostics and therapeutics. One of the most promising strategies for developing a cancer vaccine is immunotherapy based on dendritic cells (DCs). However, major challenges such as high cost and low efficiency still limit its widespread use. The cost per treatment could be reduced by using closed and automated cell culture systems to eliminate infections and reduce manual labor. Furthermore, the efficiency could be increased by using low-cost isolation methods for DC precursor cells, such as surface-immobilized capture antibodies, as well as less invasive methods for harvesting cell cultures, such as cell cultureware with nanoscale surface topography to reduce cell adhesion.

In this thesis we demonstrate the replication of sub-250 nm pillars in cyclic olefin copolymer (COC) over large surface areas by injection molding, using nanostructured mold inlays patterned by high-throughput deep-UV stepper photolithography. Injection molding at constant mold temperature below the glass transition point was significantly improved using nanostructured ceramic hydrogen silsesquioxane (HSQ) coatings on stainless steel mold inserts, compared to more traditional Ni mold inlays formed by electroplating. Numerical simulations suggested that the thermal isolation of HSQ films retards the cooling of the polymer melt, thus allowing more time to fill nanoscale cavities on the mold. In addition, the homogeneity of low surface-energy mold coatings could be improved by coating molds with silicon dioxide prior to deposition of fluorinated silanes.

We successfully demonstrated the transfer of functional proteins from a mold surface to thermoplastic replicas using injection molding in a process compatible with mass production of single-use devices for molecular analysis and cell culture. The transfer process was highly efficient, as verified by atomic force microscopy (AFM) and x-ray photoelectron spectroscopy (XPS) of the mold and replica surfaces. Both ink-jet printed sub-100 µm homogeneous spots of avidin and patches of capture antibodies were transferred using this method. Transferred avidin retained its biotin-affinity as shown by fluorescence microscopy and monocyte-capture from biotinylated anti-CD14 antibodies in a microfluidic channel. Injection molded rabbit anti-mouse IgG showed similar affinity for mouse IgG in sandwich enzyme-linked immunosorbent assay (ELISA) as capture antibodies deposited by passive adsorption to bare thermoplastic replica. The transferred proteins were stable during incubation in serum-containing cell medium for >1 week.

Finally, disposable polymer chips were fabricated by injection molding and ultrasonic welding for the generation of a large number of mature DCs in a closed microfluidic perfusion culture. By using low gas permeable tubings and chip materials, a constant pH and bubble-free culture medium was maintained for 7 days outside a CO_2 cell incubator. Numerical simulations of oxygen transport were performed to establish guidelines for medium exchange rates in an impermeable culture system. Maturation of $CD83^+$ mature DCs generated from $CD14^+$ monocytes was demonstrated inside the disposable culture chip, with a yield almost equal to standard culture procedures in an open Petri dish. This indicates that closed chip-culture systems, with further optimization of the perfusion parameters, are a promising strategy to increase automation and reduce cost of currently used procedures for cancer immunotherapy.

Resumé

Der er stigende interesse for at kombinere mikro- og nanoteknologi med massefabrikationteknikker til kliniske anvendelser såsom diagnostik og terapi. En af de lovende strategier til udvikling af en cancervaccine er immunterapi baseret på dendritceller (DC). Store udfordringer i form af høje omkostninger og lav effektivitet begrænser imidlertid dens bredere anvendelse. Prisen pr. behandling kunne reduceres ved at bruge lukkede og automatiserede systemer til celledyrkning for at undgå infektioner og for at reducere antallet af personaletimer. Effektiviteten kunne endvidere øges ved at bruge billige metoder, fx overflade-forankrede antistoffer, til isolering af forstadierne til dendritceller og ved at minimere celleskader under cellehøstning gennem brug af dyrkningsoverflader med nanoskala overfladetopografi for at minimere cellevedhæftning.

I denne afhandling demonstrerer vi replikation of sub-250 nm søjlestrukturer i cyclisk olefin copolymer (COC) over store overfladearealer ved sprøjtestøbning gennem brug af nanostrukturerede formindlæg mønstret med dyb-UV fotolitografi på en hurtig "stepper". Sprøjtestøbning ved en konstant formtemperatur lavere end polymerens glasovergang blev markant forbedret ved at anvende nanostrukturerede keramiske hydrogen silsesquioxane (HSQ) belægninger på formindlæg af rustfrit stål sammenlignet med more traditionelle formindlæg af nikkel fremstillet ved elektroplatering. Numeriske simuleringer indikerer at den termiske isolering af HSQ film forsinker afkølingen af polymersmelten, hvilket giver længere tid til at fylde nanoskala fordybningerne i formen. Endvidere kunne homogeniteten af formbelægninger bestående af fluorerede silaner med lav overfladeenergi forbedres ved at først at belægge formen med siliciumdioxid.

Vi demonstrerer overførsel af funktionelle proteiner fra en formoverflade til replika i termoplast under sprøjtestøbning i en proces der er fuldt forenelig med masseproduktion af engangs-udstyr til molekylær analyse og til celledyrkning. Overførslen er meget effektiv, hvilket blev dokumenteret med atomic force mikroskopi (AFM) og røntgen fotoelektron spektroskopi (XPS) af overfladerne på formene og replikaerne. Såvel ink-jet printede sub-100 µm diameter homogene områder af avidin som mønstre af indfangningsantistoffer blev overført med denne metode. Overført avidin bevarede sin affinitet for biotin hvilket blev vist med fluorescensmikroskopi og med indfangning af monocytter på biotinylerede anti-CD14 antistoffer i en mikrofluid kanal. Kanin anti-mus IgG overført ved sprøjtestøbning viste sammenlignelig affinitet over for mus IgG i sandwich enzyme-linked immunosorbent assay (ELISA) som de samme indfangsningsantistoffer deponeret ved passiv adsorption på rene termoplast replika. De overførte proteiner var stabile ved inkubation i serum-holdigt celledyrkningsmedium i >1 uge.

Slutteligt blev der ved sprøjtestøbning og efterfølgende ultralydssvejsning fremstillet engangs-polymerchips til produktion af store antal DCer i et lukket mikrofluidt perfusionsmiljø. Anvendelse af slange- og chip-materialer med lav gaspermeabilitet gjorde det muligt at opretholde konstant pH i et boblefrit dyrknings i 7 dage uden for en CO_2 inkubator. Numeriske simuleringer af oxygentransport blev udført for at få retningslinier for hvor ofte mediet skal udskiftes i et impermeabelt dyrkningssystem. Opmodning af $CD83^+$ modne DCer stammende fra $CD14^+$ monocytter blev demonstreret i engangs-polymerchippen med et udbytte sammenligneligt med det som blev opnået ved standard dyrkningsprocedurer i en åben

petriskål. Disse resultater tyder på at lukkede dyrkningssystemer, efter yderligere optimering af perfusionsparametrene, kan være en lovende strategi til at øge automatiseringen og til at reducere omkostningerne sammenlignet med de nuværende procedurer til cancer immunterapi.

.

Preface

This thesis is submitted in partial fulfillment of the requirements for obtaining the degree of Doctor of Philosophy (Ph.D.) at the Technical University of Denmark. The work has been carried out at the Department for Micro- and Nanotechnology (DTU Nanotech) from August 2011 to August 2014 within the group for Polymer Microsystems for Cell Processing. This work was supported by the Danish Council for Strategic Research through the Strategic Research Center PolyNano (grant no. 10-092322/DSF). The Ph.D. project was supervised by Professor Niels Bent Larsen.

I would like to thank everyone who contributed to this thesis, especially:

Niels B. Larsen for being a very dedicated and committed supervisor, and for being an inspiration and always coming with new ideas throughout the project. I would also like to thank existing and former members of the Polycell group for all the help and interesting discussions inside and outside the labs: Esben Kjær Unmack Larsen, Morten Bo Lindholm Mikkelsen, Adele Faralli, Lee MacKenzie Fischer, Johan Ulrik Lind, Maria Matschuk, Jan Kafka, Gertrud Malene Hjortø, and Mark Holm Olsen.

I would also like to thank my project partners Henrik Pranov and Guggi Kofod at InMold Biosystems for sharing their experience and letting me use the facilities at Høje Taastrup, as well as Özcan Met, Morten Hansen, and Inge Marie Svane at Herlev Hospital for generously supplying cells and for helpful advice with the cell culturing.

I would also like to thank the partners that through the Polynano project have been directly involved in my work: Jesper Nørregaard and Lasse Thamdrup at NIL Technology for their collaboration related to fabrication of masters and molds, and Kenneth Haugshøj at the Danish Technological Institute for performing surface modifications on the mold by ALD and CVD.

Thanks to all the helpful people at the administration of DTU Nanotech, especially Ina Blom, Lotte Nielsen, Ole Kristoffersen, Lene Hubert, Jannik Pedersen, and Louise Søby Møller, as well as the supporting people at DTU Danchip especially Claus Højgård Nielsen, Tage A. Larsen, Elena Khomtchenko, Matthias Keil, Rune Christiansen, and Jesper Hanberg.

Thanks to all my friends for making the life outside work more enjoyable. Especially thanks to friends from DTU and the Friday Bar: David, Adele, Kasper, Peter, Anne, François, and the Italians (Paolo, Claudia, Alexander, Ricardo, and Letizia). Thanks to my frequently visiting friends from Norway: Marius, Oddmund, Vidar, Ken, Emily, and Solveig, as well as Alex, Natalie, Timo, Claudio, Diana, Lara, Salomé, and Joana for making my stay in Copenhagen very enjoyable.

And last but not least, thanks to my girlfriend Rita and my family for their love, patience, and understanding, and for always being there and supporting me.

Thor Christian Hobæk
Kgs. Lyngby, Denmark
August 13, 2014

Table of Contents

List of Tables

List of Figures

List of Abbreviations

µCP	microcontact-printing
µTAS	micro total analysis system
4PL	four parameter logistic
7-AAD	7-aminoactinomycin D
ABTS	azino-bis(3-ethylbenzothiazoline-6-sulfonic acid)
AFM	atomic force microscopy
ALD	atomic layer deposition
APC	antigen-presenting cell
BARC	bottom anti-reflective coating
BM MNC	bone marrow mononuclear cell
BSA	bovine serum albumin
CD	clusters of differentiation
COC	cyclic olefin copolymer
DC	dendritic cell
DLD	deterministic lateral displacement
DMEM	dulbecco's modified eagle medium
DMSO	dimethyl sulfoxide
DRIE	deep reactive ion etching
DSC	differential scanning calorimetry
DUV	deep ultraviolet
EBL	electron beam lithography
ECM	extracellular matrix
ED	energy director
EDTA	ethylenediaminetetraacetic acid
ELISA	enzyme-linked immunosorbent assay
ESC	embryonic stem cell
EVA	ethylene vinyl acetate
FBS	fetal bovine serum
FDTS	perfluorodecyltrichlorosilane
FEP	fluoro ethylene propylene
GM-CSF	granulocyte-macrophage colony-stimulating factor
GMP	good manufacturing practice
HIV	human immunodeficiency virus
HRP	horseradish peroxidase
HSA	human serum albumin
HSC	hematopoietic stem cell
IC	integrated circuit
ICP-DRIE	inductively coupled plasma - deep reactive ion etching
ID	inner diameter
IL	interleukin
IR	infrared

LoD	limit of detection
MEMS	microelectromechanical systems
MFI	median fluorescence intensity
MHC	major histocompability complex
MVD	molecular vapor deposition
OD	outer diameter
OUR	oxygen uptake rate
P/S	penicillin/streptomycin
PBMC	peripheral blood mononuclear cell
PBS	phosphate buffered saline
PC	polycarbonate
PDMS	polydimethylsiloxane
PEEK	polyether ether ketone
PEG	polyethylene glycol
PGE2	prostaglandin E2
PMMA	poly(methyl methacrylate)
PO	polyolefin
PP	polypropylene
PS	polystyrene
PVC	polyvinyl chloride
RBC	red blood cell
ROS	reactive ion species
SEM	scanning electron microscopy
TMAH	tetramethylammonium hydroxide
TMB	tetramethylbenzidine
TNF	tumor necrosis factor
TR	texas red
WBC	white blood cell
XPS	x-ray photoelectron spectroscopy

Chapter 1

Introduction

1.1 Motivation

1.1.1 Cancer immunotherapy

Through evolution, our immune system has developed elaborate defense mechanisms in response to various infectious agents, such as viruses and bacteria. Inflammation is one of the earliest responses by the non-specific innate immune system, caused by "danger" signal released by damaged cells. In the case of a growing tumor, this can be triggered by toxic stress due to cell deformation and disruption of the local microenvironment [1]. However, tumors are often able to evade immune recognition; by physically excluding immune cells from tumor sites [2], reducing expression of antigen receptors of immune cells [2], secreting proteins that interfere with immune activation [3], or by blocking production of pro-inflammatory factors [4]. Cancer immunotherapy attempts to bypass these obstacles and enhance the ability of the immune system to recognize and target tumor cells.

Three main strategies exist for cancer immunotherapy: (1) activation of the innate immune system through injection of antibodies against anti-inflammatory signals, e.g. anti-cytotoxic T lymphocyte antigen-4 (CTLA-4), or cytokines (IL-2 and IL-12), (2) passive administration of antibodies or activation of B-cells to increase antibody production (humoral immunotherapy), (3) or infusion of *ex vivo* modified

immune cells to initiate an immune response (cell-based therapy) [1]. Cell-based therapies aim to create an anti-tumor response by T-cells, in order to both eliminate the tumor and achieve a long-term memory to prevent tumor recurrence. To mediate anti-tumor activity, T-cells must first be activated by antigen-presenting cells (APCs) expressing the tumor antigen on the outer cell membrane together with the major histocompatibility complex (MHC).

One of the most important APCs are the dendritic cells (DCs) [5]. They normally reside in an immature state in the peripheral tissue, such as the skin, or in the blood circulation. DCs exposed to antigens process them into small peptides expressed on the surface as they mature and start migrating towards the lymph node [6]. There they present those peptides to naïve helper T cells (CD4+) and cytotoxic T cells (CD8+), inducing a cellular response [7]. DCs are also capable of activating memory B cells [8].

Cancer vaccines that activate both the innate and adaptive immune system through DCs are very attractive. However, efficient delivery of tumor antigens *in vivo* is very challenging. Therefore, most studies are based on *ex-vivo* generated DCs, as this allows more controlled conditions for activation and delivery of antigens, which again allows a more well defined and optimized vaccination scheme. **Figure 1-1** summarizes the main steps involved in a DC-based cancer immunotherapy.

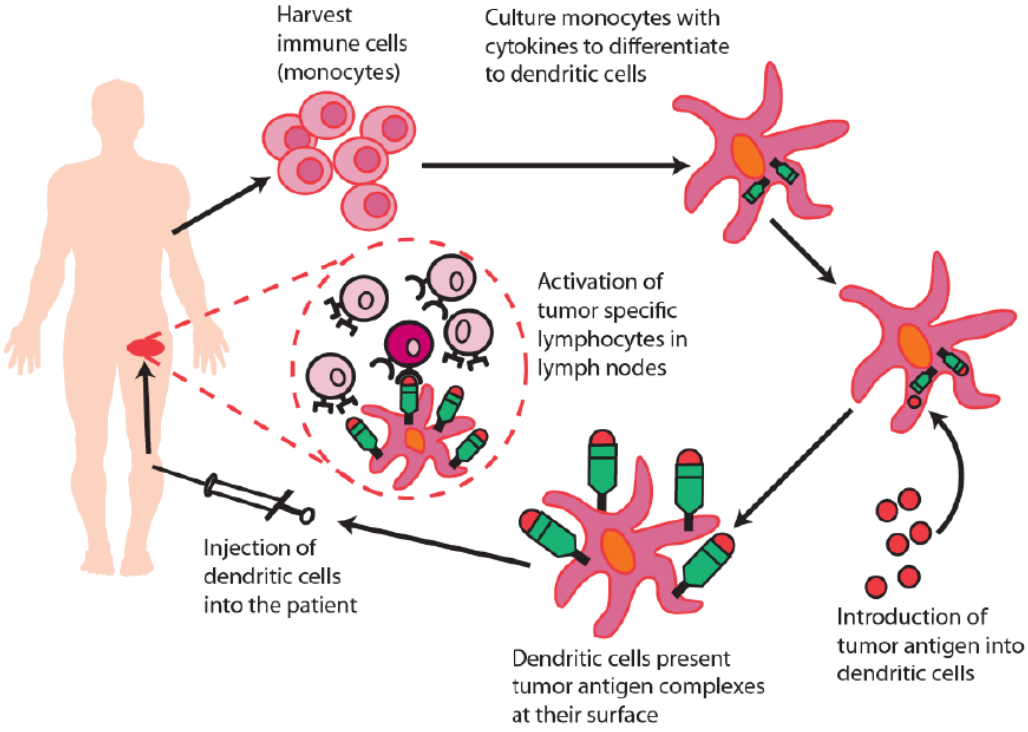

Figure 1-1. Schematic overview of the different steps in cancer immunotherapy using monocyte-derived DCs. Monocytes are extracted from the patient's blood and differentiated into dendritic cells by addition of cytokines. Matured DCs are finally transfected with mRNA encoding a tumor antigen, before they are injected back into the patient where they can trigger a specific immune response [7].

DCs can be generated by differentiation of monocytes, which are derived from peripheral blood extracted from the patient [9]–[11]. After lysing the red blood cells, the peripheral blood mononuclear cells (PBMCs) are sorted by adherence to a plastic tissue-culture dish. The non-adherent cells are removed, and the adherent cells are differentiated to immature DCs in the presence of two cytokines: granulocyte-

macrophage colony-stimulating factor (GM-CSF) and interleukin 4 (IL-4) [12].While immature DCs are able to process the antigens they are exposed to, maturation is required in order to trigger a T-cell response [7]. Maturation of DCs occurs in the presence of pro-inflammatory cytokines and prostaglandins, which are added to the culture medium after differentiation [13]. Finally, mature DCs are transfected with mRNA encoding for tumor antigens by electroporation, before they are injected back into the patient.

The first therapeutic vaccine to be approved by the FDA in 2010 to treat prostate cancer was Sipuleucel-T (trade name Provenge) manufactured by Dendreon Corporation. Although it was first reported to extend the survival by an average of 4 months in Phase III clinical trials, questions later arose whether the results were actually significant or not compared to a placebo group [14]. A drawback of the therapy is the high number of white blood cells that needs to be extracted per treatment from the patient (25 billion), which in worst case might lead to death [15]. Another drawback preventing widespread use by the public is the cost of the treatment, which was $93,000 in 2012 [14]. The reason for the high cost is that each treatment must be prepared individually for each patient, using autologous cells to avoid adverse immune reactions upon re-infusion. After extraction of blood cells from the patient, these are sent to a central manufacturing facility. Rigid safety routines must therefore be employed to avoid mixing up the cells from individual patients, and to avoid infections at any point during the treatment.

Some of the limitations preventing widespread use of cancer vaccines may be addressed using micro- and nanofabrication techniques combined with polymer injection molding, in order to improve the efficiency of the separation and to reduce the amount of manual labor required and therefore the cost. These ideas will be presented in the following sections.

1.1.2 Microfluidic cell culture on chip

In vitro culture of cells is traditionally performed in a static system, typically in a dish or culture flask, where medium is exchanged manually. In contrast, microscale cell cultures based on perfusion of medium through a chip offers a better control of the local microenvironment [16]–[18]. In fact, perfusion culture may more accurately mimic the *in vivo* environment for cells that are close to the vascular network, compared to static culture systems. The supply and removal of nutrients and secreted factors can be controlled continuously in a microfluidic system. In addition, well-defined mechanical shear stress can be applied to the cells by laminar flow. Due to the small length scales involved, several steps of traditional assays can be integrated into a so-called “micro total analysis system” (μTAS) [19], thereby eliminating the need for intensive manual handling, often required by specialized technicians. Through automation and a smaller footprint, microfabricated devices may be operated by less trained personnel and moved closer to the location of the end-user, whether it is the local hospital or the doctor’s office.

Another advantage with microfluidic perfusion culture is the possibility to integrate sensors either on-chip or further downstream, so that the state of the cell culture can be continuously monitored. The readout can be optical or electrical (impedance) and can be used to detect changes in pH, dissolved O_2 or CO_2, or to monitor phenotypic responses (secreted factors, life *vs* death, etc.) [17], [20]. In the case of DC generation, optimum culture conditions can be more quickly established as the cell response can be detected simultaneously for a range of different combinations

of parameters. For large-scale production of DCs (cell factories), the integration of sensors can serve as a quality control before the cells are infused back into the patient.

Finally, a closed microfluidic system has the advantage of potentially eliminating the risk of contamination, in contrast to traditional culture systems for adherent cells where pathogens may be introduced every time the system is opened. For the purpose of cancer immunotherapy, this is of critical importance as introduction of foreign substances with the infused cells could be potentially life threatening to already immunocompromised patients.

1.1.3 Thermoplastic materials for polymer chip fabrication

The majority of biological research data that has been published relies on cell culture with thermoplastic materials, such as polystyrene (PS) [21]. PS quickly became the material of choice as a replacement for glass, due to the low production cost and high optical transparency. Because of this, it has the major benefit that it can be disposed after use, eliminating extensive cleaning procedures and risk of contamination between experiments. High-volume commercial production of polymer parts is preferably done by injection molding. However, the use of this technique for the fabrication of microfluidic devices is not as widespread in academia, due to the high equipment costs [22]. Most academic development of microfluidic cell-based systems has been focused on using materials, which can more easily be prototyped, by microfabrication techniques, such as the elastomer polydimethylsiloxane (PDMS).

The discrepancy between the materials and the fabrication methods used for prototyping in academia and commercial production may hinder the widespread use of microfluidic devices [22]. Due to the different physical and chemical properties, results obtained with common prototyping materials cannot be directly translated into a commercial product. In fact, several researchers noted adverse effects when culturing cells in microdevices made of PDMS [23]. Therefore, there is a need to use thermoplastic microdevices fabricated by injection molding for cell culture use also in academia, in order to bridge the gap between the application and the technology.

1.1.4 Cell purification by phenotype-specific surface immobilization

The specific capture of cells based on their phenotype is important for multiplexed screening of cell populations, such as leukocytes. For instance, microarrays of antibodies specific for different surface antigens (clusters of differentiation) has been used to separate blood cells according to their phenotype [24]–[26]. A high sorting specificity has been achieved in a microfluidic device, by seeding cells on a surface covered with antibody spots, followed by washing to remove non-specifically bound cells [27]. In the case of cancer immunotherapy, monocytes are isolated from leukapheresis products. However, the total fraction of monocytes in these samples is low, and therefore they must be captured efficiently to maximize the yield. This could be achieved by coating the culture substrate with antibodies against monocyte-specific proteins, such as CD14 [28]. In addition to cell capture, antibody-coated surfaces are important for high-throughput screening applications, such as proteomics for the development of personalized medicine [29], [30], and point-of-care diagnostics [31].

Following the concept of μTAS, it is desirable to integrate the sorting step together with cell culture on the same chip. In addition, phenotypic sorting of cells should be performed on antibody immobilized thermoplastic substrates, in order to be

compatible with commercial fabrication processes, as discussed above. However, thermoplastic substrates popularly used in life science besides PS, such as polycarbonate (PC), polypropylene (PP), cyclic olefin copolymers (COC) and poly(methyl methacrylate) (PMMA), are inert in their native form and therefore need chemical modification prior to protein binding [32]. In a production line, this adds an extra process step and therefore increases the cost of the final product.

An untraditional approach for antibody immobilization is the direct entrapment of the protein on a polymer surface during injection molding, where pre-adsorbed proteins on a mold surface are transferred to the polymer replica during shaping. This method has previously been used to demonstrate successful transfer of avidin, fibronectin and horseradish peroxidase (HRP) with retained biofunctionality [33]. One of the advantages of this approach is that immobilization can be combined with replication of micro- or nanostructures in a simultaneous shaping process, making it a highly attractive approach for biochip fabrication. Moreover, with automation of the mold exchange, a cycle time below 30 s per part is achievable, which makes it compatible with mass-fabrication.

1.1.5 Nanostructured culture substrates for adherent cell harvesting

The surface topography at the nanoscale has been shown to influence cell behavior [34], generating interest in fabrication of new biomaterials for bone formation and tissue engineering [35]–[37]. *In vivo*, cells are surrounded by nanostructures in the extracellular matrix (ECM). However, culturing cells *in vitro* expose them to a physical environment far away from their natural state, since traditional cultureware does not contain nanotopography. For instance, it has been shown that introduction of nanostructures affects cell adhesion [34], [38].

Cell adhesion to the ECM is mainly mediated by integrins, a class of proteins that couple the actin filaments of the cytoskeleton to ECM proteins such as fibronectin, vitronectin, collagen and laminin. These protein complexes are known as focal adhesion points. Focal adhesion is mediated by particles on the cell membrane with a diameter of about 25 nm and a spacing of about 45 nm [39]. It has been shown that cell adhesion is dependent on the distance between focal adhesion sites; a large spacing significantly reduces the adhesion to the substrate [40]. With the introduction of surface topography, the cell membrane needs to be flexible in order to establish a sufficient number of adhesion points. The link between cell adhesion and nanotopography is likely depending on whether the cell can establish a conformal contact with the substrate or not. As the feature-size of structures on the surface becomes smaller and the roughness increases, the accessible surface area for adhesion may therefore be reduced.

Adherent cells cultured inside a microfluidic device may be challenging to harvest for further use at the end of a culture. They can be removed mechanically by applying a shear stress through laminar flow in the culture chamber. However, a high shear stress level may be detrimental for the culture and lead to cell death. Addition of calcium-chelating agents (ethylenediaminetetraacetic acid, EDTA) or peptide-cleaving enzymes (trypsin) leads to cells being loosened from the surface, but again it may either be inefficient or have detrimental effects on cell function or viability [41]. By introducing nanotopography on the culture surface, the adhesion may be lowered by reducing the surface area available for adhesion, thus, reducing the level of shear stress required to remove cells.

1.2 Project goal

The aim of the project was to contribute with technological solutions for a more efficient cell-based cancer immunotherapy. The goal of the project was divided into three main sub-tasks:

1. To fabricate a closed culture chip made entirely of injection molded plastics with integrated sorting of monocytes from PBMCs, followed by culturing for 7 days, where the monocytes should differentiate and become mature DCs, and finally to harvest viable cells with a high yield.
2. To integrate cell-binding proteins on the surface of injection molded culture substrates, with the purpose of achieving specific capture of monocytes from PBMCs.
3. To incorporate well-defined nanostructures on the surface of injection molded plastic over large length scales (~cm^2); with the purpose of reducing the shear stress necessary to harvest DCs by modifying cell adhesion.

Common to all sub-tasks is that they involve polymer fabrication using injection molding, which is the industrially preferred method for mass-fabrication. In this way, the obtained results can be more easily translated into a commercial product, since the methods and materials used are similar. Although the main application of this project was cancer immunotherapy, other possible applications should not be excluded, as discussed more detailed hereinafter.

1.3 Outline of the thesis

The following chapters in this thesis are divided into three main parts:

- The first two chapters deals with the aspects around fabrication of polymer replicas with nanostructured surface topography, as an attempt to control the behavior of adherent cells during sorting and culture. **Chapter 2** *Large Area Master and Mold Fabrication*, deals specifically with the generation of silicon masters with sub 250 nm patterns on full wafer-scale using deep-UV lithography, fabrication of nickel shims by electroplating, and finally surface modification to reduce mold adhesion. **Chapter 3** describes the replication of nanopatterns into the surface of polymer replicas, with special emphasis on using low mold temperatures to achieve higher throughput.

- The two next chapters describe protein patterning on nickel shims, functional integration on polymer replicas during the injection molding process and the application for cell capture and immunoassays. **Chapter 4** *Protein Patterning for Monocyte Isolation* deals with the deposition of micro-sized avidin spots on flat and nanostructured mold surfaces, with emphasis on how to improve spot homogeneity, and the functional transfer to polymer replicas. Finally, the cell adhesion to various functionalized surfaces under well-defined shear stress is examined. **Chapter 5** *Antibody Immobilization by Injection Molding*, describes how antibodies can be transferred from a mold surface to a polymer replica, and their retained affinity for antigen-capture demonstrated by ELISA.

- The two last chapters describe the fabrication of thermoplastic chips and the generation of a large number of DCs inside a closed microfluidic perfusion system. **Chapter 6** *Polymer chip fabrication and simulation of perfusion culture*, deals with chip fabrication using injection molding and ultrasonic bonding, simulation of oxygen transport inside a perfusion system, as well as the various challenges and possible solutions of operating a microfluidic culture system outside the environment of a traditional cell culture incubator. **Chapter 7** *On-Chip Generated Dendritic Cells* describes the selection of monocytes from a mixed cell population, and the subsequent differentiation and maturation of DCs during a perfusion culture. The constructed perfusion system is compared to culture experiments performed in a traditional Petri dish.

Chapter 2

Large Area Master and Mold Fabrication

2.1 Introduction

Production of polymer surfaces with nanoscale topography for cell culture has gained interest in the last decade, due to the increased understanding of the influence it has on cell behavior. A potential application of nanostructuring is to control the cell adhesion on culture substrates [34], [38]. Adherent cells, such as monocytes and DCs, may be generally difficult to harvest for further processing, without applying high shear forces or chemicals that may compromise the cell viability [42]. Nanoscale surface topography for reduced cell adhesion may therefore potentially be a less harmful route to harvest highly adherent cell cultures.

Cancer immunotherapy requires culture of a large amount of cells, up to around 5×10^9 cells [43]. Thus, even with a relatively high cell density of an adherent monolayer (2×10^6 cells/cm^2), culture substrates with a large surface area are required (>1000 cm^2). Nanoscale patterns can be defined with lateral resolution below 10 nm by using electron beam lithography (EBL) [44]. However, because EBL is a serial process with writing times ranging from a few h to days for ~ 1 cm^2 area depending on the density and complexity of the pattern, it is not economical feasible for the generation of large patterned areas.

Optical photolithography, which is a parallel process, is capable of patterning large areas at a significantly higher throughput compared to EBL. Industrial scale production of integrated circuits are commonly performed with projection lithography, which uses a lens system to form an image of the photomask pattern, often reduced by a factor up to five times [45]. Stepper systems are able to transfer the reticle pattern by repeated exposure across the wafer, by using a motorized stage to move or "step" the wafer in a pre-defined grid. Through a low stitching error the same pattern can be joined together to form a continuous array of nanostructures across the entire wafer. By using a stepper system based on deep ultraviolet lithography (248 nm illumination source), the fabrication of silicon masters with continuous arrays of holes with sub-250 nm feature size over ~ 100 cm^2 for mold inlay production and subsequent replication by injection molding, will be demonstrated.

For injection molding processes involving tens of thousands of replication cycles, it is important that micro- and nanostructures on the mold insert are preserved, which requires materials that are both hard and resilient to be able to withstand the high forces exerted during injection and demolding. Silicon [46] and quartz [47] has previously been used directly as mold materials, however, because these materials are very brittle, the use is limited to prototyping purposes where only few cycles are needed.

With the development of LIGA[1] fabrication processes for high aspect ratio microstructures, nickel shims formed by electroplating from a metallized silicon or photoresist master have become the standard insert material for micro- and nano-replication [22], [48]. Although LIGA processes are time-consuming, especially if thick inlays are required, it is the most suitable method to produce metal molds with features below 10 µm due to the high precision. Nickel has a high thermal conductivity like most other metals, which leads to fast heat dissipation from the polymer melt during mold filling. Although rapid cooling of the polymer leads to lower cycle times, it is detrimental to filling of nanostructures on the mold surface due to an early formation of a solidified polymer skin layer [49].

For micro- and nano-replication, it would therefore be advantageous to use mold materials that has both a high mechanical strength and a low thermal conductivity. One such material may be hydrogen silsesquioxane (HSQ), which is a soluble organosilicon compound that forms a ceramic coating after thermal curing. HSQ thin films are established in commercial integrated circuit production as a precursor for interlayer dielectrics [50] and as an EBL resist with lateral resolution down to 5 nm [51]. For polymer shaping, structured HSQ films on silicon have previously been used as stamps for nanoscale features by hot embossing [52], [53]. In addition, planar HSQ films have been used as a surface coating on steel molds to lower the surface roughness [54] with a demonstrated injection molding lifetime of at least 10 000 cycles without measurable wear. In this chapter, the fabrication of Ni shims by

[1] German acronym for ***Li****thographie* (lithography), ***G****alvanoformung* (electroplating), ***A****bformung* (molding)

electroplating as well as hybrid molds consisting of a film of HSQ with imprinted nanostructures on a stainless steel mold using master structures defined by DUV lithography, will be discussed.

Finally, the adhesion between the mold surface and polymer replica is important for the surface quality of the final part, as high stiction during demolding can lead to incomplete replication or damage to the mold surface [55], [56]. One method to reduce the mold adhesion is to coat the surface with highly non-polar fluorinated silane monolayers such as FDTS, which has routinely been applied on moving parts in microelectromechanical systems (MEMS) [57], as well as for improved separation between polymer replica and a molding surface in the format of stamps for nanoimprint lithography [55], [56], [58]–[60] or nickel inlays for injection molding [61]–[64]. However, traditional mold metals such as nickel and steel are not readily oxidized, meaning that the surface density and accessibility of surface hydroxyl groups for coupling with silanes are low [56], [65]. The result is an inhomogeneous monolayer with low coverage, which leads to insufficient shielding of the underlying substrate. One method to improve the anti-adhesive properties of metal molds further is to apply thin film coatings of SiO_2 prior to silanization, by sputter coating or atomic layer deposition (ALD), which has the effect of greatly reducing the stiction between molds and polymer. ALD has the additional advantage that conformal films are achieved even for very high aspect ratio structures, by using sequential, self-limiting surface reactions [66]. Application of HSQ thin films is another method to increase the reactivity of fluorinated silanes to the mold, as heat treated HSQ forms a silica-like material. In this chapter, the surface energy of FDTS coatings on different substrates will be characterized.

2.2 Experimental procedures

2.2.1 DUV stepper system

Nanoscale features was defined using a Canon FPA-3000 EX4 DUV stepper system. The stepper was equipped with a KrF laser (CYMER ELS-530) having a wavelength of 248 nm, with a guaranteed minimum line width of 250 nm. The numerical aperture was 0.6, with a depth of focus of around 700 nm. The mask pattern was projected onto the silicon wafers with a 5x reduction of feature size. Individual chips on the reticle could be printed by using programmable aperture blades to shadow out parts of the reticle.

2.2.2 Reticle design

The masks (6”x6”x0.25” quartz) with pellicle films for dust-protection were manufactured by Compugraphics (Glenrothes, Scotland). The reticle pattern was written using an ALTA 3900 system, which consists of a “brush” of 32 individual Ar-ion laser beams ($\lambda = 364$ nm) scanned in a raster motion, with two passes for averaging spatial variations. This method allowed writing of features with a width and separation distance down to 700 nm on the reticle.

Two different reticles were designed during the project; a first-generation design called “*9stripes*”, and later a second-generation called “*16Box*”. An overview of both reticle designs can be found in **Figure A-1** and **Figure A-2**. The chip area on the

reticle, i.e. the exposure area, was 110x110 mm^2.

The reticle "*9stripes*" consisted of nine fields spanning the full width of the chip area (**Figure A-1**). To achieve a smooth transition between different chips on the wafer when stitching in both the x- and y-direction, field 1 and 9 was made identical, with half the width compared to the other fields. Each field contained 0.2-1×10^9 squares with different side-length *d* and pitch *p*. To minimize the stitching error between different chips, it was necessary to calculate the pitch in the x- and y-direction that resulted in an integer number of squares spanning the extents of the field, with a half-pitch margin on all four borders. Because of this, the pitch for each field had to be increased by an amount of up to 0.01% of the nominal value, corresponding to less than 0.5 nm. This level of precision could not be achieved in common mask-drawing software. Therefore, a script written in IGOR Pro (Wavemetrics) was used to generate a CIF file with the mask pattern, which was converted to a GDS-II file using CleWin 4 (PhoeniX Software). Final inspection of the reticle design file was done in L-Edit 15 (Tanner EDA) before sending to DTU Danchip, which added stepper alignment marks and ordered the reticle.

The reticle "*16Box*" consisted of 15 areas filled with hexagons laid out in a hexagonal array, to allow a denser packing of features as fulfilling the requirement of a minimal spacing of 700 nm between features, as well one area with "test" patterns and horizontal and vertical gratings. Each of the sixteen areas were separated by a 1 mm wide chromium frame, so that individual exposure doses could be addressed to each field, and that the placement of each area on the wafer could be determined independently, by using aperture blades in the stepper system. The pitch between features was specified to fit exactly one half hexagonal unit cell along all four frame borders (**Figure A-2**).

2.2.3 Master fabrication

All DUV lithography steps were performed by personnel at DTU Danchip. The silicon wafers were <100>, n-doped, single-side polished, 4" or 6", with a thickness of 525 µm and 675 µm respectively. Dispensing, spin-coating, and baking of resist were performed with a Gamma 2M automated platform (Süss MicroTec AG, Garching, Germany). To minimize interference effects and to promote adhesion, a 60 nm thick bottom anti-reflective coating (BARC, DUV42S-6, Brewer Science, Rolla, USA) was applied by spin-coated, followed by baking at 175 °C for 60 sec. A positive tone photoresist (JSR-M230Y, JSR Corporation, Tokyo, Japan) was spin-coated to a thickness of 350-360 nm, and soft baked at 130 °C for 90 sec. Exposure doses ranged from 180 – 1020 J/m^2, depending on the type of structure. A post-exposure bake at 130 °C was employed for 60 sec, before developing in a 2.38% solution of tetramethylammonium hydroxide (TMAH) in water for 60 sec.

On some wafers, the resist pattern was transferred into silicon by reactive-ion etching using inductively coupled plasma (ICP-RIE), using the Bosch process with alternating plasma etching (SF_6), and plasma deposition of a passivation layer (C_4F_8), using an Advanced Silicon Etcher (ASE, STS). This was performed by NIL Technology. The fabrication of Si masters for the study of heat retardation by HSQ/steel molds, were instead performed by InMold Biosystems using a continuous RIE with a Pegasus system (STS; SF_6/ C_4F_8 = 38/75 sccm; P = 4 mTorr; coil/platen power = 800/40 W; 180 s; T = -20 °C). After etching, residual resist was removed by ashing using O_2 plasma.

2.2.4 Ni shim fabrication

Initial process development of the mold fabrication was performed by the author, while fabrication of Ni shims using the established procedures was later performed by NIL Technologies as part of the Polynano project agreement. Ni shims were fabricated by electroplating from a seed layer deposited either directly on the DUV stepper resist or on etched silicon. Metallic seed layers were sputter coated with a Lesker CMS 18 sputter system, using either NiV (1150 s, 157 W, 400 V, 3 mTorr Ar) with a predicted film thickness of about 130 nm, or with a dual layer coating of Cr (225 s, 90 W, 300 V, 5 mTorr Ar) and Au (260 s, 100 W, 500 V, 3 mTorr Ar), with a predicted thickness of about 10 nm and 60 nm, respectively. Chromium was used to improve the adhesion of gold films on the silicon wafer during electroplating.

Nickel electroplating from both 4" and 6" metallized wafers was performed with a Technotrans Microform 200 system, using a bath of nickel sulfamate, sulfamic acid and boric acid, operated at 56 °C and at pH 3.6-3.8. A detailed overview of the plating programs used for 4" and 6" samples can be found in **Figure A-3** and **Figure A-4**. The resulting Ni shims had a thickness of 320±10 µm. In those cases where etched silicon was used, the master was separated from the shim by dissolving the entire wafer in a 28% w/w KOH in water at 90 °C. When the seed layer was deposited directly on the resist, the master could easily be separated from the shim mechanically. Any residual resist was removed by plasma ashing. Shims plated from 4" masters were cut out as 85 mm disks with flats for alignment in the injection molder using a manual hydraulic press, while shims plated from 6" masters were cut out by laser (532 nm, 20W), using a microSTRUCT vario laser micromachining tool (3D-Micromag AG, Chemnitz, Germany).

2.2.5 HSQ/steel mold fabrication

Most of the fabrication steps leading to HSQ/steel molds were performed by InMold Biosystems. Stainless steel substrates with a thickness of 1 mm were cut out with alignment flats by milling. The substrates were wet polished using a series of sandpaper with grit size P500, P800 and P1200 (Norton Abrasives, Saint-Gobain), followed by Al_2O_3 paper with 5 µm and 0.3 µm mean particle size (Laser Components GmbH, Olching, Germany). The substrates were cleaned in an ultrasonic bath with 1% Triton X-100 in MilliQ water at 60 °C for 1 h, followed by a 10 min air plasma treatment to reduce hydrocarbon contamination. HSQ was subsequently spin-coated at 2000 rpm. Ni shims were electroplated from etched Si, which was patterned by the DUV stepper using a reticle provided by InMold Biosystems through "Large Area Nanostructuring Initiative" (LANI, The Danish National Advanced Technology Foundation). To transfer the patterns from the Ni shim to the HSQ film, an intermediate elastomeric stamp was fabricated by casting from the Ni shim, and curing overnight at 120 °C. The patterns of the cured elastomeric stamp were imprinted into the spin-coated HSQ film, using a spring-loaded press. Afterwards, the HSQ/steel mold was thermally cured, first at 80 °C for 24 h to remove solvent, and finally at 450 °C for 2 h to allow monomer cross-linking. The hybrid mold was cleaned with 1% Triton X-100 in de-ionized water in an ultrasonic bath for 10 min, before FDTS-coating was applied by MVD as described in **Section 2.2.7**.

2.2.6 Characterization of nanostructures

Scanning electron micrographs (SEM) of Si masters, Ni shims, and HSQ/steel mold inserts were acquired on a Supra 40 VP microscope (Carl Zeiss, Oberkochen, Germany) using 5 kV acceleration potential, and an in-lens secondary electron detector. The diameter of features (holes and pillars) was measured using the Gwyddion SPM data analysis software [67]. The edges were detected by the "Zero crossing step detection method" (**Figure A-5**), which gives pixels a value of 1 where the result of the Laplacian of a Gaussians filter changes sign, and all other pixels a value of 0. A grain threshold method was then used to mark the area inside the edge of the hole, and the diameter of each grain was calculated by grain analysis.

The HSQ film thickness was measured by optical reflectance at incidence angles of 0° and 70° using a FilmTek 4000 reflectometer (Scientific Computing International, Carlsbad, CA). Surface topography micrographs were acquired by atomic force microscopy (AFM) using BudgetSensor-300 cantilevers for low aspect ratio features (Innovative Solutions, Sofia, Bulgaria), or Nanosensors AR5T-NCHR cantilevers for high aspect ratio features (NanoAndMore, Wetzlar, Germany), on an XE-150 AFM (Park Systems, Korea) operating in intermittent contact mode.

The height/depth of features was analyzed as grains using height threshold detection in Gwyddion or SPIP 6.2.8 software package (Image Metrology, Hørsholm, Denmark). The background level, defined as the base area surrounding holes/pillars, was corrected with a 2^{nd} degree polynomial plane fit. Each of the 256 line profiles was then fitted individually with a linear curve (excluding the data above/below the threshold level). This method was the most reliable to produce a zero-level flat background. The minimum/maximum height value of each grain (hole/pillar) was recorded and used to quantify the degree of replication.

2.2.7 Surface modification of molds

The molds were coated with a monolayer of 1H,1H,2H,2H-perfluorodecyltrichlorosilane (FDTS) using molecular vapor deposition (MVD, MVD 100, Applied Microsystems Inc., San Jose, USA). The process parameters are summarized in **Table A-1**. Prior to coating, the empty MVD chamber was conditioned using oxygen plasma, and the FDTS lines were purged. Ni shims were loaded into the MVD chamber with the structured side facing upwards (up to five shims loaded per run), and coated using a multilayer recipe, consisting of oxygen plasma, followed by four cycles of FDTS and water vapor injection, which were allowed to react for 15 min each.

To improve the quality of FDTS-coatings on Ni shims, thin film coatings of SiO_2 were deposited on substrates using: (1) radio frequency sputter-coating (1825 s, 157 W, 670 V, 3.5 mTorr Ar), or (2) a two-layer coating process, using atomic layer deposition (ALD) to deposit 5 nm Al_2O_3 from $Al(CH_3)_3$ and H_2O precursors and chemical vapor deposition (CVD) to deposit 5 nm SiO_2 from $SiCl_4$ and H_2O precursors (PICOSUN R-150, Picosun Oy, Espoo, Finland). Initial deposition of Al_2O_3 was used since it was believed to improve SiO_2 adhesion to the substrate. Deposition of ALD-coatings was performed by the Danish Technological Institute (Kenneth Haugshøj). The shims were compared against FDTS-coated Ni shims, with a 50-100 nm nickel-vanadium alloy (7% w/w vanadium) seed layer, bought commercially from DVD Norden (Sakskøbing, Denmark).

Advancing and receding contact angles of water were measured optically using

an OCA 20 system (dataphysics, Germany), by the dynamic sessile drop method, through adding/removing liquid at 0.1 µL/s and calculating the average equilibrium angle while the length of the contact line increased/decreased.

The polar and dispersive components of the surface energy was calculated for FDTS coatings on NiV and NiV coated with Al_2O_3 and SiO_2, by using the Owens-Wendt method [68]. Details of this method can be found in **Section 0**. The contact angles of water, diiodomethane and benzyl alcohol, which has different polar and dispersive components of the surface tension as listed in **Table 2-1**, was measured with the sessile drop method, using a Krüss DSA100 drop shape analyzer (Krüss, Germany). Values are reported as average ± standard deviation, of at least 5 droplets of each liquid on each sample.

Table 2-1. Dispersive and polar components of the surface tension of probe liquids used to measure the surface energy of FDTS-coated samples [69], [70]. $\boldsymbol{\gamma_L^D}$ and $\boldsymbol{\gamma_L^P}$ are the dispersive and the polar components, respectively, of the surface tension, $\boldsymbol{\gamma_L}$.

Liquid	Surface tension (mN/m)		
	$\boldsymbol{\gamma_L^D}$	$\boldsymbol{\gamma_L^P}$	$\boldsymbol{\gamma_L}$
Water	21.8	51.0	72.8
Diiodomethane	50.8	2.3	48.5
Benzyl alcohol	30.3	8.7	39.0

2.3 Fabrication of Si masters

Full wafer-scale nanopatterning was achieved by the DUV stepper, as shown in the photograph of a 6” Si wafer with resist after exposure and development (**Figure 2-1**). During the initial work using the “9stripes” reticle, it was quickly discovered that different types of structures required exposure doses ranging from 270 – 1020 J/m^2, in order to get well-defined patterns. The optimal doses, defined as the dose that gave a width (diameter) closest to the nominal values on the reticle after a 5x reduction, are listed in **Table 2-2**. In general, fields on the reticle with the smallest width and largest spacing between features required a larger exposure dose. In addition, the features appeared as circular holes in the resist, even though they were defined as squares on the reticle. Therefore, the “width” of features on the reticle will be referred to as “diameter” in the resist and subsequent replication by electroplating and injection molding. SEM micrographs of resist patterns exposed with the optimal doses are displayed in **Figure A-6**.

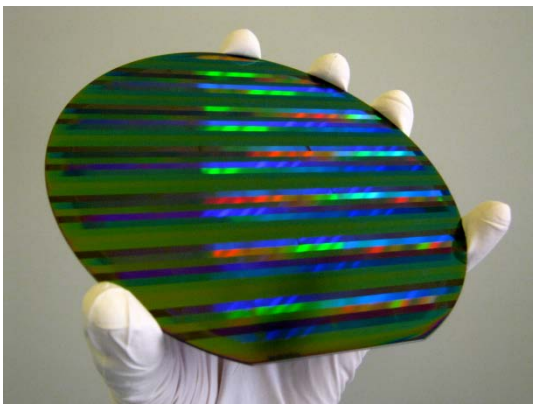

Figure 2-1. Photograph of a 6" silicon wafer with resist patterned by the DUV stepper, using motifs from the reticle "*9stripes*".

Table 2-2. Optimal exposure doses, determined for each type of structure contained on the reticle "*9stripes*". The nominal dimensions after 5x reduction by the projection system are listed next to the dimensions of holes in resist after development measured by SEM, given as the average value ± standard deviation. In general, the fields with small width and/or large spacing required a higher exposure dose.

	Nominal dimensions			**Measured dimensions**		**Exposure dose [J/cm2]**
Field	**Width [nm]**	**Spacing [nm]**	**Pitch [nm]**	**Width [nm]**	**Spacing [nm]**	
1/9	160	320	480	179±15	301	1020
2	160	160	320	190±14	130	800
3	240	140	380	239±11	141	270
4	240	240	480	242±7	238	300
5	240	480	720	239±11	481	410
6	200	140	340	201±12	139	400
7	200	200	400	199±10	201	440
8	160	140	300	-	-	-

Part of the motivation behind using the "*9stripes*" reticle was to establish a resolution limit for the lowest hole diameter and spacing that could be achieved with the DUV stepper. **Figure 2-2** shows SEM micrographs of some of the smallest features on the mask that could be achieved after exposure and development. Field 8, with a nominal diameter of 160 nm and a spacing of 140 nm, could not be defined for any exposure dose (**a**). For structures with a nominal diameter of 160 nm and a spacing of 160 nm and 320 nm (Fields 2 and 1/9, **b** and **c**), it was possible to get well-defined patterns in the resist only if they were overexposed, giving a minimum hole diameter of about 180 nm and 190 nm, respectively. In addition, underexposure of field 6 with a nominal diameter of 200 nm, gave a diameter of about 180 nm (**d**). Finally, the spacing between larger features could be reduced down to about 80 nm by overexposure (Field 3, **e**). In general, the resist pattern for the smallest features was more sensitive to variations in the exposure dose, making the process window very narrow. In addition, it was also observed that the diameter had a spatial variation across the exposed chips.

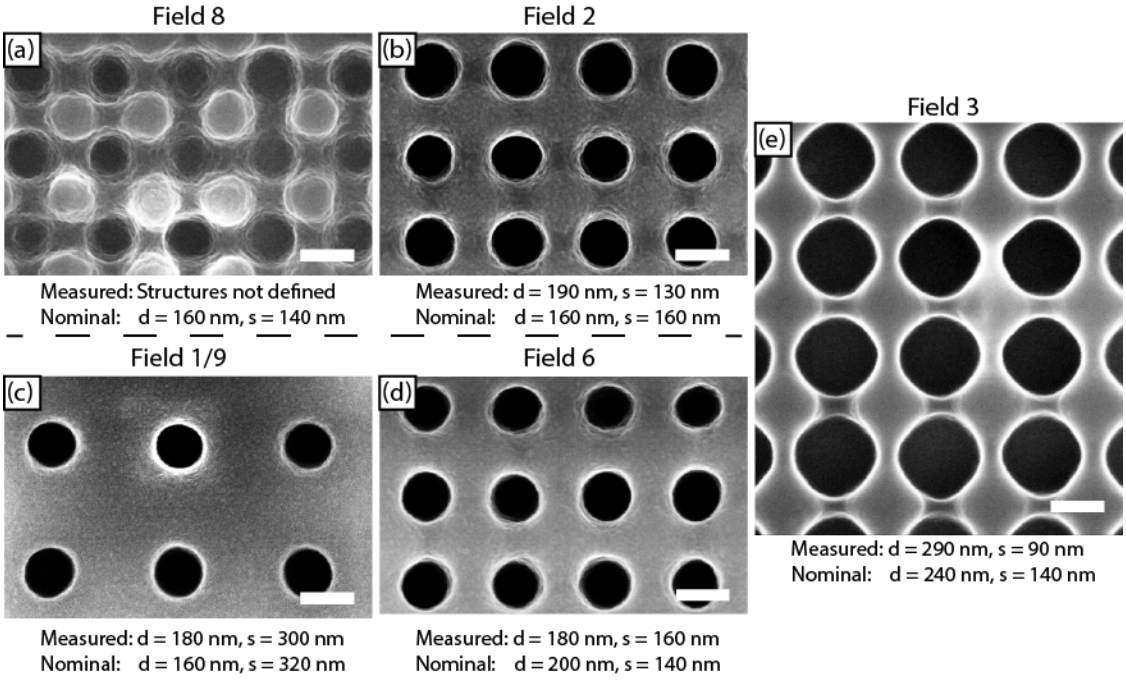

Figure 2-2. SEM micrographs of patterns in DUV resist after development with feature size below 200 nm. (**a**) Holes using reticle field 8 (160/300 nm) could not be clearly defined. (**b, c**) Holes in field 2 and 1/9 (nominal dimensions: 160/320 nm and 160/480 nm) could only be defined by overexposure (dose: 800 J/m^2 and 1020 J/m^2), leading to holes with a diameter down to 180 nm and a minimal spacing of 130 nm could be defined. (**d**) With underexposure (380 J/m^2) of field 6 (200/340 nm), holes with a diameter and spacing of 180 nm and 160 nm respectively, could be defined. (**e**) By overexposure (320 J/m^2) of field 3 (240/380 nm), the spacing between holes could be pushed down to about 80 nm. Error bars are 250 nm.

An AFM topography micrograph of holes in the DUV resist on Si after exposure and development (240/720, field 5) is shown in **Figure 2-3**. On average, the depth was measured to be 330 nm, slightly lower than the expected resist thickness after spin-coating of 360 nm.

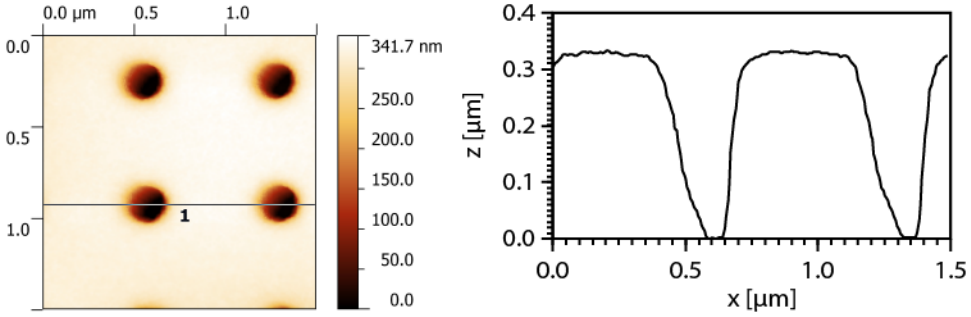

Figure 2-3. AFM topography micrograph of holes in DUV resist (240/720, field 5) after exposure and development. The average hole depth was measured to be 330 nm.

In order to pattern large nanopatterned continuous areas, it was desirable to expose the individual parts of the reticle independently, since it was discovered that the different structures required widely different exposure doses. This was achieved by using shutter blades, to block certain parts of the reticle from being exposed. However, it was discovered that the position of the blades had an inaccuracy of about ± 100 µm,

as well as having a certain edge roughness. Therefore, it was decided to make a second design, *"16Box"*, which contained 16 different types of structures separated by a chromium frame of 1000 µm width. To be able to increase the density of features, while maintaining the minimum spacing of 700 nm required by the mask writing process, the features were defined as hexagons instead of squares, and placed in a hexagonal array.

The flexibility of patterning nm-scale features over cm^2 areas was demonstrated as shown in **Figure 2-4**, where patterns from the resist were transferred to a 6" Si wafer by dry etching. The center of the wafer contains four rectangular areas that each consist of a 2x10 array of chips from fields 9, 10, 11, 13, with average hole diameters after etching of 251 nm, 249 nm, 255 nm, and 268 nm respectively as measured by SEM, as well as test structures (field 16), stitched together.

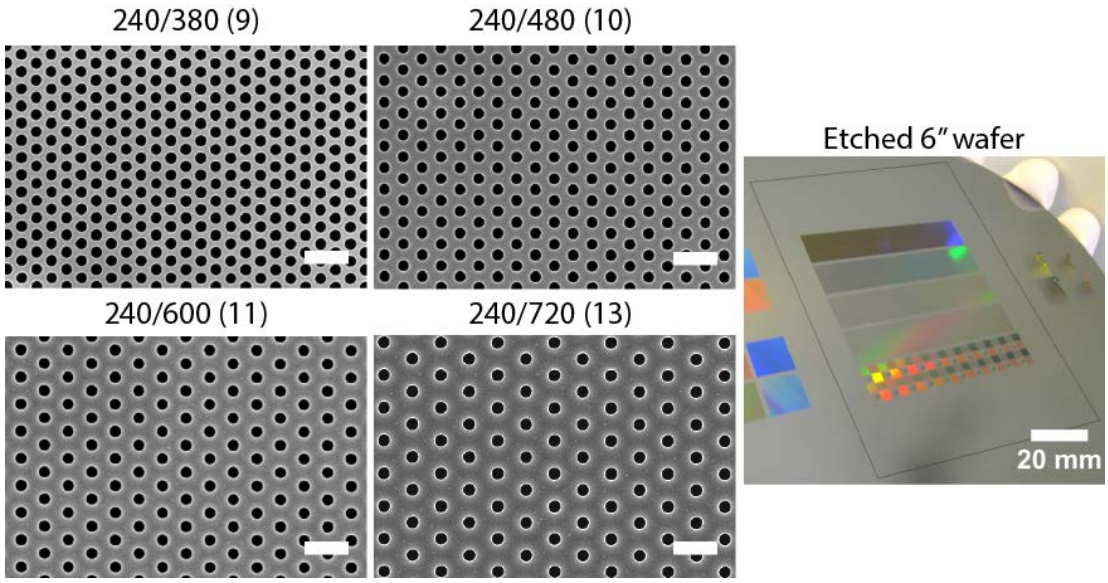

Figure 2-4. Left: SEM micrographs of homogeneous 240 nm patterns from the "16Box" reticle, etched into silicon by reactive-ion etching. Scale bars are 1 µm. **Right:** A photograph of the etched Si wafer with rectangular fields (10.5x52.5 mm^2), comprised of 2x10 arrays of chips stitched together, patterned with structures from different parts of the reticle. The stipulated line indicates the position of the mold inlay that was later cut out from the electroplated shim.

The depth of holes etched into silicon from the 240/380 nm pattern (field 9) was 474 nm as measured by AFM (**Figure 2-5**). The depth of holes from the other patterns was also measured, although it was not possible to reach the bottom due to convolution of the cantilever tip.

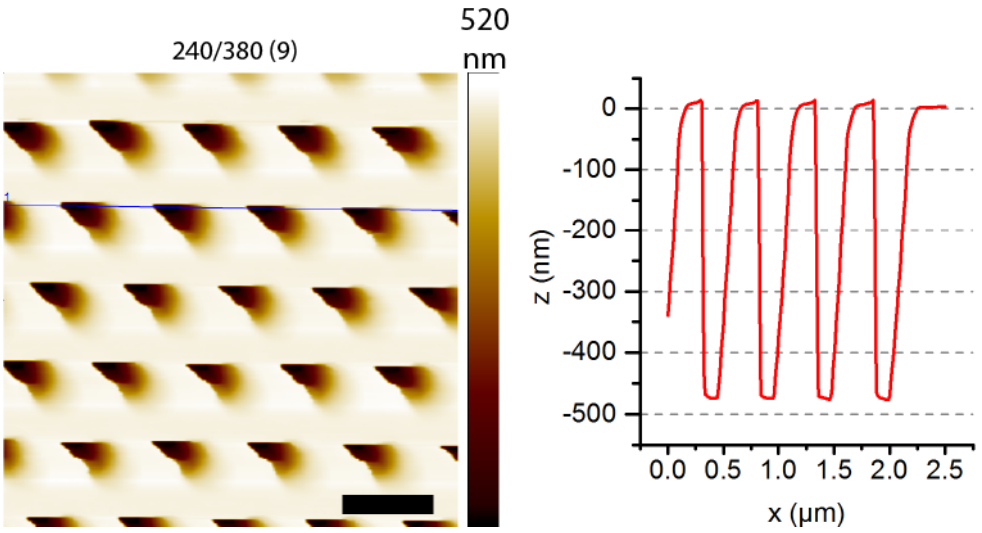

Figure 2-5. AFM topography micrograph and line profile of 240/380 nm pattern after silicon etching. The average hole depth was measured to be 474 nm. The scale bar is 500 nm and the vertical color scale is 520 nm.

For the development of large, continuous nanoscale patterns for cell cultureware, it was important to achieve a high positioning accuracy of individual chips. The interface of two neighboring exposure fields stitched together is marked by the stipulated line in **Figure 2-6** (image is from the electroplated Ni shim). The diameter of features at the interface were larger compared to the rest, due to a higher total exposure dose by the overlapping fields. The stitching error was determined as the offset in the center to center distance, measured from line profiles drawn across features in a direction perpendicular to the interface. A minimal stitching error of about 41 nm was found, although this varied from wafer to wafer.

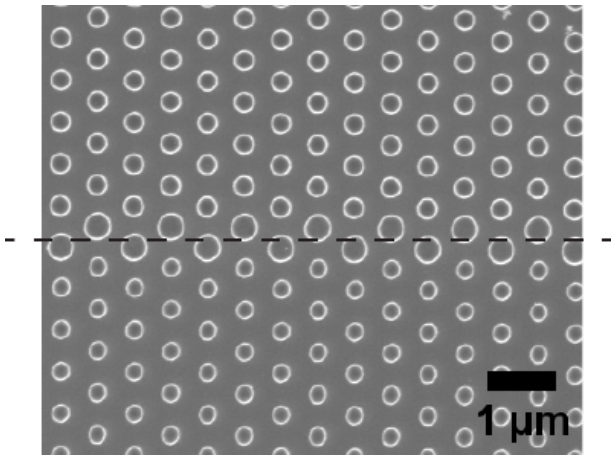

Figure 2-6. SEM micrograph of two neighboring chips stitched together at a position approximately where the dashed line is drawn. The stitching error, determined as the offset in vertical pitch (center to center distance) was on average 41 nm.

While the exposure was homogeneous across large areas for features with a nominal diameter of 240 nm and larger, spatial inhomogeneity in the pattern was observed for features with a diameter of 200 nm and a spacing of 140 nm (200/340, field 3, **Figure 2-7**). Along the indicated line, the diameter increased gradually from 195 nm to 230 nm. This patterned was periodic with a frequency of 65 µm across the exposed area. The same phenomenon was also observed for 240 nm features

underexposed to give a sub-200 nm diameter, as well as features with a nominal diameter of 180 nm and the same spacing (180/320 nm, field 1), where the pattern was even more inhomogeneous due to the narrow process window.

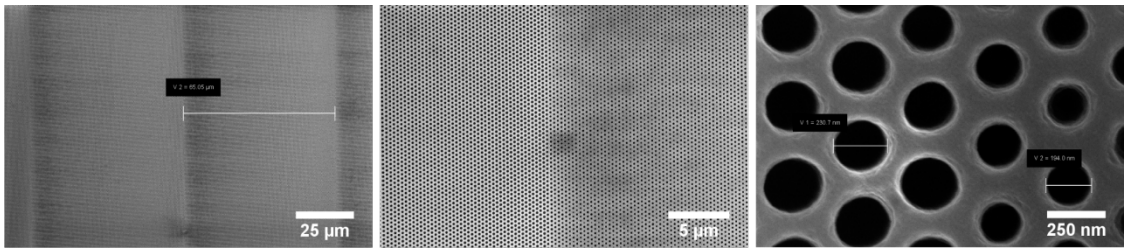

Figure 2-7. SEM micrographs of 200/340 nm patterns in DUV exposed resist (field 3, *"16Box"* reticle). The measured diameter of holes varied gradually between 195 nm and 230 nm, and was repeated with a spatial frequency of 65 µm. This inhomogeneity was also observed for the 180/320 nm pattern (field 1). Images provided by NIL Technology.

2.4 Electroplating of Ni shims

Fabrication of the first Ni shims was done by electroplating from NiV sputter-coated on DUV resist after development. After plating, the shim easily separated from the Si wafer due to thermal stress occurring when the shim, still warm from the electroplating bath, was rinsed with cold water. Some of the resist was transferred to the Ni shim after separation, and was subsequently removed by plasma ashing, although some parts of the patterned areas were damaged during the mechanical separation (**Figure A-7**).

SEM micrographs of some of the nanostructures transferred to Ni are shown in **Figure 2-8**. Hollow nanopillars were observed on several of the plated shims, with a slightly smaller diameter compared to those pillars with a flat top. In some areas the pillars were either partially or completely removed from the surface (**d).** The non-uniformity of pillars was in general worse for the smallest structures (**f,** field 7). This structure had on average a lower protrusion height (197 nm) as measured by AFM (**Figure A-8**) compared to the other structures, which had an average height of around 275 nm (fields 2 and 6), 290 nm (field 3), and 327 nm (field 5), which was close to the depth of holes measured in the resist (**Figure 2-3**). On certain occasions, NiV delaminated from the resist during the plating process causing large holes in the shim, while when it was electroplated from NiV on etched Si, some large patches of the nanostructured areas was gone after the Si wafer had been etched away (**Figure A-9**).

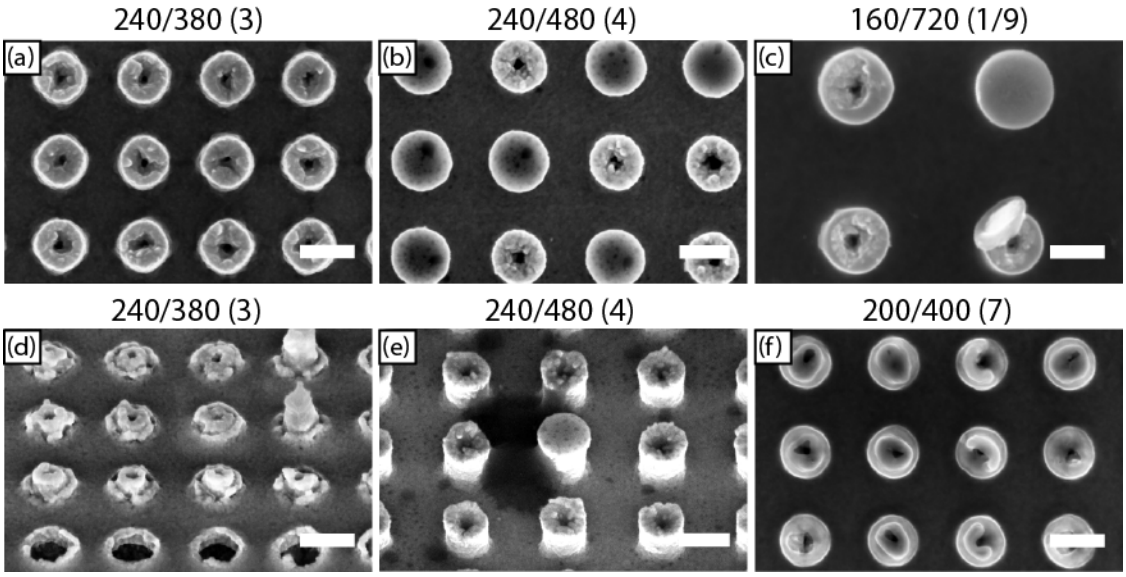

Figure 2-8. SEM micrographs of hollow nanopillars (**a-f**) on Ni shims electroplated from resist sputter coated with a layer of 130 nm NiV. Some of the protruding pillars had a flat top with a larger diameter than the hollow ones (300 *vs.* 270 nm) (**b, e**), while some pillars reveal a hollow structure beneath the flat top (**c,** diameter larger than nominal value due to overexposure of resist). In some areas, the pillars had been partially or completely delaminated from the surface of the shim (**d**). Ni pillars electroplated from resist patterns with smaller hole diameter, were lower and with a narrow top. The scale bars are 250 nm.

Due to the problems with delamination and hollow nanopillars, the material for the seed layer was instead changed to Cr (~10 nm) and Au (~60 nm). After this, the plating of Ni shims was significantly improved. **Figure 2-9** shows a photograph of a laser-cut shim plated from a similar master to that shown in **Figure 2-4**. SEM micrographs in **Figure 2-10** show the protruding Ni pillars with an average diameter of 263 nm, 257 nm, 275, and 291 nm for field 9, 10, 11, and 13 respectively. The height of pillars in field 10, 11, and 13 was 484 nm, 483 nm, and 472 nm as measured by AFM, which was essentially the same as the depth of holes in the etched silicon master (474 nm, **Figure 2-5**), corresponding to an aspect ratio of around 1.8. The results of replication by injection molding using this shim are presented in **Section 0**.

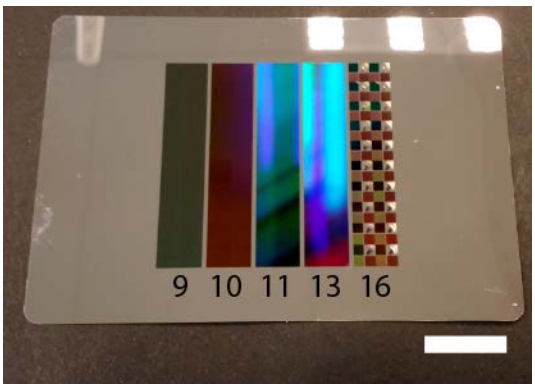

Figure 2-9. Photograph of a laser-cut Ni shim for molding polymer replicas in microtiter plate, plated from the Si master shown in **Figure 2-4**. The nanostructures are numbered according to the different areas on the reticle in **Figure A-2**. The indicated scale bar is 20 mm.

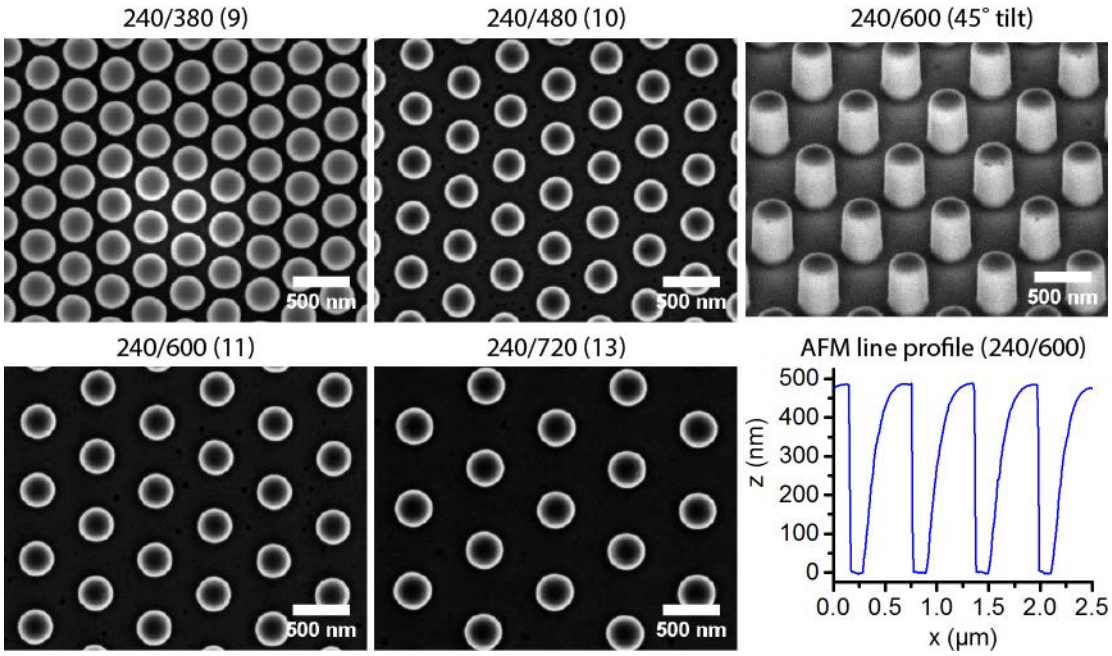

Figure 2-10. SEM micrographs of nanostructures (top-view and 45° stage tilt) on Ni shim electroplated from Cr/Au seed layer sputter-coated on etched Si. The structures are annotated by nominal values of diameter/pitch defined after 5x reduction in the reticle design (**Figure A-2**). A line profile drawn across Ni protrusions from an AFM scan is included in the bottom right.

2.5 Patterning of HSQ films on steel molds

Figure 2-11 shows the electroplated Ni mold (**a**) that was plated from etched Si patterned by the DUV stepper using a different reticle provided by InMold Biosystems, and the imprinted HSQ film on a stainless steel substrate (**b**). The presented pattern consists of squares in a checkerboard pattern with a nominal width of 500 nm and with a periodicity of 1000 nm. The equivalent square side length from grain analysis of the SEM images gave an average hole width in Ni and HSQ of 334 nm and 394 nm respectively. The structures in HSQ had more rounded edges due to

the different fabrication processes between the two molds. Charging effects were observed during SEM imaging of the HSQ film due to its low electrical conductivity leading to reduced image contrast. The average HSQ film thickness in the patterned area was ~500 nm as measured by optical reflectometry.

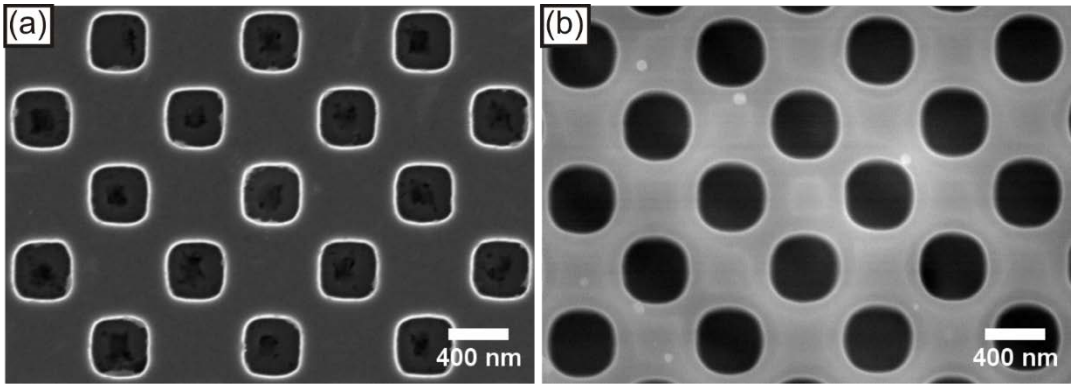

Figure 2-11. SEM micrographs of hole arrays in (**a**) the Ni shim and (**b**) the HSQ/steel mold insert.

Figure 2-12 shows AFM topography micrographs of the Ni mold (**a**), the elastomeric stamp obtained by casting (**b**), and the imprinted HSQ surface (**c**). The color scale was inverted for the elastomeric stamp respective to the Ni and HSQ molds, as it contains protruding pillars instead of holes. The average hole depth in Ni was measured to be 397 nm, while the average pillar height on the elastomeric stamp was measured to be 367 nm, a reduction of about 8% from the nominal height expected for full replication. Furthermore, the depth of holes in HSQ was measured to be 325 nm, which was a reduction of about 11% relative to the height of elastomeric pillars, and 18% relative to the hole depth in Ni. Similarly, the pitch distance of the patterns on the stamp was measured to be 956 nm, which is a reduction of about 4% relative to Ni. The pitch distance in HSQ was 953 nm, which is almost the same as for the stamp.

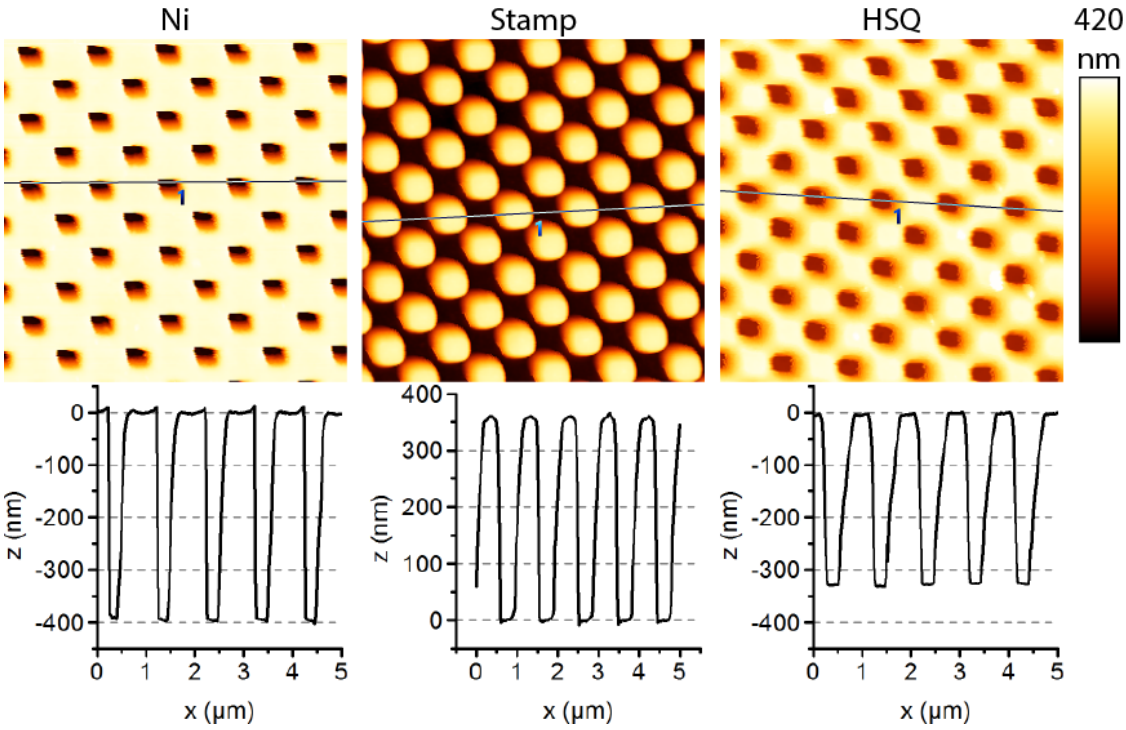

Figure 2-12. AFM topography micrograph of holes in the Ni mold, pillars on the elastomeric stamp, and imprinted holes in the HSQ mold. The color scale for the elastomeric stamp micrograph was inverted with respect to the Ni and HSQ molds. The average step height for holes/pillars was measured to be 397 nm, 367 nm, and 325 nm for the Ni mold, elastomeric stamp, and HSQ mold respectively.

2.6 Anti-stiction coating on mold surfaces

Water contact angles were used to compare the quality of FDTS-coatings on native NiV (n = 7) and NiV coated with Al_2O_3 and SiO_2 by ALD (n = 3) (**Figure 2-13**). The static contact angle was slightly higher for FDTS on the dual-layer coating, compared to native NiV (111.7° *vs.* 97.1°). However a large variation of the FDTS quality was observed on NiV, with contact angles ranging from 75° to 105°. The advancing contact angle was comparable, while the largest difference was observed for the receding angle, which was 65.9° for FDTS on native NiV compared to 96.2° for the dual-layer coating. Thus, there was a contact angle hysteresis of 50.0° and 14.6° for the two surfaces respectively.

Furthermore, contact angles measured with three probe liquids having different polarity and surface tension (**Table 2-1**), was measured on FDTS applied on native NiV, NiV- Al_2O_3-SiO_2, a Si wafer, and HSQ after thermal curing (**Table 2-3**). In addition, contact angles on native TOPAS 8007 and PS was measured for comparison. Contact angles of diiodomethane (~99°) and benzyl alcohol (~86°) were similar for all surfaces with FDTS. With water, however, the contact angle on NiV-FDTS was only 77.3°, while the contact angle on FDTS on Si, HSQ, and silica-coated NiV shim were notably higher. This could be related to the varying FDTS quality on NiV as previously mentioned.

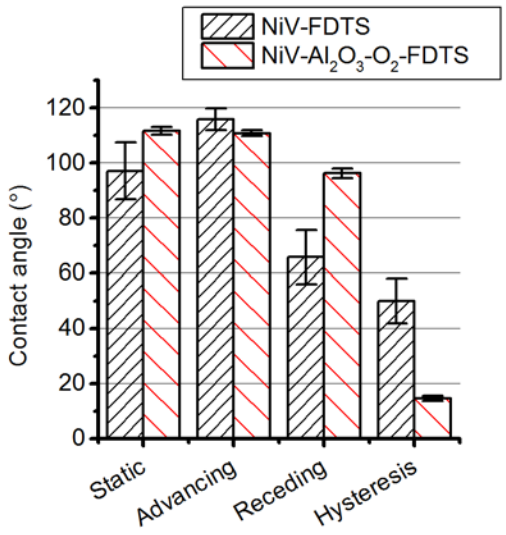

Figure 2-13. Static, advancing, receding, and contact angle hysteresis of water measured on native NiV and NiV coated with Al_2O_3 and SiO_2 by ALD. Error bars indicate the standard deviation (n=7 and n=3 respectively).

The lowest estimated surface energy was found on FDTS-coated Si and FDTS-coated NiV-Al_2O_3-SiO_2 (**Table 2-4**). Due to the low water contact angle measured on NiV-FDTS, the surface energy was estimated to be almost three times larger, with a dominating polar component. Furthermore, the surface energies of TOPAS and PS were noticeably higher, even though they also had a high water contact angle.

Contact angle measurements revealed no substantial difference between Ni coated with SiO2 using the Lesker system followed by MVD, or Ni coated with the Al_2O_3-SiO_2-FDTS trilayer using ALD and CVD (data not shown). However, ALD-coating was the preferred choice due its ability to achieve a very homogeneous film thickness on shim nanostructures.

Table 2-3. Static contact angles of water, diiodomethane, and benzyl alcohol on different substrates with FDTS-coating. In addition, contact angles on TOPAS 8007 and PS are shown for comparison (benzyl alcohol contact angle was too low to be measured).

	Contact angle, θ (°)		
Material	**Water**	**Diiodomethane**	**Benzyl alcohol**
NiV-FDTS	77.3±2.6	99.7±2.6	85.2±1.2
NiV-Al_2O_3-SiO_2-FDTS	115.2±0.9	98.5±1.8	85.9±1.1
Si-FDTS	109.0±0.9	98.0±1.1	85.4±0.4
Steel – HSQ – FDTS	115.4±1.8	102.2±1.5	90.4±3.2
TOPAS 8007	95.7±3.8	37.9±3.1	-
PS	92.5±1.8	27.9±3.1	-

Table 2-4. Surface energy with polar and dispersive components calculated by Owens-Wendt method, using contact angles from Table 2-3, together with the coefficient of determination, R^2, for the linear regression fit (**Section 0**). R^2 values for TOPAS and PS are not included since only contact angles for two liquids were fitted.

Material	Surface energy (mJ/m2)			
	γ_S^D	γ_S^P	γ_S	R^2
NiV-FDTS	2.2	26.4	28.6	0.98
NiV-Al_2O_3-SiO_2-FDTS	9.4	0.9	10.3	0.91
Si-FDTS	8.3	2.5	10.7	0.99
Steel – HSQ – FDTS	8.3	1.1	9.4	0.99
TOPAS 8007	41.5	0.1	41.6	-
PS	45.9	0.2	46.1	-

2.7 Discussion

The spatial resolution of optical lithography exposure systems is often linked to the Rayleigh criterion [71], which is defined as the minimum distance *d* between two point sources in the object plane that can be distinguished in the image plane for light with a wavelength λ and numerical aperture *NA*

$$d = 0.61\frac{\lambda}{NA} \quad \textbf{(2-1)}$$

For the DUV stepper system with λ = 248 nm and NA = 0.6, the Rayleigh resolution is therefore about 250 nm. The overlapping intensity profiles of the Fraunhofer diffraction patterns (far field) for light from a point source through two neighboring circular apertures, separated by this distance are shown in **Figure 2-14**. However, the resolution of the exposed reticle image is also dependent on the resist contrast, i.e. its ability to distinguish between light and dark portions of the mask. From the producer of the DUV resist, it was informed that the exposure latitude, i.e. the range of exposure dose between overexposure and underexposure relative to the optimal dose, was 14% for lines with 130 nm width and spacing (260 nm pitch), while it was 7% for lines with 110 nm width and spacing (220 nm pitch) [72]. For two objects separated by the distance corresponding to the Rayleigh resolution limit, the summed intensity profile has a local minimum with a 25% lower intensity than the two maxima. This means that features in theory could be resolved even if they are spaced closer together than what the Rayleigh resolution predicts, as long as the relative intensity difference between maxima and minima of the overlapping intensity profiles are larger than the exposure latitude of the resist.

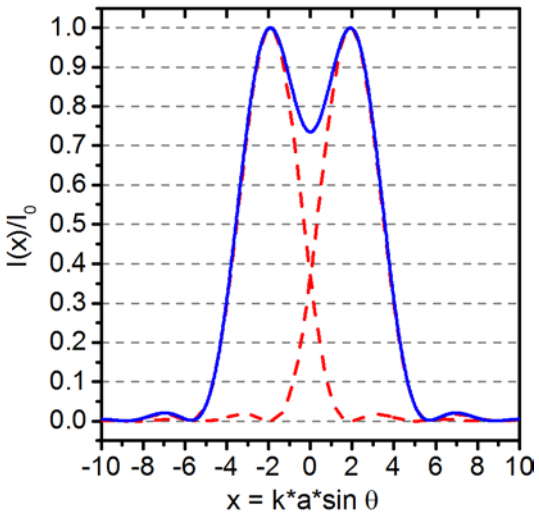

Figure 2-14. The overlapping intensity profiles from Fraunhofer diffraction patterns for two circular apertures separated by a distance corresponding to the Rayleigh resolution criterion.

In practice, however, the optical resolution is worse than the theoretical limit due to several factors such as having a finite size of the illumination source, meaning that the light striking the mask will not be plane waves (spatial coherence), non-uniformity in the illumination intensity, as well as imperfections in the lens system (aberrations). In addition, the resolution will be affected by several process conditions such as wafer roughness and tilt, resist bake temperature, and resist development. SEM micrographs of the smallest features in resist (**Figure 2-2**) shows a partial exposure of the area between holes with a pitch of 320 nm on the resist, because of too much overlap between intensity profiles of adjacent features. By increasing the pitch to 340 nm, the contrast was sufficient to obtain well-defined holes arranged in a square array. Generally, exposure of smaller features resulted in larger variations in the diameter, likely due to the narrower process window of the resist When 1000 nm features were arranged in a hexagonal array with a pitch of 1700 nm on the reticle, producing 200 nm holes on a 340 nm pitch, a systematic variation in the diameter was observed after exposure (**Figure 2-7**). After discussion with the reticle manufacturer (Compugraphics), it was believed that this effect could be due to the mask writing process using a multi-beam brush, which produces a small spatial variation to the critical dimensions. Due to the narrow process window, this variation became more apparent as the feature size approach the resolution limit. Since the DUV resist was positive tone, overexposure led to a widening of holes and therefore spacing down to about 80 nm could be achieved, before overlapping of the intensity profiles of adjacent features on the mask occurred.

As was seen in **Figure 2-8**, electroplating from DUV resist metallized with NiV, led to the formation of hollow and inhomogeneous nanopillars. The quality of replication of the resist pattern is likely highly dependent on the sputter coating process, since the thickness of the seed layer was comparable to the hole diameter in the master. Target atoms arrive at the substrates in a wide range of angles. Due to geometry of the structures, more material will be deposited at convex corners since a wider range of arrival angles are possible leading to cusping, while only those atoms that have a close to vertical direction will reach the bottom of holes (**Figure 2-15**) [73]. As the layer thickness at the edge of the holes grows disproportionally, the opening of the holes becomes smaller, which further reduces the amount of material deposited at

the bottom of holes. At some point, the growing edges may close off the hole and form an empty void, which in the case of the Ni shim leads to hollow pillars. This effect is expectedly worse for structures with smaller diameter (higher aspect ratio). Since the thickness of the deposited NiV seed layer was estimated to be 130 nm on a horizontal surface, this is a likely explanation. It should be noted, however, that measurements of sputter deposition rates were performed on flat silicon wafers. The deposition rate might be lower on the DUV resist, especially if some of the target atoms have energy high enough to sputter etch the substrate. After the seed material was changed to Cr and Au, hollow nanopillars on the shims were no longer observed, neither for holes in resist nor for holes in silicon with an aspect ratio of up to 1.8. As the total thickness of the sputtered layer was changed from about 130 nm to 70 nm at the same time, it is not possible to derive whether one seed material were better than the other, although a thinner seed layer would be expected to reduce the effect of cusping. The uniformity of the seed layer may be further improved by applying a DC bias to the wafer chuck, in order to allow plasma etching of the substrate, preferably reducing material overhang and allow re-deposition of material on vertical sidewalls.

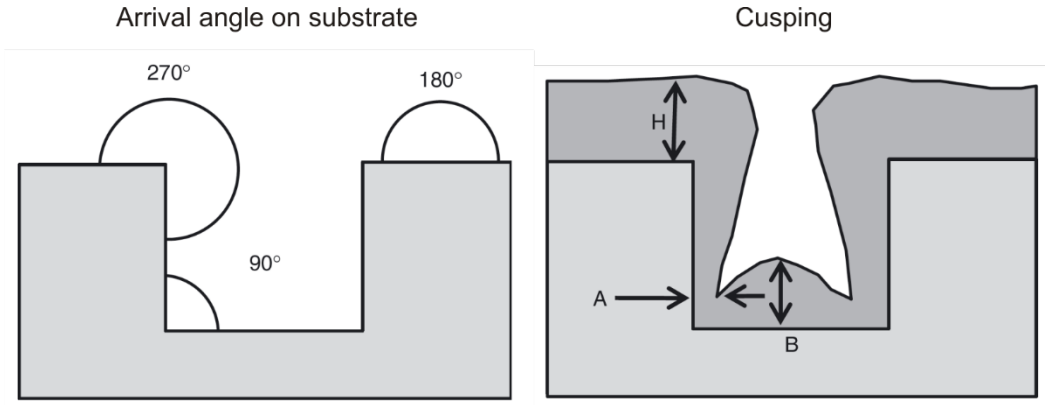

Figure 2-15. Left: The range of possible arrival angles of atoms deposited by sputter coating are generally higher at convex and lower at concave corners compared to a horizontal surface. **Right:** Because sputter coating leads to a wide distribution of arrival angles, the film thickness at sidewalls (A) and at bottom (B) of holes are lower than on a horizontal surface (H), leading to cusping. Reproduced from [73].

Some of the failed productions of Ni shims shown in **Figure A-9** were likely caused by delamination of the NiV seed layer due to poor adhesion to resist. In addition, removal of some of the structured areas during separation from one of the etched silicon master may suggest a poor adhesion between NiV and electroplated Ni, possibly caused by surface contamination between sputter coating and plating. After the seed material was changed, no delamination was observed on shims was observed, possibly because gold has a high electrical conductivity and a high resistance against oxidation, which is beneficial for the electroplating process.

In **Section 2.5** it was observed that DUV-defined patterns were transferred to the HSQ film through imprinting by an intermediate elastomeric stamp. However, holes in HSQ had slightly different dimensions compared to the Ni mold, with the depth being 18% smaller and the width being 18% larger. The change in dimensions could be attributed to the two extra replication steps that were employed in order to make HSQ molds with similar patterns as the electroplated Ni shims. Shrinkage of the elastomer stamp was observed during thermal crosslinking, leading to a reduction of 7.6% of the protrusion height on the stamp relative to the depth of holes on the Ni mold. In addition, a 7% shrinkage for HSQ films shrink curing at 450 °C has been

reported [74]. This gives in total a shrinkage of 15%, which is similar to the 18% that was observed.

Another reason for why the imprint depth in the HSQ might be lower than the height of pillars in the stamp could be the compressive forces required to displace the HSQ monomer. Elastomers are often considered incompressible, having a Poisson's ratio of ~ 0.5 [75]. This means that a compressive force acting perpendicular to the top plane of pillars on the stamp during imprinting, leading to a height reduction of 5%, should be accompanied by an increase in the lateral width by 2.5% due to conservation of volume. However, the width of holes in HSQ was 18% larger than for Ni, which means that the increase in lateral size cannot be explained by compression during imprinting alone. In addition, the imprinted squares appeared more rounded in HSQ compared to Ni, suggesting that some re-flow of the monomer could be occurring between removal of the stamp and thermal curing, which contributes to the increased hole width. It should, however, be noted that the lateral dimensions that was measured by SEM could be influenced by charging, due to the much lower HSQ film conductivity compared to Ni shims.

Finally, it was demonstrated that coating Ni molds with SiO_2 improved the density of FDTS, demonstrated by a lower surface energy and a low contact angle hysteresis. When FDTS was applied directly to a nickel mold with a NiV seed layer, static water contact angles varied between 75° and 105° and was generally lower compared to that of FDTS on silicon wafers or NiV coated with SiO_2. The large variations on NiV may be due to different levels of contaminations on the shim as they were bought from a commercial supplier, even though all shims were protected by a laminar film, and cleaned with water and oxygen plasma before FDTS-coating. The low receding contact angle and correspondingly large hysteresis on NiV suggests that water was pinned at defects in the FDTS monolayer coating, suggesting that the density was relatively low. This was not surprising as Ni does not readily react with silane chemistry. Deposition of SiO_2 onto Ni molds led to a more dense FDTS monolayer, which were able to shield most of the polar interactions from the underlying substrate.

Other chemical coupling agents than silanes might be suitable for surface modifications on Ni or NiV, such as phosphates, which has been used to demonstrate dense monolayers of a fluorinated alkyl phosphoric acid derivative by wet chemical deposition [76]. Another route might be to use hydridosilane coupling, which have been used to deposit fluorinated monolayers on oxide-free metal substrates [77]. However, this method has not been demonstrated so far on Ni.

2.8 Conclusion

In this chapter, it was shown that large areas on silicon (~100 cm^2) could be patterned with 240 nm holes, and transferred to a Ni shim by electroplating. Hole diameters down to 180 nm in diameter and 340 nm in pitch was reached, although with a large spatial variation in feature size. Holes in the resist metallized with 130 nm NiV by sputter coating, led to hollow pillars during separation of shim and master, but not when holes in etched silicon was metallized with 70 nm of Cr and Au. Furthermore, imprinted HSQ films on stainless steel substrates were fabricated from an elastomeric stamp, although with some loss in lateral and vertical resolution with respect to the master. Finally, it was demonstrated that NiV coated with Al_2O_3 and SiO_2 by ALD and CVD prior to FDTS deposition, led to shielding of polar interactions and a lower

surface energy, compared to FDTS on bare NiV. This might be advantageous for the release of polymer replicas with large-area nanoscale topography, as well as and protein transfer from mold to replica, which will be discussed in the next chapters.

Chapter 3

Replication of Nanostructures by Injection Molding

3.1 Introduction

Injection molding has been the preferred industrial process for polymer shaping for decades due to low cycle times and the multitude of technologies established for full process automation [78], [79]. Considerable know-how and experience is established on replication on the macroscopic scale using this technique. During the last two decades this knowledge base has been extended to replication of micro- and nanoscale features. A wide range of applications has been explored including microfluidic devices [22], [80], diffractive optical elements [48], anti-reflective surfaces [64], superhydrophobic surfaces [81]–[83], and functional cell culture substrates [35]–[37], [84]. Commercial injection molding is routinely used to replicate features with details down to 150 nm in the case of Blu-Ray discs, while replication demonstrating lateral resolution as low as 5 nm has been demonstrated in research

[47], [62], [63], [85]–[87]. This suggests that the lower limit of replication is determined by the structural detail of the mold surface.

Replication of nanoscale features is more challenging when targeting height-to-width aspect ratios above 1. A limiting factor in the replication of higher aspect ratio structures is the rapid formation of a solidified skin layer after the hot polymer melt contacts the cold mold surface [49], resulting in a significant increase in the flow resistance inside micro- and nano-scale cavities due to the high viscosity. A general strategy for improving replication of high aspect-ratio features is to increase the melt and mold temperature as well as the injection speed, which reduces the thickness of the skin layer formed prior to filling of the cavity. Additionally, high injection pressures also help to force the melt into cavities even after skin formation [62], [63], [88], [89]

The most important factor for achieving good replication appears to be the mold temperature, $T_{mold,}$ [63], [86], [88] that often needs to be above the glass-transition temperature, T_g, of the polymer for replicating high aspect ratio structures [90], [91]. This calls for the use of a variothermal process, i.e. active heating and cooling of the mold with each replication cycle. The main disadvantage is longer process cycle times: While conventional injection molding uses cycle times from 4-30 s, variothermal processes may require 100-300 s for each replication [90]. The repeated thermal cycling can also lead to lower mold lifetime due to thermal stresses [91], as well as higher energy consumption, which both contribute to overall higher production costs.

Several authors have reported on methods to reduce the thermal cycling time for variothermal processes. These involves heating of the stamper material itself by electrical (Joule heating) [92]–[94] or induction heating [95], [96]. Other methods involve external heating of the stamper surface, such as infrared heating [97], [98] or steam heating [99]. Laser-heating of the mold has been used to achieve extremely rapid mold heating (300 °C/s) [100], although the heated area was rather small and inhomogeneous. Although several of these methods have demonstrated cycle times comparable to conventional injection molding, they add complexity to the mold and the machine, making it more expensive to set up and maintain a production line.

A simpler alternative to variothermal processes involves the use of heat retardant materials to impede the heat transfer from the polymer melt to the cold mold. Nickel shims formed by electroplating from a metallized silicon master have become the standard insert material for micro- and nano-replication, due to its ease of replication and good durability [22], [48]. Nickel has a high thermal conductivity like most other metals, which leads to fast heat dissipation from the polymer melt during mold filling and rapid formation of a solidified polymer skin layer. Adding a heat-insulating plate on the backside of a nickel shim has been shown to slow the heat transfer resulting in increased replication quality [101], [102]. Likewise, a polymer foil covering one of the mold halves allowed fabrication of high-aspect ratio microcantilevers through an isothermal process [103]. Furthermore, polymeric stampers with imprinted micro- [104] and nano-structures [105] showed improved filling at low mold temperatures compared to a nickel stamper. Although these examples demonstrated impressive replication without the need for a variothermal process, they are likely not suitable for high-volume production as the mold materials used lack the mechanical durability that is required in an industrial setting.

In this chapter, nanoreplication in COC polymer using both Ni and HSQ/steel mold inlays derived from DUV stepper lithography, will be demonstrated. It is shown that an isothermal process with $T_{mold} = T_g - 10$ °C of the polymer, results in holes with an aspect ratio from 0.3 – 1.2, when the spacing between 260-290 nm wide protrusions on the surface increase from 120 to 430 nm. With a variothermal mold cycling using

T_{mold} = T_g + 30 °C, full replication of structures with an aspect ratio of 1.8 was achieved for all patterns. Finally, it will be shown that improved filling of nanoscale holes was achieved using heat treated nanopatterned HSQ films under isothermal mold conditions compared to an electroplated nickel shim with an outer chromium/gold coating. Simulation of the heat transfer between polymer melt and mold shows that the HSQ-layer significantly retards the cooling after thermal contact between the materials was established, thus enabling improved nanoscale replication.

3.2 Experimental procedures

3.2.1 Injection molding

Polymer replicas in microtiter plate format (110x75x1 mm^3, **Figure 3-1a**) were injection molded with an Engel e-motion 55 injection molder (Engel, Austria) at the facilities of InMold Biosystems in Høje Taastrup, Denmark, using TOPAS 8007-S04 cyclic olefin copolymer (TOPAS Advanced Polymers, Germany) with T_g of 78 °C. The parameters used for injection molding are summarized in **Table 3-1**. The mold was heated by an external water supply, and the mold temperature (T_{mold}) was kept constant at 70 °C. A holding pressure (P_{hold}) of 700 bar was used, as this was the highest value that could be employed without significant over-packing and creation of flashes at the replica edges. A start-up cycle of at least 30 replicas was run before samples were collected for analysis.

Table 3-1. Experimental parameters for isothermal injection molding using the microtiter format tool.

T_{mold}	T_{melt}	V_{inject}	P_{inject}	P_{hold}	F_{clamp}	t_{hold}	t_{cool}	t_{cycle}
70 °C	270 °C	130 cm^3/s	880 bar	700 bar	550 kN	3 s	30 s	45 s

Polymer replicas in microscope slide format (76.7x26.3x1 mm^3, **Figure 3-1b**) were injection molded with an Engel Victory 80/45 Tech injection molder (Engel, Austria) at the facilities of DTU Danchip, using TOPAS 8007-S04 and TOPAS 5013L-10 cyclic olefin copolymer (TOPAS Advanced Polymers, Germany) with T_g of 78 °C and 134 °C respectively. The parameters used for variothermal injection molding are summarized in **Table 3-2**. The mold parts were heated by heating elements (resistive heating), which was controlled via a feedback loop using a thermistor in each mold half. Cooling was achieved using an external water supply, with the opening/closing of valves for the water supply being controlled by the operating software. The mold temperature was cycled, using a temperature (T_{mold}) of 110 °C (T_g + 30 °C) and 150 °C (T_g + 15 °C) during injection, and a temperature (T_{demold}) of 40 °C (T_g - 40 °C) and 100 °C (T_g - 35 °C) during ejection for the two grades of COC respectively. Mold temperatures higher than 150 °C were not allowed with the current machine configuration. Holding pressures (P_{hold}) of 900 bar and 600 bar for TOPAS 8007 and TOPAS 5013 respectively, were the maximum allowed values while running the machine in automatic mode. A start-up cycle of at least 30 replicas was performed before samples were collected for analysis.

Table 3-2. Parameters for variothermal injection molding with the microscope slide format tool, with TOPAS 8007 (T8007) and TOPAS 5013 (T5013).

Polymer	T_{mold} (°C)	T_{demold} (°C)	T_{melt} (°C)	V_{inject} (cm^3/s)	P_{inject} (bar)	P_{hold} (bar)	F_{clamp} (kN)	t_{hold} (s)	t_{cool} (s)	t_{cycle} (s)
T8007	110	40	250	43	1100	900	450	15	50	147
T5013	150	100	300	43	1500	600	450	10	30	140

Polymer replicas for the demonstration of heat retardation by HSQ/steel molds compared to a Ni mold, were injection molded in TOPAS 8007-S04 in a circular disc format (Ø = 50 mm, t = 2 mm, **Figure 3-2**) using an Engel Victory 80/45 Tech injection molder (Engel, Austria) at the facilities of DTU Danchip. The injection molding parameters used are summarized in **Table 3-3**. The Ni shim was installed with a 1.0 mm steel backplate, while the HSQ/steel insert was installed with a 0.33 mm Ni backplate. Thus, both inlay assemblies had a total thickness of 1.33 mm. The mold temperature was varied from 40 °C - 70 °C in a random sequential order. A start-up cycle of at least 40 replicas was performed between each parameter change before samples were collected for analysis.

Table 3-3. Parameters used for the demonstration of heat retardation of HSQ/steel molds compared to Ni mold, under isothermal injection molding conditions.

T_{mold} (°C)	T_{melt} (°C)	V_{inject} (cm^3/s)	P_{inject} (bar)	P_{hold} (bar)	t_{hold} (s)	t_{cool} (s)	t_{cycle} (s)
40 – 70	250	45	1300	800	10	29	60

3.2.2 Replica analysis

Polymer replicas were sputter coated with a 5 nm Au/Pd alloy (80/20 %) film, using a Balzers SCD 004 sputter coater (50 mm working distance, 0.05 mbar argon, 15 mA, 60 s), before SEM imaging (Zeiss Supra 40 VP, Carl Zeiss, Oberkochen, Germany). Surface topography micrographs were acquired by AFM and analyzed in the same way as described in **Section 2.2.6** (page 14). Unless otherwise noted, topography values are reported as average ± standard deviation.

3.2.3 Mold heat transfer simulations

Finite element modeling of the polymer melt cooling was performed with the COMSOL Multiphysics 4.4 software package (COMSOL, Sweden) by numerically solving the one-dimensional heat equation:

$$\frac{\partial T}{\partial t} - \alpha \frac{\partial^2 T}{\partial x^2} = 0 \tag{3-1}$$

$$\alpha = \frac{k}{\rho c_p} \tag{3-2}$$

where T is the temperature, α the thermal diffusivity, k the thermal conductivity, ρ the mass density, and c_p the specific heat capacity at constant pressure. The initial contact temperature, T, between two semi-infinite bodies at temperature T_1 and T_2,

respectively, can be calculated analytically from their thermal effusivities *e*:

$$T = T_1 + \frac{(T_2 - T_1)e_2}{e_2 + e_1} \tag{3-3}$$

$$e = \left(k\rho c_p\right)^{\frac{1}{2}} \tag{3-4}$$

The material constants used for Cr, Au, Ni, HSQ, stainless steel, and COC are shown in **Table 3-4**, together with the calculated thermal diffusivities and thermal effusivities. All material constants used were values reported at room temperature [106], except the thermal conductivity and heat capacity of COC where values for TOPAS 5013 between 150 °C – 200 °C were used [107]. The outer layer of the mold surface used for injection molding consisted of ~15 nm Cr and ~45 nm Au on top of the bulk electroplated Ni. In the numerical simulations, the outermost two layers were approximated by a single 100 nm thick Au layer, as the chromium layer is extremely thin and has similar thermal transport properties as gold. A boundary probe for the temporal development of the temperature was defined at a location inside the polymer melt at a distance of 50 nm from the mold/melt interface. Perfect thermal contact between the mold and the polymer melt was assumed, with T_{mold} = 70 °C and T_{melt} = 250 °C as initial temperatures. The initial mold temperature of 70 °C was maintained within the mold at a distance of 500 µm from the mold/melt interface, and a symmetry plane was defined within the polymer melt at a distance of 500 µm from the mold/melt interface. No movement of material was included in the simulations, thus heat dissipation by viscous effects was not considered.

Table 3-4. Material constants used for numerical heat transfer analysis in COMSOL.

	Thermal conductivity, k ($W \cdot m^{-1} \cdot K^{-1}$)	**Heat capacity, c_p ($J \cdot kg^{-1} K^{-1}$)**	**Density, ρ ($kg \cdot m^{-3}$)**	**Thermal diffusivity, α ($m^2 \cdot s^{-1}$)**	**Thermal effusivity, e ($W \cdot s^{1/2} \cdot m^{-2} \cdot K^{-1}$)**
Cr	93.7	448	7150	$2.92 \cdot 10^{-5}$	$1.73 \cdot 10^{4}$
Au	317	129	19300	$1.27 \cdot 10^{-4}$	$2.81 \cdot 10^{4}$
Ni	90.7	445	8900	$2.29 \cdot 10^{-5}$	$1.90 \cdot 10^{4}$
HSQ	0.15	730	1400	$1.46 \cdot 10^{-7}$	$3.92 \cdot 10^{2}$
Stainless steel	16.2	500	8000	$4.05 \cdot 10^{-6}$	$8.05 \cdot 10^{3}$
COC	0.21	2200	1003	$9.51 \cdot 10^{-8}$	$6.81 \cdot 10^{2}$

3.3 Results

Parts were injection molded in microtiter plate (**Figure 3-1a**), microscope slide (**Figure 3-1b**), and round disc format (**Figure 3-2**). The different nanostructured areas in the plastic can be seen by structural coloration, caused by interference effects when light was shined upon the surface. Samples were for any given mold temperature injection molded using the maximum injection speed, injection pressure, and holding pressure allowed while running in automated mode. For replicas in microtiter plate format at holding pressures higher than 700 bar using maximum injection velocity, the polymer melt flowed outside the mold cavity. This resulted in flashes, even though the maximum clamping force of the machine were used, which made the polymer replicas stick to the stationary part of the mold and therefore preventing complete ejection.

The maximum injection velocity was also used for injection molding replicas in the microscope slide and round disc format, which was almost 3 times slower than for the microtiter plate replicas. This was due to the differences between the two machines, with the one at InMold Biosystems having an electrical motor, while the machine at DTU Danchip was hydraulic, thus displaying a slower movement of the screw. At high injection and holding pressure, before the onset of flashes, the parts tended to get stuck in the mold cavity around the inlet region, leading to the gate or the sprue being broken when the two mold halves opened. A higher pressure was allowed when using TOPAS 8007, since this grade led to a more elastic sprue part during demolding compared to TOPAS 5013, which meant that this part of the replica was mechanically deformed instead of breaking, thus allowing the machine to run in automatic mode. The structured parts were not macroscopically deformed due to a lower adhesion to the mold in this region of the cavity.

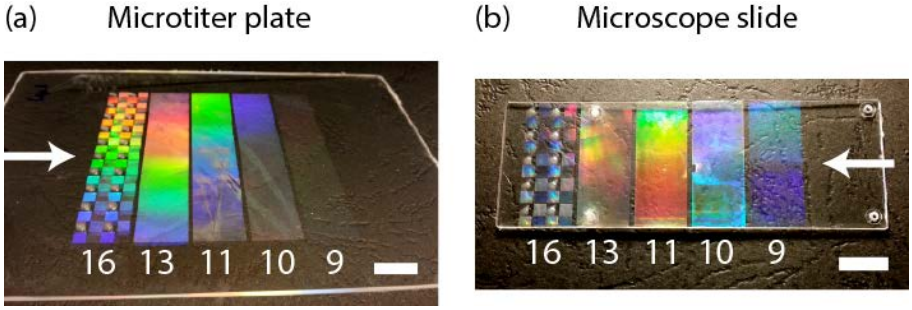

Figure 3-1. Photographs of COC replicas in **(a)** microtiter plate and **(b)** microscope slide format, with nanostructures injection molded from the shim in **Figure 2-9** and **Figure A-10** respectively. The nanostructures are numbered according to the different areas on the reticle in **Figure A-2**. The arrows show the direction of polymer melt being injected into the mold cavity. The scale bars are 10 mm.

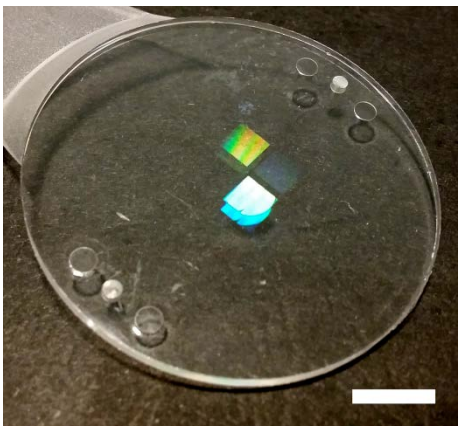

Figure 3-2. Photograph of a COC replicas in circular disc format, used to demonstrate heat retardation with HSQ. The scale bar is 10 mm.

3.3.1 Replication at isothermal injection molding

As mentioned in the introduction, injection molding at a constant mold temperature can significantly shorten production cycle times compared to variothermal processes, as well as being compatible with protein transfer if the temperature is kept low, as will be discussed in further detail in **Chapter 5**. In addition, cycling of the mold temperature was not possible for the microtiter plate format, since the tool could only be heated with the current machine configuration at InMold Biosystems. To achieve as high replication quality as possible, a constant mold temperature just below the glass transition temperature of TOPAS 8007 was chosen (T_{mold} = 70 °C, T_g = 78 °C).

Figure 3-3 shows SEM micrographs of nano-sized holes injection molded against the Ni shim shown in **Figure 2-10**. Images were captured at 12 positions, distributed across an area of (2.6×3.5 cm^2), with origin defined as the geometrical center of the replicas (**Figure 3-1a**). Three different positions evenly distributed along the y-axis, defined as being perpendicular to the melt flow direction (negative x-direction), are displayed for each structure. Replicated holes were very shallow when molded against the area on the shim with the most densely packed features (field 9). As the spacing between features increases, the hole depth appears to increase as seen by the higher image contrast. In addition, holes in some of the images were deformed, especially for field 11 at y = 0 and y = 13.1 mm.

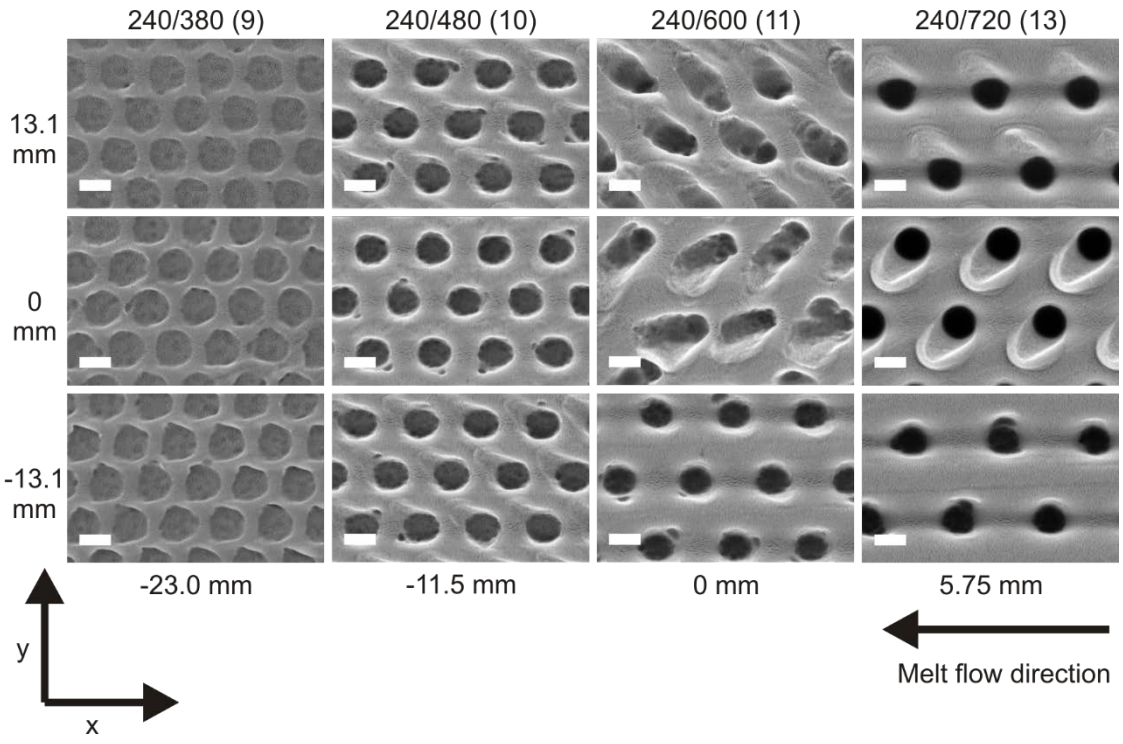

Figure 3-3. SEM micrographs of injection molded nanostructures produced from a Ni shim (**Figure 2-10**) at the facilities of InMold Biosystems, using an isothermal process with T_{mold} = 70 °C. The different structures are annotated as diameter/pitch according to the nominal values in the mask design, with the field number in parenthesis (**Figure A-2**). Qualitatively, the hole depth increased as the spacing between features increased. Severe deformation of the replicated structures was observed especially for field 11. The indicated scale bars are 250 nm.

AFM topography micrographs were obtained for polymer replicas at three positions, separated by at least 6 mm for each field for two individual replicas. Representative scans are shown in **Figure 3-4**, and reveal the same trend as observed with SEM: the replicated holes were deeper, visualized by a darker color, as the spacing between features increased Also, it should be noted that the deformations in these scans were not as severe as those observed in **Figure 3-3**.

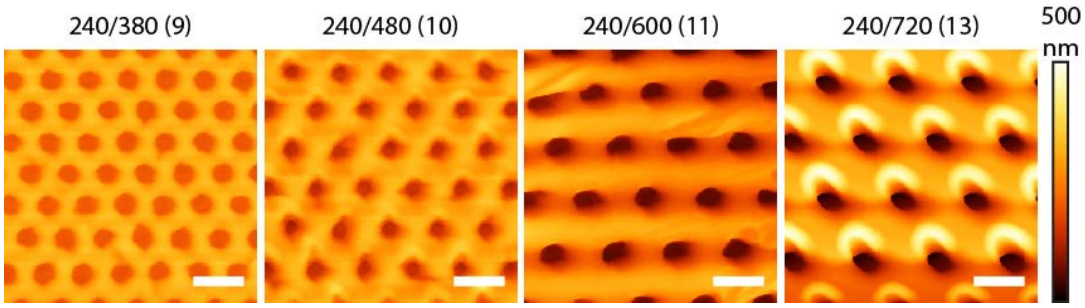

Figure 3-4. AFM topography micrographs of injection molded nanostructures produced from a Ni shim (**Figure 2-10**) at the facilities of InMold Biosystems, using an isothermal process with T_{mold} = 70 °C. The different structures are annotated as diameter/pitch according to the nominal values in the mask design (**Figure A-2**). The hole depth increased (darker color) as the spacing between features increased. The vertical color-scale is 500 nm. The indicated scale bars are 500 nm.

The average hole depth for each field is shown in **Figure 3-5**, together with the nominal height of the Ni shim (483 nm, **Figure 2-10**). For the most densely packed structure (240/380 nm, field 9), which had a replication depth of 74 nm that is only 15% of the protrusion height on the shim, the degree of replication increased with increased spacing. For structures with a pitch of 480 nm, 600 nm, and 720 nm, the depth was 157 nm, 230 nm, and 349 nm, respectively, which corresponds to 33 %, 48 %, and 72 % filling. The corresponding aspect ratio of the holes was 0.3 – 1.2. The error bars, which show the standard deviation of the measured depth, also increase as the total replication depth increases.

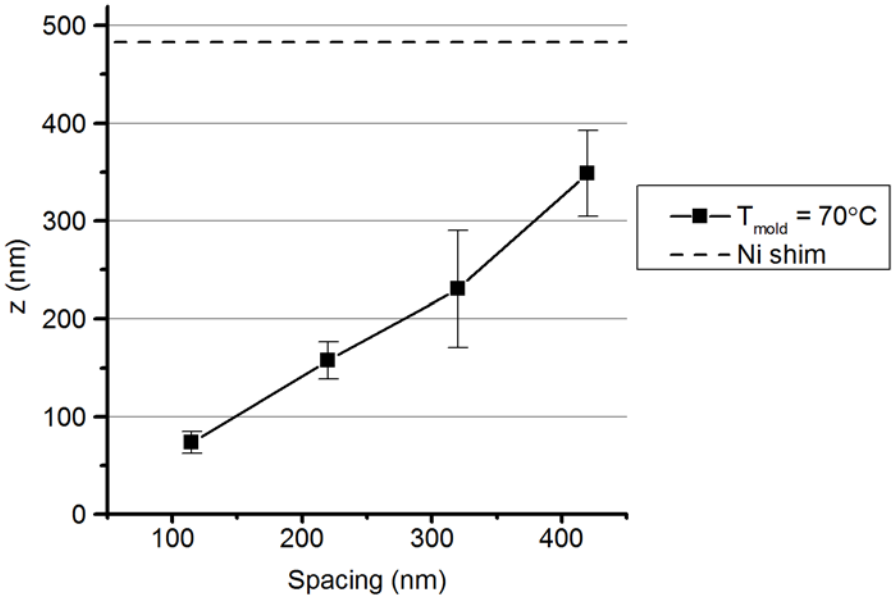

Figure 3-5. Average hole depth as measured by AFM in TOPAS 8007 replicas using an isothermal process with T_{mold} = 70 °C. The nominal height of pillars in the Ni mold (483 nm) is shown as dashed lines (**Figure 2-10**). The hole depth decreases as the spacing between features of similar diameter decreases. The error bars indicate the standard deviation (n=2).

Furthermore, the replication of gratings (300/600 nm, field 16), with axis parallel with and perpendicular to the flow direction of the injected polymer melt was characterized. The measured average step height was 166.0±1.2 nm and 102.0±18.5

nm respectively, for three independent replicas.

3.3.2 Replication with variothermal mold cycling

Based on the results presented so far, it seems that full replication could be achieved at isothermal injection molding, with T_{mold} just below T_g of the polymer; only if the spacing between protrusions on the mold inlay is larger than the diameter and the aspect ratio is lower than 1. For structures with smaller spacing or higher aspect ratio, variothermal processes seems to be required. The first indication of increased replication by using higher mold temperatures, was the stronger interference effect observed for field 9 and 10 (**Figure 3-1b**), compared to replicas injection molded at $T_{mold} < T_g$ (**Figure 3-1a**).

Figure 3-6 shows SEM micrographs of nano-sized holes in TOPAS 8007 microscope slides injection molded against the same Ni inlay **(Figure 2-10)**, using T_{mold} = 110 °C (T_g + 30 °C) and T_{demold} = 40 °C (T_g - 40 °C). Images were captured at 12 positions, distributed across an area of (1.2x3.5 cm^2) with origin in the geometrical center of the microscope slide replicas (**Figure 3-1**). Filling was significantly improved with the use of higher mold temperatures. The deformations earlier observed for structures with a pitch of 600 and 720 nm (fields 11 and 13) were less severe. However, features with 380 and 480 nm pitch (fields 9 and 10) appeared to be more deformed than before. The area “behind” protruding pillars on the Ni shim, were not completely filled for 240/480 nm structures at y = 6.6 mm, or for 240/380 nm. The result was that the topography appeared to be holes with a superimposed ridge pattern, which for the 240/380 nm structure had a width from 70 - 120 nm. Like before, the deformations seemed to have an orientation parallel to the flow direction of polymer melt during the injection phase.

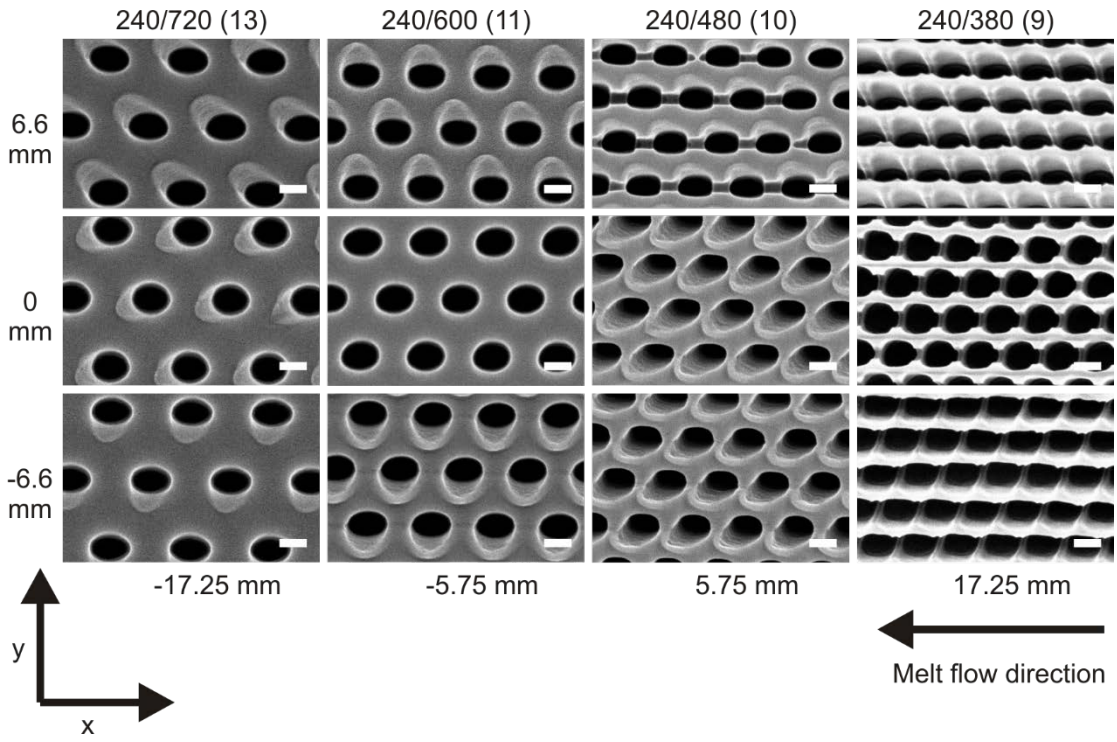

Figure 3-6. SEM micrographs of injection molded nanostructures replicated in TOPAS 8007 produced from a Ni shim (**Figure 2-10**), using a variothermal process with T_{mold} = 110 °C. The different structures are annotated with diameter/pitch according to the nominal values (**Figure A-2**). The position of each image is given relative to the center of the microscope slide replica. The indicated scale bars are 250 nm.

AFM topography micrographs were obtained for polymer replicas fabricated in the same injection molding series at the center of each field (y = 0), and are shown in **Figure 3-7**. The average hole depth was measured to be 483 nm, 486 nm, 491 nm, and 492 nm, for structures with a pitch of 380 nm, 480 nm, 600 nm, and 720 nm, respectively. An overview of the maximum depth/height of holes/pillars measured by AFM for the Si master, the Ni shim, and TOPAS 8007 replicas injection molded using isothermal and variothermal injection molding, is shown in **Table 3-5**.

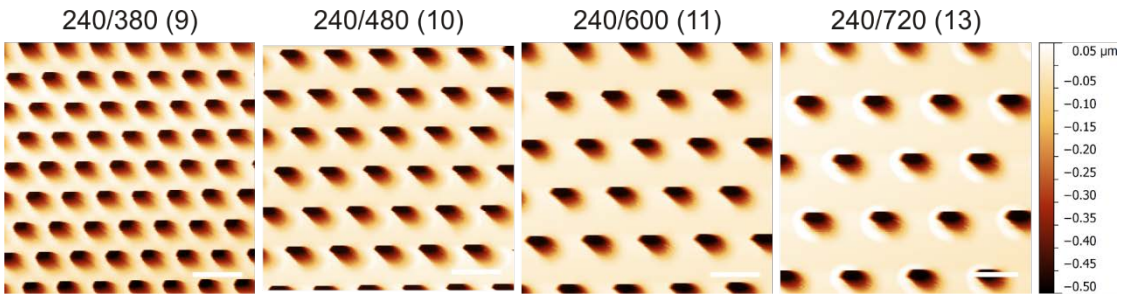

Figure 3-7. AFM topography micrographs of injection molded nanostructures produced from a Ni shim (**Figure 2-10**), using a variothermal process with T_{mold} = 110 °C. The different structures are annotated as diameter/pitch according to the nominal values (**Figure A-2**). The average hole depth was measured to be 483 nm, 486 nm, 491 nm, and 492 nm, for structures with a pitch distance of 380 nm, 480 nm, 600 nm, and 720 nm, respectively. The vertical color-scale is 550 nm. The indicated scale bars are 500 nm.

Table 3-5. Overview of the maximum depth/height of holes/pillars in the etched Si master, Ni shim, and TOPAS 8007 replicas injection molded at T_{mold} = 70 °C and T_{mold} = 110 °C, as measured by AFM. The correct height information could not be obtained for all structures due to tip convolution.

		Depth/height [nm]			
	Polarity	**240/380**	**240/480**	**240/600**	**240/720**
Si master	Holes	474	-	-	-
Ni shim	Pillars	-	484	483	472
TOPAS 8007 T_{mold} = 70 °C	Holes	74	157	230	349
TOPAS 8007 T_{mold} = 110 °C	Holes	483	486	491	492

Furthermore, gratings (300/600 nm, field 16) with axis parallel with the flow direction of the injected polymer melt was also fully replicated against the shim (474 nm average step height) (**Figure 3-8a**). However, for gratings with axis perpendicular to the flow direction (**Figure 3-8b**), replication was incomplete and with a large variation in the step height (228.1±92.6 nm, 4 scans). The average width for the parallel and perpendicular ridges on the replica was measured to be 146 nm and 150 nm respectively, which was significantly smaller than the nominal width of 300 nm, likely achieved by overexposure of the resist on the Si master. The pitch on the replica was measured to be 591 and 593 nm, which is 1.5 % and 1.1 % from the nominal pitch of 600 nm.

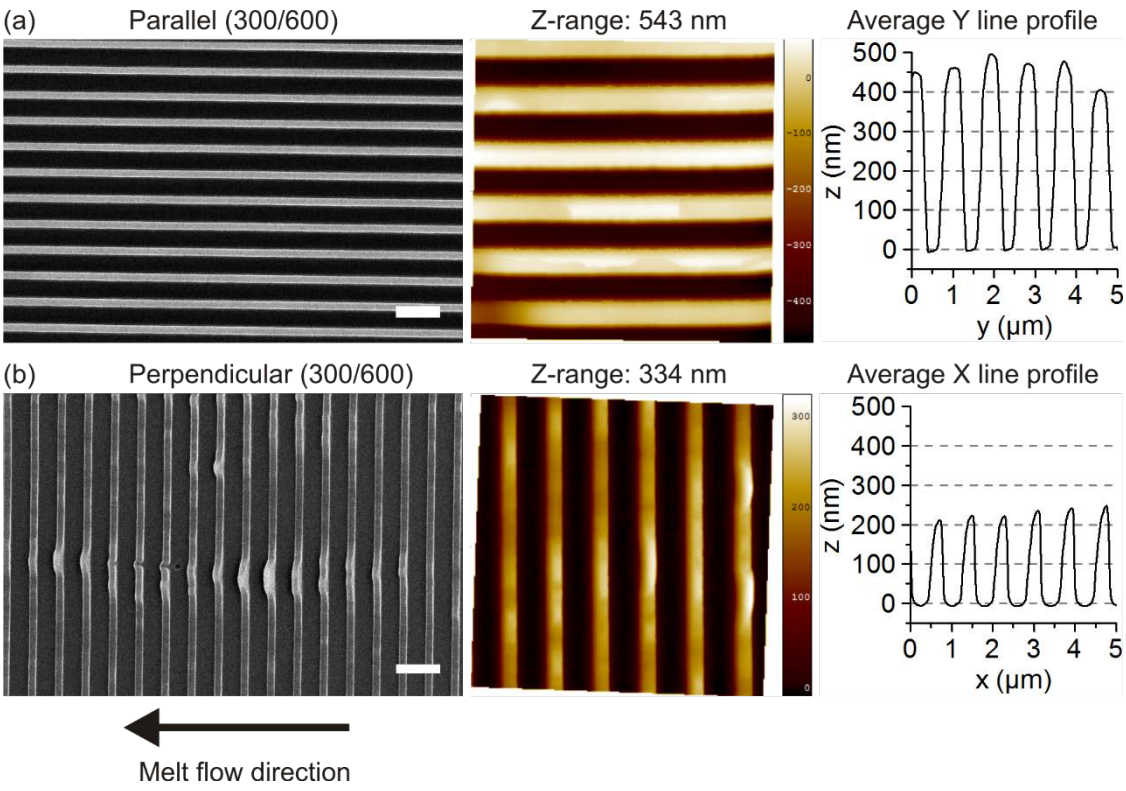

Figure 3-8. SEM micrographs, AFM topography micrographs, and average line profiles for gratings replicated in TOPAS 8007 **(a)** parallel with and **(b)** perpendicular to the melt flow direction indicated by the arrow. The scale bars in the SEM micrographs are 1 µm. The AFM topography scan size were 5x5 µm.

Figure 3-9 shows SEM micrographs of nano-sized holes in TOPAS 5013 microscope slides, using T_{mold} = 150 °C (T_g + 15 °C) and T_{demold} = 100 °C (T_g -35 °C). Images were captured at 12 positions, distributed across an area of (1.2x3.5 cm^2) with origin in the geometrical center of the microscope slide replicas (**Figure 3-1**). Full replication with this COC grade was also achieved by a variothermal process. However, the same type of deformations as mentioned before was also observed for these replicas, with the deformation becoming increasingly more severe as the spacing between features in the Ni mold was reduced. For the 240/380 nm structure, the width of the protruding area between holes seems to be below 50 nm. Compared to variothermal injection molding with TOPAS 8007 (**Figure 3-6**), the features in this experimental series seemed to be more distorted.

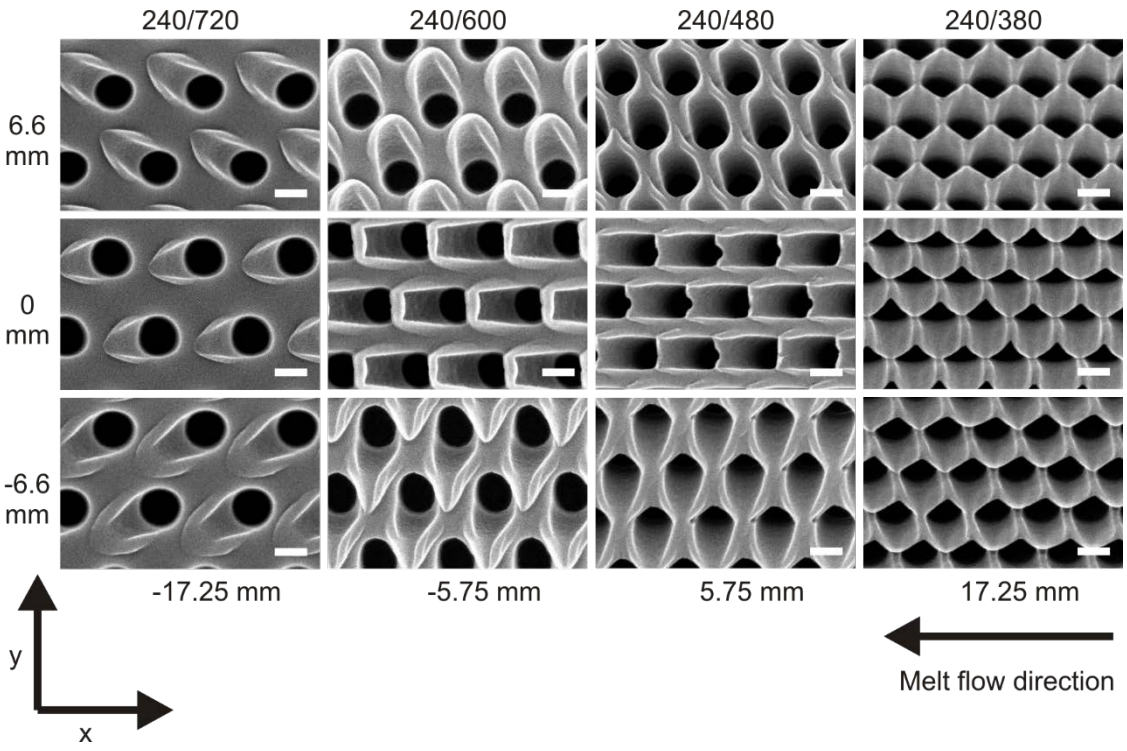

Figure 3-9. SEM micrographs of injection molded nanostructures replicated in TOPAS 5013 produced from a Ni shim (**Figure 2-10**), using a variothermal process with T_{mold} = 150 °C. The different structures are annotated as diameter/pitch according to the nominal values in the mask design (**Figure A-2**). The position of each image is given relative to the center of the microscope slide replica. The scale bars are 250 nm.

3.3.3 HSQ improves replication by heat retardation of polymer melt

SEM micrographs of TOPAS 8007 replicas injection molded from the Ni shim (**a**) and HSQ/steel mold (**b**), using a constant mold temperature of 70 °C, are shown in **Figure 3-10**. Similarly to what was observed for the HSQ/steel mold nanopatterns, the squares in these replica appear more rounded than the corresponding replica from the Ni mold. The average width of pillars in the replica was measured to be 366 nm and 400 nm from the Ni and HSQ molds respectively.

The lower heat conductivity of HSQ was expected to retard the heat dissipation between the polymer melt and the mold during the initial phase of the cavity filling, and thus delay the formation of a solidified skin layer. **Figure 3-11** shows AFM micrographs of polymer replicas injection molded against the structured mold inserts at different mold temperatures. The micrographs show that the mean pillar height increases monotonically with increasing mold temperature and was generally higher for HSQ than for a Ni shim. Injection molding with a Ni shim at mold temperatures ≤ 60 °C leads to a spatially inhomogeneous distribution of pillar heights over the scan area and with some features not being replicated at all. Replicas from the HSQ/steel mold insert also show some pillar height variations but to a much smaller extent and only at lower mold temperatures.

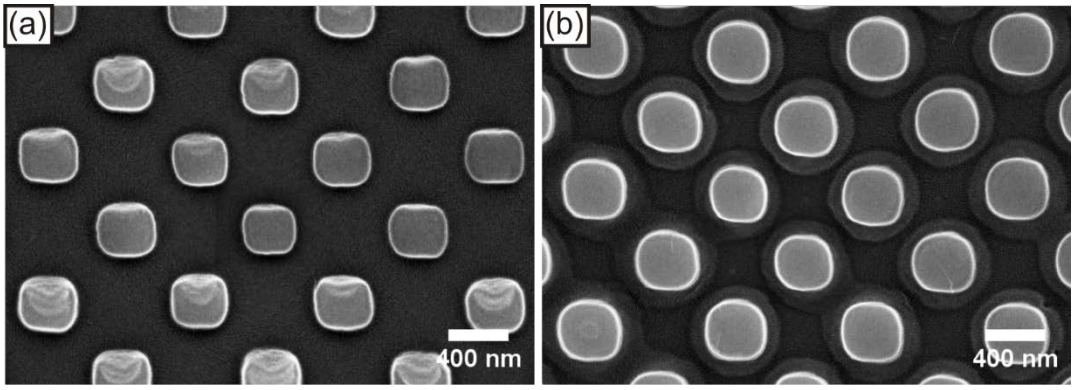

Figure 3-10. SEM micrographs of injection molded nanostructures replicated in TOPAS 8007 produced from the Ni shim (**a**) and HSQ/steel mold (**b**) shown in **Figure 2-11**, using a constant mold temperature (T_{mold}) of 70 °C.

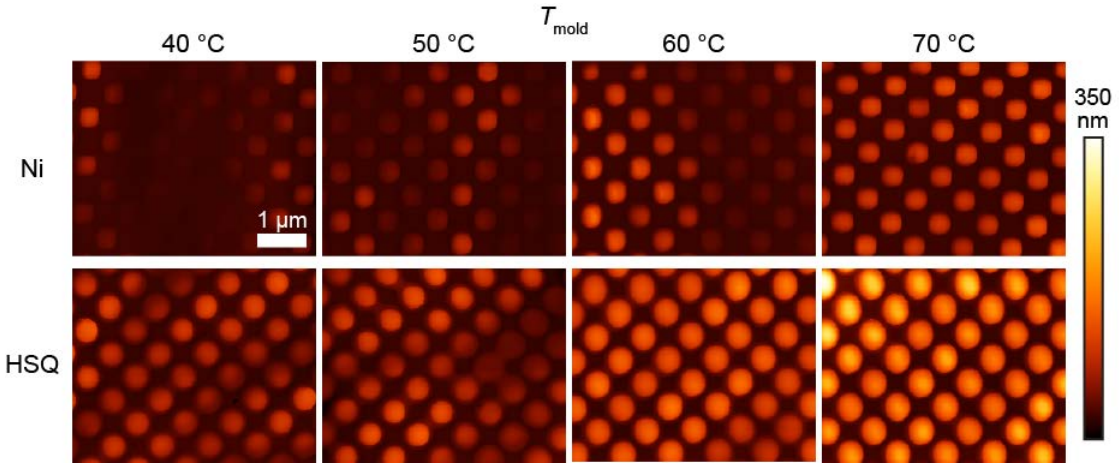

Figure 3-11. AFM micrographs of TOPAS 8007 replicas injection molded on a Ni mold insert (upper row) or a HSQ/steel mold insert (lower row) at different mold temperatures. The displayed scan areas are 5×4 µm^2 and the height scale is 350 nm.

The replication was quantified and is plotted in **Figure 3-12** for Ni and HSQ/steel mold inserts based on height measurements of at least 300 replicated pillars from 3 individual samples, at each mold temperature. These measurements confirm that structured HSQ molds results in better replication than Ni molds at all mold temperatures, as visually apparent in **Figure 3-11**. At mold temperatures of 40 °C and 50 °C, i.e. ~40 °C and ~30 °C lower than the polymer T_g, the mean replicated pillar height was increased by 100% compared to the Ni mold, while the improvement at 70 °C, close to T_g, was 50%. Full replication was still not achieved at this temperature as the HSQ hole structures (**Figure 2-11**) had a mean depth of 326 nm as determined by AFM (**Figure 2-12**).

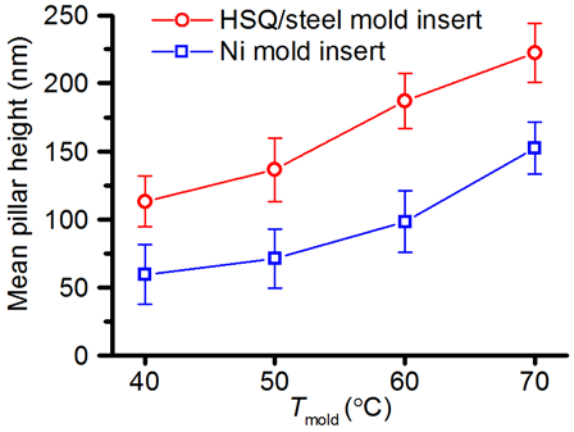

Figure 3-12. Mean pillar height of polymer replicas from structured Ni and HSQ/steel mold inserts at various mold temperatures. The mean depth of the mold structures are 398 nm and 326 nm for the Ni shim and the HSQ/steel mold insert, respectively. Error bars show the standard error of the mean (n=3).

Table 3-6 shows the calculated coefficient of variation (CV) of the pillar height, defined as the ratio of the standard deviation to the mean. These data confirm a more homogeneous pillar replication with the HSQ/steel mold insert than with the Ni shim at all mold temperatures and especially at the lower temperatures investigated.

A total cycle time (t_{cycle}) of 60 s was the shortest achievable at T_{mold} = 70 °C. With shorter cooling times, the sprue part of the replicas was still too soft for the replica to be reliably picked up by the robot arm in automatic machine mode. However, at T_{mold} = 40 °C the cooling time could be significantly reduced resulting in a minimum cycle time of 31.6 s. Despite this possibility to shorten the production time, the total cycle time was kept constant at 60 s in this study to allow a direct comparison between the different mold temperatures. The HSQ/steel mold inserts were used during 900 injection molding cycles, after which no damage to the surface could be observed by SEM analysis (data not shown).

Table 3-6. Coefficient of variation (%) of the replicated pillar height at the different mold temperatures.

	T_{mold}			
	40 °C	50 °C	60 °C	70 °C
Ni shim insert	64%	53%	40%	22%
HSQ/steel mold insert	28%	30%	19%	17%

3.3.4 Heat transfer simulations confirm heat retardation by HSQ

The initial contact temperature between the COC polymer melt and the mold surface can be calculated using **Equation (3-3)**. The results for initial temperatures T_{mold} = 70 °C and T_{melt} = 250 °C were 77 °C for COC/Cr and 184 °C for COC/HSQ, which gives a first indication that HSQ may support sustained polymer flow after initial contact. The simulated cooling of a polymer melt at a position 50 nm from the polymer/mold interface is shown in **Figure 3-13** for a Ni mold and a stainless steel mold insert with a 500 nm thick HSQ layer. The Ni mold was modeled as consisting of

a 100 nm thick Au layer on a nickel support, thus disregarding the minute influences expected from having a Cr/Au layer instead of pure gold on the actual mold used for injection molding. Upon thermal contact with the Ni shim, the polymer melt cools rapidly from an initial temperature of 250 °C and reaches T_g after only 10 µs. In contrast, the polymer melt remains at temperatures above T_g for about 100 ms when contacting the HSQ/steel mold surface, i.e. 4 orders of magnitude longer.

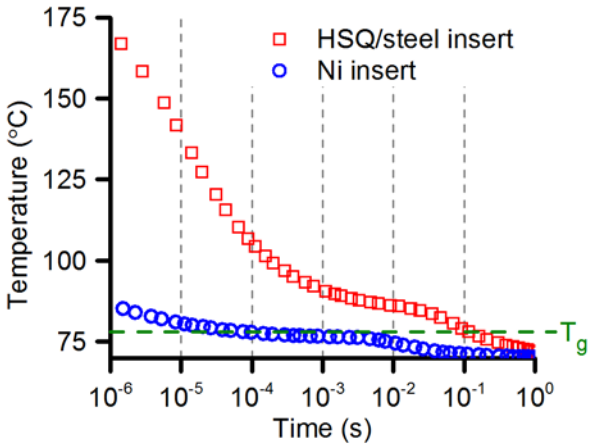

Figure 3-13. Finite element modeling of polymer melt cooling at a position 50 nm from the polymer melt/mold interface after the polymer melt at 250 °C is brought in thermal contact with a Ni insert or a HSQ/steel mold insert at 70 °C.

Figure 3-14 shows the results of modeling the time-dependent spatial temperature distribution across the polymer/mold interface. The Ni mold (**Figure 3-14a**) gives rise to a sharp transition in temperature across the polymer/mold interface with the melt temperature reaching 100 °C (T_g + 20 °C) after 10 µs at a distance of 200 nm from the mold surface, i.e. about half the nanopillar diameter in **Figure 3-11**. The temperature at the mold surface barely increases from 70 °C to 76 °C during this time period. In contrast, the HSQ/steel mold insert (**Figure 3-14b**) causes much slower cooling of the polymer melt with a polymer/HSQ interface temperature of 184 °C at 100 ns after initial contact and reaching 160 °C (T_g + 80 °C) after 10 µs at a distance of 200 nm from the mold surface. A temperature gradient arises across the HSQ film after 10 µs, with the outer surface being at 139 °C and the inner surface (towards stainless steel) still being at 70 °C. After 1 ms, the steel surface reaches a temperature of 83 °C.

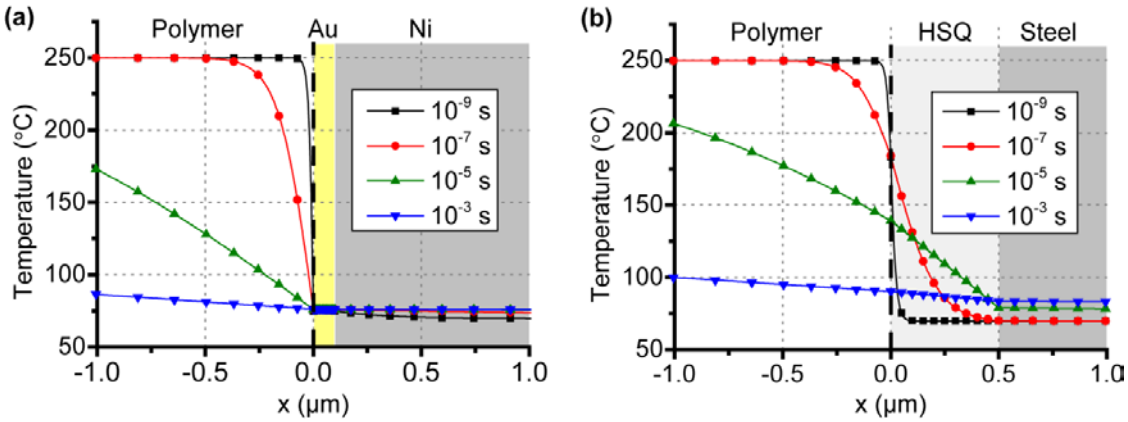

Figure 3-14. Finite element modeling of the spatial temperature distribution across the polymer/mold interface (x = 0) at different time points for (**a**) Ni insert and (**b**) HSQ/steel mold insert. In (**a**), x < 0 µm: COC, 0 µm < x < 0.1 µm: Au, 0.1 µm < x: Ni. In (**b**), x < 0 µm: COC, 0 µm < x < 0.5 µm: HSQ, 0.5 µm < x: stainless steel.

The effect of heat retardation by HSQ coatings could likely be increased by increasing the film thickness above 500 nm. **Figure 3-15** shows the simulated cooling of a polymer melt at a position of 50 nm from the polymer/mold interface, with HSQ film thicknesses of 0.5, 1, 2, 5, and 10 µm. As expected, the time duration at which polymer melt 50 nm from the mold surface remains at elevated temperatures increases with the thickness. After 10 ms from initial contact, the temperature was 86 °C, 88 °C, 92 °C, 104 °C, and 120 °C for 0.5, 1, 2, 5, and 10 µm thick HSQ films respectively.

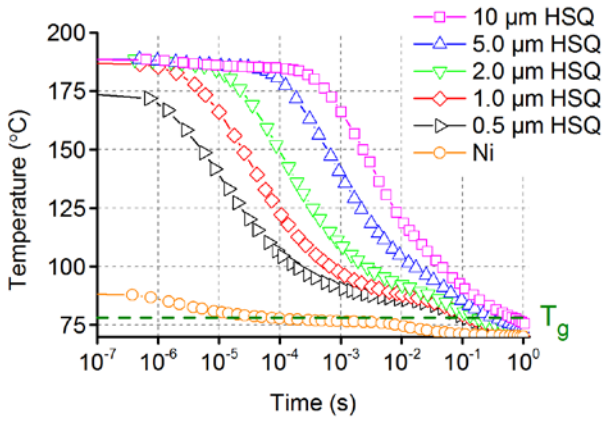

Figure 3-15. Finite element modeling of polymer melt cooling at a position 50 nm from the polymer melt/mold interface after the polymer melt at 250 °C is brought in thermal contact with a Ni insert or a steel mold inserts with different HSQ film thicknesses at 70 °C.

3.4 Discussion

Injection molding using both Ni and HSQ molds at isothermal and variothermal conditions was presented in this chapter. With a constant mold temperature (T_g – 10 °C), replication of protruding pillars on the Ni shim increased from 15 % to 72 % as the spacing was increased from 120 nm to 430 nm for TOPAS 8007. This was expected, due to the higher surface to volume ratio at low spacing,

leading to a faster cooling of the polymer melt at the mold interface. Not surprisingly, the replication was greatly improved by increasing the mold temperature to T_g + 30 °C, leading to a full replication depth even for 240/380 nm structures due to the slower cooling of the melt, allowing more time for the polymer to flow and replicate the mold surface before the onset of a solid skin layer.

However, the increased depth of the replicated holes also led to a more distorted surface topography, especially for the most densely packed features. The deformations in **Figure 3-3**, **Figure 3-6**, and **Figure 3-9** seem to have an orientation along the flow direction of injected polymer, since the space "behind" Ni protrusions with respect to the direction of the injected polymer melt was only partially filled. Similarly, replication of linear gratings also revealed a dependence on the orientation relative to the direction of the flow front (**Figure 3-8**). While ridges in the polymer parallel to the direction of the flow front had a replication height of 166 nm and 474 nm at T_{mold} = 70 °C and T_{mold} = 110 °C respectively, ridges aligned perpendicular to the flow direction had a replication height of 102 nm and 228 nm for the two different mold temperatures. The same orientation-dependence on the replication quality has previously been observed for replications of channels (on the mold) with a width below 500 nm in one study [89], and with widths ranging from 0.3 µm to 4 µm in another study [108]. In the latter reference, the difference in replication for two differently aligned gratings became stronger as the mold channel width became smaller, with the vertical height of 300 nm polymer ridges perpendicular to the flow direction being only 1/3 of the height of parallel ridges. An unstable filling flow has previously been observed during replication of channels with a width below 30 µm, leading to creation of spherical features on top of incompletely replicated ridges in the polymer [109]. The explanation was having a non-uniform elastic skin layer, which at weaker points could be forced into the mold channels by the hydrostatic pressure from the injection gate. This type of non-uniformity was also observed for ridges perpendicular to the flow direction in **Figure 3-8**. It is likely that the deformations observed for both holes and ridges in the polymer are related to the pressure gradients that arise from the gate to the end of the mold cavity during packing.

These deformations could also be occurring during separation of the two mold halves. This has previously been observed for the replication of microfluidic channels, where the edge at one side of the channel had a "bump" with buildup of additional material [110]. If the molds are not completely aligned to each other, they may move by a small amount in the plane perpendicular to the withdrawal direction, thus scratching the surface of the polymer replica. Alignment could be improved by using mold tools with tie bars.

Finally, the observed deformations could be partially related to shrinkage of the polymer melt during cooling from T_{melt} to T_{demold}. Shrinkage was compensated by applying a holding pressure after the mold was filled. However, once the melt at the gate of the tool is frozen, the applied pressure inside the cavity drops to zero and any subsequent cooling beyond this point leads to dimensional changes. For the microscope slide format, replicas in **Figure 3-6**, and **Figure 3-9** were mechanically fixed by four ejector pins (close to the gate and inside field 13, **Figure 3-1b**). Thus, it is expected that significant shrinkage should have an orientation relative to the pin positions. However, this is not obvious from the presented results. Shrinkage is also depending on the thermal and mechanical history of the melt at any particular point, and no attempt to simulate this was made in this study.

By using an imprinted HSQ film on a stainless steel mold insert the replication quality of nanoscale features was significantly improved compared to a nickel mold insert fabricated by electroplating (**Figure 3-11** and **Figure 3-12**). The replicated

pillars were taller at all mold temperatures and with the difference being largest for T_{mold} = 40 °C or 50 °C, i.e. well below T_g of the polymer. Due to the lower thermal diffusivity of the HSQ film (**Table 3-4**), heat dissipation across the polymer/mold surface was retarded. The melt was allowed to stay in a flowable state for a longer time and could therefore penetrate longer into the nanostructured holes before it solidified. This was exemplified by the modelling results presented in **Figure 3-13** where a difference in melt temperature of T_g + 20 °C vs T_g + 80 °C on the Ni mold vs HSQ/steel mold after 10 µs corresponds to a reduction in melt flow viscosity by several orders of magnitude [111].

These findings agree well with previous literature on other heat-retarding mold materials. For instance, by using a nano-imprinted layer of SU-8 on a 740 µm polyimide (PI) sheet as a mold inlay, full replication of 100 nm holes in polycarbonate (PC) with an aspect ratio of 1 was achieved at T_{mold} = 60 °C [105]. Injection molding using a Ni mold with the same surface pattern resulted in replicated pillars with only about 30% of the nominal height. Another study demonstrated replication of 1 µm wide polymer gratings with an aspect ratio of 9 using a patterned polyurethane acrylate (PUA) layer on a 40 µm thick polyethylene terephthalate (PET) film, although the replication quality was not uniform [104].

The non-uniform replication at low mold temperatures with a Ni shim (**Figure 3-11** and **Table 3-6**) may be explained by thermally induced flow instabilities that have previously been observed at low injection velocities and large differences between T_{melt} and T_{mold} (high cooling rates) [112]. With the onset of flow instability, the polymer solidifies before the cavity is completely filled, causing surface waviness with a periodicity of several micrometers. Flow instability was not observed to the same degree when using the HSQ-coated mold, and the surface topography was more uniformly replicated.

Numerical simulation of the heat transfer showed that the polymer melt close to the mold surface stayed above T_g significantly longer for HSQ/stainless steel compared to Ni, due to the much lower thermal diffusivity (**Figure 3-13**). The initial temperatures for the Ni/COC and the HSQ/COC as predicted by the simulations fit perfectly with the analytical solution in **Equation (3-3)**. It was also demonstrated that by increasing the film thickness of HSQ, the effect of heat retardation could likely be enhanced and therefore further improve replication at low mold temperatures (**Figure 3-15**). The effect of viscous heat dissipation was not included in these simulations, although for replication of microstructures they have previously been assumed to be negligible [107]. Also, a perfect thermal contact between the melt and the mold surface has been assumed, which is a good approximation during the initial filling phase when the viscosity is low [113]. The polymer contracts during cooling, which is compensated by the holding pressure as long as polymer melt is allowed to move through the gate. After the gate is frozen, the polymer may separate from the mold due to continuous shrinking. Thus, a thermal contact resistance arises. However, as the replication of nanoscale features happens at a much shorter timescale, this is likely of less relevance for our study.

The materials used to demonstrate heat retardation in an injection molding process have so far only been polymer-based. These materials may be suitable for prototyping or small-volume productions. However, for high-volume productions that could involve more than 100 000 cycles, they lack the wear-resistance offered by those materials typically used in industry, such as tool steel. Thermally cured HSQ has previously demonstrated a lifetime of at least 10 000 cycles in an injection molding process [54] and has also shown to be mechanically stable during hot embossing [52]. Above 400 °C, the Si-H bonds in the monomer dissociates and a cross-linked silica

network is formed resulting in an increase in hardness to 2-15 GPa depending on the curing conditions [74]. This ceramic-like coating is highly scratch resistant and is a robust candidate for mold coatings.

Another advantage of using HSQ as a heat-retardant mold coating is its ability to reduce surface roughness of the mold due to its high flowability, an important factor for the production of optically smooth polymer replica [54]. In addition, HSQ was shown to be fully compatible with silane surface chemistry. Thus, an anti-stiction coating like FDTS can be applied without any intermediate process steps. This is an important finding as a strong adhesion between polymer and mold can lead to incomplete replication or in worst case damage to the mold surface [63] [52].

3.5 Conclusion

In this chapter, it was demonstrated that large-area nanopatterns could be transferred to polymer replicas by injection molding. By isothermal injection molding with short cycle times, 250 nm features could be replicated in COC with an aspect ratio above 1 using a large pitch distance. For more closely spaced features, the replication quality fell significantly. By raising the mold temperature to 30 °C above the glass-transition temperature of the polymer, features with a spacing down to 120 nm could be filled to an aspect ratio of 1.8, although with a significantly longer cycle time (45 s *vs.* 2.5 min). In addition, nanoscale deformations of the hole structure was observed, which were likely caused by rapid onset of an elastic skin layer or scratching during demolding. Finally, replication was improved with a HSQ-coated steel mold compared to a Ni mold formed by sputtering and electroplating, both in terms of a larger mean height and more uniformly distributed height of pillars in the polymer. In contrast to the rapid formation of skin layers caused by the high cooling rates during isothermal molding, the HSQ film acted as an insulating layer that allowed more time for the melt to flow before solidifying. In addition, the coated films have demonstrated sufficient durability for high-volume fabrication processes. Thus, HSQ-coatings have the potential to improve nanoscale replication in an industrially relevant setting, by reducing the need for variothermal mold cycling.

Chapter 4

Protein Patterning for Monocyte Isolation

4.1 Introduction

Isolation of leukocyte subpopulations is important for a range of clinical applications, such as the diagnosis of human immunodeficiency virus (HIV), malaria and leukemia. Using microarrays of cell-specific ligands, such as antibodies for the clusters of differentiation (CD), leukocyte subpopulations can be captured at distinct spots on the same substrate [24]–[27]. After an incubation period where cells are

allowed to bind specifically to the antibody-coated surface, loosely bound cells are removed by washing with buffers. It is advantageous to perform cell sorting in a microfluidic device, as well-defined mechanical shear stress can be applied to achieve the optimal separation between specifically and non-specifically adhered cells. In a parallel plate channel of width much longer than its height, the wall shear stress τ that cells experience may be calculated as:

$$\tau = \frac{6\mu Q}{wh^2} \qquad (4\text{-}1)$$

where μ is the dynamic viscosity of the liquid, Q is the flow rate, and h and w is the chamber height and width respectively.

One of the most common and simplest methods to isolate monocytes for the generation of mature DCs is by adherence to plastic substrates [41], since they have a relatively higher adherence to tissue culture PS compared to other PBMCs, which are more easily removed after several washing steps [114], [115]. A more sophisticated method that results in a higher purity is elutriation, which is based on counterflow centrifugation to separate cells based on both size and density [116]. With this method, it has been demonstrated that monocytes can be sorted with a purity of 83%, which is the total fraction of monocytes in the sample after sorting, and a recovery of 75%, which is defined as the total number of monocytes after sorting relative to the initial amount [116].

However, elutriation systems are expensive in capital investment as well as per purification step. If anti-CD14 antibodies, with CD14 being a cell surface antigen specific to monocytes, could be integrated on cell-culture substrates by methods compatible with industrial mass production, the purity of DC-based cancer vaccines could be improved while keeping costs low. In addition, microarrays open new possibilities for a more defined cell-culture microenvironment, such as the co-culture of T-cells and DCs in spatially different positions. This could be used for T-cell activation *ex vivo*, thereby omitting some of the problems connected with the lack of migration to the lymph nodes, which is often experienced by infused DCs [7].

The most common technique for producing microarrays are by spotting or ink-jet printing [117], where droplets containing aqueous solutions of proteins are ejected through a narrow nozzle by piezo-electric actuation. One of the advantages of this method is the high degree of freedom for the spatial positioning of protein spots. Furthermore, it involves no physical contact between the nozzle and the substrate to be printed, thereby reducing contamination. In addition, low volumes can be deposited (pL to nL), which is advantageous for applications where expensive reagents are required.

One challenge with the fabrication of protein microarrays is the ring formation of deposited material that occurs during drying of droplets, popularly known as the coffee ring effect [118]. It is caused by contact-line pinning of the droplets, leading to a radial flow outward from the center during faster evaporation at the droplet periphery in order to compensate for the volume lost. The consequence of this phenomenon is that most of the protein is deposited at the edge of the spot, while the center part has a low coverage. This can decrease the sensitivity of spot readout when for instance the amount of fluorescently bound material is low [119], or decrease the capture efficiency for cellular microarrays.

Ring formation can be avoided by reducing the evaporation rate of droplets, in order to allow sufficient protein adsorption to happen before droplets dry out completely, so that excess amounts can be removed by a wash step. Due to the increased surface-volume ratio of droplets as the diameter is reduced, evaporation becomes increasingly problematic for pL droplets. Drying is significantly slowed when

the temperature is close to the dew point, which could be achieved by cooling the printing substrate and/or printing inside a closed humidity chamber. In addition, solvents with a low vapor pressure, such as dimethyl sulfoxide (DMSO) or glycerol can be added to the spotting buffer [120]. Finally, the spot homogeneity can be increased by printing on hydrophobic surfaces, which reduces the evaporation rate locally at the contact line due to higher contact angles [121].

Previous work in the group has demonstrated direct entrapment of avidin, fibronectin, and horseradish peroxidase (HRP) on the surface of PP and PMMA replicas formed during injection molding, a process termed "InMold transfer" [33]. With this method, pre-adsorbed proteins on a mold surface are transferred to the polymer replica during shaping, with some retained biochemical activity. One advantage of this approach is that immobilization can be combined with replication of micro- or nanostructures in a simultaneous process, making it a highly attractive approach for microfluidic biochip fabrication. Moreover, with automated robot replacement of mold inserts, a cycle time below 30 s per part is achievable in an in-line process.

In this chapter, printing of < 100 µm homogeneous avidin spots on FDTS-coated Ni shims, with and without nanostructures, and subsequent transfer with retained biofunctionality will be discussed. Furthermore, the capture of monocytes on biotin-anti-CD14 patches immobilized on avidin deposited by passive adsorption or transferred from mold inlay will be described by the adhesion under a range of shear stresses in a parallel flow chamber. Finally, monocyte adhesion on injection molded plastics with nanoscale topography, with the purpose of increasing the harvest efficiency by restricting the effective surface area between the cell and the surface for adhesion, will be briefly described.

4.2 Avidin spotting for InMold transfer

4.2.1 Experimental procedures

Proteins in buffer were spotted using a Nano-Plotter NP 2.1 operated by NPC16 software (GeSiM, Germany). The instrument included a microscope slide deck, a microplate sample holder, a washing station, a drying pad, and a robotic arm with a four-channel pipette head. A micro-milled PMMA carrier was used to align Ni shims to the slide deck.

Dispensing of droplets was performed using a piezoelectric micropipette (Nano Tip A), consisting of a microstructured silicon channel bonded to a glass lid. Droplets were ejected through a 20 µm opening at a frequency of 30-100 Hz, using a piezoelectric pulse width of 50 µs, and an amplitude of 80-150 V. The optimal parameters for stable spotting of single droplets varied considerably with the viscosity of the protein buffer and the "cleanliness" of the pipette. Therefore, the frequency and the amplitude had to be adjusted for each experiment, for which a camera (stroboscope) was used to monitor droplet formation (**Figure 4-1**).

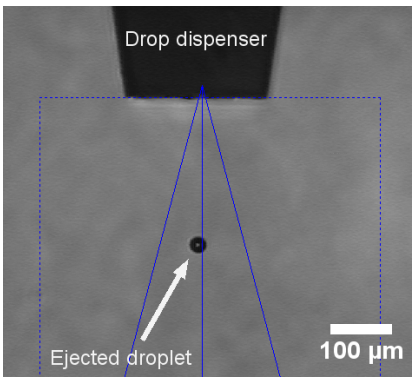

Figure 4-1. Stable, single-droplet ejection from a micropipette as verified by the stroboscope.

Two different deposition programs were used – a high-precision protocol where the movement of the pipette arm were stopped at each spot position, and a high-speed protocol where droplets were deposited on-the-fly. Spotting close to the dew point was achieved by controlling the humidity, using a humidifier and a humidity sensor inside the covering hood, and by decreasing the temperature of the slide deck using circulation of cooling liquid (50% v/v glycerol in water). The temperature at the shim surface T_s and the surrounding air T was continuously measured by a digital thermometer, and the relative humidity RH was adjusted to be just below the value required for the dew point, using the formula [122]:

$$RH = 100 \times \exp\left(\frac{17.62T_s}{243.12 + T_s} - \frac{17.62T}{243.12 + T}\right) \qquad (4\text{-}2)$$

For protein spotting, both avidin labelled with the fluorophore TexasRed (TR) and unlabeled, deglycosylated avidin (ExtrAvidin), mixed in a 1:9 weight ratio, was used. Droplets with protein solution were deposited on Ni shims first sputter-coated with SiO_2 and subsequently FDTS-coated by MVD (**Section 2.6**). Afterwards, an incubation period of 10 min was used to allow protein adsorption. The shims were immersed in MilliQ water to remove unbound protein, before drying with an air gun. For InMold transfer, the injection molder was kept running in automatic mode using a "dummy" shim. After spotting, the shims were immediately installed in the tool casing and protein on the mold surface was transferred to TOPAS 8007, using a mold temperature (T_{mold}) of 30 °C. Otherwise, the parameters for injection molding were equal to those listed in **Table 3-1**. The polymer replica with transferred protein was protected from light and stored in a refrigerator before analysis. To avoid non-specific adsorption, bovine serum albumin (BSA) in PBS was added at 1 mg/mL at room temperature for 30 min. Excess protein was removed by washing in MilliQ water and the polymer replica was dried. Biotin-fluorescein conjugate in PBS was added at 1 µM for 1 h, before the replica was again washed and dried. Detection of fluorescent avidin and biotin was performed with a Zeiss LSM 5 confocal microscope (Carl Zeiss, Oberkochen, Germany), using both a 488 nm Ar and a 543 nm HeNe excitation laser. Image analysis was performed with the ImageJ software package.

Materials used:

Avidin-sulforhodamine 101 (avidin-Texas Red®) (#A2348), ExtrAvidin® (#E2511), bovine serum albumin (#A2153), biotin (5-fluorescein) conjugate (#53608), dimethyl sulfoxide (#D8418), and Dulbecco's Phosphate Buffered Saline (#D8537) purchased from Sigma-Aldrich.

4.2.2 Optimization of avidin spotting

For some cell capture applications, such as the co-culture of two or more different types of cells, printing over relatively large areas (cm^2) within a short time is attractive. By using on-the-fly spotting of droplets, the required time for a 330x30 spot array was reduced from 2.5 h to 9 min, compared to the normal spotting program. To determine the precision of the high-speed program, two arrays of PBS droplets were deposited on a shim with a pitch of 150 µm and 200 µm (**Figure 4-2**). At 150 µm spacing, the pattern of dried salt crystals was clearly distorted, showing merging of droplets likely due to positioning inaccuracy. At 200 µm, the spacing was large enough to allow small individual droplet displacements while maintaining individual spots.

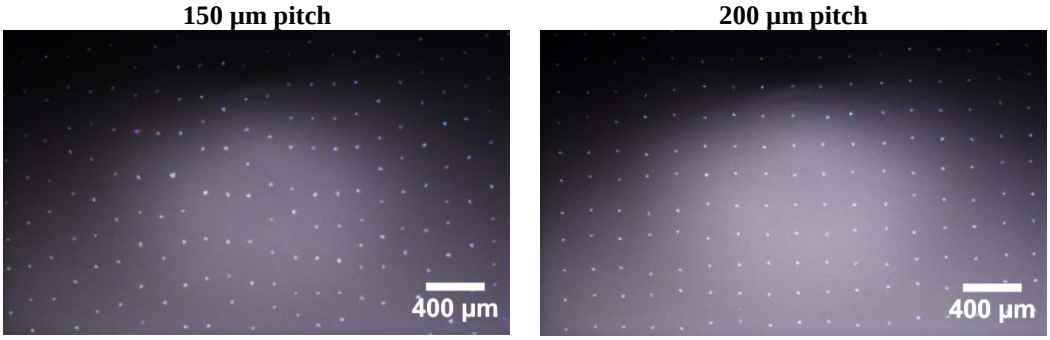

Figure 4-2. Arrays of salt crystals from dried PBS droplets spotted on a Ni shim with the high-speed program (18.5 spots/second) using different pitch. **Left:** A pitch of 150 µm leads to droplet merging. **Right:** A regular array of single droplets was achieved when the pitch was increased to 200 µm.

Operating at the dew point was problematic as humidity fluctuations caused condensation on the shim surface. Therefore, the humidity was set a bit lower than the dew point. However, at these conditions the deposited droplets dried out within 1 min. During spotting of avidin in PBS on a FDTS-coated Ni shim, the spot size was found to increase with increasing concentration of protein in the range 10-300 µg/mL, while at higher concentrations the spot size remained constant (**Figure A-12**). Furthermore, it was found that each spot consisted of a larger ring with a low fluorescence intensity and center part with a high intensity (**Figure 4-3**). By spotting on native PS, the size was constant above 100 µg/mL, and decreasing for lower concentrations (**Figure A-13**).

To achieve more homogeneous spots, DMSO was added to the protein buffer (**Figure 4-4**). Combined with cooling of the substrate and using a high humidity, deposited droplets remained in a liquid state for at least 10 min, before the shim was immersed in MilliQ water. By using 10% v/v DMSO in PBS, the fluorescence intensity was more evenly distributed than using PBS, although the coffee-ring effect leads to a thin ring on the edge of the spot with a slightly higher intensity. For PBS, the outer ring had a diameter 85 µm and the inner part a diameter of 55 µm, while the average spot size with a 10% DMSO spotting buffer was 90 µm. The spot size was constant in the range of 80-500 µg/mL avidin with higher concentrations leading to larger spot sizes (**Figure A-14**).

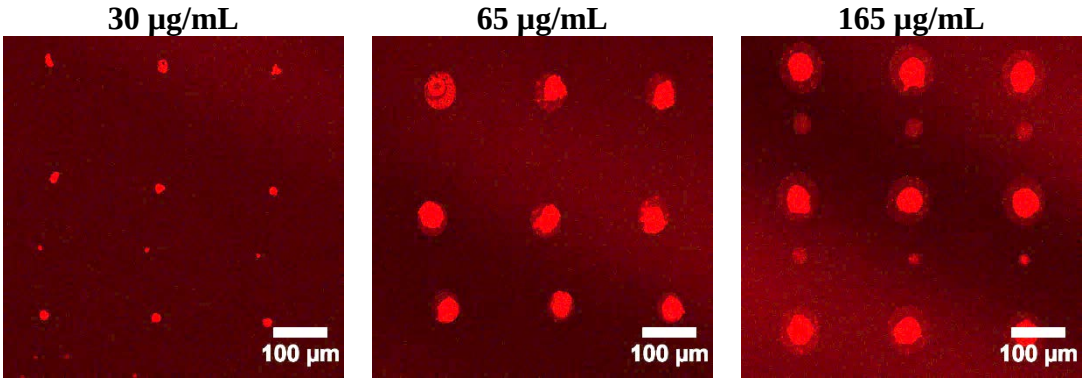

Figure 4-3. Confocal microscope images of fluorescently labelled avidin. The spot size on shim decreased as the avidin concentration in droplets decreased. For 65 and 165 µg/mL, a larger ring can be seen with a lower intensity, followed by a smaller center spot with a higher signal.

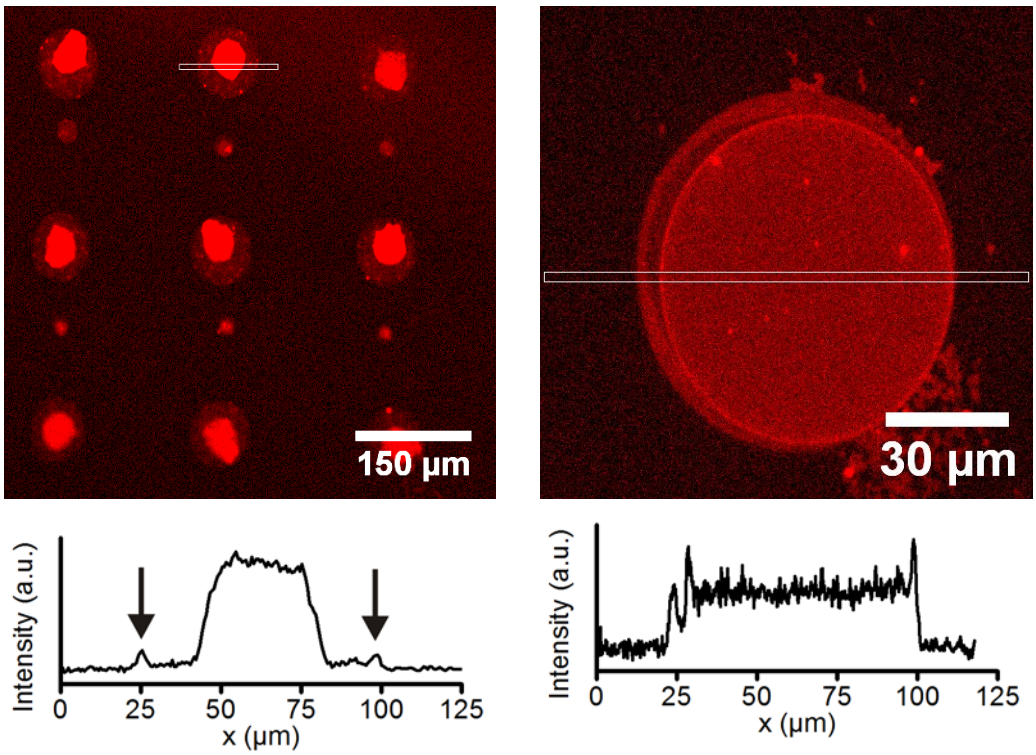

Figure 4-4. Confocal microscope images of fluorescently labelled avidin. **Left:** Spotting on a FDTS-coated shim of 140 µg/mL avidin in PBS leads to an outer low-intensity ring indicated by the arrows and a center high-intensity part. **Right:** Spotting at the same concentration in PBS + 10% DMSO buffer leads to improved spot homogeneity by delaying evaporation.

4.2.3 Avidin spotting on nanostructured shim

Droplets were also spotted on a nanostructured SiO_2+FDTS-coated Ni shim. The diameter *d* and spacing *s* of the different structures are summarized in **Table 4-1**, along with a filling factor *f* defined as the percentage of the projected area consisting of protrusions, and a roughness factor *r* defined as the real area relative to the projected

area. A protrusion height of 330 nm was assumed, which was the depth of photoresist after development (**Figure 2-3**). A droplet array with a pitch of 300 µm was spotted across unstructured and structured fields (fields 3-7). While deposition of avidin was achieved for some of the structures (fields 3, 5, and 6), no proteins were found on others (fields 4 and 7). During spotting, no droplets were placed on these fields in contrast to the neighboring fields. In addition, these two fields did not become hydrophilic after 30 min of incubation with 1 mg/mL BSA. Advancing and receding contact angles for the different fields were measured. All the structured fields had a higher water contact angle relative to the unstructured area. In addition, field 4, 6 and 7 displayed a higher contact angle and a lower hysteresis than field 3 and 5.

Table 4-1. Static (θ), advancing (θ_{adv}), receding (θ_{rec}), and contact angle hysteresis ($\Delta\theta$) of SiO2+FDTS-coated Ni nanostructures, with different diameter *d*, spacing *s*, filling factor *f*, defined as the projected area comprising of protrusions, and roughness factor *r*, defined as the real area relative to the projected area. *Structures were holes instead of protruding pillars.

Field	d [nm]	s [nm]	f [%]	r	θ [°]	θ_{adv} [°]	θ_{rec} [°]	Δθ [°]
Flat	-	-	-		111.7±1.4	110.8±1.1	96.2±1.8	14.6
3*	210	170	76	2.5	136.9±3.0	143.1±0.9	92.9±2.7	50.2
4	264	216	24	2.2	149.8±1.7	159.5±0.9	125.3±3.7	34.2
5	243	477	9	1.5	145.2±3.5	149.6±0.8	95.2±18.8	54.4
6	151	189	15	2.4	153.1±1.4	159.2±0.7	138.8±4.5	20.4
7	128	272	8	1.8	157.4±3.1	160.5±0.1	142.9±0.8	17.6

To increase the wetting of the most hydrophobic structures, 0.001-0.01% of Triton X-100 was added to the spotting buffer. During spotting, all fields were wetted, except 4 and 6. In addition, no adsorbed protein was found during inspection of the wetted fields by confocal microscopy, suggesting that the surfactant may have blocked adsorption on FDTS (not shown).

By addition of 10% v/v DMSO to PBS, protein spots could be deposited on all types of structures, as verified in **Figure 4-5**. The average spot size depends on the surface topography with droplets on especially field 4 and 6 having a small diameter.

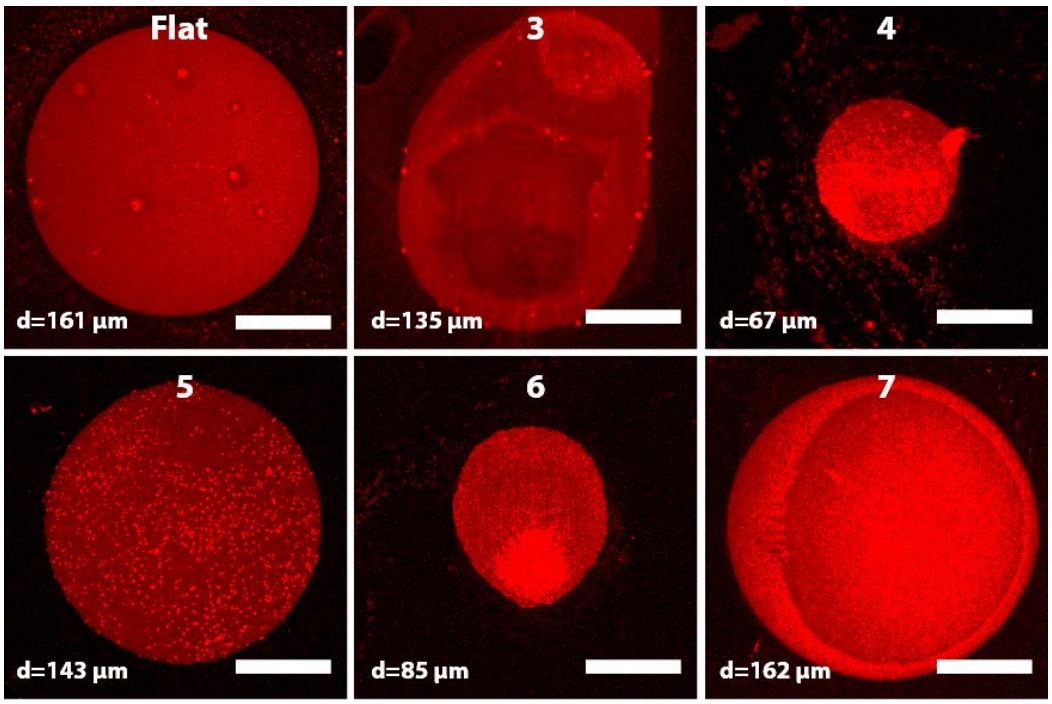

Figure 4-5. Confocal microscope images of fluorescently labelled avidin on a nanostructured Ni shim. Addition of 10% DMSO enables deposition of protein spots on nanostructures that were otherwise not wetted by PBS. On each image, the average diameter of five droplets on the same structure is annotated. The scale bars are 50 µm.

4.2.4 Functional InMold transfer of avidin

The retained biotin-binding affinity of avidin after InMold transfer is demonstrated in **Figure 4-6**. In this experiment, 100 µg/mL of ExtrAvidin (unlabeled) in 10% v/v DMSO was spotted with a pitch of 200 µm on the mold surface. Then, an array of 50 µg/mL avidin-TexasRed (TR) was superimposed with a pitch of 400 µm. After injection molding, the polymer replica was labelled with 1 µM biotin-FITC. Biotin was observed to bind to all spots, while fluorescently labelled avidin was only found on one out of four positions as expected. These spots were naturally larger as the volume of liquid was twice as large. The fluorescent signal of avidin was lower in the middle of the droplet, likely due to adsorption of ExtrAvidin prior to deposition of avidin-TR.

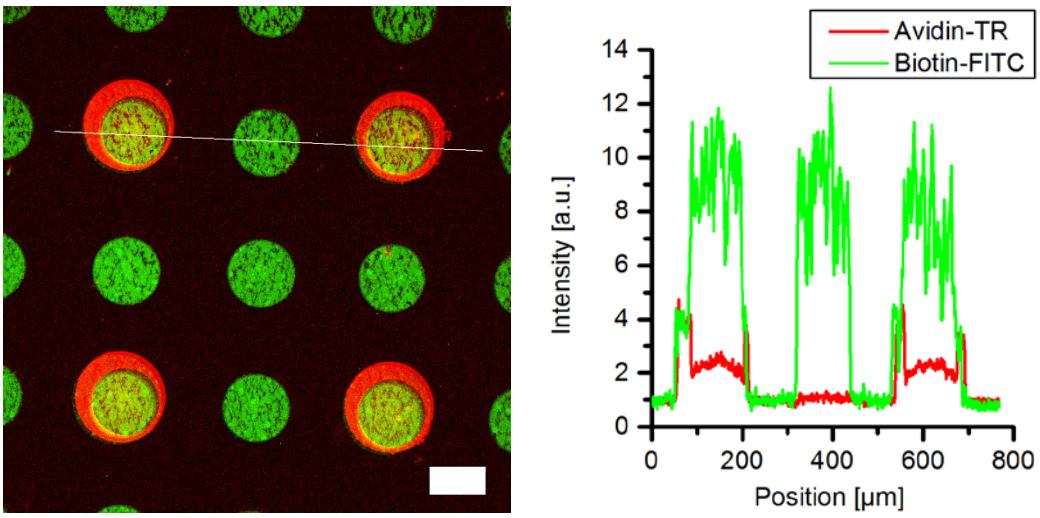

Figure 4-6. Confocal microscope image of InMold transferred unlabeled and fluorescently labelled avidin, as well as fluorescently labelled biotin added after transfer, demonstrates retained biofunctionality after transfer. First, ExtrAvidin was spotted with a pitch of 200 µm. Then, avidin-TR was spotted with a pitch of 400 µm on the mold surface in register with the ExtrAvidin spots. The intensity profile (graph on the right) drawn across spots in the microscope image shows co-localization of fluorescent biotin and avidin at every second spot.

4.3 Cell capture and adhesion in flow chamber

As mentioned in the introduction, integration of phenotypic-specific antibodies on plastic cultureware for cell capture using low-cost production methods, which in the case of DC vaccines would be anti-CD14 specific against monocytes, could be an alternative to more sophisticated and expensive sorting systems such as elutriation. For monocyte isolation, both a high purity and recovery are desired, defined as the total fraction of monocytes in the sample after sorting and the total number of monocytes after sorting relative to the initial amount respectively. In addition, control of adhesion is important for the harvest of captured cells at the end of culture. In this section, PBMC and monocyte adhesion to different protein patches and nanoscale topography integrated in a parallel plate flow chamber will be described.

4.3.1 Experimental procedures

4.3.1.1 Protein patches on TOPAS slides

Casted PDMS wells or 12 well silicone sticky slides (ibidi, Munich, Germany) were attached to injection molded TOPAS slides to create different protein patches. Prior to all experiments using biotinylated antibodies, all wells were incubated with 1 mg/mL ExtrAvidin in PBS overnight at 4 °C. Wells were washed three times with dPBS + 0.05% Tween-20 (PBS-T) between each incubation step to remove excess protein. Recombinant human serum albumin (HSA) (#A9731, Sigma-Aldrich) was used to block remaining adsorption sites by 30-60 min incubation at room temperature. Biotinylated mouse anti-human CD14 (#C1496) or mouse IgG2a isotype control (#I-

129), both from Leinco Technologies (St. Louis, USA), were incubated for 1 h at room temperature. Finally, wells were washed before the silicone chamber was detached and the flow chamber assembled.

4.3.1.2 InMold transfer of avidin

ExtrAvidin was InMold transferred using the procedure shown in **Figure 4-7**. Droplets with 50 µg/mL in PBS were deposited on the shim surface (step 1). Due to the high surface hydrophobicity, a TOPAS microscope slide was laid on top to spread the liquid out (step 2). After 10 min of incubation at room temperature, the slide was removed and the shim was washed with MilliQ water to remove unbound protein (step 3). Polymer replicas were molded as described in **Section 4.2.1**.

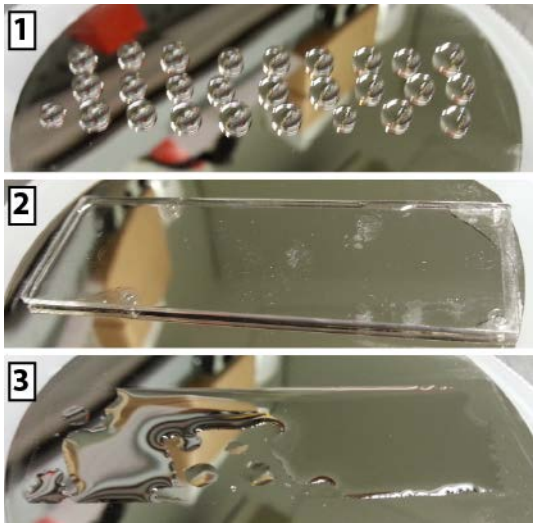

Figure 4-7. Protein deposition on SiO_2+FDTS-coated Ni mold. **Step 1:** Droplets of protein in PBS were deposited on the shim by pipetting. **Step 2:** A TOPAS microscope slide was laid on top to facilitate wetting of the hydrophobic surface. **Step 3:** After protein adsorption, the shim was washed with MilliQ water and dried.

4.3.1.3 Cell adhesion studies in parallel plate flow chamber

The experimental procedure was based on the work of two previous master students in the group [123]. The adherence of PBMCs and monocytes were examined using a rectangular flow chamber kit for microscope slides (GlycoTech, Gaithersburg, USA). A silicone rubber gasket with a thickness of 127 µm (0.005 inch) was sandwiched between injection molded TOPAS slides and a PMMA flow deck (**Figure 4-8**). The flow chamber was sealed by applying vacuum (V) to the tubings. A Y-splitter was attached to the inlet, to allow injection of PBS wash buffer (W) and cell suspension (I) separately.

To avoid bubbles inside the flow chamber, the level of dissolved gas in the PBS buffer was reduced overnight inside a desiccator. Before cells were injected, the chamber was primed with buffer. Bubbles were removed using pressure from a syringe attached to (I), by pulling back and forth. Frozen PBMCs and monocytes from Herlev Hospital were thawed and washed according to the protocol in **Section A.4**. PBMCs from donor #1 were used for the adhesion studies, and the fraction of $CD14^+$ monocytes was determined to be 19.8% (data not shown). In some experiments, cell

suspensions containing around 90% monocytes (obtained from separation by elutriation) were used instead. Cells were resuspended in either 500 µL PBS or Dulbecco's Modified Eagle Medium (DMEM, D5030) + 10% fetal bovine serum (FBS, F2442) (both from Sigma-Aldrich) at a concentration of 2×10^7 cells/mL, injected into the flow chamber, and allowed to adhere for 30-60 min before the chamber was flushed with wash buffer by a Masterflex L/S peristaltic pump (Cole-Parmer). Cells were observed in a Zeiss Axiovert S100 phase contrast microscope (Carl Zeiss, Oberkochen, Germany), using a 20x 0.4 NA objective. The microscope was operated using software developed by David Selmeczi, a previous group member, using the LabView platform. Images were captured at pre-defined stage positions between each flow step, using an ANDOR iXon camera. The cell count for each image was recorded using a macro written in ImageJ. With the employed seeding density, 300-500 cells were counted before flow was initiated. Flow rates between 0.05-12.8 mL/min, corresponding to a shear stress of 0.03-8.0 Pa, were used. Each flow step lasted for 2-5 min.

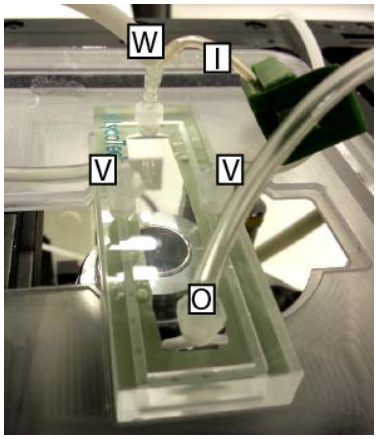

Figure 4-8. The parallel plate flow chamber used for measuring cell adherence. W: Tube for wash buffer. I: Tube for cell injection. V: Tube for vacuum sealing. O: Outlet tubing.

4.3.2 PBMC adhesion to HSA blocked TOPAS

To demonstrate sorting by the specific capture of monocytes from a PBMC population on anti-CD14 spots, a low non-specific adhesion to TOPAS was required. The adhesion was measured on patches blocked with HSA at different concentrations

. First, thawed cells were re-suspended and seeded in PBS (**Figure 4-9a**). Unexpectedly, the majority of cells adhered to the surface for all blocking concentrations. Even at 2.0 Pa, 85-90% of all the seeded cells remained inside the flow chamber. The situation was clearly different when cells were suspended in DMEM+10% fetal bovine serum (FBS) (**Figure 4-9b**). Here, about 50% of all cells were removed at the lowest shear stress when using a blocking concentration above 1 mg/mL, while for lower blocking concentrations, the fraction of adherent cells were below 10%. At high shear stress, less than 10% of all cells remained for all blocking concentrations. For the following experiments cells were only seeded in serum-containing medium.

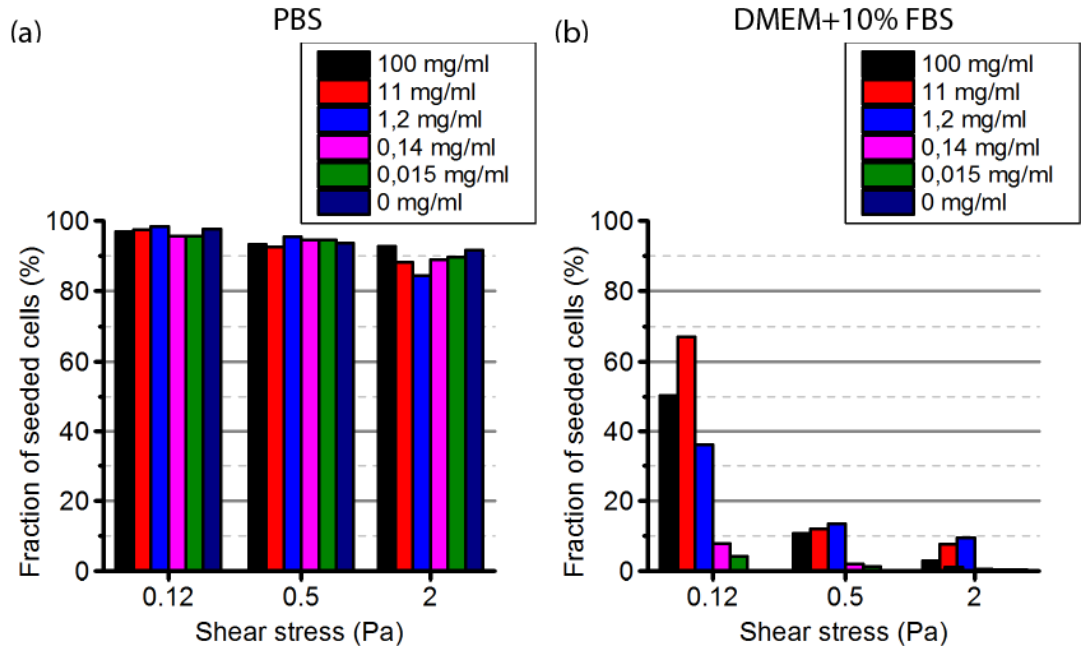

Figure 4-9. Adhesion of PBMCs on patches pre-blocked with different concentrations of HSA (0-100 mg/mL) when seeded in (**a**) PBS (n=2) and (**b**) DMEM+10% FBS (n=1). By suspending cells in serum-containing medium, cells were only loosely bound to patches blocked with more than 1 mg/mL of HSA, and non-adherent to patches with lower blocking concentrations.

4.3.3 Monocyte adhesion to anti-CD14 patches

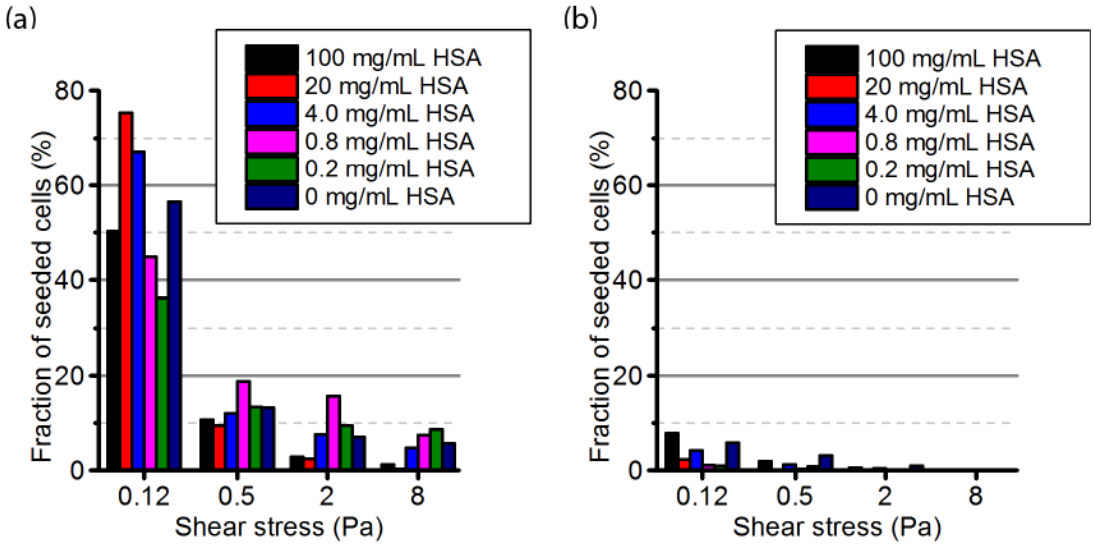

Figure 4-10. Monocyte adhesion to patches coated with (**a**) and without (**b**) avidin. All patches were blocked with the specified concentration of HSA, followed by coating with 100 µg/mL biotin mouse anti-human CD14 for 1 h. Plot shows average values of two independent experiments (n=2).

Figure 4-10 shows adhesion of elutriation-separated monocytes (~90% purity) to TOPAS slides with (**a**), or without (**b**) avidin, blocked with HSA at different concentrations and incubated with 100 µg/mL biotin-anti-CD14. Monocytes bound

loosely to avidin-biotin-anti-CD14 irrespective of the blocking concentration (**a**). When no avidin was present on the surface (**b**), the monocyte adhesion was below 10% at low shear stress for all blocking concentrations, and was further reduced by increasing the flow rate.

Images of monocytes adhered to biotin-anti-CD14 antibody, biotin-isotype control antibody, and avidin after 0, 0.03 and 8.0 Pa shear stress, are shown in **Figure 4-11**. No HSA blocking or wash step was employed between avidin and biotinylated antibody incubation in this experiment. Before sorting, cells adhering to the anti-CD14 patches appeared larger than other cells, indicating that they were spread out (cells with a bright periphery and a dark center). This was seen to some degree also for the isotype control. By applying a low level of shear stress, most of cells on the avidin patch were removed. In contrast, most cells remain on anti-CD14 even at high shear stress. Monocytes also adhere to the isotype control, although with a lower strength.

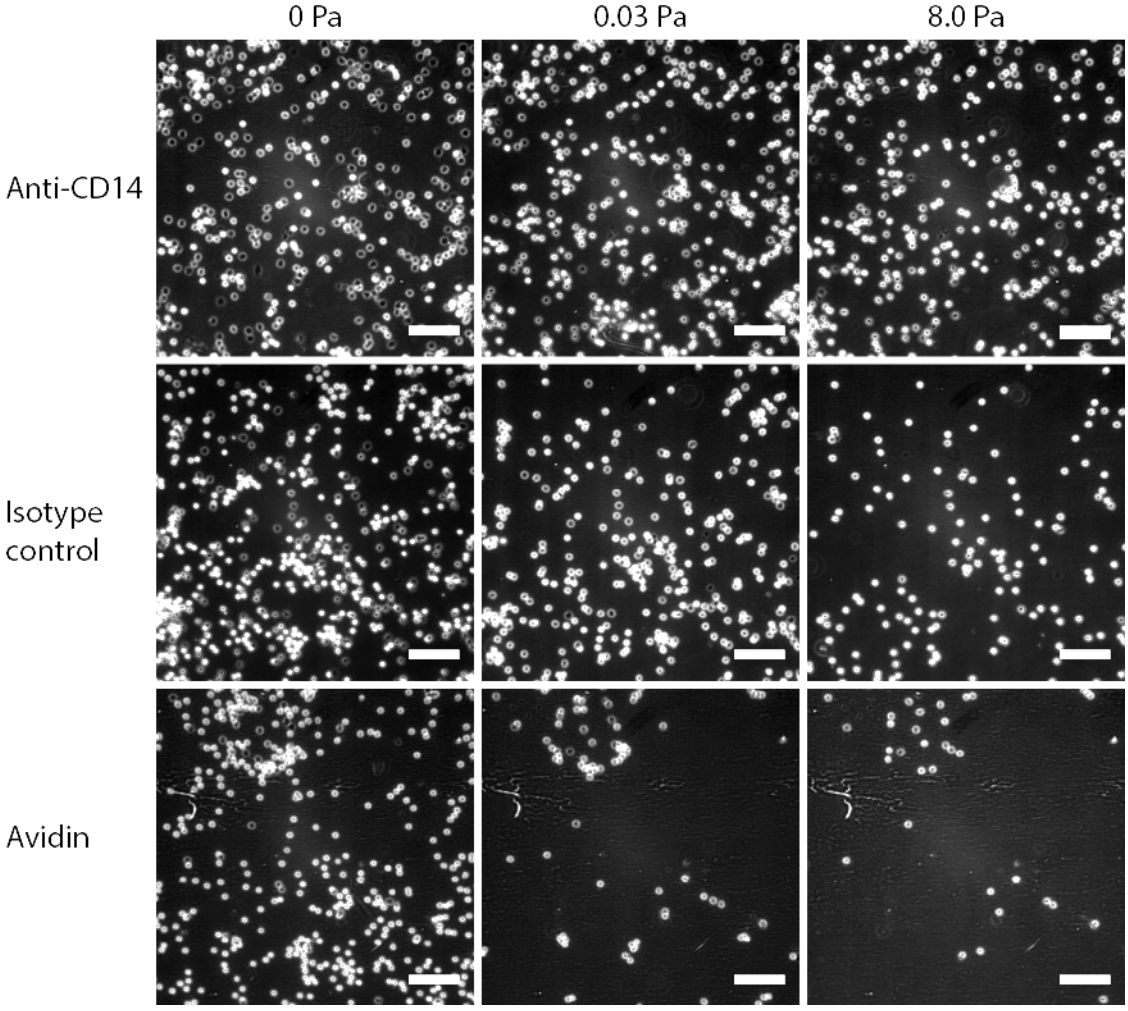

Figure 4-11. Monocyte adhesion on anti-CD14, isotype control, and avidin patches on native TOPAS, under low (0.03 Pa) and high (8.0 Pa) stress. Monocytes adhered firmly to anti-CD14 and spread out as seen the by the larger cell size before flow was initiated. The majority of cells remained attached even at high flow rates, while around 50% of those attached to the isotype control were washed out. Monocytes were mostly non-adherent to avidin patches even at low shear stress.

Figure 4-12 shows monocyte adhesion to patches with bound (**a**) anti-CD14 and (**b**) isotype IgG control through the avidin-biotin link from the same experiment as presented in **Figure 4-11**. Monocytes bound strongly to anti-CD14 at concentrations

above 10 µg/mL; at 0.5 Pa, more than 90% of cells were remaining. In (**b**), more than 60% of monocytes adhered non-specifically to the isotype control antibody after washing with 0.5 Pa. At 1 µg/mL antibody concentration the adhesion of anti-CD14 and isotype control was similar to that of avidin (0 µg/mL).

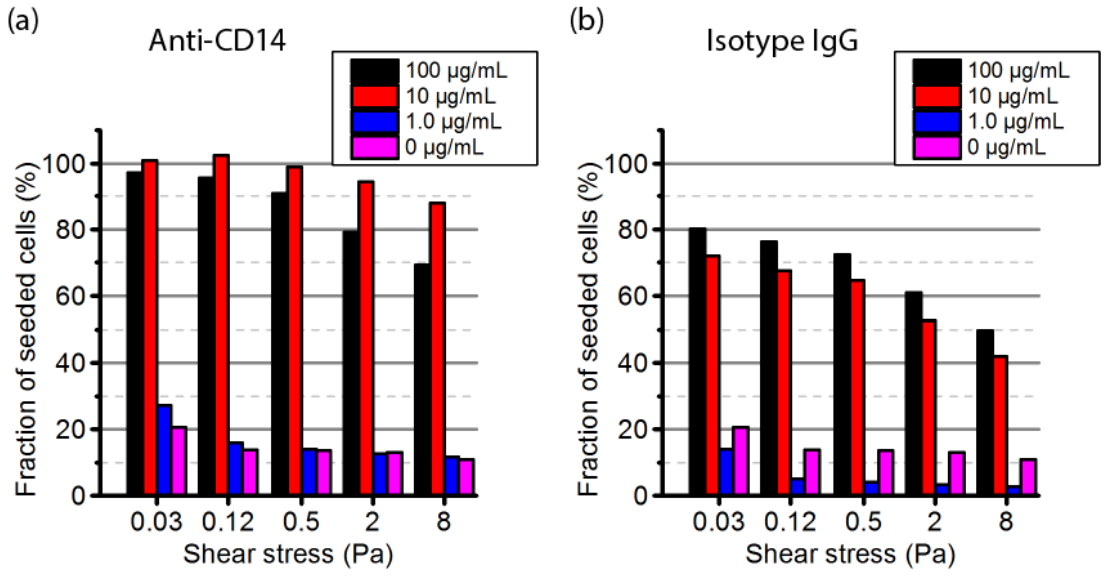

Figure 4-12. Monocyte adhesion to patches coated with (**a**) biotin-anti-CD14 and (**b**) biotin-isotype IgG at the indicated concentrations. All patches were incubated overnight with avidin prior to antibody-coating for 1 h. Plots show average values of two independent experiments (n=2).

4.3.4 InMold transferred avidin for monocyte capture

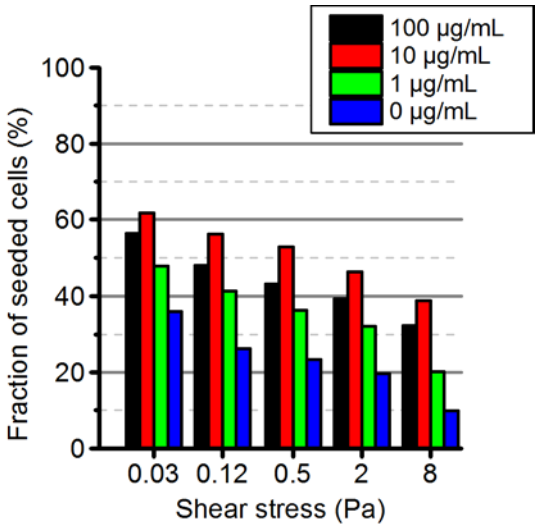

Figure 4-13. Monocyte adhesion to biotin-anti-CD14 on slides with InMold transferred avidin (n=1) was slightly higher on than avidin.

Figure 4-13 shows monocyte adhesion to patches with different concentrations of biotin-anti-CD14 on InMold transferred avidin. The highest difference in adhesion was observed between 10 and 0 µg/mL, where the fraction of adhered monocytes was 62% and 36% at 0.03 Pa, and 32% and 10% at 8.0 Pa respectively. However, the adhesion

to antibodies was not as strong compared to when avidin was immobilized directly on the polymer surface by passive adsorption (**Figure 4-12**). In addition, the difference between coated and non-coated anti-CD14 areas was smaller than what was observed for passive adsorption.

4.3.5 Monocyte-adhesion on nanostructures

The adhesion of monocytes to a microscope slide with nanoscale topography injection molded with the same conditions as for the sample shown in **Figure 3-1b** and **Figure 3-6**, were studied using the parallel plate flow chamber. The microscope slide was treated with air plasma (50 W, 10 min) immediately before the experiment. No protein coating was applied to the surface prior to cell seeding. The nanostructured areas could easily be distinguished in the microscope due to the interference pattern generated when illuminated.

Figure 4-14 shows the relative number of monocytes adhering to the different fields patterned with 240 nm holes, with respect to the initial cell count before any shear stress was applied. At a shear level of 0.03 Pa, the relative density was only slightly lower for 240/380 nm and 240/720 nm structures. However, at 8.0 Pa, the cell density was greatly reduced for the 240/380 nm structure relative to the unstructured field (36 % *vs.* 96 %), while for the other nanopatterned fields there was almost no change.

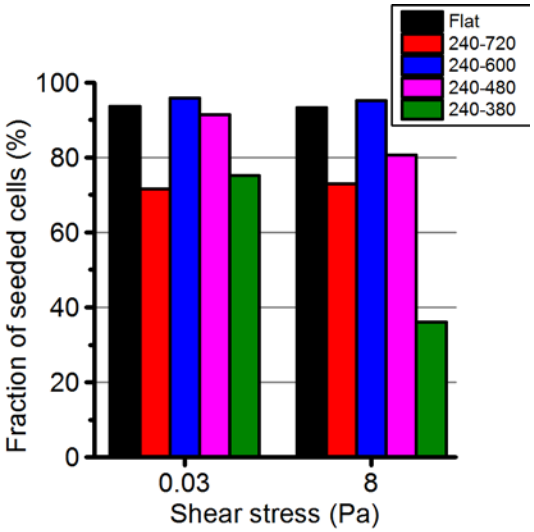

Figure 4-14. Monocyte adhesion to the different nanostructured areas, annotated by nominal hole diameter and center to center pitch, under different shear stress levels. The lowest cell adhesion was observed for the 240-380 nm structure, where 36% remained after a shear stress of 8 Pa was applied.

Figure 4-15 shows adherent cells on different topographies after 1 h incubation inside the flow chamber. Compared to the unstructured area, cells appeared slightly more elongated on the field with 240 nm wide holes on a pitch of 380 nm. A strong orientation-specific elongation was observed for cells adhering to the linear gratings, where several cells were elongated along the axis of the gratings.

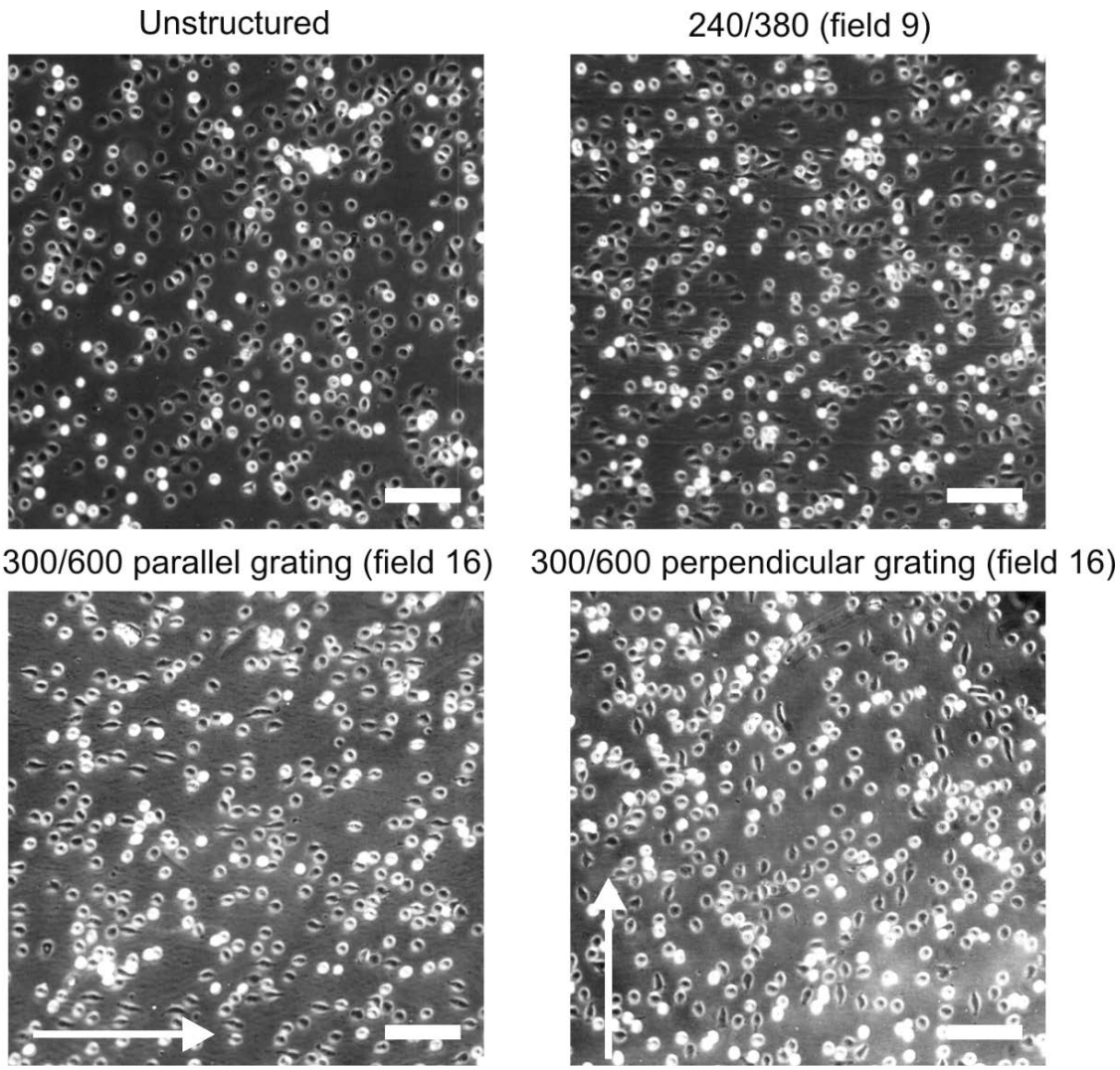

Figure 4-15. Phase contrast micrographs of adherent monocytes after 1 h incubation in serum-containing cell medium at room temperature, before shear stress was applied. Cells appear more elongated when adhering to the 240/380 nm (diameter/pitch) structure, compared to an unstructured part of the surface. In addition, it appears as if cells align along the axis of 300/600 nm parallel and perpendicular gratings, indicated by the white arrows. The scale bars are 100 µm.

4.4 Discussion

4.4.1 Avidin patterning and InMold transfer of protein

The first experiments using PBS as spotting buffer produced irregular spots on FDTS with a diameter decreasing with the concentration (**Figure 4-3**). In contrast to the coffee-ring effect where most of the material is deposited along the drop perimeter, spots at a concentration above 65 µg/mL displayed an outer ring with a fluorescence intensity barely above the background level, while the center part had a high intensity, suggesting that most of the material was deposited there. This is often referred to as spiking [124]. Due to the fast evaporation of the droplets (< 1 min), it could be suggested that the amount of initially adsorbed protein was not sufficient to pin the

contact line. As the droplet evaporates, the contact line retracts with a constant receding angle (**Table 4-1**). Due to the rapidly shrinking volume and the low amount of adsorbed protein, the protein concentration in solution increases until a point where the droplet becomes self-pinned. From this point on, the droplet evaporates with decreasing contact angle and a constant contact area. The idea that a threshold concentration for droplet pinning exists is supported by **Figure A-12**, which shows a constant spot size on FDTS above 300 µg/mL, suggesting that droplets in this concentration range were initially self-pinned. At lower initial protein concentrations, pinning only occurred after a certain amount of liquid had evaporated, when the threshold concentration was reached. A similar behavior was seen when spotting on PS, only that the threshold concentration for self-pinning was lower (< 100 µg/mL).

Choi and Kim [125] studied the contact angle over time for evaporating droplets on Teflon-coated surfaces. Water droplets initially maintained a constant contact area with a contact angle decreasing from 116° to 110°, before switching over to a constant receding angle with a continuously decreasing contact area. For droplets of DMEM containing 10% FBS (corresponding to about 4 mg/mL protein [126]), the contact line was pinned throughout the entire evaporation process, with the contact angle continuously decreasing from 111° to 0°. This study does not describe pinning at lower protein concentrations however.

The fact that the droplets were not completely dried out likely explains the homogeneous spot in **Figure 4-4**. Addition of 10% v/v DMSO (mole fraction X_{DMSO} = 0.027) to the spotting buffer significantly reduced the evaporation rate of the droplets. Since DMSO has a lower vapor pressure compared to water ($P_{V,DMSO}$ = 0.051 kPa, $P_{V,water}$ = 2.372 kPa at 20 °C), the addition of 17% v/v DMSO (X_{DMSO} = 0.049) has been reported to reduce the vapor pressure to 2.145 kPa [127]. At the conditions inside the cover of the Nanospotter (25 °C and 70% relative humidity), the partial pressure of water vapor is 2.226 kPa [128]. It is therefore likely that the vapor pressure of droplets of 10% v/v DMSO in PBS, sitting on the shim at 20 °C, is very close to being saturated. In addition, DMSO and water mixtures does not form azeotropes, which means that X_{DMSO} will increase during evaporation due to the higher vapor pressure of water [127], which means that at some point evaporation from protein-containing droplets will stop. It should be added that due to the large surface to volume ratio of the droplets, the evaporation is likely highly sensitive to small fluctuations in the surrounding atmosphere, so parameters like temperature and humidity must be carefully controlled.

As mentioned, deposition of PBS was not possible on field 4 and 7 for the nanostructured shim, which were two of the structures with the highest contact angle and a low hysteresis (**Table 4-1**). On the other hand, droplets could be deposited on field 6, which also had a high contact angle and a low hysteresis. **Table 4-2** shows the measured static contact angles θ of the different structures together with theoretical contact angles θ_W and θ_C, according to a wetting (Wenzel) [129] and non-wetting state (Cassie-Baxter) [130], which can be calculated by the two formulas:

$$\cos\theta_W = r\cos\theta \tag{4-3}$$

$$\cos\theta_C = f(\cos\theta + 1) - 1 \tag{4-4}$$

where r is the roughness factor and f is the fraction of the projected surface area that is wetted. In the calculations for the Cassie-Baxter state, it was assumed that the droplet only touches the top of the pillars, which was assumed to be flat and smooth. The contact angles measured on field 4 and 7 was close to the predicted angle for the non-wetted state. A Cassie-Baxter state for these structures is also supported by the low contact angle hysteresis (**Table 4-1**). Field 6 had a contact angle close to both θ_W and

θ_C, while field 3 and 5 might be in a partially wetted state as the measured angle was somewhere in between the two states.

Table 4-2. Static contact angle together with contact angles according to the Wenzel (θ_W) and Cassie-Baxter model (θ_C) for SiO_2+FDTS-coated Ni nanostructures, with different diameter *d*, spacing *s*, filling factor *f* of protrusions, and roughness factor *r*. *Structures were holes instead of protruding pillars.

Field	d [nm]	s [nm]	f	r	θ [°]	θ_W [°]	θ_C [°]
Flat	-	-	-		111.7±1.4	-	
3*	210	170	0.76	2.5	136.9±3.0	158	121
4	264	216	0.24	2.2	149.8±1.7	144	148
5	243	477	0.09	1.5	145.2±3.5	124	161
6	151	189	0.15	2.4	153.1±1.4	153	155
7	128	272	0.08	1.8	157.4±3.1	132	162

Droplets of radius ~ 1 mm used for measuring contact angles were in the Cassie-Baxter state, but smaller droplets might not be in the same state. The Laplace pressure due to the curved air-liquid interface is given by

$$\Delta P = \frac{2\gamma}{R} \tag{4-5}$$

where γ is the surface tension and *R* is the droplet radius. For droplets with a radius of 1 mm, the pressure difference across the liquid-air interface is 146 Pa, while it is 2.9 kPa for a radius of 50 µm. It is known that transition from the non-wetting to the wetting state can be induced by an external pressure [131], which might be caused by the increased Laplace pressure as the droplet size decreases [132]. Therefore, it is more likely that pL droplets printed on the shim exist in a fully wetted or partially wetted state, than what is predicted by macroscopic contact angle measurements.

By addition of 10% v/v DMSO, which lowers the surface tension slightly from 72.8 mN/m to 67.5 mN/m [133], it was possible to spot on all nanostructures. As the DMSO content increases during evaporation, the surface tension is also approaching the surface tension of pure DMSO, which is 43.5 mN/m. This could explain why the avidin spot size on a flat surface was slightly larger compared to when PBS was used as the spotting buffer (**Figure 4-4**). Since the size was constant for 50-500 µg/mL protein (**Figure A-14**), it could be suggested that the contact line was pinned throughout the incubation period.

Finally, it was demonstrated that InMold transfer of homogeneous avidin spots with retained biotin-recognition could be reproduced from earlier work. In an earlier PhD project in the group, areas on the shim with a high density of proteins caused by drying of the liquid solution were poorly replicated [134]. Therefore, the addition of DMSO to the spotting buffer could also be beneficial for the InMold transfer process. InMold transfer of functional capture antibodies will be further described in Chapter 5.

4.4.2 Cell capture on injection molded thermoplastics

PBMCs were observed to be highly adherent to untreated TOPAS with and without pre-adsorbed HAS when cells were seeded in PBS, while they were non-adherent to the same surface when re-suspended in serum-containing medium. This was in line with previous observations of leukocytes adhering equally well to tissue culture grade and native PS in serum-free medium [135]. In that study, cells became

highly adherent to PS containing hydroxyl surface groups and non-adherent to native PS when serum proteins were added. It might therefore be possible that metabolically active cells secrete their own adhesion-promoting proteins that proteins adsorbs effectively to hydrophobic PS without competition from serum, or that proteins on the membrane adsorb directly to the polymer. In addition, serum proteins likely adsorb at different amount and with a different orientation on hydrophobic and hydrophilic culture dishes. In another study, fibronectin, albumin, alpha-1-antitrypsin and alpha-2-macroglobulin, but not transferrin, pre-adsorbed to untreated PS decreased leukocyte adhesion in serum-free media, while for tissue-culture grade PS no change was observed [136].

It is not clear why HSA blocking of hydrophobic TOPAS did not reduce cell adhesion in PBS, although it might be explained by cell binding to proteins that denature during drying of the slides. Indeed, it has previously been found that monocytes adhere better to denatured BSA compared to native BSA [137].

Monocytes did not adhere to native TOPAS pre-coated with 100 µg/mL biotin-anti-CD14 when avidin was not present (**Figure 4-10**), which could suggest that either a too low amount of physisorbed antibody was present after the washing steps, or that the orientation was not ideal for cell capture. When avidin was adsorbed prior to the antibody, monocytes was efficiently captured on the polymer surface. Furthermore, by omitting the wash step between avidin and biotin-anti-CD14 incubations, an even higher fraction of monocytes could be captured (**Figure 4-12**). A concentration of 10 µg/mL seemed optimal, while at 1 µg/mL there was no improved cell adhesion. However, the adhesion through CD14 recognition was not very specific, as a large fraction of cells also adhered to the isotype control. This could be explained by the binding to adsorbed IgG molecules through monocyte Fc receptors [138]. Although this is not a disadvantage for monocyte isolation, IgG recognition through the Fc fragment should be reduced for co-culture applications where monocyte capture together with other cells on distinct spots is targeted. A way to avoid this could be to block the Fc receptors prior to seeding by human AB serum [24], which contains a higher amount of IgG than FBS. The largest separation between monocytes adhering specifically and non-specifically occurred at the highest shear rate, indicating that cells had a higher avidity to anti-CD14 antibodies than the isotype control.

Monocyte adhesion was also increased when anti-CD14 antibody was incubated on slides with InMold transferred avidin. However, the difference between coated and non-coated areas was smaller than for passive adsorption of avidin, even though biotin-recognition was demonstrated in **Figure 4-6**. The reason could be both due to a lower amount of avidin adsorbed on the surface (50 µg/mL for 10 min at 25 °C on the shim, versus 1 mg/mL overnight at 4 °C on the plastic), and/or that a lower fraction of avidin was able to recognize biotin after injection molding. However, time did not permit optimization of the concentration or incubation time for InMold transferred avidin with the purpose of achieving cell capture. Also, one should also be careful to draw conclusion between different experimental series, as the applied shear rate is highly dependent on changes in the chamber height, which might be caused by small folds in the silicone gasket made during assembly of the flow chamber.

Previously, Sekine et al. demonstrated panning of multiple leukocyte subsets on spots with anti-CD4, anti-CD8, anti-CD36, and anti-CD16b antibodies physisorbed on polyethylene glycol (PEG) coated glass slides [27]. A purity of 97.2% of $CD14^+$ monocytes re-suspended in PBS from red blood cell (RBC)-lysed whole blood was achieved on anti-CD36 spots, after applying a shear stress of 0.16 Pa. However, the yield was not mentioned in this study. The high specificity is likely due to the high resistance of PEG against non-specific leukocyte adhesion, which was demonstrated

by a cell density after washing of only 0.07% relative to cell-adhesive poly-L-lysine. PEG-coated glass slides with antibody spots have also been used for efficient CD4 and CD8 T-cell separation [139], [140]. In another study, monocytes from RBC-lysed whole blood were efficiently captured at shear stresses below 0.05 Pa, using 75 µg/mL anti-CD14 on glass slides, although the purity was not described [141]. To anchor the antibodies, the glass slides were surface functionalized in a two-step process with a silane and a coupling agent containing an amine-reactive group. Although several devices has demonstrated selective capture of leukocyte subpopulations, the fabrication processes are rather cumbersome, involving several process steps in order to achieve the high specificity. Instead of using glass, it would be advantageous to use injection molded thermoplastics for disposable devices. In the next chapter, functional transfer of polyclonal antibodies by injection molding will be discussed.

Finally, monocyte adhesion on plasma oxidized TOPAS with nanoscale topography was briefly described. Cell adherence to 240 nm holes with 380 nm pitch was noticeably reduced, while for structures with increased spacing between holes, the adhesion was not much different from an unstructured surface. The lower cell adhesion might be explained by the reduced surface area available for cell adhesion, when holes on the surface were brought closer together. In addition, the replicated features appeared more as parallel ridges having a width of only 70-120 nm, with the hole pattern buried deeper into the surface (**Figure 3-6**), which could explain why this pattern led to a noticeable lower adhesion. This could also explain why the cells appeared more elongated in the horizontal direction, as cells are known to align along linear gratings below a certain size [142], [143]. A summary of some literature reporting on cell adhesion on nanostructured surfaces is shown in **Table 4-3**. Most studies report a reduced adhesion, although the largest difference appears for hole diameter below a certain limit. Similarly, it has been observed that with small protrusions on the surface having a large separation distance, the cell membrane is able to conform to the topography, while for pillars more closely spaced, the cell-substrate contact area is reduced [144]. For the 240 nm hole structures which was fully replicated in this thesis, it may be that the hole diameter was too large to reduce the surface area available for cell adhesion.

Table 4-3. Summary of selected literature on cell adhesion on different nanostructured polymer surfaces. A reduced adhesion is denoted by "÷", no difference by "0", and increased adhesion by "+".*Topography was disordered and with a wide distribution in feature size. PLGA = poly(lactic-co-glycolic acid); PCL = polycaprolactone; HUVEC = human umbilical vein endothelial cell; CPAE = calf pulmonary artery endothelial cell.

Cell type	Material	Feature type	Width [nm]	Depth/ height [nm]	Pitch [nm]	Adh.	Ref
Osteoblasts	PC	Holes	120	100	300	÷	[145]
Osteoblasts	PS	Holes/pillars	200	500	500	+	[146]*
Fibroblasts	PCL, PMMA	Holes	35-120	50-100	100-300	÷	[147] [148]
Fibroblasts	PCL	Holes	150	80	300	÷	[149]
Astrocytes	PS	Grooves	10.000	3.000	20.000	÷	[142]
HUVECs	PLGA	Grooves	350-1750	500	750-2100	÷	[143]
CPAEs	PLGA	Grooves	350-1750	500	750-2100	0	[143]

4.5 Conclusion

Avidin spots with a diameter lower than 100 µm and a pitch of 200 µm can be printed on an FDTS-coated Ni shim at a speed greater than 18 spots/s. When proteins were spotted in PBS, the resulting pattern was inhomogeneous, with a higher intensity at the center of the spot. The spot diameter changed with protein concentration, indicating that a threshold level for droplet pinning exists. By addition of 10% DMSO, the spot homogeneity was improved, likely due to a reduced evaporation rate of the droplets. This also enabled spotting on nanostructured Ni structures displaying superhydrophobicity. Finally, the transfer of avidin spots by injection molding was achieved with retained biotin recognition.

By shear stress studies of PBMCs in a parallel plate flow showed that cells were highly adherent to native TOPAS without serum proteins, while they became non-adherent when serum was added. Blocking of the surface with HSA did not appear to have any effect in either case. Furthermore, capture of monocytes to anti-CD14 spots were achieved, although with a low level of specificity. Biotinylated anti-CD14 bound to InMold transferred avidin also demonstrated the ability to capture monocytes, although for further optimization of the transfer process is needed to reach the same capture efficiency as antibodies bound to avidin passively adsorbed on plastic. Finally, reduced monocyte adhesion was shown on one of the injection molded nanostructures, although more experiments are needed before any conclusion can be made.

Chapter 5
Antibody Immobilization by Injection Molding

5.1 Introduction

Immobilization of antibodies to solid substrates is of great importance for various applications, such as protein microarrays for proteomics [29], development of personalized drugs [30] and point-of-care diagnostics [31], immunoassays such as the enzyme-linked immunosorbent assay (ELISA) [150], in addition to cell capture through surface antigen-recognition as previously discussed. Most biochips employing covalent protein immobilization are made from materials such as glass or silicon [151], [152]. However, it is advantageous to use thermoplastic polymers instead due to lower

production cost, which is especially important for disposable devices.

Thermoplastic substrates popularly used in life science applications such as PS, PC, COC, PP and PMMA are inert in their native form and therefore need to be chemically activated prior to protein binding [32]. This can be done by introducing functional groups on the surface like epoxy or amines by photoactivation [153]–[155], by forming functionalized polymer adlayers [156], [157] prior to protein linkage, or by direct photoimmobilization of proteins using a photoiniator [158]. However, these methods inevitably add extra steps to a production line, increasing both time and cost.

It would be advantageous if the protein deposition could be readily integrated in the injection molding process (**Figure 5-1**). The direct entrapment of avidin, fibronectin, and HRP on the surface of PP and PMMA replicas formed during injection molding, with some retained biofunctionality, and the transfer of fluorescently labelled IgG has previously been reported [33], [134], [159]. In addition, transfer of avidin micro-patterns deposited by spotting was also demonstrated in the previous chapter. Through the avidin-biotin link, it is therefore possible to immobilize antibodies to the polymer surface. This route, however, still adds extra process steps. Therefore it would be advantageous to integrate antibodies directly in the polymer surface through InMold transfer.

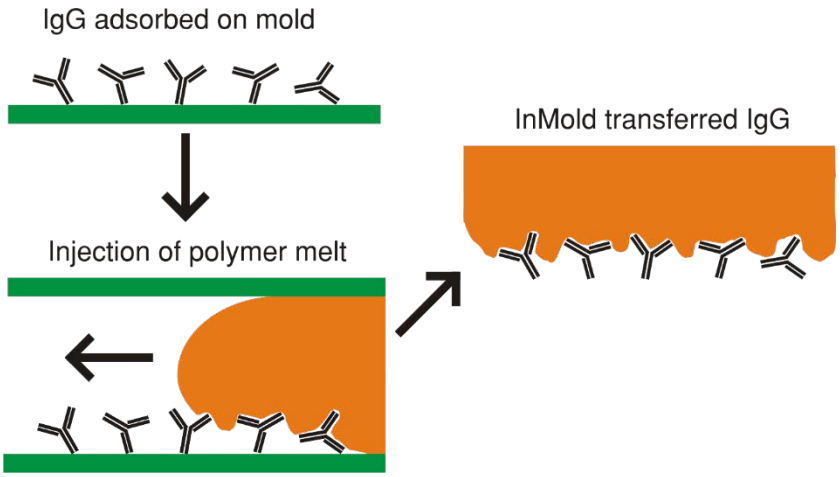

Figure 5-1. Schematic overview of the transfer of IgG by injection molding. IgG is adsorbed to the mold surface, before the inlay is installed and melted polymer is injected into the cavity. After de-molding, the IgG molecules are transferred to the polymer surface.

In this chapter, the transfer of functionally active antibodies, specifically anti-mouse IgG, from the mold surface to a COC replica by injection molding is demonstrated. The high transfer efficiency procedure mediated by the anti-stiction coating on the mold surface is characterized using AFM, x-ray photoelectron spectroscopy (XPS) and contact angle measurements. Furthermore, the retained antigen-binding affinity of the transferred antibody is at a level that is comparable to that of antibodies deposited on the polymer surface by conventional passive adsorption, as demonstrated by ELISA.

5.2 Experimental procedures

5.2.1 Materials

dPBS (D8537), DMEM (D5030), IgG from mouse serum (I5381), anti-mouse IgG (whole molecule) antibody produced in rabbit (M7023), anti-mouse IgG (whole molecule)-peroxidase antibody produced in goat (A4416), BSA (≤25 ng IgG/mg BSA, A9085), FBS (F2442), penicillin/streptomycin (P/S, P4333), 3,3',5,5'-Tetramethylbenzidine liquid substrate system for ELISA (TMB, T0440), and 2,2′-Azino-bis(3-ethylbenzothiazoline-6-sulfonic acid) (ABTS, A3219) liquid substrate system for ELISA were purchased from Sigma Aldrich (St. Louis, MO). Rabbit anti-mouse IgG antibody conjugated with HRP (P0260) was purchased from Dako (Glostrup, Denmark). All water used was purified with a Millipore MilliQ system (Boston, MA). The blocking buffer consisted of 0.05% v/v Tween 20 (Merck-Schuchardt, Hohenbrunn, Germany) and 0.1% w/v BSA in 1x dPBS. The wash buffer consisted of 0.05% v/v Tween 20 in 1x dPBS. The colorimetric reaction was stopped by addition of 0.5 M H_2SO_4 in MilliQ water. Protein stability tests used an incubation buffer of 10% v/v FBS and 100 U/mL P/S in DMEM. All incubation steps were done at room temperature (25 °C) unless otherwise stated. 12-well removable silicone chambers (81201) and 8-well sticky-slide chambers (80828) was purchased from ibidi (Martinsried, Germany). Nunc 96-well polystyrene plates (260860) were acquired from Fischer Scientific (Roskilde, Denmark). For injection molding, TOPAS ® 8007-S04 (COC) was purchased from Topas Advanced Polymers (Frankfurt-Höchst, Germany) and shims of electroplated nickel were obtained from DVD Norden (Sakskøbing, Denmark).

5.2.2 InMold transfer of antigen

IgG from mouse serum was deposited by passive adsorption on the FDTS-coated mold inlays, by dispensing protein solutions in a titration series (0-100 µg/mL) in dPBS for 10 min, using the 12-well chamber attached to the mold (**Figure A-15**). Excess protein and salts from the buffer were removed by immersing the molds in 30 mL MilliQ water for 1 min, before the inlay surfaces were dried with a pressurized air gun. The protein-coated mold inlays were immediately installed and TOPAS 8007 was injected into the mold, which was kept at a temperature (T_{mold}) of 20 °C. Otherwise, similar parameters as those described in **Table 3-1** were used. The replicas with transferred protein were kept in a sealed zip-lock bag in a refrigerator at 4 °C until analysis. After each transfer cycle, the mold inlay was treated with oxygen plasma to remove any residual proteins, and a new FDTS layer was deposited by MVD.

The functionality of immobilized protein was assessed using indirect ELISA. The patches with transferred proteins were identified by wetting the replica surface with PBS, and the 12-well silicone chamber was mounted by manual alignment to the hydrophilic areas. Blocking buffer was added to each well (300 µL) and incubated for 1 h. After blocking, each well was washed 6 x 3 min with washing buffer, and 100 µL 0.5 µg/mL goat anti-mouse IgG-HRP (detection antibody) in blocking buffer was added and incubated for 1 h. Afterwards, the same washing procedure was repeated followed by addition of 100 µL ABTS substrate. The enzymatic conversion by the peroxidase enzyme was measured by continuously recording the absorbance during 10

min in the silicone wells at 405 nm using a Victor3 plate reader (Perkin Elmer, Santa Clara, USA). The change in absorbance values over time were fitted by linear regression and the slope was correlated to the amount of antigen present on the surface.

5.2.3 InMold transfer of capture antibodies

Rabbit anti-mouse IgG was deposited by passive adsorption on the FDTS-coated mold inlays by dispensing a solution of 10 µg/mL protein in dPBS for 10 or 60 min. A microscope slide was used to spread liquid over the shim area (**Figure 4-7**). The transfer procedure of capture antibody was otherwise performed similarly to antigen transfer. For the experimental series studying the ability to re-use the same mold without plasma treatment and FDTS-coating, new protein solution was added after each transfer without cleaning the mold surface.

The functionality of the immobilized antibody was assessed using a sandwich ELISA. The silicone chamber was mounted on the polymer replica slides with transferred antibody, before adding 300 µL of blocking buffer to each well and incubating for 1 h. After blocking, the excess solution was tapped out and 100 µL mouse IgG (antigen) in blocking buffer was added and incubated for 16 h at 4 °C. Each well was washed 6 x 3 min with washing buffer, and 100 µL 0.5 µg/mL rabbit anti-mouse IgG-HRP (detection antibody) in blocking buffer was added and incubated for 1 h. Afterwards, the same washing procedure was repeated followed by adding 100 µL TMB substrate and incubating for 10 min on a shaking table. 100 µL 0.5 M aqueous H_2SO_4 was added to stop the enzymatic reaction, and 100 µL supernatant was transferred from each well on the polymer replicas to a transparent 96 well PS plate, where the absorbance was read at 450 nm. For comparison, capture antibody was deposited on uncoated polymer replica slides by passive adsorption from solution, using the same coating procedure and concentrations as for the mold inlays, before washing with MilliQ water, drying and mounting the silicone well chambers.

For the protein stability tests, a bottomless 8-well slide was attached to the polymer replicas by adhesive tape and 500 µL of DMEM with 10% v/v FBS and 100 U/mL P/S was added. The slides were incubated in a sealed bag in the refrigerator at 4 °C for 9 days, before performing a sandwich ELISA as described. It should be noted that the slides with transferred proteins were stored in the dried state for 3 weeks at 4 °C before the stability tests were initiated.

5.2.4 Characterization of the transfer efficiency

The mold inlay surface before protein deposition, after protein deposition, and after protein transfer by injection molding, as well as the surface of the polymer replicas with and without transferred proteins was characterized by AFM (XE-100, Park Systems, South Korea) using BudgetSensor-300 cantilevers operated in intermittent contact mode. The recorded micrographs were adjusted with a plane fit at an average zero height. XPS was performed with a K-Alpha spectrometer (Thermo Scientific, U.K.) using a 400 µm wide monochromatized Al K_α X-ray beam spot and pass energies of 50 and 200 eV for high resolution and survey spectra respectively. Elemental composition analysis and deconvolution of C1s spectra were performed using the instrument manufacturer's Avantage software package. Advancing and receding contact angles of water were measured optically using an OCA 20 system (dataphysics, Germany), by the dynamic sessile drop method, through

adding/removing liquid at 0.1 µL/s and calculating the average angle while the length of the contact line increased/decreased. Static contact angles of water, diiodomethane, and benzyl alcohol were measured using a Drop Shape Analyzer DSA100S (Krüss, Germany) inside cleanroom-facilities. The surface energy with dispersive and polar components was calculated using the Owens-Wendt method [68]. At least 5 drops on different positions on each sample were measured.

5.2.5 Data Analysis and Curve Fitting

Quantitative data are reported as mean ± standard error of the mean (SE) unless otherwise stated. Statistical significance was evaluated using Welch's t-test for two samples having possibly unequal variances [160]. The antigen standard curves were quantified using a Four Parameter Logistic (4PL) curve fit, $A = A_0 + (A_{max} - A_0)/\left(1 + \left(\frac{c}{EC_{50}}\right)^{\alpha}\right)$, where A is the measured absorbance, A_0 the absorbance at zero analyte concentration, A_{max} the saturation absorbance from the analyte, c the analyte concentration, EC_{50} the half maximum effective concentration, and α is the Hill curve steepness [161]. A limit of detection (LoD) for each assay was defined as the mean value + 3x the standard deviation of the zero antigen well [162].

5.3 Results

5.3.1 IgG transfer efficiency from mold to replica

Efficient transfer of antibodies during the injection molding process is essential to produce replicas with biofunctionally highly active surfaces and to establish an automatable process sequence. Earlier experiments in the group compared IgG transfer from mold inlays of native hydrophilic nickel to inlays of nickel with FDTS at the surface. Native nickel inlays resulted in markedly poorer transfer efficiency (data not shown). Thus, only FDTS-coated mold inlays were considered in the further work.

The transfer efficiency of rabbit anti-mouse IgG was evaluated qualitatively by AFM and contact angle analysis, and quantitatively by XPS on both the mold inlay and replica surfaces. **Figure 5-2 (**a-c) compares the topography of the mold inlay surface before and after protein transfer. Freshly prepared FDTS-coating on a Ni mold had a certain surface roughness (**Figure 5-2**a). Proteins adsorbed on the inlay surface (**Figure 5-2**b) appear as surface protrusions (bright dots and lines) of an apparent width <50 nm, superimposed on the FDTS-layer. The mold inlay surface after transfer (**Figure 5-2**c) shows again a similar topography to a clean Ni mold, with lower surface roughness and on a longer lateral length scale, indicating that most of the proteins were removed during transfer. **Figure 5-2** (d + e) compares the topographies of polymer replicas molded against inlays with or without adsorbed protein. The surface roughness was higher and dominated by features on a shorter length scale for the replica surface molded against an IgG-coated inlay (**Figure 5-2**e) than the replica from an uncoated inlay (**Figure 5-2**d). The topography of the replica with molded protein (**Figure 5-2**e) was similar in appearance to proteins adsorbed on the mold surface (**Figure 5-2**b); although the peak-to-valley heights on the associated line profiles appear to be smaller on the replica. Five line profiles were measured across proteins on both mold inlay and polymer replica (**Figure A-16**), and the average peak height against a flat background

was 5.3 nm and 3.6 nm respectively, suggesting partial embedding of the protein in the polymer surface.

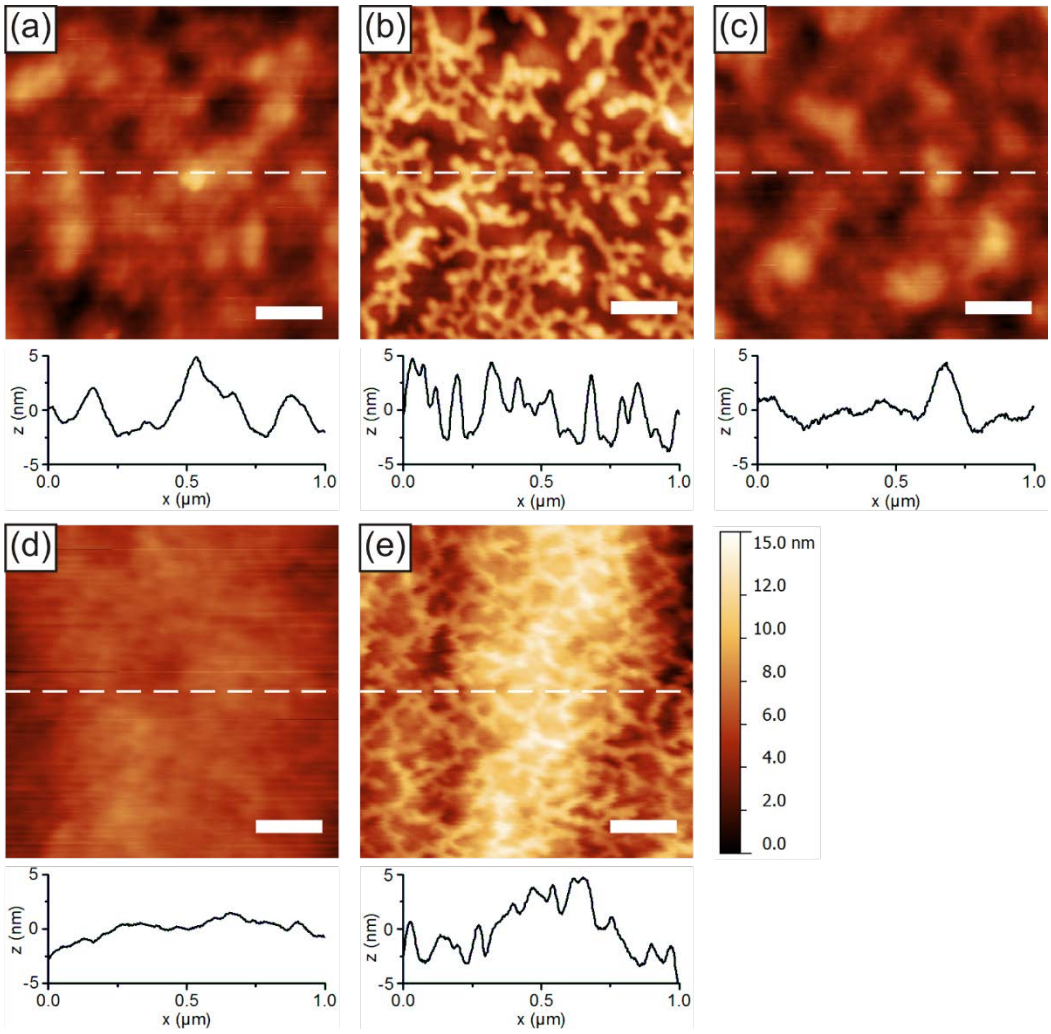

Figure 5-2. Adsorbed protein molecules were efficiently transferred to polymer replicas during injection molding. AFM topography micrographs of the mold inlay surface and polymer replica surface with or without protein (IgG) coating. The height profiles were extracted along the stipulated lines in the micrographs. (a) A clean FDTS-coated mold inlay surface, (b) IgG coated mold inlay surface prior to injection molding, and (c) after injection molding. (d) Polymer replica injection molded from an inlay without IgG coating and (e) with IgG coating. The height scale of the topography images is 15 nm. Scale bars are 200 nm.

XPS analysis was employed to obtain quantitative information on the amount of proteins transferred, the elemental composition of the mold surface before and after deposition of IgG, and after injection molding, as well as the polymer replicas with and without InMold transferred IgG (**Table 5-1**). The analysis showed a distinct increase in carbon and nitrogen surface concentrations after IgG adsorption on the mold, as expected from the polyamide backbone of the proteins. After injection molding, the chemical composition was close to the initial values, with no detectable nitrogen (<0.3 atom %), and only a small increase in the surface concentrations of carbon and fluorine, and a small decrease in the amount of oxygen. The signals from oxygen, fluorine, and silicon originate presumably from the FDTS monolayer and the

underlying SiO_2 adhesion promoter layer on the mold inlay surface. Correspondingly, nitrogen and oxygen signals were detected on a COC polymer replica molded against an IgG-coated inlay but not on a COC (hydrocarbon) replica against an uncoated replica. The amount of adsorbed or transferred protein can be semi-quantitated by the nitrogen surface concentration. Similar concentrations were detected on the IgG-coated mold inlay (2.8 atom %) and on the polymer replica (3.6 atom %), which is in agreement with highly efficient transfer from the FDTS-coated inlay.

Table 5-1. Elemental composition as determined by XPS of mold and replica surfaces with or without protein (IgG) coating before or after injection molding. The values are the average of two measurement points on each sample. The detection limit is estimated to be 0.3 atom%.

	Elemental composition (atom %)				
	C	**N**	**O**	**F**	**Si**
Mold inlay surface (FDTS on SiO_2)	11.4	-	39.5	24.4	24.8
IgG-coated mold inlay	21.4	2.8	34.2	21.2	21.0
IgG-coated mold inlay after injection molding	11.9	-	38.6	24.7	24.8
Polymer replica from uncoated mold inlay	100	-	-	-	-
Polymer replica from IgG-coated mold inlay	90.7	3.6	5.3	-	-

High resolution XPS analysis of the carbon signals from the mold inlay surfaces supported the results of the elemental analysis (**Figure 5-3**). Peak contributions from the mold inlay surface components and from the adsorbed protein were extracted by curve fitting, and subsequently fitted in combination to C_{1s} spectra from the mold inlay in different process stages. More details on the peak deconvolution can be found in **Section A.3**. In brief, mold inlay peak contributions to the carbon spectra were from the fluorocarbon part of the FDTS monolayer at 294.2 eV (C^*F_3-) and 291.9 eV (-C^*F_2-) and from the two methylene units closest to the SiO_2 layer at 286.3 (-CH_2-C^*H_2-CF_2-) and 285.6 eV (-Si-C^*H_2-CH_2-). Adsorbed proteins were assigned to peaks at 288.4 eV, 286.6 eV, and 285.2 eV originating from the amide carbon (-NH-CR-C*(=O)-) in the protein backbone, the nitrogen-bound α-carbon (-NH-C*R-C(=O)-) in the backbone as well as oxygen- and nitrogen-bonded carbon in the side groups, and carbon-carbon bonds in the side groups, respectively. A strong increase in the protein-associated peaks was evident after protein deposition, while contributions from these peaks were hardly detectable for the mold inlay surface after protein transfer.

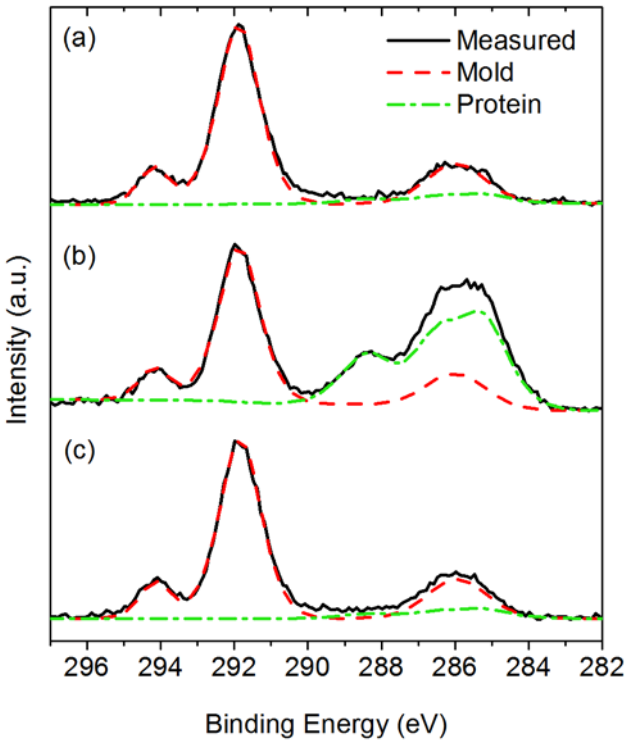

Figure 5-3. C1s high-resolution XPS spectra support complete transfer of protein from the mold inlay during injection molding. (a) Mold inlay surface (FDTS on SiO_2) without proteins, (b) after protein deposition, and (c) after protein transfer to the polymer replica by injection molding. The photoelectron contributions from the mold inlay FDTS layer and the protein coating were fitted by the dashed and dash-dotted curves, respectively.

The transfer efficiency was additionally evaluated by contact angle measurements of water droplets on the mold inlays (**Figure 5-4**). The bare surface, i.e. FDTS-coated SiO_2, exhibited mean advancing and receding water contact angles of 110.8 ± 0.6° and 96.2 ± 1.0° respectively. The total surface energy from contact angle measurement of water, diiodomethane, and benzyl alcohol was calculated to be 10.3 ± 0.1 mJ/m^2, with a polar component of 0.9 ± 0.1 mJ/m^2 and a dispersive component of 9.4 ± 0.2 mJ/m^2 (

). Protein adsorption and transfer to a replica did not give rise to a significant change in the advancing angle on the mold inlay, while the receding contact angle was significantly reduced to 87.7 ± 1.0° ($p < 0.002$,). After plasma treatment and re-coating of the inlay surface with FDTS, both the advancing and receding contact angles returned to their original values. In addition, the static contact angle for water, diiodomethane and benzyl alcohol after re-coating was measured to be 114.2 ± 0.9°, 98.0 ± 0.6°, and 85.8 ± 1.0° respectively, which was similar to what was measured before protein deposition (**Table 2-3**).

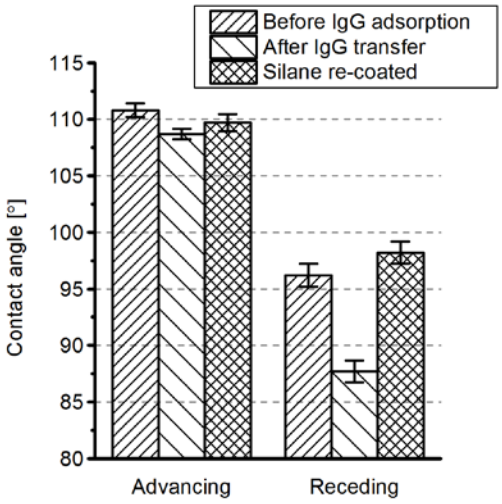

Figure 5-4. Advancing and receding contact angles of water on mold inlay surfaces (FDTS-coated SiO_2) before adsorption of IgG, after IgG transfer to a polymer replica during injection molding, and after a new FDTS-coating was applied. Error bars show the SE (n=3).

Although low surface energies were measured on Ni after applying ALD-coatings, delamination of the SiO_2 layer during protein transfer was observed for a few of the mold inlays as shown in **Figure 5-5**. Through measurements by XPS inside and outside the delaminated patches, removal of silicon accompanied by detection of aluminum and a small amount of nickel, together with an increased signal of oxygen, was observed. Furthermore, fluorine from the FDTS-coating was greatly reduced.

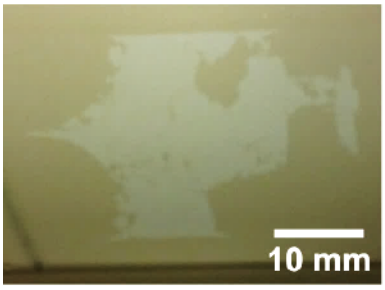

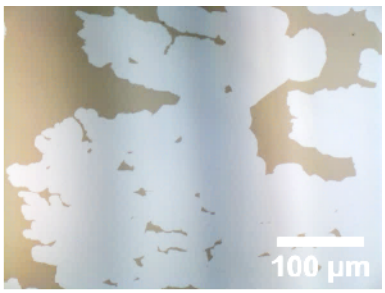

	Atom %					
	O	F	Si	C	Al	Ni
Inside patch	53.3	6.8	-	11.5	26.7	1.3
Outside patch	41.5	21.8	25.3	11.0	-	-

Figure 5-5. Delamination of SiO_2 deposited by CVD. After a few protein transfer cycles, brighter patches within the mold area started appearing. After XPS characterization, it was found that the SiO_2 layer was completely removed together with most of the FDTS, accompanied by a clear signal from the underlying Al_2O_3-layer.

5.3.2 Functionality of InMold transferred IgG

5.3.2.1 InMold transfer of antigen

Antibodies were efficiently transferred from the mold surface to the polymer replica. However, for applications relying on biomolecular recognition such as immunoassays and cell panning, it is crucial to know how well the antibody retains its antigen-binding affinity after the injection molding process. For the first experiments, an indirect ELISA was used to measure the amount of transferred IgG from mouse serum that could be recognized by a detection antibody. Patches incubated with 11, 33 and 100 µg/mL protein in PBS for 10 min were hydrophilic; both on the mold and the replica, while surface areas incubated at lower concentrations remained non-wettable (**Figure A-15**). The conversion rate of ABTS substrate measured by the rate of change in optical density, which is proportional to the amount of bound detection antibody, is shown in **Figure 5-6**. A more rapid color development occurred at higher antigen concentrations, and the data show a close to logarithmic correlation between antigen in solution and transferred antigen recognized by the detection antibody. However, there was a relatively large spread between each replication, as seen by the error bars. It was believed that some of this spread was due to differences in the optical transmission of the polymer between each injection molded replica. Therefore, for the next experiments, the substrate conversion was stopped after 10 min and the liquid was transferred to standard 96 well PS plates.

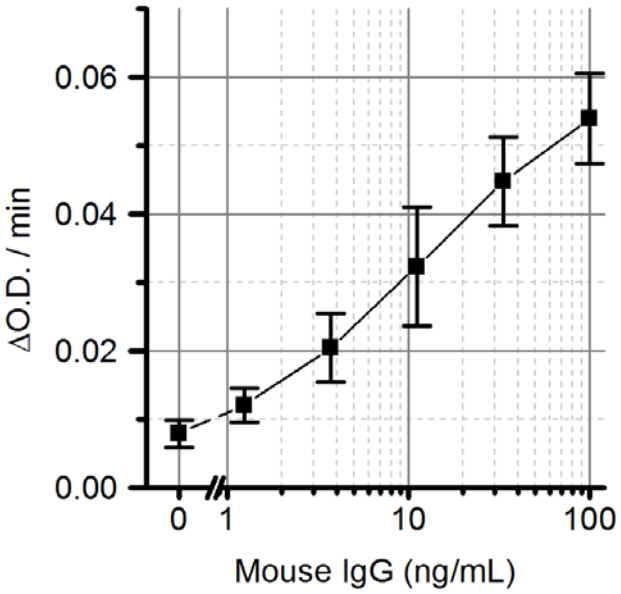

Figure 5-6. Detection curve of InMold transferred mouse IgG at different concentrations. The signal was recorded as the rate of increase in optical density at 405 nm in a continuous enzymatic reaction. Error bars show the SE (n=3).

5.3.2.2 InMold transfer of capture antibody

To evaluate the specific antigen-avidity of transferred IgG, a sandwich ELISA was employed. Initially, transferred goat anti-mouse was used as a capture antibody. However, a low sensitivity was observed due to cross-reaction between the capture and detection antibody without the presence of antigen (data not shown). Therefore, the detection antibody was changed to rabbit anti-mouse (same as capture antibody), which resulted in no detectable assay interference. ELISA analysis was performed on polymer replica slides with molded antibodies and compared to replica slides with antibodies deposited by passive adsorption from PBS. To increase sensitivity, TMB substrate was used instead of ABTS and the reaction was stopped by addition of H_2SO_4.

The antigen response curves, fitted with 4PL curves in **Figure 5-7**, show no significant difference between the two methods of capture antibody immobilization for antigen concentrations below 100 ng/mL. The linear range was from 10-75 ng/mL, and the LoD was 0.30 ng/mL antigen for both immobilization methods. The EC_{50} obtained from the curve fits were 27 and 21 ng/mL antigen for passive adsorption and transfer from mold inlay respectively.

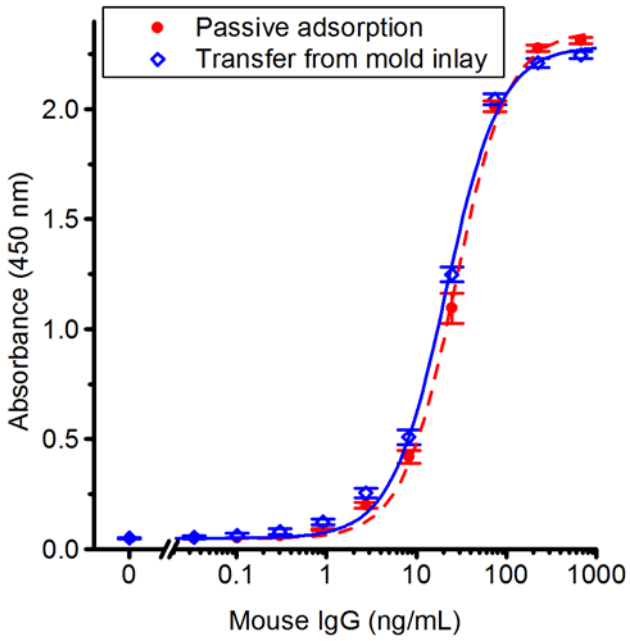

Figure 5-7. ELISA assays using antibodies immobilized during injection molding or by passive adsorption show equal sensitivity and response range. Standard curves for mouse IgG as antigen, comparing the antigen-binding capacity of capture antibodies adsorbed passively to a blank polymer replica surface to antibodies transferred from a mold inlay. The data points were fitted to a 4PL curve. Error bars show the SE (n=3 for passive adsorption; n=4 for transfer from mold inlay).

5.3.2.3 Transfer comparing long and short and incubation times

Robot replacement of a number of insertable mold parts during production is a standard process technology, but long mold inlay incubation times would be a major challenge for viable automation and industrial application of the proposed technology, as the required number of inlays would be large to sustain low process cycle times. An injection molding cycle time of 30 s using 20 replaceable mold inlays was targeted, thus calling for an individual inlay incubation time of 10 min in comparison to 60 min incubation used for the results presented in **Figure 5-7**. Antigen response curves using transferred antibodies with the two incubation times prior to injection molding are displayed in **Figure 5-8**. Replicas only showed significant differences in the response curves between the two incubation times for antigen concentrations ≥75 ng/mL ($p < 0.04$).

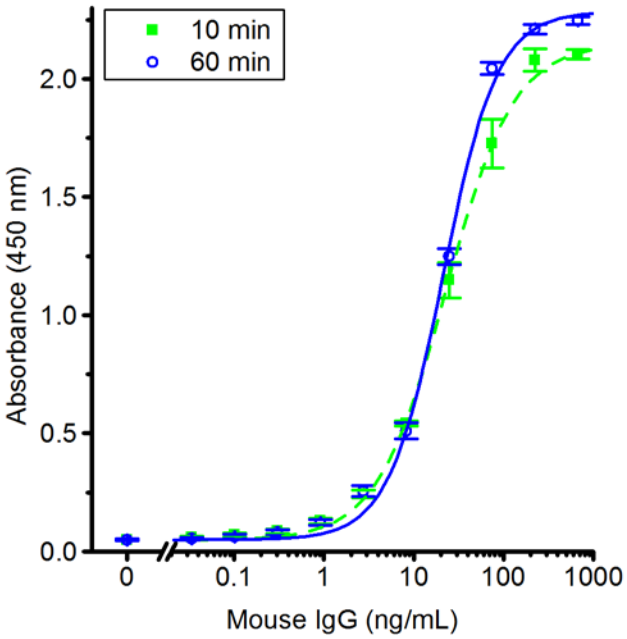

Figure 5-8. Highly sensitive ELSA assays can be produced by short incubation times prior to injection molding. Standard curves for mouse IgG comparing the effect of incubating the capture antibody on the mold inlay surface for 10 min and 60 min prior to transfer by injection molding. The data points were fitted by 4PL curves. Error bars shows the SE (n=5 for 10 min; n=4 for 60 min).

5.3.2.4 Repetitive InMold transfer from the same shim

In the experiments presented so far, the mold inlays was treated with oxygen plasma and re-application of the FDTS-coating between each injection mold cycle. However, for the process to be industrially relevant, it is important to evaluate the transfer efficiency and the biofunctionality of IgG that is transferred from re-used molds. **Figure 5-9a** shows a standard curve for antigen bound to transferred capture antibodies after 1, 3, and 6 consecutive cycles. After the third cycle, the amount of antigen captured by the transferred IgG was slightly lower both at low and high concentrations. There was no noticeable difference between the third and the sixth cycle. **Figure 5-9b** shows the water contact angles on the mold inlay before transfer and after 6 cycles. The advancing contact angle was reduced slightly from 111.8° to 102.5°, while the receding angle was reduced from 97.2° to 74.2°. Correspondingly, the contact angle hysteresis was increased from 14.6° to 28.4°.

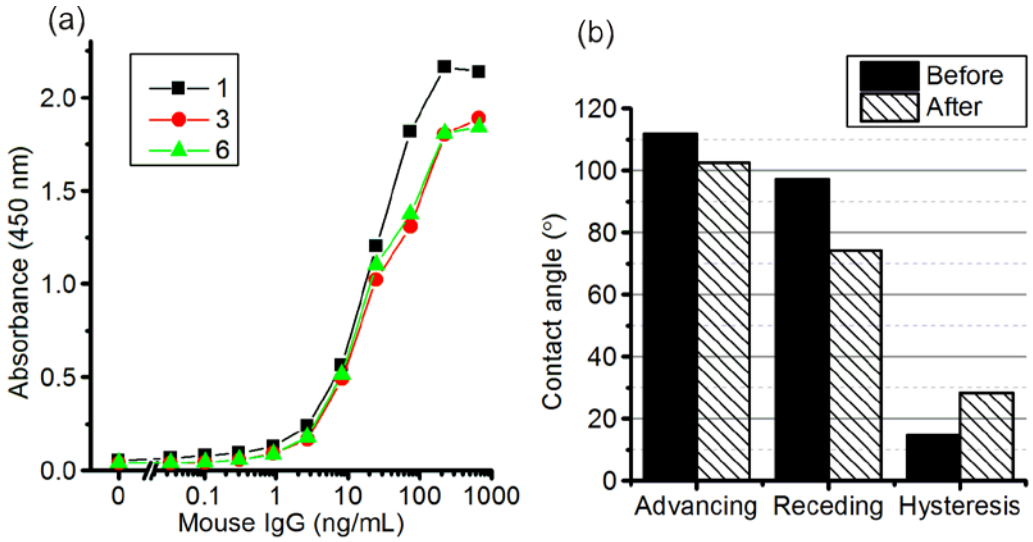

Figure 5-9. Repetitive InMold transfers from the same shim. **(a):** Standard curves generated for mouse IgG with InMold transfers after 1, 3, and 6 cycles, without plasma cleaning and re-deposition of FDTS between each cycle. **(b):** Advancing, receding, and contact angle hysteresis of the mold surface before, and after six consecutive transfer cycles (n=1).

5.3.2.5 Stability of immobilized IgG in cell culture medium

The stability of transferred antibodies over time was investigated by incubating the wells in DMEM with 10% v/v FBS and 1% v/v P/S for 9 days at 4 °C. The reduced temperature was chosen to minimize the risk of bacterial growth. Subsequently, the wells were washed and a sandwich ELISA performed as described in **Section 5.2**. **Figure 5-10** shows that capture IgG transferred from mold inlays had a similar response as passively adsorbed capture IgG at antigen concentrations below 10 ng/mL. However, at higher antigen concentrations the response was significantly lower ($p < 0.05$). It should be noted that the polymer slides with transferred capture IgG were stored in a dried state at 4 °C for 3 weeks before addition of medium, while slides with passively adsorbed capture IgG were analyzed immediately after protein deposition. The extended storage time of the transferred IgG may have reduced the protein activity.

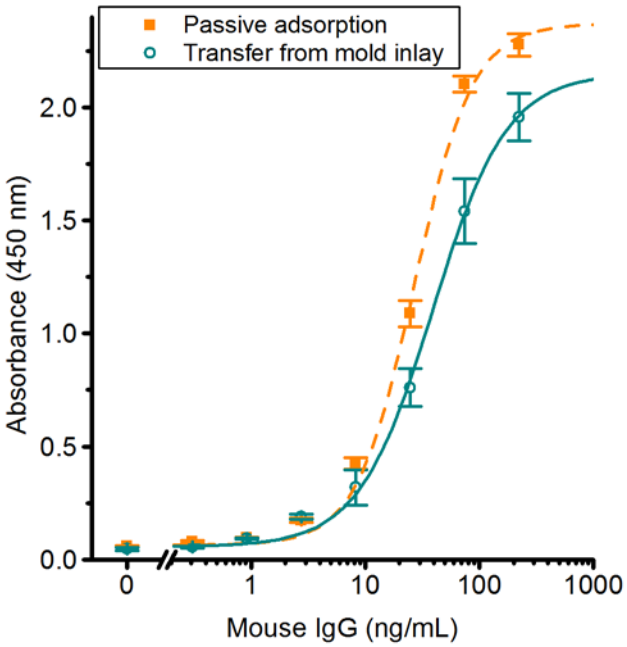

Figure 5-10. Antibodies transferred during injection molding retain their function in cell culture medium for >1 week. Standard curves for mouse IgG bound to capture antibody immobilized by passive adsorption or molded in the plastic, and stored for 9 days in DMEM + 10% v/v FBS + 1% v/v P/S at 4 °C. Error bars show the SE (n=3).

5.4 Discussion

AFM and XPS revealed a change in topography and elemental composition associated with the presence of proteins on the surface of the InMold polymer replica. In, addition there was no detectable difference, neither in terms of surface topography, nor elemental composition, between the mold inlay before and after transfer.

The reason behind the efficient transfer process is presumably that the proteins interact more strongly with the polymer than with the mold inlay surface. Due to the fact that dispersive contributions are dominating the surface energy of the fluorinated mold inlay (**Table 2-3** and **Table 2-4**, page 25), it is assumed that adsorbed proteins interact mainly by weak van der Waals forces. The olefinic COC polymer is also dominated by dispersive surface energy components in its native form. However the measured contact angle of water was lower (95.7°) and the surface energy was four times higher than for FDTS (41.5 mJ/cm^2). In the field of microcontact-printing (µCP) of proteins, successful pattern transfer depends on a lower wettability of the printing stamp surface than on the printed substrate [163]. Although the difference in water contact angle was small between the mold and the polymer compared to what is usually reported between stamp and substrate for µCP, the transfer of antibodies might be facilitated by the significantly lower surface energy of the FDTS-coated mold.

Another explanation for the efficient transfer could be partial embedding of the proteins into the polymer during injection molding, as suggested by the line scans of IgG on a FDTS-coated mold and after transfer to a polymer replica, where a reduction in the average peak height of about 30% was observed (**Figure A-16**). This partial embedding would increase the protein-polymer interface area and therefore also the total interaction energy, facilitating transfer of proteins from the low-binding mold

inlay surface.

Although no residual protein after transfer was detected by AFM and XPS probing of the mold surface, a small, but significant decrease in the receding contact angle, and a corresponding increase in the contact angle hysteresis on the mold after protein transfer was observed (**Figure 5-4**). It is well known that heterogeneity in either topography or surface energy may cause hysteresis, where the hydrophilic groups on a surface dictates the receding angle [164]. Introduction of hydrophilic groups by adsorbed proteins could therefore explain the apparent increase in contact angle hysteresis [165]. Furthermore, after six repetitive cycles, the contact angle was reduced from 87.7° to 74.2° compared to after a single cycle (**Figure 5-9**). This could suggest that there was a small amount of residual protein left on the mold inlay after transfer. In addition, a slightly lower response in the antigen standard curve was observed after three repetitive cycles, which could be related to a lower amount of transferred IgG, caused by residual adherent proteins occupying adsorption sites on the surface.

Wiseman and Frank [166] studied the orientation of IgG adsorbed on a hydrophobic CH_3-terminated surface. Their results suggested that initially adsorbed antibodies were rigidly mechanically coupled to the surface with a horizontal orientation (flat-on), while later adsorption occurred by filling of the interstitial spaces with more vertically oriented and loosely bound protein. For the InMold transfer process, it is therefore reasonable to believe that the orientation of any residual proteins is preferentially horizontal, since they are likely the most adherent.

However, the lower receding contact angle could also be related to other types of surface inhomogeneities, such as residual COC-polymer on the mold surface or the partial delamination of the SiO_2 layer + FDTS layer. As Al_2O_3 has a similar reactivity with silanes as SiO_2 [65] and apparently a higher adhesion to NiV, a better mold functionalization strategy could be to deposit FDTS directly on Al_2O_3. In either case, the surface properties could be completely restored by plasma oxidation and subsequent vapor phase deposition of FDTS.

In this study, no optimization of the IgG concentration (10 µg/mL) on the mold inlay was performed. It has been shown that 10 min adsorption time on a hydrophobic surface followed by subsequent rinsing led to a constant coverage density (monolayer) when the concentration was 5-100 µg/mL, while lower concentrations led to a sharp decrease in coverage, down to 20% of a full monolayer at 1 µg/mL [166]. For InMold transfer, the slightly higher antigen-response when incubating for 60 min compared to 10 min could therefore be due to structural re-arrangement over time [167], rather than a higher amount of adsorbed protein. Additionally, the uncertainty in the antigen-response was higher for the shorter incubation time, most notably seen most in the upper part of the sigmoidal curve, suggesting that the density of capture antibodies was less homogeneous. However, for applications where a lower detection range is targeted, the shorter incubation time does not seem to affect the assay performance.

The results presented so far suggest that there was no apparent reduction of the antigen-affinity of the transferred capture antibodies related to the injection molding process. This might seem surprising as the proteins on the mold inlay are brought in contact with a polymer melt initially at 250 °C. Earlier differential scanning calorimetry (DSC) studies showed irreversible denaturation of the F_{ab}-domain of IgG above 61 °C at a heating rate of 0.5 °C/min, while a higher heating rate of 5 °C/min increased the denaturation temperature to 65 °C [168]. Thus, denaturation kinetics is clearly limiting the extent of irreversible function loss. The cooling rates of polymer melt in the immediate vicinity of the mold inlay metal surfaces may exceed 10^4 °C/s [107] due to the high thermal conductivity of nickel, thereby only exposing the

adsorbed protein to high temperatures for extremely short time periods. Indeed, modelling has predicted that the first nanometers of polymer melt at 270 °C brought in thermal contact with a metal mold surface maintained at 30 °C was cooled to 50 °C within 100 ns [33]. Molecular dynamics simulations predicted that the unfolding of a 61-residue α-helical protein at 225 °C is on the order of tens of nanoseconds [169], although generally the protein folding speed limit increases with increasing number of residues in the polypeptide chain [170]. Similarly, prior experimental work demonstrated that peak temperatures of 290 °C are required to decrease the activity of horseradish peroxidase by 50% using multiple nanosecond laser pulses [171]. Antibodies transferred from the mold inlay during injection molding may therefore avoid irreversible loss of function, due to heating by the polymer melt and subsequent cooling by the mold being on a sufficiently short timescale to avoid denaturation.

5.5 Conclusion

Antibodies passively adsorbed on a surface functionalized mold inlay can be transferred with a high efficiency to a COC replica slide by injection molding. Insignificant amounts of protein residuals remain on the mold surface after transfer, as verified by AFM and XPS, thus making multiple subsequent protein transfers using the same mold possible. The antigen-binding affinity of the transferred capture antibody was similar to that of antibodies adsorbed by passive adsorption directly on polymer surfaces, as verified by sandwich ELISA. In addition, short incubation times (10 min) of antibody solution on the mold surface prior to transfer results in fully satisfactory antigen response curves on replicas with transferred antibody. Also, it was possible to re-use the same mold for at least six consecutive protein transfers, while retaining antigen-binding affinity. However, it would be advantageous to extend this study to determine the “lifetime” of a mold before FDTS-coating has to be re-applied. Finally, antibodies transferred during injection molding retained their functionality after 3 weeks of dry storage followed by 9 days of immersion in standard serum-containing cell culture medium. Thus, direct immobilization of antibodies at polymer surface during injection molding is a promising approach for high-volume production of protein functionalized disposable polymer biochips for immunoassay or cell capture applications.

Chapter 6

Polymer Chip Fabrication and Perfusion Culture Simulation

6.1 Introduction

There are several advantages to culturing cells on chip as compared to a static culture dish, as mentioned in **Section 1.1.2**. The higher degree of control over the local microenvironment allows a closer approximation to *in vivo* conditions. Most importantly, using laminar flow allows a well-defined mechanical shear stress, mass transport of soluble factors and the creation of concentration gradients. Some cell types, such as epithelial cells lining the veins, hepatocytes, or renal cells, experience a high level of perfusion in the body [18], which is difficult to mimic in a static system.

Moreover, the application of shear stress caused by laminar flow can affect the cell phenotype [172], which opens up new possibilities in research and therapy.

Cell cultures in closed microfluidic devices impose different requirements to mass transport of nutrients than what is experienced in static cultures. Due to the small volumes involved and relatively high cell concentrations, it is critical to develop an optimal perfusion strategy in order to avoid depletion of nutrients or accumulation of waste products above toxic limits. At the same time, cell proliferation and differentiation are in many cases dependent on the secretion of autocrine and paracrine factors. Removing these factors by continuous perfusion may affect the culture. In this chapter, a perfusion strategy for culture of DCs on chip will be discussed based on numerical simulations of oxygen consumption in a closed microfluidic system.

Maintaining a pH of the culture medium in the physiological range is also a requirement. Using a closed microfluidic system gives the possibility of moving the culture outside the environment of a CO_2 incubator. However, this requires a careful selection of materials and design of the culture system especially concerning gas permeability, which will be further discussed in this chapter. Finally, the fabrication of thermoplastic polymer chips by injection molding and ultrasonic welding will be demonstrated.

6.1.1 Mass transport of soluble factors

By laminar flow, the delivery of soluble factors can be controlled by tuning the flow rate. At constant unidirectional flow in a microfluidic channel, the soluble factors enters from one side and exit on the other (**Figure 6-1**). The time scales for reaction τ_r, diffusion τ_d, and convection τ_c can be given as

$$\tau_r = \frac{c_0 h}{R\rho} \tag{6-1}$$

$$\tau_d = \frac{h^2}{D} \tag{6-2}$$

$$\tau_c = \frac{L}{U_m} \tag{6-3}$$

where $c_0$is the initial concentration, h is the height of the microfluidic channel, R is the cellular uptake rate, ρ is the cell density, D is the diffusivity of the substrate, L is the length of the channel from inlet to outlet, and $U_m$is the flow velocity [16]. For microfluidic culture system, the diffusion timescale is relatively short due to small channel heights, meaning that the substrate concentration is uniform between the top and the bottom of the channel.

A small channel height can lead to rapid depletion of soluble factors if the flow rate is too low. From the inlet to the outlet, the concentration varies linearly with L at the bottom of the channel, if the uptake rate R is constant [16]. A dimensionless parameter κ has been used to compare the ratio of the convective timescale to the reactive timescale:

$$\kappa = \frac{\tau_c}{\tau_r} = \frac{LR\rho}{U_m c_0 h} \tag{6-4}$$

If $\kappa > 1$, for instance at low flow rates, nutrients are depleted before they reach the end of the channel. Similarly, a large κ may lead to insufficient removal of waste products such as CO_2 and lactate, which may inhibit normal cell functions at high concentrations [173].

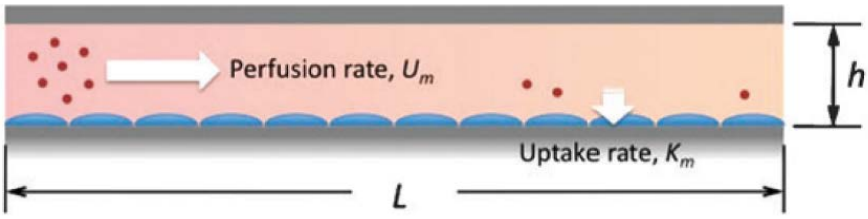

Figure 6-1. Schematic of a microfluidic channel in cross-section with cultured cells shown in blue and soluble factors in red. In a microfluidic cell culture with continuous perfusion, the perfusion rate U_m, must be large enough to ensure that the soluble factors are not depleted at the end of the channel. Reproduced from [16].

A suitable perfusion strategy for mass transport of nutrients and waste products is one of the greatest challenges for high-density cell cultures [174]. The optimal perfusion rate depends on the sum of the metabolic activity for all cells, and is therefore individual for each culture system. For instance, different cells require different level of dissolved oxygen in the culture medium: hepatocytes require high levels (21%) [175], while embryonic stem cells require low levels (3-5%) [176]. The uptake rate R of oxygen by cells may be predicted by Michaelis-Menten saturation kinetics [177]:

$$R_{O_2} = \frac{V_{max}\, c_{O_2}}{c_{O_2} + K_m}\rho \tag{6-5}$$

where $V_{\max}$ and K_m are kinetic constants, c_{O_2} is the oxygen concentration, and ρ is the surface density of cells.

Gradients of soluble factors such as certain cytokines may be deliberately created to study cell migration [178]. However, for long-term culture this may lead to different cell behavior upstream and downstream in the culture channel. A high flow rate can be used to reduce gradients of soluble factors, but may lead to depletion of autocrine factors secreted locally by cells, which may lead to culture failure as was demonstrated for embryonic stem cells (ESC) [179]. An alternative perfusion strategy compared to continuous flow is that of periodic, short-pulsed medium exchange, which was shown to result in a more homogeneous long-term culture of shear-sensitive cells such as ESC [20], [180], [181]. With this method, relatively high flow rates are applied for a short amount of time to exchange the culture medium, followed by a long incubation period where secreted signaling factors are allowed to accumulate locally.

6.1.2 Maintaining physiological pH of culture media

Mammalian cell cultures are conventionally maintained at 37 °C and pH 7.4 by using media containing sodium bicarbonate buffer ($NaHCO_3$) in a 5% CO_2 incubator [182]. For most microfluidic cultures, the whole culture system (including pumps, tubes, chip, reservoir etc.) is placed inside the incubator. However, this adds extra experimental constraints, and the principle of “lab on a chip” becomes “chip in a lab” instead. Exposing the culture medium to normal atmospheric conditions, which contains only 0.04% CO_2, will rapidly increase the pH. Atmospheric CO_2 dissolves in an amount that is proportional to the partial pressure according to Henry’s law:

$$p = k_H c \tag{6-6}$$

Dissolved CO_2 forms carbonic acid, which in turn dissociates to form bicarbonate according to the reaction:

$$H_2O_{(l)} + CO_{2\,(g)} \leftrightarrow H_2CO_{3\,(aq)} \leftrightarrow H^+_{(aq)} + HCO^-_{3\,(aq)} \quad (6\text{-}7)$$

By lowering the amount of CO_2, the equilibrium of the bicarbonate system is shifted to the left in the equation above. Alternatively, addition of HEPES buffer can be used to maintain physiological pH without the need for CO_2-supply [183], as it has a p*Ka* of 7.3 at 37 °C [184]. However, there are indications that cells in culture require CO_2 as an essential nutrient for growth [185]. In addition, HEPES may be toxic for some cell types at concentrations above 40 mM [186], and is known to generate reactive oxygen species (ROS) when exposed to light [187].

Alternatively, a closed microfluidic system can be used to retain appropriate levels of dissolved CO_2 in normal atmosphere. However, all polymer materials are gas permeable, which needs to be taken into account especially for long-term cultures with low flow-rates. From equation (6-6), the equilibrium concentration of dissolved CO_2 at p_{CO_2}= 0.05 atm and T=37 °C is 1.2 mM. However, in normal atmosphere, the equilibrium is only 0.013 mM. Thus, there is a driving force for permeation, for which the rate can be defined as a permeability coefficient *P* for different materials [188]:

$$P = \frac{M\ d}{A\ t\ \Delta p} \quad (6\text{-}8)$$

where *M* is the amount of permeated gas, *d* is the membrane thickness, *A* is the membrane area, *t* is time, and Δp is the pressure gradient across the membrane. The permeability for O_2 and CO_2 for selected types of polymers used in microfabrication are listed in **Table 6-1**. PDMS is markedly more permeable than the thermoplastic materials (PMMA, COC, PC, PS), which may be beneficial in systems where a rapid gas diffusion is desired [189], for instance for high-density cultures of hepatocytes. However, if operation in normal atmosphere while maintaining a constant pH over time is desired, thermoplastic materials are the best choice. The effect of gas permeability for tubing materials will be discussed later.

Table 6-1. Gas permeability for selected polymers at 23 °C used for microfabrication of cell culture devices. *Permeability values are for T = 35 °C.

	Gas permeability (cm^3 mm / m^2 day atm)	
	O_2	**CO_2**
PMMA [188]	6	43
COC [190]*	47	128
PC [188]	91	609
PS [188]	129	597
PDMS [188]	40,700	212,000

6.1.3 Additional material considerations

In addition to gas permeability, it is also important to consider permeation of water vapor, especially for microscale systems that have a high surface to volume ratio. Evaporation will lead to increased concentrations and osmolality of the medium, which could significantly affect the culture [191]. PDMS shows a high evaporation loss (18 g mm m^{-2} day^{-1}) [64] , which is three order of magnitudes higher than COC [60].

Furthermore, the high compliance of PDMS (~ 1 MPa) compared to common

thermoplastic materials (~2-3 GPa) becomes a limitation when fabricating low aspect ratio channels [193]. Due to sagging of the ceiling under its own weight, the local flow resistance and therefore the medium exchange rate becomes inhomogeneous across the width of the channel.

Curing of PMDS never leads to 100% crosslinking [23]. Remains of low-molecular weight oligomers of uncrosslinked siloxanes may have several adverse effects on cell cultures. Due to a high mobility, these chains tend to migrate from bulk to the surface. After 24 h of incubation with water, uncrosslinked chains were found to leach out into solution [23]. It is suspected that these chains may interfere with cellular signaling by incorporating into the cell membrane or bind to hydrophobic compounds [23], [194]. The high mobility of uncrosslinked chains also makes it challenging to achieve stable surface modification, such as surface hydrophilization by plasma oxidation due to hydrophobic recovery [195]. Additionally, in contrast to thermoplastic materials that only experience surface adsorption, PDMS also tends to absorb small, hydrophobic molecules such as hormones [23] or drugs [196] into the bulk.

Even though PDMS has been extensively used for many microfluidic cell-based devices, it has several potentially critical drawbacks that make it unsuitable to be integrated in a clinical treatment. In contrast, COC polymers (e.g. TOPAS 8007) have in addition to a high optical transparency a low gas and water vapor permeability [197], low water uptake, allow long-term stable surface modifications [198], and present a high biological inertness (USP Class VI approved), which are all important requirements for long-term cell cultures. Therefore, chips for DC cell culture were injection molded using this material.

6.2 Chip fabrication using mass production techniques

6.2.1 Ultrasonic welding

Ultrasonic welding is a commonly used industrial bonding method of injection molded macroscale parts, such as automotive parts, battery housing and wrist watches [199]. During the last 5 years, it has been increasingly used for bonding of thermoplastic microfluidic parts [200]–[206]. One of the strongest advantages associated with ultrasonic welding is high productivity due to low cycle times (less than 1 second). Additionally, it is based on localized heating, which allows bonding of parts with immobilized heat-sensitive proteins, if the weld seams are located far away from the functionalized sites.

The two parts to be bonded are clamped together as electrical energy is converted into mechanical vibrations at ultrasonic frequencies (**Figure 6-2**a). The vibrational energy induces friction and thereby heating of the parts in contact, causing entanglement of polymer chains at the interface. Low-temperature ultrasonic bonding requires the integration of sharp contact points, also called energy directors (EDs), to focus the vibrational energy in a small area. EDs are most commonly designed as triangular shaped ridges with a sharp apex running alongside the weld seam (**Figure 6-2**b). As vibrational energy is applied together with compression, the EDs collapse and leaves a thin residual layer covering the width of the welded seam (**Figure 6-2**c) [199]. For the sealing of microfluidic channels, EDs with a height of 100-200 µm has been fabricated by milling or etching of the mold [205], [207].

Critical parameters in ultrasonic welding include the welding energy, which is the product of the weld time and power, the amplitude of the vibrations and the weld

pressure, which is applied to the polymer parts by the welding horn (also called sonotrode). The quality of the weld is usually improved by increasing the weld energy and the amplitude. However, if excessive energy is applied the polymer may be degraded, causing leaky seams.

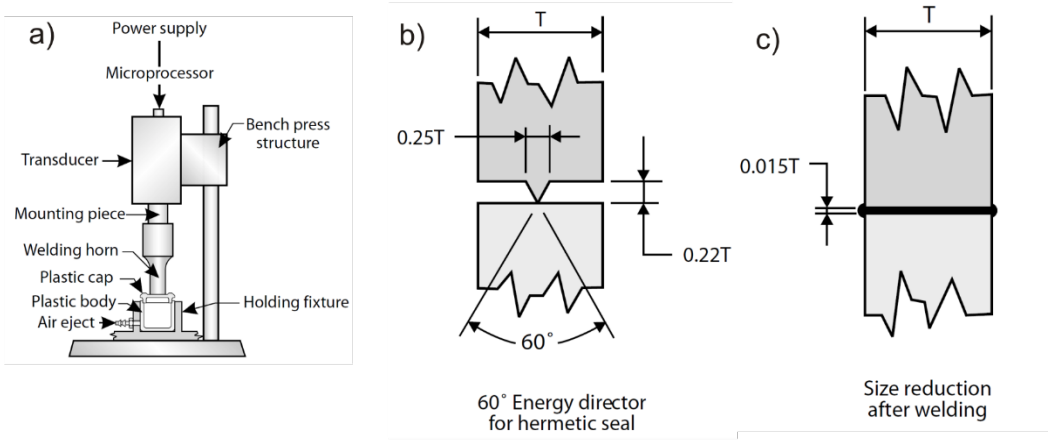

Figure 6-2. a) The basic components of an ultrasonic welder. b) Design of triangular-shaped EDs, with recommended geometrical dimensions for a seam of width *T*. c) A residual polymer layer remains after simultaneous melting and compression of the EDs. Reproduced from [199].

6.2.2 Experimental procedure

The mold used for injection molding of the culture chip was milled from a 3 mm thick plate of aluminum grade 2017. An AutoCAD drawing of the mold design (**Figure 6-3**) was exported to Cimatron E 10.0, used to make the milling job. A CNC micro-miller was used with a 3 mm end mill to make structures for the inlet and outlet through-holes (elevated by 1 mm) and the culture chamber (elevated by 0.25 mm). The EDs was milled with a 60° engraving tool (DIXI 7024), to a depth of 250 µm. To facilitate demolding, all sidewalls were trimmed to have a positively tapered angle of 30°. The center part of the plate was milled out to have a diameter of 85 mm, including flats for alignment in the injection molder. Finally, a metal polish (Autosol) was applied to the chamber part to achieve a smoother finish.

The aluminum mold insert was installed in the injection molder, and chips were replicated in TOPAS 8007-S04 using a constant mold temperature of 40 °C. To interface with fluidic tubings, 50 mm chips integrated with 12 Luer-lock connectors and EDs were injection molded using a different tool (**Figure A-17**). Afterwards, each connector was milled out directly using a 1 mm end mill tool.

Ultrasonic welding of the polymer chips was done by a Telsonic Ultrasonics USP-3000 welding press, capable of delivering a maximal amplitude of 60 µm with 20 kHz frequency (a 14 µm amplitude from the transducer was amplified 2.0x by a booster and further 2.1x by a sonotrode). Welding was performed in two separate steps: first the chamber was sealed by bonding to a flat microscope slide, then two luer lock connectors with integrated EDs were welded on the assembly. To align the chips with the ultrasonic welder, two separate aluminum holders were made (**Figure A-18**). The optimized parameters listed in **Table 6-2** were used for chip welding.

Table 6-2. Welding parameters for microfluidic chamber (two microscope slides) and connectors on the final assembly.

	Trigger force [N]	Energy [Ws]	Hold time [s]	Amplitude [%]	Weld pressure [bar]
Chamber	300	75	0.5	80	2
Connectors	300	75	0.5	85	2

The cross-section of a bonded microfluidic chamber was imaged in an optical microscope (Zeiss Axioscope 40), by cutting out a small piece of the plastic with a scissor and tilting 90° by fixing to a metal object by double-sided tape.

The height of a liquid-filled fluidic chamber can be measured with a confocal microscope, due to reflections created at the interface between the polymer (n = 1.53) and water (n = 1.33). The distance required to move the stage between the two reflection maxima can be converted to the real chamber height by correcting for the refractive index and the numerical aperture of the objective [208]. Fifteen positions evenly distributed in a 3x5 array across the chamber area (Δx = 11.875 mm, Δy = 5.0 mm) were mapped, using a LSM 700 confocal microscope (Carl Zeiss, Oberkochen, Germany) with a 20x / 0.5 NA objective, and the homogeneity was characterized as the coefficient of variation (CV), which is the ratio of the standard deviation to the mean.

6.2.3 Design of the culture chip

The microfluidic cell culture chip was designed to have the footprint of a standard microscope slide, with a single inlet and outlet on each end and a large chamber in the center, enclosed by the red curve in **Figure 6-3**. An inlet and outlet width of 1 mm was chosen to give mechanical support during bonding of luer-lock fluidic connectors. All corners were rounded with a radius of curvature of 3 mm, in order to avoid sharp transitions in flow rate and possible nucleation sites for bubbles. A large culture chamber was designed for the purpose of containing as many cells as possible within the slide area. The nominal depth of the culture chamber was 250 µm, the total culture area 10.8 cm^2 and the total volume 270 µL. Two parallel EDs, marked by the blue curves, were placed with an offset distance of 0.625 mm and 1.95 mm from the chamber wall. Based on the ED height (250 µm) and weld design recommendations [199], each weld seam was expected to have a total width of about 1.1 mm.

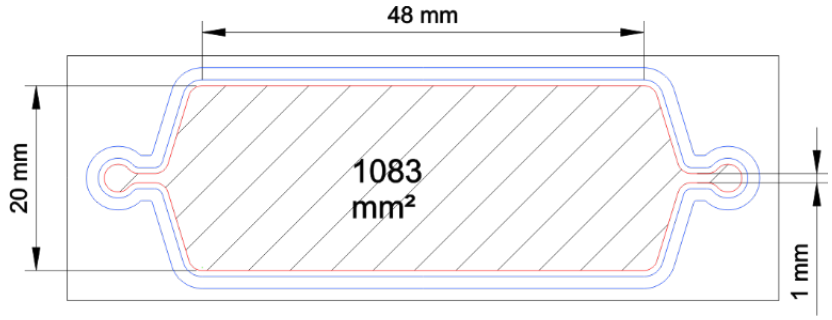

Figure 6-3. Design and dimensions of the microfluidic culture chamber (red) and the EDs for ultrasonic bonding (blue) to be injection molded in COC in a microscope slide format.

6.2.4 Results and discussion

The micro-milled aluminum mold and the injection molded chip half containing the culture chamber is shown in **Figure 6-4**. The first version of the mold (not shown) did not have tapered sidewalls for the 1 mm tall pillars, which led to the lower end of the replicated polymer chip consistently breaking into pieces during de-molding. After incorporating a 30° wall-angle, this was no longer a problem.

Figure 6-4. Left: Micro-milled aluminum mold for the molding of culture chamber, EDs and through holes to make fluidic connectors. **Right:** Injection molded replica.

A cross-section of the innermost ED and the culture chamber wall in the molded replica can be seen in **Figure 6-5**. The replica dimensions corresponded well to the mold dimensions. The height of the chamber and EDs was 235 µm and 245 µm respectively. Due to the 60° engraving tool having a finite width at the tip, the top of the EDs was flat, having a width of 155 µm.

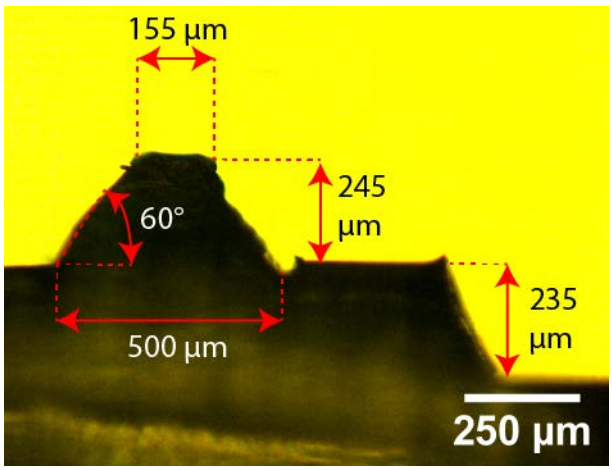

Figure 6-5. Optical micrograph of the injection molded ED and the chamber sidewall seen in cross-section. The EDs to the left were 155 µm wide at the top and 500 µm at the bottom, with a height of 245 µm and a side-angle of 60°. The culture chamber to the right was 235 µm deep, with a wall-angle also of 60°.

A bonded chip with optimal weld parameters is shown in **Figure 6-6**. The weld seam was completely sealed as seen in **Figure 6-7**. The weld was widest halfway between the two connectors (left image), and the two parallel EDs were completely welded together in several places, making the total width about 2.5 mm. The weld seam was narrower at the rounded corners, where a 100-200 µm wide air gap was present. Welding led to polymer being pushed about 200 µm into the culture chamber; however, this can be neglected due to the large chamber width (20 mm).

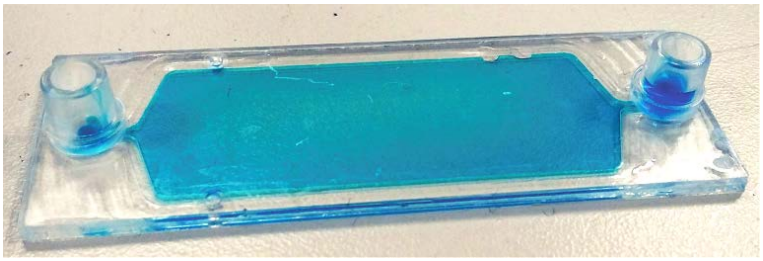

Figure 6-6. A welded cell culture chip with fluidic connectors, in this case filled with a blue color dye for visualization.

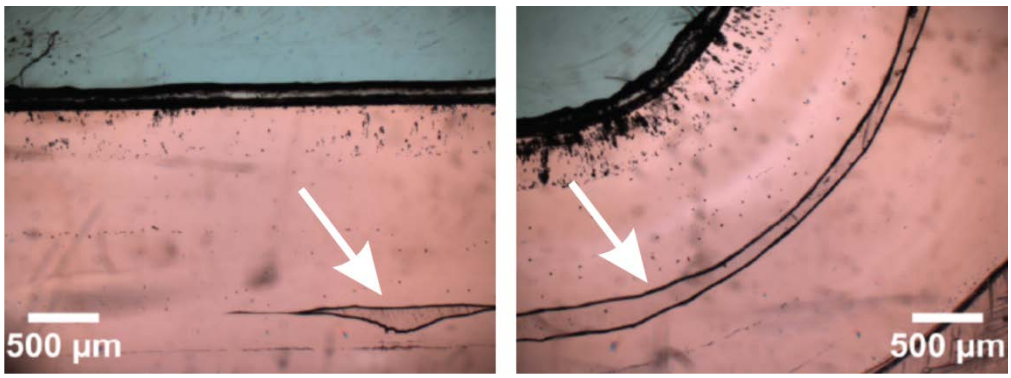

Figure 6-7. Chip after ultrasonic welding. The culture chamber was filled with a blue food color for better contrast. **Left:** The two parallel EDs were almost completely melted together at the middle of the long side of the chip. **Right:** At corners, the weld seam was narrower, leaving a small air gap between the parallel EDs.

The chamber height as measured by confocal scanning at 15 different positions is presented in **Figure 6-8**. The average height was 289 µm and the CV was 7%. The chamber was lower in the center part and one of the long sides was consistently lower than the other.

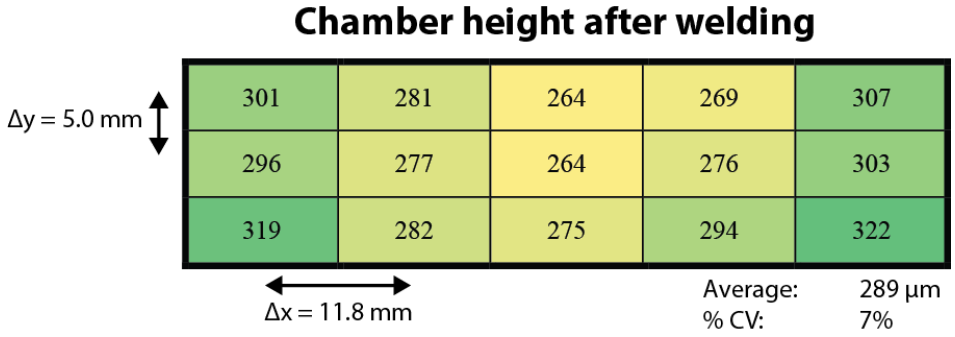

Figure 6-8. Mapping of chamber height after ultrasonic welding as measured by confocal microscopy. The average height was 289 µm, with a CV of 7%.

Generally, increasing the energy and/or the amplitude improved the quality of the weld seam. However, excessive energy led to mechanical deformation (sagging) of the free-hanging chamber ceiling, as seen in **Figure 6-9**.

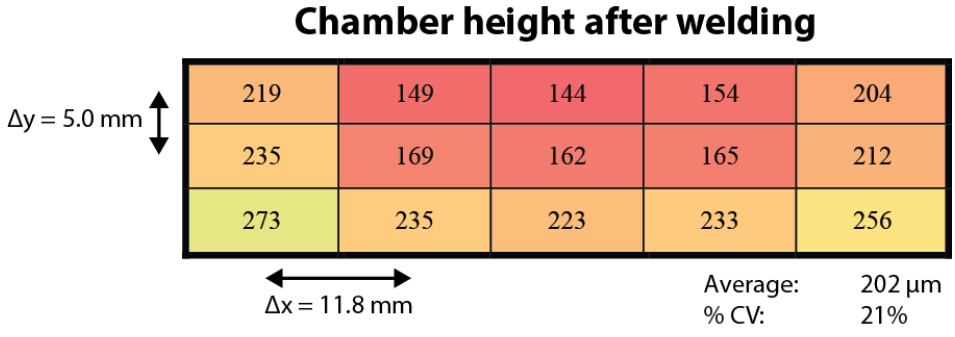

Figure 6-9. Mapping of the chamber height after ultrasonic welding with excessive energy, as measured by confocal microscopy. The average height was 202 µm, with a CV of 21%.

The hydrodynamic resistance R_H in a rectangular channel is for h << w equal to

$$R_H = \frac{12\mu L}{wh^3} \tag{6-9}$$

where μ is the dynamic viscosity, L is the length, w is the width, and h is the height of the channel. Therefore, a height variation of ±7% leads to a variation of the hydraulic resistance of ±22.5%. For a height variation of ±21% however, the resistance in the channel varies by ±77%. This will again significantly affect the local flow velocity inside the chip, and therefore the mass transport and shear stress applied to cells during culture. The consequence of high flow velocity variations was demonstrated by injecting a blue food color dye into a chip that was previously filled with water (**Figure 6-10**). Close to the inlet and outlet and along the sidewalls of the chamber, the color turned blue due to liquid exchange, while in the center part of the chamber, where the flow velocity was relatively low due to the lower height, the color did not change to the same degree.

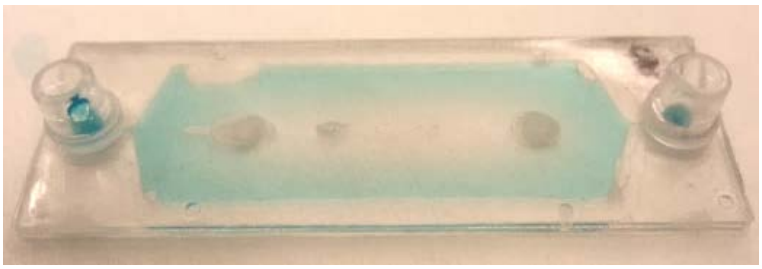

Figure 6-10 An excessive weld energy led to stress and deformation in the polymer, gave a lower chamber height in the center and therefore an increased local hydraulic resistance. This affected the flow velocity, demonstrated by a slower replacement of water inside the microfluidic chamber when a blue colored liquid was injected.

It is believed that the inhomogeneous channel height was due to the energy dissipated during welding not being equally distributed along the EDs. The relatively wider seams along the long sides of the chamber suggest more deformation of the EDs and therefore a smaller distance between the two bonded plates. Close to the four corners of the chamber the weld seam was not as wide, so the separation distance was likely higher here. Additionally, the chip might not have been perfectly parallel with the sonotrode during welding, leading to more energy being dissipated at one side than the other. Furthermore, sagging might be due to residual stress in the two polymer plates arising from non-uniform thermal cooling during the injection molding process, known as warpage [80]. It might also be induced by mechanical deformation during de-molding when the polymer is still soft [209]. Indeed, warpage is especially critical to the fabrication of microfluidic devices with low height-to-width aspect ratio channels, which for the presented system is 1:60.

Possible solutions to avoid sagging might be to reduce the weld energy required to make hermetical seals. This might be achieved by increasing the sharpness of the ED apex, for instance by using laser milling of the mold instead of mechanical milling. A few tests of milling sharp grooves in a Ni inlay were performed, where a width at the bottom of only 8 µm was achieved (**Figure A-19**). However, due to lack of time it was not possible to compare ultrasonic welding using polymer replicas from this mold. Additionally, the size of the EDs might be reduced and several parallel lines included to keep the width of the weld seam constant [204]. Alternatively, support structures with the same height as the channel wall might be incorporated in the center part, to reduce the bending. It should be noted that it is also possible to omit EDs entirely if the plastic parts are pre-heated to a temperature 20-30 °C lower than T_g. [201], [202]. However, heating is not compatible with surfaces that are

biofunctionalized with for instance antibodies.

Finally, infrared (IR) laser welding is another industrial compatible bonding technique based on localized heating that might be considered instead of ultrasonic welding to bond the microfluidic chip [210]. With this method, an IR-transparent layer is bonded to an opaque IR-adsorbing layer by local heating from a focused laser. However, efficient bonding requires addition of infrared-absorbing pigments in the polymer, such as carbon black [211]. For long-term cell culture applications, this is unwanted since pigments may leak out into the cell medium over time, which may have adverse biological effects.

6.3 Simulation of oxygen uptake during perfusion culture

In this section, the transport of oxygen by perfusion of culture medium and the oxygen uptake by cells in a microfluidic chamber will be discussed. In a gas impermeable system, such as a COC chip, convection of medium is the only source of oxygen. Thus, to sustain a long-term cell culture it is important to estimate the oxygen consumption, in order to determine a flow rate through the chip sufficiently high of preventing depletion at the end of the culture chamber. Simulations of the oxygen uptake by PBMCs during constant perfusion and periods with no convection will be presented in this section.

COMSOL 4.4 software was used to solve the convection-diffusion equation and the Navier-Stokes equation for laminar incompressible flow. The oxygen uptake by a 2D monolayer of cells was simulated using Michaelis-Menten kinetics. The oxygen uptake rate (OUR) has previously been measured for primary bone marrow mononuclear cells (BM MNCs) [212], which include the hematopoietic stem cell lineage (HSC) that give rise to lymphocytes and monocytes [7], [213]. At the beginning of the culture the rate was 0.0075 ± 0.0025 μmol/10^6 cells/h, and increased to 0.038 ± 0.006 μmol/10^6 cells/h after 8 to 10 days. Although monocytes from donor blood might be in a different metabolic state than BM MNCS, these parameters were used in the following simulations for the oxygen uptake through the chip (**Table 6-3**).

Table 6-3. Parameters used for simulations of oxygen uptake rate during culture. V_{max} and K_m are kinetic constants, ρ_{cell} is the surface density of cells, $[O_2]_0$ is the initial oxygen concentration, and D_{O_2} is the diffusion coefficient of oxygen in water at 37 °C.

	V_{max} (mol cell^{-1} s^{-1})	ρ_{cell} (cell m^{-2})	$[O_2]_0$ (mol m^{-3})	K_m (mol m^{-3})	D_{O_2} (m^2 s^{-1})
Before sorting	1.4-2.8×10^{-18}	1.7×10^{10}			
After sorting	1.4-2.8×10^{-18}	1.0×10^{10}	2.1×10^{-1}	5.0×10^{-3}	3.3×10^{-9}
End of culture	8.9-12.2×10^{-18}	3.4×10^{9}			

6.3.1 Constant perfusion

As discussed in **Section 6.1.1**, a reactive and convective time scale for the presented system can be defined at different flow rates (Equation (6-1) and (6-3), page 94). These time scales are plotted in **Figure 6-11** for a range of flow rates using the dimensions of the chip in Section 6.2 (h = 0.3 mm, L = 50 mm, w = 20 mm), V_{max} = 2.1×10^{-18} mol cell^{-1} s^{-1}, ρ_{cell} = 1.0×10^{10} cell m^{-2}, and c_0 = 2.1×10^{-1} mol m^{-3} (a maximal uptake rate of oxygen R_{O_2} = 2.1×10^{-1} mol m^{-2} s^{-1}). The cross-over point where the two time scales are equally contributing is at 6 µL/min (κ = 1) (**Figure 6-11**). For flow rates below this value, τ_c is longer than τ_r (κ > 1), which means that oxygen is depleted before reaching the end of the channel. Oppositely, above 6 µL/min, the flow rate is sufficiently high to supply oxygen to the cells (κ < 1).

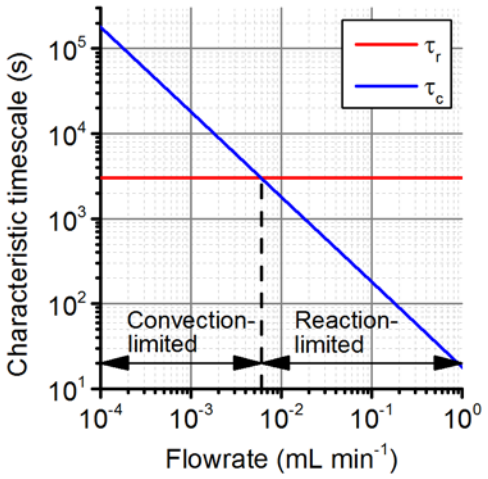

Figure 6-11. Reactive and convective time scales for the chip system at different medium flow rates, using a channel width, length, and height of 20 mm, 50 mm and 0.3 mm respectively, V_{max} = 2.1×10^{-18} mol cell^{-1} s^{-1} and ρ_{cell} = 1×10^{10} cell m^{-2}.

Due to the low channel height, diffusion is expected to be fast. This can be predicted by the ratio between diffusion (τ_d) and reaction (τ_r) time scales, also known as the Damköhler number *Da* [16]:

$$Da = \tau_d/\tau_r \quad (6\text{-}10)$$

Being Da ~ 0.01 for the presented system, a homogeneous oxygen distribution along the height of the microfluidic culture chamber was predicted. The steady-state

solutions for different flow rates close to the cross-over point were solved. The inlet was placed on the left side of the channel, with a fixed boundary concentration at $[O_2]_0$. The flux at the top surface was assumed zero, as TOPAS has a very low permeability coefficient (**Table 6-1**). A boundary flux following Michaelis-Menten kinetics was added to the bottom surface (equation (6-5), page 95). Cells were simulated as being present at a density of 1.0×10^{10} cells m^{-2} with an uptake rate of 2.1×10^{-18} mol $cell^{-1}$ s^{-1}.

The color plot in **Figure 6-12** shows the spatial distribution of oxygen along the length of the channel (*x)*, for 1, 6 and 36 µL/min. The simulations correspond well to what was expected based on comparison of the characteristic time scales in **Figure 6-11**. At 36 µL/min, the level of dissolved oxygen at the channel end was 17%, while it was only 1% at 6 µL/min. At 1 µL/min, the concentration drops to zero after 10 mm from the inlet (**Figure A-20**). Also, the relatively homogeneous distribution of oxygen along the vertical height (*y*) of the channel corresponds well to that predicted by a low Damköhler number.

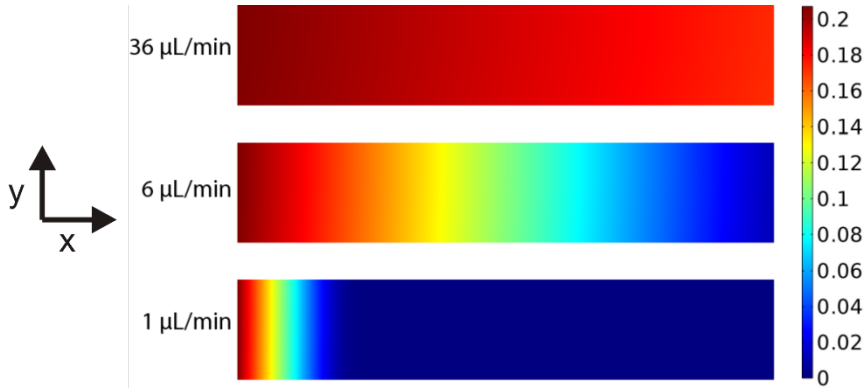

Figure 6-12. Finite element modeling of the oxygen concentration in a microfluidic channel shown in cross-section. Steady-state solutions of the concentration of dissolved oxygen throughout the channel, at three different flow rates. These cases corresponds to long (1 µL/min), medium (6 µL/min) and short (36 µL/min) convective time scales relative to the reaction time scale. The channel height (300 µm) has been scaled by a factor of 30 compared to the channel length (50 mm) for a more clear visualization.

6.3.2 Temporal oxygen uptake without convection

Based on the simulations, it is evident that high flow rates are necessary to provide a homogeneous oxygen distribution across the length of the channel. However, as discussed in **Section 6.1.1**, high flow rates could lead to high shear stress and vital signaling factors being depleted. Thus, periodic, pulsating flow may be a promising perfusion strategy leading to a more spatially homogeneous cell culture. In this section, the simulations of oxygen levels over time when there is no convection inside the chip are presented. The goal of these simulations was to establish some guidelines for how long incubation time was allowed between each medium exchange for DCs culture on chip, while maintaining the level of dissolved oxygen above or equal to the physiological relevant range.

At the start of the culture, a high cell density and a relatively low metabolic rate are expected. **Figure 6-13** shows the decrease in oxygen level at different cell densities and oxygen uptake rates. The cell densities after sorting are reported as the relative fraction of the cell seeding density, which was assumed to be 1.7×10^{10} cells m^{-2}. Due to the uncertainty in the reported oxygen uptake rate, two curves are plotted for each

density, to indicate the upper and lower limits. The physiological levels of dissolved oxygen are different for different types of tissue [214]. For venous blood, where PBMCs circulate, the normal physiological level is 0.05 mM. With the kinetic parameters expected at the beginning of the culture, the level of dissolved oxygen fell below this value after 25-50 min at 60% density, and 40-75 min at 40% density.

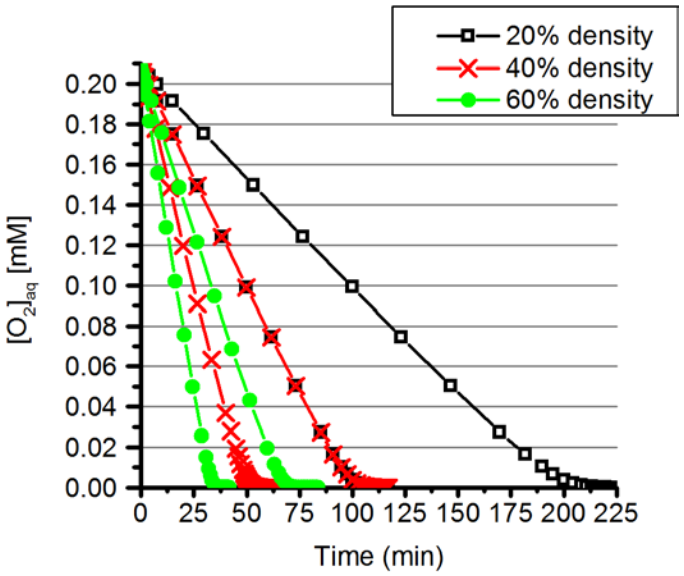

Figure 6-13. Time-dependence of the dissolved oxygen concentration at the channel bottom with no convection, during the beginning of the culture. There are two curves for each cell density relative to the seeding density, showing the upper and lower limits. Note that the upper limit for 40% density (red) and the lower limit for 20% density (black) overlap.

Furthermore, **Figure 6-14** predicts the oxygen consumption close to the end of the culture. The metabolic activity is expected to be higher for the matured DCs, but at the same time the cell density is expectedly lower since loosely adherent cells may be removed by flow. For dermal skin, where certain types of DCs reside (Langerhans DCs [7]), the physiological level is 0.03 mM. From the numerical simulations the level of dissolved oxygen fell below this value after about 20-25 min.

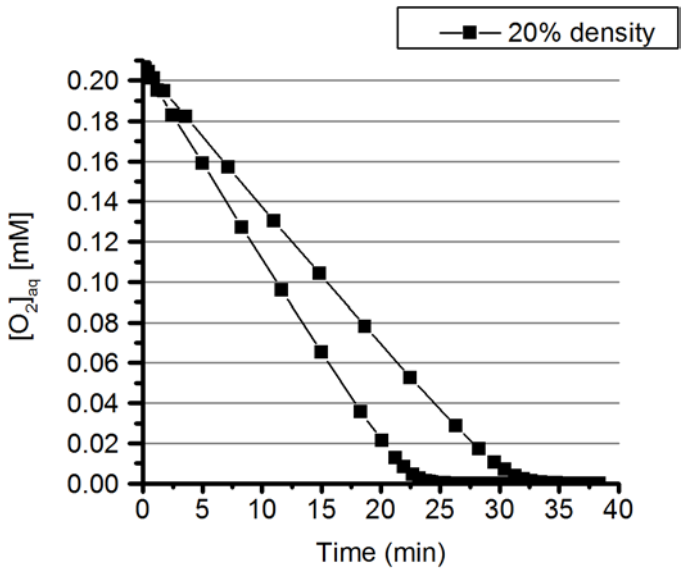

Figure 6-14. Time-dependence of the upper and lower limits of dissolved oxygen concentration at stationary conditions, calculated for the bottom cell chamber surface during the end of the culture. The simulation assumes a cell density 20% of the initial seeding density.

Based on these results, it was decided to use 25 min incubation time between each medium exchange, to prevent the oxygen level to fall below the normal physiological range. By using a flow-pulse of 80 µL/min for 5 min after each incubation period, a volume of 400 µL was exchanged every 30 min, which gives an average flow rate of 13 µL/min. With this configuration, $\kappa < 1$, and convective transport of oxygen is expected to be sufficient to avoid depletion as discussed in **Section 6.1.1**. It should be stressed that these simulations only discuss the metabolic consumption of oxygen. The uptake rates for other factors may be faster or slower, and thus the optimal perfusion strategy is likely a compromise between ensuring sufficient replenishment of nutrients, allowing accumulation of cellular signaling factors, and removal of waste products.

6.4 Continuous pH measurements with perfusion

As discussed in **Section 6.1.2**, maintaining an optimal pH during perfusion culture outside a CO2 incubator requires that the system has low gas permeability, in order to prevent equilibration with normal atmosphere. Since it is difficult to predict how low permeability is required, the pH was continuously measured during a "dummy" culture. In most culture media, phenol red acts as a visual pH indicator. Accurate pH-values can be determined by the relative absorbance values at two distinct peaks (436 nm and 560 nm), measured inside an optical cell [215].

6.4.1 Experimental procedures

An optical cell was connected to the fluidic system as shown in **Figure 6-15**. The absorbance of medium flowing through the cell was measured by an AvaSpec-

3648 spectrometer and an AvaLight-DH-S-BAL deuterium halogen light source (both from Avantes, Netherlands). A 100 mL glass bottle containing 15 mL X-vivo 15 culture medium (Lonza, Switzerland) was heated to 37 °C in a water bath. A mixture of 95% air and 5% CO2 was supplied by an external gas source with silicone tubing inserted through a milled hole in the bottle cap. To avoid evaporation of the medium, the gas passed through a humidifying chamber, consisting of a 250 mL glass bottle filled with MilliQ water, before entering the medium reservoir. Furthermore, a 0.22 µm sterile filter was attached to the end of the gas tube to prevent bacteria from entering the reservoir. Medium was pumped from the reservoir through the optical cell by a Masterflex L/S peristaltic pump before being re-circulated as shown by the arrows in the figure.

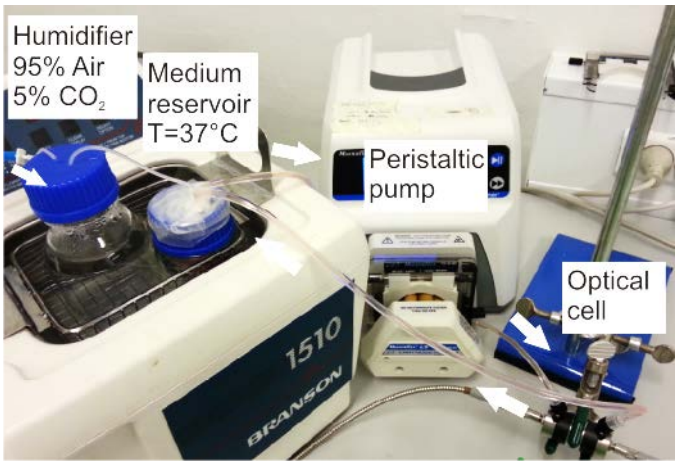

Figure 6-15. Experimental setup for the absorbance measurement of phenol red in cell medium during flow used to calculate the pH. The arrows show the direction of the circulating medium.

The permeability coefficients for the two different tubing materials that were tested are listed in **Table 6-4**.

Table 6-4. Gas permeability coefficients for two different peristaltic tubing materials [216].

	Gas permeability (cm^3 mm / m^2 day atm)		
	N_2	**O_2**	**CO_2**
Pharmed® BPT	530	1300	7900
Tygon® E-3603	260	530	2400

6.4.2 Results

Pharmed® BPT peristaltic pump tubing from Saint-Gobain has met USP Class VI and FDA requirements [217], and was therefore initially considered an ideal candidate for DC production. However, the steady-state pH of medium after flowing through a 80 cm segment at 60, 150 and 500 µL/h, was measured to be 7.8, 7.6 and 7.5 respectively (**Figure A-21**), which was considered too high for cell culture. Therefore, it was decided to repeat the experiment with the less permeable tubing.

Tygon E-3603 tubing are based on polyvinyl chloride (PVC) and use a non-

phthalate plasticizer [218]. For this tubing, the inner diameter (ID) was 1.6 mm, and the outer diameter (OD) was 4.8 mm, with a total internal volume of 1.6 mL. The flow was pulsating, consisting of one 5 min period with a flow rate of 80 µL/min followed by a 25 min stationary period (no flow). The average flow rate was 800 µL/h, which means that the medium residence time from the reservoir to the optical cell was 2 h. With these parameters, a constant pH could be maintained within an acceptable range (pH = 7.2-7.4) for at least 66 h (**Figure 6-16**). However, the absolute absorbance values for both peaks started to increase after 30 h (**Figure A-22**). After flushing with medium at high flow rates, the absorbance returned to the initial values. Therefore, the hypothesis is that the increased absorbance was due to formation of bubbles inside the optical cell, created by gas permeation through the tubing. This phenomenon will be discussed further in the next chapter.

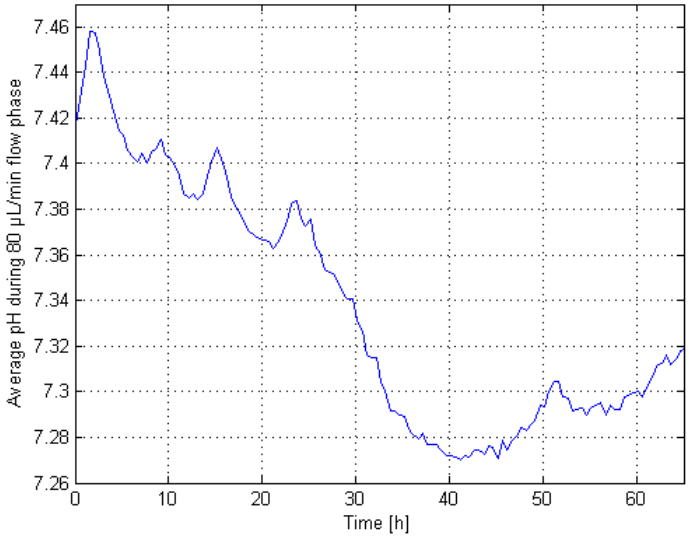

Figure 6-16. Calculated pH over time for pulsating flow of culture medium through a Tygon E-3603 tubing.

6.5 Conclusion

In this chapter, the fabrication of a COC microfluidic culture device, using micro-milling of an aluminum mold, injection molding, and ultrasonic welding, was presented. With an optimization of welding parameters, the chamber height variation over an area of 10 cm^2 could be reduced from 21% to 7% CV, leading to an expected variation in flow rate of 20%. In addition, the oxygen uptake by monocytes/DCs in a gas impermeable chip was predicted for both different flow rates and stationary conditions, which were used to give guidelines for further cell experiments. It was found that in order to maintain a normal physiological range of oxygen along the entire channel, the flow rate has to be higher than 6 µL/min at constant flow, or that the medium inside the chamber has to be exchanged every 25 min by pulsating flow. To achieve homogeneous oxygen levels, pulsating flow was chosen as the perfusion strategy for DC culture on chip. Finally, it was demonstrated that Tygon peristaltic tubings had a sufficiently low CO_2-permeation to maintain acceptable pH during periodic flow at an average rate of 800 µL/h.

Chapter 7
On-Chip Generated Dendritic Cells by Microfluidic Perfusion

7.1 Introduction

The requirement of DC-based vaccines to conform with current good manufacturing practice (GMP), calls for the use of closed systems to reduce the risk of pathogen infections, which also enables handling to be performed in lower class cleanroom environment [116], [219]. In addition to being safer, closed systems can also be made easier to handle, thus reducing the manual workload. For DC vaccines, up to 5×10^9 PBMCs may be required [43]. Due to the large culture area needed, a total of 20 traditional culture dishes (Ø = 140 mm, 1.7×10^6 cells/cm^2) may be required. Considering that washing, medium exchange and harvest needs to be done manually, it

imposes an immense workload that prohibits upscaling of DC-based cancer vaccines.

Isolation of monocytes from the patient normally starts with leukapheresis, where whole blood passes through a centrifugation apparatus that continuously depletes the white blood cells (WBCs), while RBCs and plasma are re-infused into the bloodstream. A typical leukapheresis product may consist of about 1×10^{10} WBCs and 1×10^{11} RBCs [219]. One of the most common and simplest methods to isolate monocytes for the generation of mature DCs is by density gradient centrifugation followed by adherence to plastic substrates [41]. Density gradient centrifugation is used to separate the leukapheresis product into three components: erythrocytes and granulocytes (high density), mononuclear cells (medium density), and plasma (low density). PBMCs are isolated by collecting the middle layer and added to a culture dish. The monocyte fraction can then be further enriched due to the relatively higher adherence to tissue culture PS compared to other PBMCs, which are more easily removed after washing [114], [115].

It is well established that culture of $CD14^+$ monocytes with GM-CSF and IL-4 leads to differentiation into immature DCs [12]. After 5-7 days of culture, the majority of cells are reported to form loosely adherent clusters with a typical dendritic morphology and an increased motility. Addition of the pro-inflammatory cytokines tumor necrosis factor alpha (TNF-α), IL-1β and IL-6 has been shown to be important for DC maturation and their ability to stimulate cytokine production by T-cells [9], [13]. Addition of prostaglandin E2 (PGE2) to the medium further enhances the stability, immunostimulatory and migratory activity of DCs. Surface expression of CD83 is one of the known markers for mature DCs [220]. At the same time, expression of CD14 is down-regulated during differentiation when IL-4 is added to the culture medium [221].

In this chapter, DC generated both in conventional culture dishes and inside injection molded microfluidic chips will be presented. Selective sorting of monocytes by adhesion, as well as differentiation and maturation to DCs will be demonstrated for both systems. Challenges encountered during set-up of the perfusion system, seeding cells from different donors with a varying degree of lymphocyte and monocyte purity, maintaining a long-term perfusion cell culture, and finally harvesting cells after 7 days, will be discussed.

7.2 DC generation in culture dish

7.2.1 Experimental procedures

The experimental methods used to generate DCs from monocytes in dish were based on previous work [9]. PBMCs from healthy donors were kindly provided from Center for Cancer Immunotherapy (CCIT), Herlev Hospital, Denmark. Frozen cells at a concentration of 6×10^7 cells/mL were transported in cryovials containing 90% human AB-serum + 10% DMSO and were stored at -140 °C upon arrival.

At the start of each experiment, frozen cells were thawed by adding warm X-VIVO 15 medium (Lonza, Switzerland) and washed twice by centrifugation at 400 g for 10 min. The cells were counted manually using a hemocytometer (Bürker-Türk) Finally, the cells were resuspended in X-VIVO 15 with 2% human AB-serum (Herlev Hospital) and 2 mM L-alanyl-L-glutamine (GlutaMax Supplement, Life Technologies) to a final concentration of 7×10^6 cells/mL, and added to a 50 mm tissue culture polystyrene dish (Nunc, Roskilde, Denmark). A fraction of the cells were separated

and kept on ice for analysis by flow cytometry. After 1 h of incubation at 37 °C, non-adherent cells were removed by washing the culture dish twice with X-VIVO 15. Analyzing adherent cells in the dish was not possible without disrupting the culture. Therefore, the fraction of $CD14^+$ cells remaining in the culture dish was estimated indirectly from cell counting and flow cytometry data from samples taken before and after sorting.

The medium was supplemented with 1000 U/mL GM-CSF and 250 U/mL IL-4 (both from CellGenix, Germany) and the adherent cells were cultured for 5 days at 37 °C, 5% CO_2. On day 5, the medium was further supplemented by IL-1β (1000 U/mL), IL-6 (1000 U/mL), TNF-α (1000 U/mL), and PGE2 (1 µg/mL) and cultured for 2 more days. On day 7, adherent cells were harvested by adding cold 0.2% Na-EDTA in PBS to the culture dish and incubating for 30 min at 4 °C, in order to chelate Ca^{2+} ions. Remaining adherent cells were removed mechanically using a cell scraper.

Cells were stained with PE Mouse Anti-Human CD14 (#555398), APC Mouse Anti-Human CD83 (#551073), PE Mouse IgG isotype control (#555574), APC Mouse IgG isotype control (#555751), as well as 7AAD for dead cell-staining (#559925), from BD Pharmingen (BD Biosciences), before being analyzed with a Gallios flow cytometer (Beckman Coulter, USA). A threshold level was set on the forward scatter detector to exclude smaller cell fragments arising from lysed erythrocytes and granulocytes. Therefore, all fractions presented here include only monocytes and lymphocytes. The level of CD83-expression for cells gated as DCs was defined as the median fluorescence intensity (MFI) of anti-CD83 PE-stained cells relative to cells stained with the isotype control. For more detailed information on the experimental procedures, refer to **Section A.4** for the full protocol.

7.2.2 Cell sorting by adherence

Figure 7-1 and **Table 7-1** show the $CD14^+$ fraction before and after sorting, as well as a statistical comparison for three independent experiments from donor #2. The fraction of $CD14^+$ cells were significantly lower for the non-adherent cells (6.2%), compared to the total cell population before seeding (17.8%, $p < 0.05$). On average, 45.9% of the seeded cells were removed by sorting, and from these numbers it was estimated that the recovery of $CD14^+$ monocytes after sorting, that is the fraction of remaining cells relative to the initial number, was 84.6±5.1%. An estimated 27.6% of adherent cells after sorting were $CD14^+$, corresponding to an increase in purity of 59%, which was significantly higher than the initial fraction ($p < 0.05$). The density of adherent cells was estimated to be 1.1×10^6 cells/cm^2 on average. It should be noted that experiment #3 was done in a 35 mm dish. However, the seeding density and the volume concentration was the same as for the two other experiments.

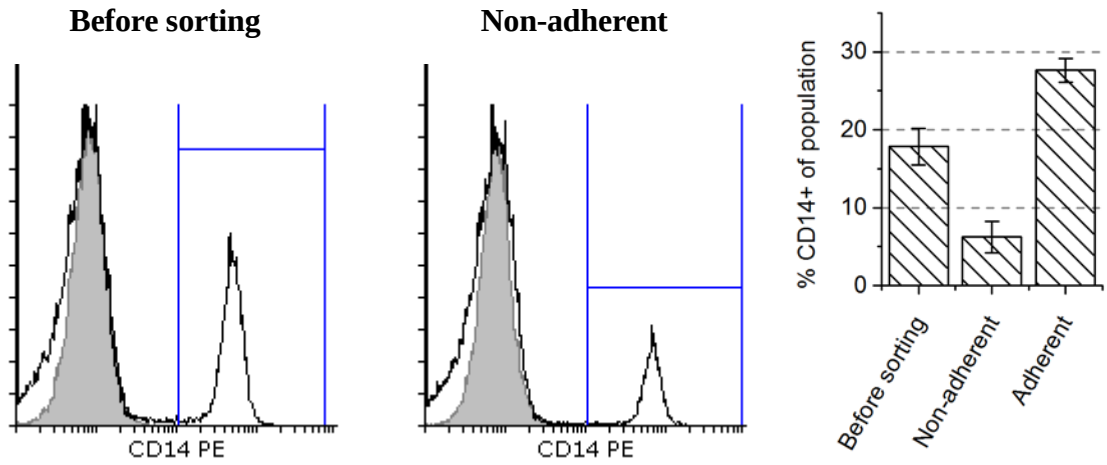

Figure 7-1. Flow cytometry analysis of CD14-expressing cells before and after **s**orting of adherent PBMCs in a Petri dish. Cells were stained with anti-CD14 PE and an isotype control. The fraction of $CD14^+$ monocytes adherent to the Petri dish increases from an average of 18% to 28%. This percentage was estimated indirectly from cell counting and flow cytometry data from samples taken before and after sorting. The error bars are the SE (n=3) for cells from donor #2.

Table 7-1. Flow cytometry analysis and counting of cells from donor #2, before and after sorting of PBMCs, as well as an estimate of the fraction of $CD14^+$ adherent cells remaining in culture.

	Experiment			
	1	**2**	**3**	**Average±SE**
Before sorting				
Seeding density (x $10^6/cm^2$)	2.0	2.1	1.7	1.9
Viability (%)	99.1	99.1	99.5	99.2±0.1
$CD14^+$ (%)	22.1	17.3	14.1	17.8±2.3
Non-adherent cells				
Fraction of cells seeded (%)	35.9	48.8	53.1	45.9±5.2
Viable cells (%)	99.9	99.6	99.8	99.8±0.1
$CD14^+$ (%)	7.2	9.1	2.4	6.2±2.0
$CD14^+$ recovery (%)	88.3	74.6	90.9	84.6±5.1
Adherent cells (estimate)				
Cell density (x $10^6/cm^2$)	1.3	1.1	0.8	1.1
$CD14^+$ (%)	30.4	25.2	27.3	27.6±1.5
$\Delta CD14^+$ (%)	37.6	45.7	93.6	59.0±17.5

Table 7-2 shows the results for experiments performed with cells from three individual donors. The values used for donor #2 were the average values from the three experiments that were presented in **Table 7-1**. For donor #1 and #3, only one experiment was performed. The data was similar to what was presented for donor #2, except that the viability was slightly lower.

Table 7-2. Flow cytometry analysis and counting of cells from donor #1, #2,and #3, before and after sorting of PBMCs, as well as an estimate of the fraction of $CD14^+$ adherent cells remaining in culture.

	Donor			
	1	**2**	**3**	**Average±SE**
Before sorting				
Seeding density (x $10^6/cm^2$)	1.2	1.9	2.1	1.7
Viability (%)	97.3	99.2	95.0	97.2±1.2
$CD14^+$ (%)	20.7	17.8	16.8	18.4±1.2
Non-adherent cells				
Fraction of cells seeded (%)	41.7	45.9	53.6	47.1±3.5
Viable cells (%)	98.5	99.8	98.0	98.8±0.5
$CD14^+$ (%)	2.9	6.2	9.3	6.1±1.8
$CD14^+$ recovery (%)	94.4	84.5	70.3	83.2±7.1
Adherent cells (estimate)				
Cell density (x $10^6/cm^2$)	0.7	1.0	1.0	0.9
$CD14^+$ (%)	32.6	27.6	25.0	28.6±2.1
$\Delta CD14^+$ (%)	57.5	59.0	48.8	53.8±2.6

7.2.3 DC maturation in culture dish

The flow cytometry forward-scatter (cell-size) *vs.* side-scatter (cell granularity) plot for PBMCs at day 0 show two populations - lymphocytes and monocytes (**Figure 7-2**a). After 7 days, lymphocytes were still present while a new population with larger size and granularity appeared which was gated as being DCs (**Figure 7-2b**). The data in **Table 7-3** (donor #2) shows that 46.6% of all cells fall within the DC gate region. Of those cells, 96.6% were $CD83^+$. The median fluorescence intensity (MFI) from CD83 expression relative to the isotype control was on average 62.7. Similarly, an absence of CD14 expression can be seen (MFI = 1.01). Due to signal overlap, the threshold for $CD83^+$ was set to include a maximum of 2% of the control (**Figure 7-4**). The yield, which is defined as the total number of $CD83^+$ DCs relative to $CD14^+$ monocytes at the start of the culture, was on average 28.6%.

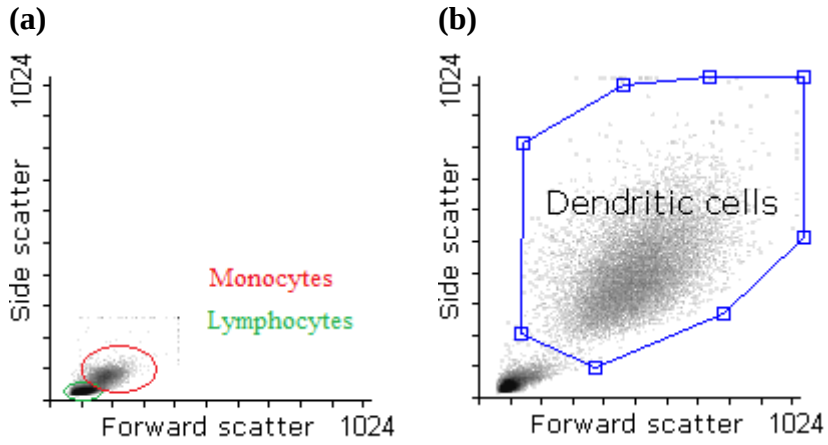

Figure 7-2. Forward *vs.* side-scatter plot from flow cytometry of cells at (a) the beginning of culture, showing monocyte and lymphocyte sub-populations, and (b) after 7 days (donor #2), showing a distinct population of larger and more granular cells believed to be DCs.

Table 7-3. Flow cytometry analysis after 5+2 days of differentiation + maturation of DCs in a petri dish, from three independent experiments using cells from donor #2. The uncertainty is reported as ± SE (n=3).

	Experiment			
	1	**2**	**3**	**Average**
Viability (%)	95.2	96.5	94.3	95.3±0.6
DCs from gating (%)	60.5	44.8	42.6	49.3±9.8
$CD83^+$ from DC gating (%)	98.2	96.9	94.6	96.6±1.1
$CD83^+$ total (%)	56.1	43.3	40.3	46.6±4.8
MFI, CD83	96.5	48.3	43.3	62.7±29.4
MFI, CD14			1.01	
Yield (%)	18.6	25.4	41.7	28.6±6.9

Microscope images taken at different days during culture of cells from donor #1 shows a clear change in cell morphology after 3 days and onwards (**Figure 7-3**). After cell sorting, both lymphocytes (small and circular) and monocytes (large and irregular) adhere to the culture dish. The lymphocytes did not change morphology during 7 days of culture, while monocytes became increasingly larger in size and with a more irregular shape. At Day 5 and Day 7, several cells became elongated and displayed branched projections (dendrites).

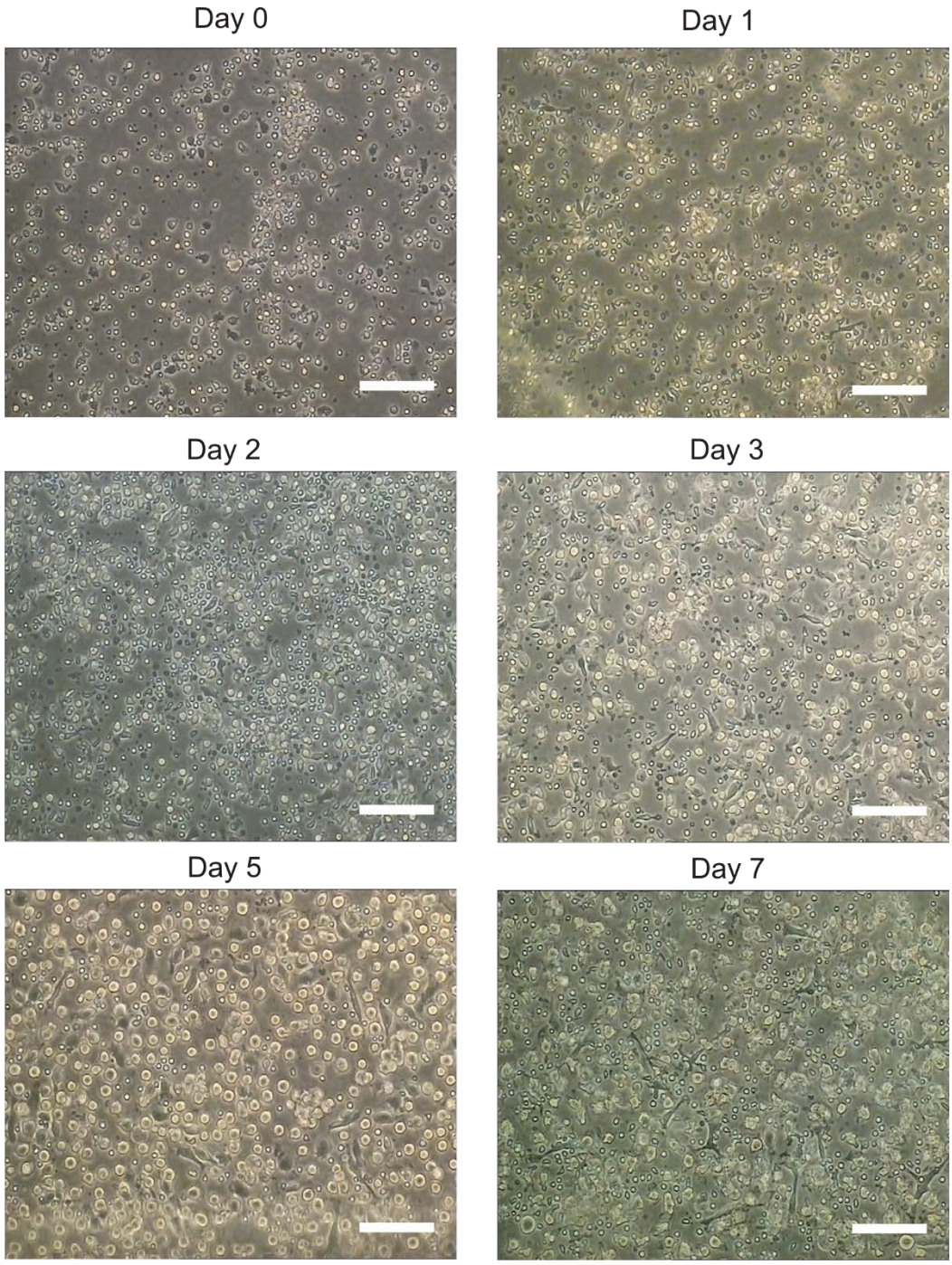

Figure 7-3. Phase contrast micrographs of DCs generated from adherent PBMCs (donor #1) during a 7-day culture (5 days differentiation + 2 days maturation) in a culture dish. Scale bars are 50 µm.

The generation of DCs was more variable when using PBMCs from different donors (**Table 7-4**). Harvested cells from donor #1 and #3 show a larger fraction of DCs than donor #2. However, the $CD83^+$ fraction from donor #1 was lower. Fluorescence intensity histograms (**Figure 7-4**), show a bimodal distribution for donor #1. As estimated by Gaussian curve fit (**Figure A-23**), about 46% of DCs show a modest CD83 expression (MFI = 4.9), while 54% show a high expression (MFI = 79.9). A bimodal population was also present to a lesser degree for donor #3.

Table 7-4. Flow cytometry analysis after 5+2 days of differentiation + maturation of DCs in a petri dish, comparing cells from donor #1, #2 and #3. The uncertainty is reported as ± SE (n=3).

	Donor			
	1	**2**	**3**	**Average**
Viability (%)	99.5	95.3	95.0	96.6±1.4
DCs from gating (%)	75.5	49.3	70.9	65.2±14.0
$CD83^+$ from DC gating (%)	85.6	96.6	98.0	93.4±3.9
$CD83^+$ total (%)	64.2	46.6	66.9	59.2±6.4
MFI, CD83	37.2	62.7	63.2	54.4±14.9
MFI, CD14	1.12	1.01	0.99	1.04±0.07
Yield (%)	55.3	28.6	25.0	36.3±9.5

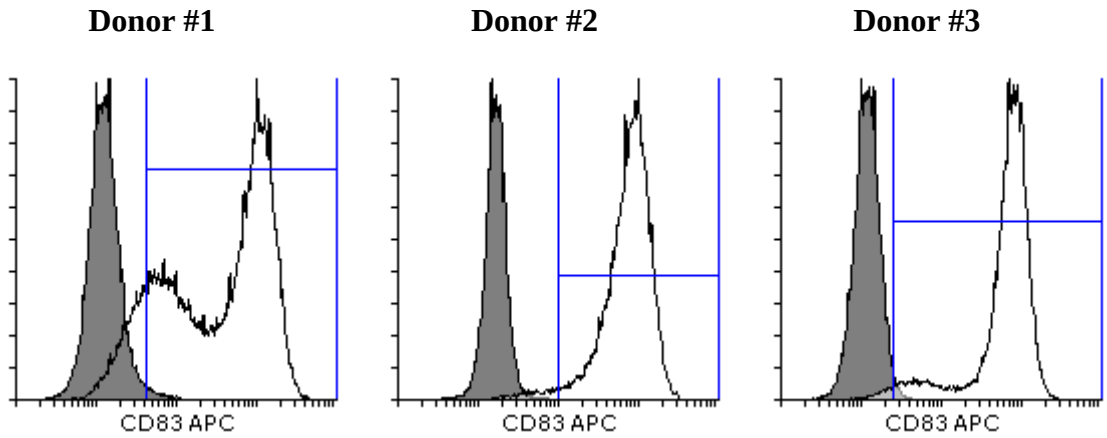

Figure 7-4. Fluorescence histograms from flow cytometry of harvested DCs from donor #1, #2 and #3, stained with anti-CD83 APC against an isotype control. Cells were gated by size, granularity and 7AAD to include viable DCs (**Figure 7-2**). Thresholds for $CD83^+$ were consistently set to include maximum 2% unspecific staining. A peak at medium fluorescence intensity appeared for donor #1 and to a slight degree also for donor #3, but was absent for donor #2.

7.3 DC generation by microfluidic perfusion culture on chip

7.3.1 System design

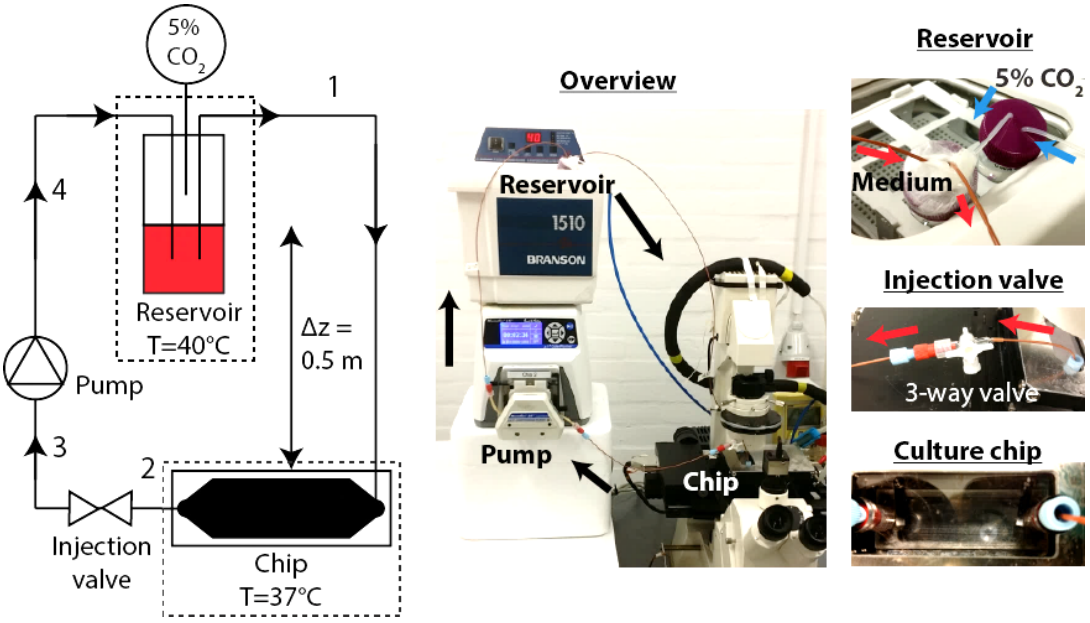

Figure 7-5. Microfluidic perfusion system for long-term cell culture. The culture medium reservoir was elevated by 50 cm relative to the chip in order to pressurize the system. The reservoir was continuously fed with a 5% CO_2 humidified gas mixture to maintain pH and to limit evaporation. The medium was recirculated through the chip by an automated peristaltic pump. The chip was fixed inside a stage incubator with circulation of warm water to maintain 37 °C. A 3-way injection valve was included to allow injection of cell suspension into the chip.

Numerous trials and errors were done before arriving upon a microfluidic system which could automatically exchange medium, maintain constant pH, avoid bubbles and provide an injection port with minimal dead volume. The final system used for generation of DCs on chip is shown in **Figure 7-5**. The system contained a separate medium reservoir, consisting of a 50 mL centrifuge tube with holes drilled in the cap for tubings. An external supply of 95% air and 5% CO_2 was used to maintain constant pH, similar to the setup presented in **Section 6.4**. An extra centrifuge tube filled with water was used to humidify the gas mixture before entering the reservoir, in order to avoid evaporation of medium. A 0.22 µm sterile filter was connected at the end of the gas tubings. A water bath was used to heat up both the reservoir and the humidifying chamber. The reservoir was elevated by a height of 50 cm relative to the chip, creating a hydrostatic pressure difference of 50 mbar. Pressurizing the system has previously been used to collapse bubbles trapped during priming of the system, and to suppress bubble formation during culture [18].

A peristaltic pump was used to create a pressure gradient in order to push medium through the chip and back into the reservoir. With recirculating flow, factors secreted by cells are being washed out, diluted in the medium reservoir and transported back to the culture chip, instead of being constantly removed by non-recirculating

flow. Furthermore, recirculation reduces the overall consumption of the culture medium especially at high flow rates.

The different materials used, along with the length and internal volumes of the different system parts are summarized in **Table 7-5**. Polyether ether ketone (PEEK) tubings (Upchurch Scientific, #1532) with 0.5 mm ID and Pharmed BPT peristaltic pump tubing with 0.8 mm ID was used for medium transport. Male nuts (P-206), 1/16" Ferrule (P-200), 1/4-28 Female to Male Luer Lock (P-675) and 1/4-28 Female to Female Luer Lock (P-678) from Upchurch Scientific, and Male Luer Lock Connector Barbed 1/16" (#10826) from ibidi, was used as connectors.

Table 7-5. Length (L) of tubing parts and internal volume including dead volume (V), of different parts of the system. Numbers correspond to those indicated in **Figure 7-5**.

	Material	**L [mm]**	**V [µL]**
Inlet tube (1)	PEEK	860	190
Chip	TOPAS	-	310
Chip-to-injection valve (2)	PEEK/PVC	105	70
Injection valve to pump (3)	PEEK/PVC	300	175
Peristaltic tubing	Pharmed BPT	185	120
Outlet tube (4)	PEEK	625	155
Total			1020

The chip was contained inside a microscope stage incubator, which was heated by warm, circulating water. The polymer chip was clamped mechanically on top a microscope glass slide, using a custom-milled aluminum holder. The top cover of the incubator consisted of a PMMA and an aluminum plate sandwiched together, with holes milled to fit fluidic connectors. Finally, a 3-way injection valve (BD Connecta #394982) was inserted close to the inlet of the chip, to allow injection of cells into the chip using a Luer-Lock syringe without the need to disconnect any fluidic connectors. This reduces the risk of introducing both air bubbles and infectious agents into the chip during seeding.

7.3.2 Experimental procedure

The procedure used to culture DCs on chip was based on those used for culture dish, although with several modifications. Before the start of each experiment, all the material that would be in direct contact with the culture medium was autoclaved at 121 °C for 15 min, except the culture chip. As TOPAS is hydrophobic in its native state, the chips were exposed to air plasma (50W, 10 min) to render it hydrophilic as well as sterile. The culture medium was equilibrated inside a CO_2-incubator overnight before the start of the experiment. After sterilization, as much sample handling as possible were performed inside a laminar flow bench.

PBMCs were thawed and analyzed in the same way as described in **Section 7.2.1**. After washing, cells were resuspended to a concentration to 7×10^7 cells/mL in 400-500 µL culture medium. By injection with a Luer-Lock syringe, cells were seeded into the empty chip by capillary filling. After 1 h incubation at 37 °C, non-adherent cells were removed by pumping medium at 2 mL/min for 10 min. Subsequently, the pump was set to periodic flow, with a rate of 80 µL/min for 5 min followed by a 25 min incubation period. After 5 days of culture, the reservoir content was replaced with new medium containing maturation cytokines, in addition to IL-4/GM-CSF, and the

culture was continued for 2 more days. At day 7, cells were harvested by flowing cold Na-EDTA through the chip and incubated for 30 min. Adherent cells remaining were harvested by pumping at 12.5 mL/min for 3 min. For more detailed information on the experimental procedures, refer to **Section A.5** for the full protocol.

7.3.3 Cell seeding and sorting

Figure 7-6 shows the cells seeded inside the chip before and after sorting by applying a flow rate of 2 mL/min. The bar diagram shows the fraction of $CD14^+$ cells before sorting (16.3%), non-adherent (5.9%), and adherent cells (25.1%) for a total of five experiments with cells from donor #2. These experiments are further presented in **Table 7-6**, as two seeding methods were tested: direct injection into the chip, and injection through the 3-way valve. The fraction of $CD14^+$ lost during sorting was smaller for direct injection (6.6%), compared to when using the injection valve (26.4%). The dead volume from the injection point to the chip inlet was measured to be 70 µL, comprising about 18% of the total volume before the chip outlet. However, the sorting specificity seems to be similar for both methods, as the fractional increase in $CD14^+$ cells before and after sorting was similar (55% *vs.* 53%).

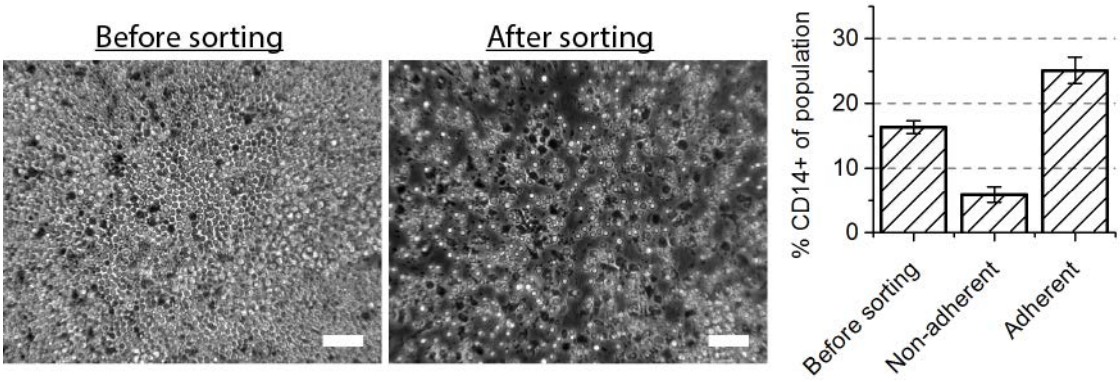

Figure 7-6. Phase contrast micrographs of cells inside the chip before and after removal of non-adherent cells by laminar flow. The fraction of $CD14^+$ non-adherent cells as determined by flow cytometry was 5.9% on average compared to 16.3% for the total population (donor #2). The estimated fraction of $CD14^+$ cells remaining on chip was estimated to increase to 25.1%. The error bars are the SE (n=5). The scale bars are 50 µm.

Table 7-6. Comparison of 5 experiments using two different seeding methods on chip. Flow cytometry data is from donor #2, before and after sorting of PBMCs on chip, as well as an estimate of the fraction of $CD14^+$ adherent cells remaining in culture.

	Direct loading			Injection valve			
Experiment	**1**	**2**	**Average**	**3**	**4**	**5**	**Average±SE**
Before sorting							
Seeding density (x $10^6/cm^2$)	1.46	1.57	1.51	2.12	1.61	1.45	1.7
Viability (%)	99.4	99.5	99.5	99.2	99.5	99.5	99.4±0.1
$CD14^+$ (%)	19.6	17.7	18.7	15.4	14.5	14.5	14.8±0.3
Non-adherent cells							
Fraction of cells seeded (%)	27.8	43.3	35.6	55.5	49.3	48.7	51.2±2.2
Viability (%)	99.0	99.9	99.5	99.6	99.7	99.6	99.6±0.1
$CD14^+$ (%)	2.6	3.9	3.3	7.4	5.9	9.7	7.7±1.1
$CD14^+$ recovery (%)	96.3	90.4	93.4	73.3	79.9	67.4	73.7±3.6
Adherent cells (estimate)							
Cell density (x $10^6/cm^2$)	1.29	1.09	1.2	1.45	1.01	0.91	1.1
$CD14^+$ (%)	26.2	31.2	28.7	26.3	22.8	19.0	22.7±2.1
$\Delta CD14^+$ (%)	33.7	76.3	55.0	70.8	57.2	31.0	53.0±11.7

Homogeneous seeding on chip was not possible for cells from all donors. The fraction of granulocytes in the buffy coat prepared by Herlev Hospital is normally around 10%, while for donor #3 and #4, the number was 20-30%. In addition, the fraction of erythrocytes was higher than normal for donor #3 and #4. This led to spontaneous cell aggregation during thawing. The aggregates could be dispersed by pipetting, but this did not prevent re-aggregation. Cells also aggregated inside the chip after injection. Sorting by laminar flow led to the formation of visible clumps being pushed against the sidewalls of the chamber and obstructing the flow (**Figure 7-7**). Cells from donors #3 and #4 were therefore not used for DC generation.

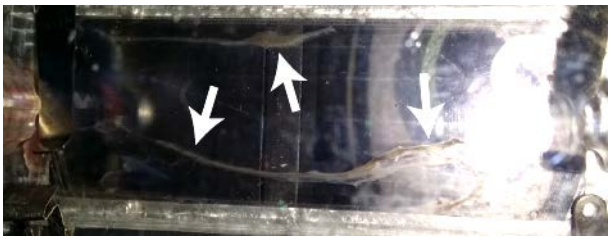

Figure 7-7. Spontaneous aggregation with cells from donor #3 led to formation of zones with extremely high cell density after sorting.

7.3.4 Bubble formation during culture

During the first perfusion culture experiments using Pharmed BPT and Tygon

E-3603 tubings, large pockets of air consistently started to appear close to the inlet of the chip after about 1 day (**Figure 7-8**). As the perfusion culture progressed, the air pocket continued to grow, constituting 50% of the chamber volume at day 4. This led to the number of harvested DCs being very low (data not shown), and was therefore considered a considerable fault with the first version of the perfusion system.

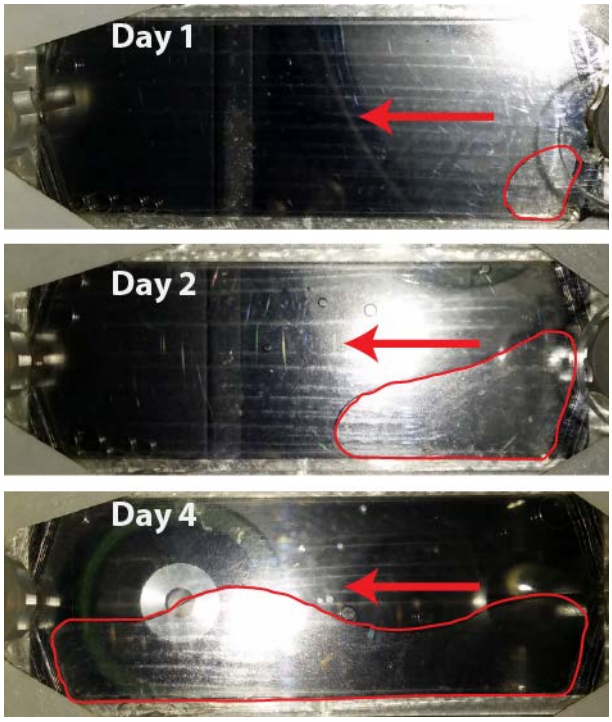

Figure 7-8. Bubble propagation through chip during flow. The air-liquid interface has been colored red for visualization. The arrows show the flow direction.

To prevent bubble growth, it was decided to dedicate some effort to discover the mechanisms behind this phenomenon. Several "dummy" experiments were performed; medium or PBS was recirculated through the chip at a constant rate, while a time-lapse series of the chamber inlet was recorded to determine at what time, t_B, bubbles started to enter the chamber. PTFE tubings were used for all experiments (ID=0.8mm, OD=1.6mm). The results for different configurations are summarized in **Table 7-7**. The annotation "IV" means that the injection valve in **Figure 7-5** was inserted immediately before the chip inlet. Bubbles appeared independently of the pump direction (run #1 and #2). In addition, external CO_2 supplied to the reservoir led to bubble formation independently of reservoir and incubator temperature, and occurred for both X-VIVO 15 and PBS. There was one exception (#3) where no bubbles were observed during 67 h when both heaters were turned off. However, two similar experiments (#6 and #7) led to bubble formation after 30 and 21 h respectively, where the only difference being the removal of the injection valve.

Table 7-7. Summary of different perfusion system configurations and the influence of bubble formation at the chip inlet. The flow direction was defined as positive when liquid was transported from the pump to the chip, and negative when it was sucked from the chip to the pump. The annotations "IV" and "X-V" mean injection valve and X-VIVO15 respectively.

Run	**Reservoir** T (°C)	CO_2	**Chip** T (°C)	**Flow** Rate (mL/min)	Dir.	**Liquid**	**Tubing**	**t_B (h)**
1	40	ON	36	0.8	Pos.	X-V	PTFE+IV	15.5
2	40	ON	36	0.8	Neg.	X-V	PTFE+IV	10
3	25	ON	25	0.8	Neg.	X-V	PTFE+IV	>67
4	25	ON	36	0.8	Neg.	X-V	PTFE+IV	14.5
5	40	ON	36	0.8	Neg.	X-V	PTFE	18
6	25	ON	25	0.8	Neg.	X-V	PTFE	30
7	25	ON	25	0.8	Neg.	X-V	PTFE	21
8	25	OFF	25	0.8	Neg.	PBS	PTFE	>62
9	40	OFF	25	0.8	Neg.	PBS	PTFE	>86
10	40	OFF	36	0.8	Neg.	PBS	PTFE	>66
11	40	ON	36	0.8	Neg.	PBS	PTFE	12

The introduction of bubbles was finally solved PEEK was used between the reservoir and the inlet. This material has much lower gas permeability as will be discussed later in this chapter.

7.3.5 DC maturation on chip

After the tubing material was changed to PEEK, it was possible to culture cells for 7 days without bubbles appearing at the chamber inlet. **Table 7-8** shows an overview of two DC culture experiments reaching day 7 performed on chip with cells from donor #2.

Table 7-8. Flow cytometry analysis after 5+2 days of differentiation + maturation of DCs on chip, using PBMCs from donor #2.

	Exp. 3	**Exp. 6**
Viable cells (%)	82.7	97.8
DCs from gating (%)	36.6	16.9
$CD83^+$ from DC gating (%)	82.8	81.2
$CD83^+$ total (%)	25.0	12.7
MFI, CD83	22.9	20.2
MFI, CD14	1.06	
Yield (%)	15.7	6.0

Figure 7-9 shows flow cytometry data from harvested cells at the end of culture (experiment #3, donor #2). A total of 3.2×10^6 cells were harvested. Of these, a fraction of 82.7% was viable as determined by 7AAD staining. Furthermore, a fraction of 36.6% of the viable cells were gated as DCs, for which 82.8% was determined to be $CD83^+$, a total of 25.0% of all harvested cells. The MFI for anti-CD83 APC and anti-CD14 PE relative to the isotype controls, was to 22.9 and 1.06 respectively, suggesting

that the harvested DCs showed a moderate level of CD83-expression, compared to DCs cultured in petri dish, and no expression of CD14. The yield of $CD83^+$ DCs relative to the initial number of $CD14^+$ monocytes was 15.7%.

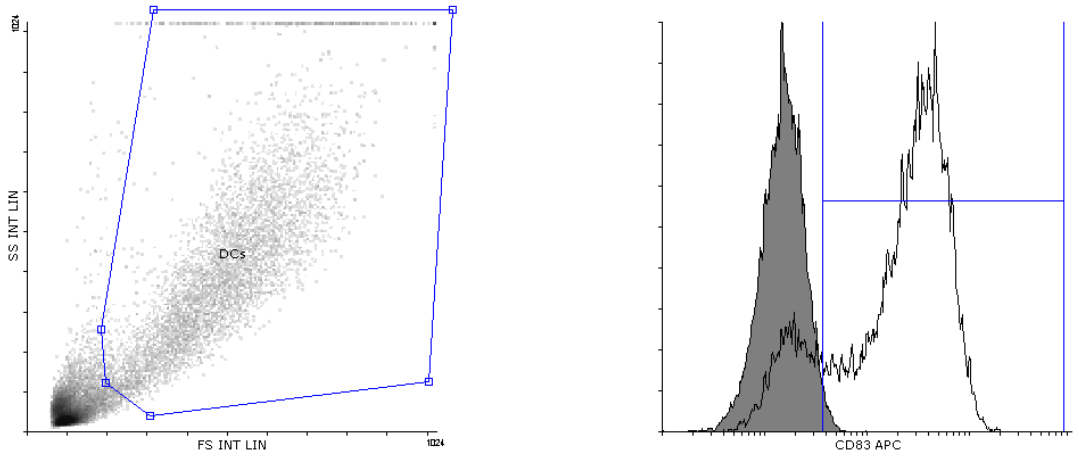

Figure 7-9. Forward vs side-scatter plot of harvested cells (experiment 3, donor #2), shows a distinct DC population. Cells stained with anti-CD83 APC and an isotype control shows that the majority of DCs were matured at the end of culture (82.8%).

Time-lapse microscope images were taken every 15 min at 15 different positions across the chip area. Images taken in the center of the chamber at a distance of 4 mm (upstream), 27.5 mm (middle), and 51 mm (downstream) from the inlet, at day 0 (after sorting), 1, 3, 5 and 7, are shown in **Figure 7-10** (available as videos on the attached CD, folder "*Time-lapse of microfluidic perfusion culture*", and online: Upstream.avi, Middle.avi, and Downstream.avi). After 1 day of culture, the cell density was considerably lower than immediately after sorting. After 2-3 days of culture, several cells became more elongated, reaching lengths over 100 µm in some cases. After 5 days, when maturation cytokines were added to the culture medium, cells became markedly more mobile as can be seen in the time-lapse videos (Downstream.avi and Middle.avi). Furthermore, it appears as if the cell density was reduced closer to the inlet of the chip after day 1, as compared to further downstream.

The change in morphology was highly dependent on the local cell density, as seen in **Figure 7-11** (available as videos on the attached CD, folder "*Inhomogeneous cell seeding*", and online: High density.avi and Low density.avi). Due to cell aggregation in experiment 6, extremely high densities were created, while a low density was observed elsewhere on the chip. In total, 71.4% of all cells remained inside the chip after sorting. Flow cytometry data from sorting is not shown because the instrument was out of order at that time. Therefore, the average fraction of $CD14^+$ cells from frozen PBMCs used in earlier experiments was used to estimate the yield. At high densities, cells became more elongated, similar to what was observed in experiment 3. In addition, at day 7, the cells were highly mobile (High density.avi) and formed clusters, as indicated by the arrows. In other areas of the chip where the density was low after sorting, cells were continuously removed over time by laminar flow and no morphology change was observed (Low density.avi).

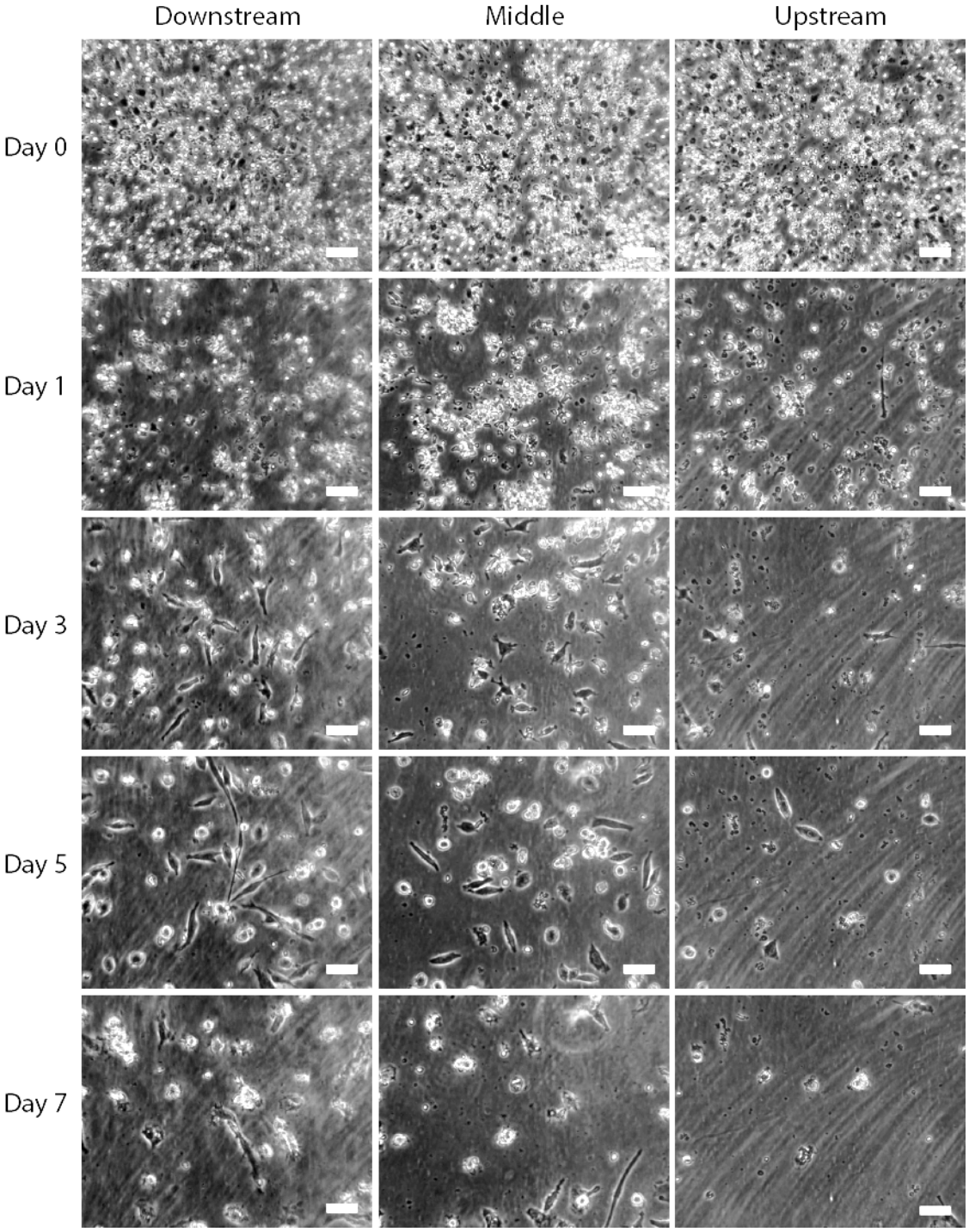

Figure 7-10. Phase contrast micrographs taken at the center of the channel at 4 mm (upstream), 27.5 mm (middle) and 51 mm (downstream) from the chamber inlet. It appears that the cell density after day 1 was lower closer to the inlet than the outlet. The scale bars are 50 μm.

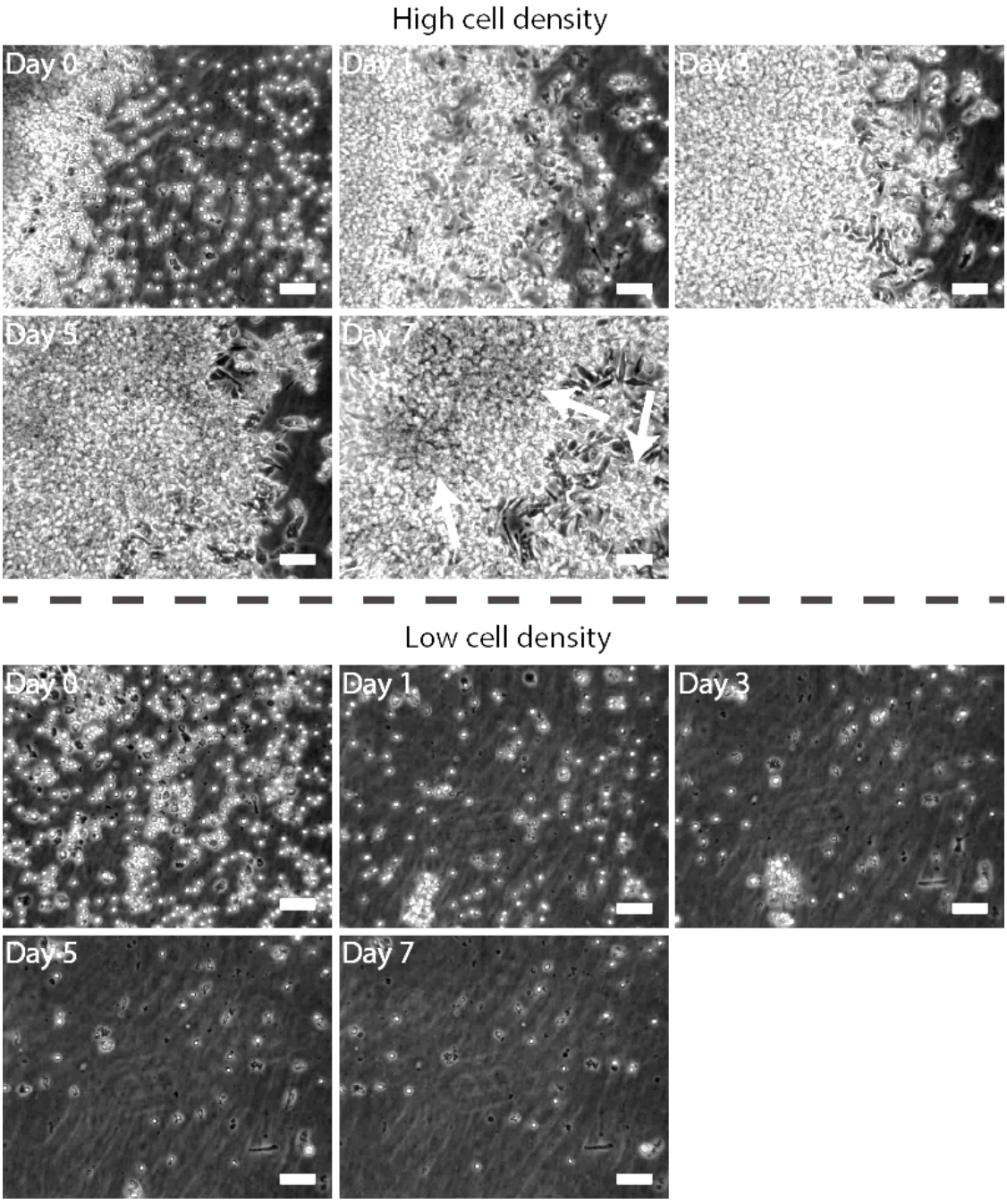

Figure 7-11. Phase contrast micrographs showing that cell morphology during culture was highly dependent on the local density. At extremely high densities caused by aggregation, cells became more elongated and arranged in clusters as indicated by the arrows. At low densities however, cells were removed by laminar flow and the cell morphology did not change. The scale bars are 50 µm.

The fraction of cells that could be harvested at the end of culture was dependent on the position across the culture chamber width as shown in **Figure 7-12** (experiment #3, donor #2). In the middle of the chamber, all cells were completely removed by laminar flow. At a distance of 5 mm away from the chamber wall, a higher fraction of cells remained after harvest; 24% and 27% for the left and right side respectively. At very high densities (**Figure 7-13**), a large number of cells remained inside the chip after harvest (experiment #6, donor #2). In this experiment, a total of 2.6×10^6 cells were harvested, of which 12.7% were viable, $CD83^+$ DCs (**Figure 7-14**

and **Table 7-8**). However, a large fraction of the population above the 2% non-specific threshold was weakly stained (bimodal population). The relative MFI was determined to be 20.2.The total yield of mature DCs was 6.0% relative to the number of seeded $CD14^+$ monocytes.

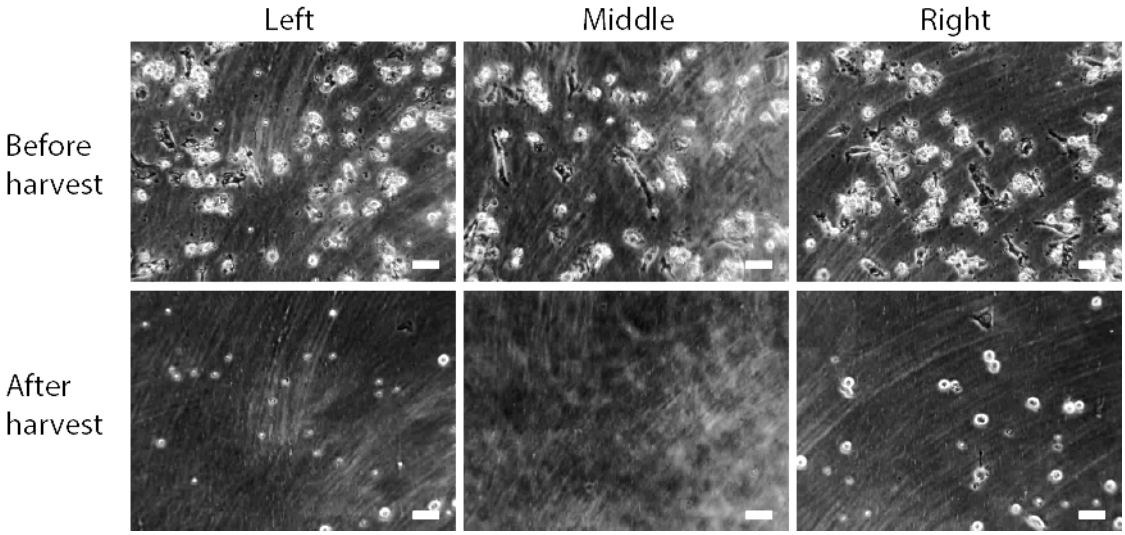

Figure 7-12. Phase contrast micrographs showing a different cell harvest efficiency at different positions separated by 5 mm across the chamber width (experiment 3, donor #2). After 30 min incubation and flushing with Na-EDTA, the fraction of cells remaining after harvest was 24%, 0% and 27% at the left, middle and right section of the chamber. The scale bars are 50 µm.

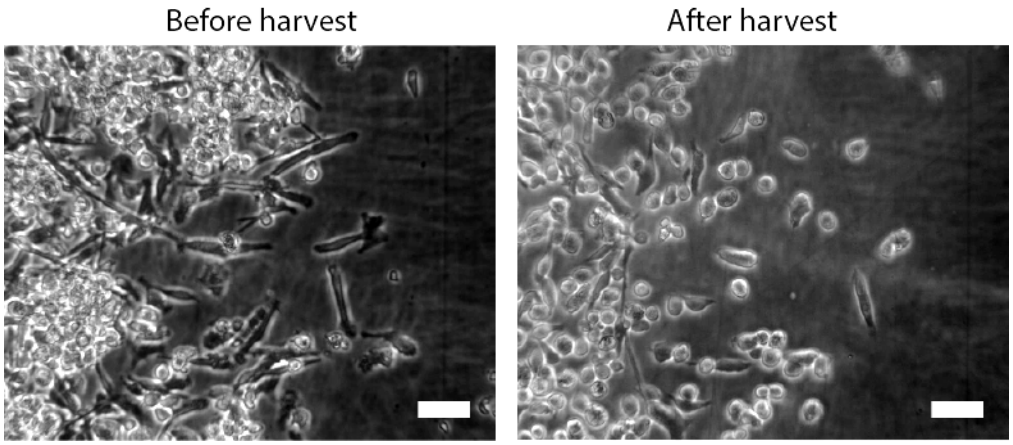

Figure 7-13. Phase contrast micrographs showing a low cell harvesting efficiency where the local cell density was high (experiment #6, donor #2). The scale bars are 50 µm.

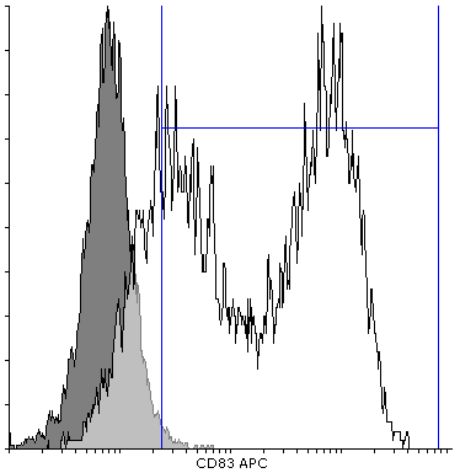

Figure 7-14. Fluorescence histograms from flow cytometry of harvested DCs from a culture with non-uniform density (experiment #6, donor #2), stained with anti-CD83 APC against an isotype control. A non-uniform density resulted in a weak maturation as seen by the bimodal distribution.

7.4 Discussion

7.4.1 Monocyte enrichment by adherence sorting

The relative higher monocyte adherence to plastic surfaces compared to other PBMCs was used to increase the purity in both culture dish and chip. By sorting of cells from donor #2 in culture dish, an increase of 59% for the $CD14^+$ fraction after sorting was observed, ending up with a purity of 27.6%. With cells from donor# 1 and #3, the results were similar.

Two different seeding methods on chip were employed: direct injection using a syringe connected to the chip Luer Lock connector, and injection through the injection valve. The increase in purity after sorting was on average 55% and 53% for the two methods, ending up at a purity of 28.7% and 22.7% respectively. The difference in purity was caused by a higher initial fraction of CD14+ for the cells seeded directly. Although, there was no apparent difference in sorting specificity between the two methods, a lower recovery for injection through the valve was observed (73.7% *vs.* 93.4%) due to dead volume, which meant that about 18% of the cells were not seeded inside the chip. Since PEEK tubings and connectors are bioinert [222], it is likely that most of these cells were removed during washing. Despite the lower recovery, this seeding method was preferred, due to the risk of introducing bubbles and contaminants when removing and attaching fluidic connectors associated with direct injection. For comparison, sorting in Petri dish led to a purity of 27.6% and a recovery of 84.6% (donor #2, **Table 7-1**), which is comparable to on-chip sorting.

Sorting at a flow rate of 2 mL/min, corresponding to a wall shear stress of about 0.1 Pa on average (equation (4-1)), did not result in any difference in purity compared to sorting in dish. However, the sorting on chip was not optimized and a higher shear stress could lead to an increased purity of adherent monocytes, although with the risk of achieving a lower recovery and damaged cells. Sorting of cells in a culture dish is highly dependent on the hand movements and pipetting of the operator,

and is therefore difficult to optimize.

Large cell aggregates were formed during thawing of PBMCs from donors having a higher fraction of granulocytes and erythrocytes. This was a detrimental problem when culturing on-chip, since large cell aggregates led to obstruction of the flow through the microchannel, creating non-uniform culture conditions. It is known that cell aggregation can be caused by DNA released by granulocytes and erythrocytes that are lysed during the freezing/thawing cycle [223]. Cell clumping can be reduced by adding DNAse to the wash medium [223]. However, this would increase the experimental costs and was therefore not exploited in this study.

Although sorting by adherence has been the most common and simple method of monocyte enrichment, other more advanced techniques exists. Using positive selection with anti-CD14 functionalized magnetic beads, it has been demonstrated that the $CD14^+$ monocyte purity from an apheresis product can be increased from 18% to 97% of all WBCs, with a recovery of 82% [224]. Monocytes can also be enriched by depletion of lymphocytes using anti-CD2 and anti-CD19 beads, although with a lower purity (61%) and a lower recovery (41%), likely due to CD2 expression of some monocyte subsets or non-specific binding [225].

Another method is elutriation, which is based on counterflow centrifugation to separate cells based on both size and density [116]. With this method, the centrifugation speed is kept constant while the counterflow velocity of a buffer is increased step-wise, to collect cells into separate fractions according to their size. It has been demonstrated that monocytes can be sorted with a purity of 83% and a recovery of 75% [116]. Both magnetic- and elutriation-sorting of monocytes can be performed within a closed system. However, it is not clear how the magnetic nanoparticles affect DCs and it is therefore not very suitable for clinical applications since the cells are injected back into the patient. In contrast, elutriation keeps the monocytes “untouched” for later cell culture, therefore generating a more defined product in compliance with GMP. Among the disadvantages are that elutriation systems are expensive in capital investment as well as per purification step, and that monocytes are sorted by size/density and not by phenotype, potentially causing selective isolation of certain monocyte sub-populations [41].

There are other label-free alternatives to cell sorting by size, which can be integrated on-chip [226]. One method is using deterministic lateral displacement (DLD), where fluid flows through an array of microposts, where each row is slightly offset laterally relative to the previous. Depending on the spacing between posts and the relative row shift, particles smaller than a critical hydrodynamic radius will follow streamlines through the gaps, while larger particles will be displaced at each obstacle and bump into the neighboring streamline [227]. This principle has been used to separate WBCs from RBCs and plasma in whole blood [228]. The advantage of this method is that it is passive, however it has only been demonstrated using low flow rates (1 µL/min). Also, imperfections in the array tended to blur the streams of differently sized particles into a continuous distribution [229].

Another method is dielectrophoretic field-flow fractionation, which separates cells based on a combination of density and dielectric properties [230]. In a pressure-driven flow, leukocyte subpopulations were levitated to different heights based on different density and membrane dielectric properties. Due to the parabolic flow profile, lymphocytes, monocytes and granulocytes from a buffy coat were therefore eluted at the end of the channel at different times. High flow rates could be attained (mL/min) at medium cell concentrations (10^6 cells/mL).

7.4.2 Gas permeability

As previously mentioned, the problem with large air pockets close to the chip inlet was overcome by switching to PEEK tubings. Although it was shown in **Section 6.4** that Tygon tubings could maintain a constant pH of the medium, it is believed that gas permeation caused bubbles to nucleate, merge and collect at the chip inlet. Since the medium was equilibrated at a 5% CO_2 atmosphere in the reservoir, it was supersaturated with dissolved CO_2 during transport through the tubings, creating a driving force for bubble nucleation on the inside of the tubing wall. As seen from equation (6-8), permeation is not only dependent on the material type. A proportionality constant k for the amount of permeated gas M can be found by re-arranging and inserting for the flow rate Q, the gradient of CO_2 partial pressure Δp_{CO_2}, the tube radius r and length L

$$M \propto k = \frac{P \times r^3 \times L^2 \times \Delta p_{CO_2}}{Q \times d} \tag{7-1}$$

By assuming that Δp_{CO_2}, Q and L are constant for the different tubing materials, the proportionality constant can be simplified to:

$$k' = \frac{P \times r^3}{d} \tag{7-2}$$

The values of k' for all the tubing materials tested for perfusion cell culture are listed in **Table 7-9**. By changing to PEEK tubings, permeation was reduced significantly due to a combination of material properties and reduced ID. Since no bubbles were observed, it is therefore believed that the time scale for bubble nucleation and growth was reduced to be shorter than the time scale for medium transport to the chip.

Table 7-9. The ability to permeate dissolved CO_2 during transport through different tubing materials for a given length (L), flow rate (Q), and pressure gradient ($\boldsymbol{\Delta p_{CO_2}}$), is characterized by the proportionality constant k', given by a combination of material permeability (P), inner radius (r) and wall thickness (d).

	***P* (cm^3 mm / m^2 day atm)**	***r* [mm]**	***d* [mm]**	***k'***
Pharmed BPT	7900	0.4	1.6	316
Tygon	2400	0.4	1.6	96
PTFE	604	0.4	0.4	97
PEEK	10.8	0.25	0.55	0.31

7.4.3 Generation of DCs on chip compared to culture dish

Due to the effort required to set up the perfusion system and unforeseen problems with cell clumping from certain donors, there was not enough time to perform the experiments required to make a statistical comparison between DC generation in dish and chip. Therefore, only trends from two experiments on chip will be discussed in this section.

Generally, the DC fraction of cells harvested on day 7 was lower for chip culture than for culture dish. In addition, the harvested DCs cultured on chip had a

lower CD83 expression than dish-culture, both in terms of $CD83^+$ fraction (82% *vs*. 97%) and MFI relative to isotype control (22 *vs*. 63) for the total DC population. DCs cultured in both systems showed a similar down-regulation of CD14. The total yield of harvested $CD83^+$ cells relative to $CD14^+$ monocytes were lower for the two chip-culture experiments (6% and 16%) compared to culture dish (28.6±6.9%).

Based on cell morphology and motility, it appears that a high cell density was beneficial for DC differentiation and maturation (**Figure 7-11**). However, achieving a homogeneous monolayer with a higher density than what was used in these experiments is likely not feasible. By using closest packing of 8 µm diameter circles, the maximum density of a non-attached cell monolayer is 1.8×10^6 cm^{-2}. In reality, however, lymphocytes and monocytes have different size (about 7 and 10 µm respectively) and are not perfectly round. In addition, they are randomly seeded on the surface, thus leading to a packing density lower than the theoretical predicted value. It is therefore likely that for the results presented here, a multi-layer was formed and that increasing the seeding density will only lead to stacking of more cells on top of each other. To achieve a higher density during culture, a more efficient enrichment of monocytes is therefore required before seeding.

Although the yield of matured DCs was apparently lower for culture on chip than culture dish, it is difficult to make a direct comparison since it was not possible to harvest all cells in the closed system. There could be several explanations for this. One could be that the shear stress generated by laminar flow during harvest, which was estimated to be ~ 0.5 Pa, is not sufficient to remove adherent cells. In addition, since the culture chamber had a varying height (**Figure 6-8**), the local shear stress was likely different at various positions. This could explain the varying number of cells remaining across the channel width (**Figure 7-12**). Also, it was more difficult to remove high density cell clusters, possibly because they alter the local hydraulic resistance of the channel (**Figure 7-13**). One way to detach adherent cells more effectively is by addition of trypsin. However, this method could modify the cell surface expression of membrane proteins [42], which is not in conformity with GMP.

After one day of culture on chip, a lower density than immediately after seeding was observed (**Figure 7-10**). From the time-lapse videos (see Upstream.avi, Middle.avi, and Downstream.avi), removal of non-adherent cells during the first day by the pulsating flow was observed. In addition, the density was higher downstream than upstream inside the culture chamber. It has previously been observed that monocyte adherence to the culture plastic was reduced during the first days after start of culture [115], [231]. A possible explanation to why the density was higher downstream, could therefore be that loosely attached cells upstream were removed over time and transported together with the flow, before re-adhering when the flow stopped.

In contrast to perfusion culture, where non-adherent cells were continuously removed by the flow, the cell density was higher throughout the culture in dish, since washing was only performed on day 0 and day 7. This, together with incomplete harvesting could explain why the number of DCs was higher for the dish culture. Also, as **Figure 7-11** indicates that a high density may be beneficial for DC generation, it could explain why the DCs cultured in dish expresses a higher level of CD83.

It is known that adherence is an important regulator of monocyte behavior, and could be used to promote activation [232]. Adherent monocytes cultured overnight demonstrated a transient expression of CD83 without the addition of cytokines (*fast*DCs), reaching a maximal level after 16-24 h before turning to baseline levels after 48 h [233]. The activated monocytes displayed reactivation of T-cells, although they were not as potent as mature DCs. Furthermore, Zhou *et al.* observed that after

TNF-α was added to a GM-CSF/IL-4 monocyte culture on day 5, cells became firmly adherent to the culture dish [220]. Also, at the end of culture, the adherence of DCs seems to be dependent on their maturation stage, as immature DCs are reported to be firmly attached while mature DCs are less adherent [234]. If a large number of DCs cannot be easily harvested, it may therefore be a sign that they are not fully matured, although adhesion depends on a combination of material properties, medium composition, and mechanical stimulus.

It is not established in what way the application of shear stress induced by laminar flow could affect monocyte differentiation and DC maturation. It is known that shear stress increases the expression of adhesion-mediating molecules of endothelial cells, thereby increasing monocyte-binding [235], but it is not known in which way it affects the binding of monocytes directly to culture plastic. In addition, adherence and differentiation could be affected by the mass transport during perfusion. The choice of medium exchange rate was based on simulations of the oxygen consumption, although the actual consumption during culture was not verified. Therefore, a longer incubation time might be used, thereby allowing a higher accumulation of secreted factors, which again could be beneficial for the differentiation and maturation process.

There are other closed systems that have been used for DC generation, which are not based on perfusion culture. The use of gas-permeable bags for generation of monocyte-derived DCs, for example, has been explored by several groups [116], [219], [236], [237]. An advantage of culture in bags is that monocytes can be directly loaded through tubings while maintaining sterility. It is also believed that cells cultured in bags adhere less firmly to the container surface; therefore they can be more easily harvested than adherent culture. Several bag materials have been used, such as ethylene vinyl acetate (EVA), fluoro ethylene propylene (FEP) and polyolefin (PO). However, it is not established whether bag-cultured DCs are more clinically suitable than adherent-cultured DCs or not. One study showed comparable DC maturation by phenotype for cells cultured in PO bags and tissue culture PS flasks [236], while another showed a lack of CD1a and CD25 expression for DCs cultured in FEP bags but not in EVA [116]. In addition, it was demonstrated that DCs cultured in flasks secreted IL-12, which is an important T-cell stimulatory factor, but not when they were cultured in PO or FEP bags [238]. Therefore, it is likely that adhesion plays an important role in generation of DC vaccines. Finally, a system that allows both aseptic transfer and cell adhesion is the Nunc Cell Factories, which essentially consists of culture plates stacked on top of each other. This has been used to generate a large number of DCs with similar surface marker expression and functionality as DCs cultured in flask [43], [239]. However, harvest of adherent cells using this system could be more challenging as culture surfaces are not easily accessible.

7.5 Conclusion

In this chapter, it has been shown that $CD83^+$ mature DCs can be generated from $CD14^+$ monocytes in a microfluidic perfusion culture chip, which can easily be upscaled for industrial mass fabrication. The culture can be run outside conventional CO_2-incubators, thereby potentially reducing the bulkiness of the system. In addition, with a more careful design of the medium reservoir, the system can be truly closed to eliminate infections. Further optimization of the perfusion strategy is required in terms of improved purity after sorting, appropriate flow rates during different stages of

culture, and improved procedures for cell harvesting, preferably with integrated feedback systems to monitor the status of the culture.

Chapter 8

Conclusion and outlook

One of the goals of this thesis was to produce polymer substrates with nanoscale surface topography over a large area, using techniques compatible with industrial mass fabrication, with the potential application of increasing the efficiency of adherent cell culture harvesting. By using DUV stepper lithography, homogeneous areas (~100 cm^2) with sub-250 nm holes on a Si master could be defined. Holes with a diameter down to 180 nm and a pitch of 340 nm were achieved, although with a larger spatial variation in the photoresist pattern. The nanoscale topography was successfully transferred to a Ni mold inlay by electroplating from the metallized master. Defect-free pillars were achieved when inlays were plated from Cr and Au sputter coated on etched Si, compared to plating from photoresist or etched silicon metallized with NiV. Furthermore, patterns could be transferred to a HSQ films on stainless steel substrates by imprinting of an elastomeric stamp, although with some loss in resolution. Deposition of an FDTS monolayer on HSQ or NiV coated with Al_2O_3 and SiO_2 by ALD and CVD, led to shielding of polar interactions and a lower surface energy, compared to FDTS deposited on bare NiV.

Nanoscale patterns were transferred to COC by injection molding, although complete replication of mold protrusions with an aspect ratio of 1.8 was not achieved with a mold temperature below the glass-transition point of the polymer. By using variothermal mold cycling, full replication was achieved, at the cost of systematic deformations of the pattern and a considerably longer process cycle time. Indications that monocyte adhesion may be greatly reduced on these replicas were observed, when the spacing between holes was smaller than 140 nm, although more systematic studies are needed. Replication using an isothermal process was improved with a HSQ-coated steel mold compared to a Ni mold, both in terms of a larger mean height and more uniformly distributed height of pillars in the polymer. By simulation of the heat transfer from the polymer melt to the mold surface, the HSQ film was shown to act as an insulating layer that allowed more time for the melt to flow before solidifying. HSQ may therefore have the potential to improve nanoscale replication in an industrially relevant setting, by reducing the need for variothermal mold cycling.

Another goal in this thesis was to physically integrate proteins with retained biofunctionality on the surface of inert thermoplastics, using high-throughput fabrication methods, and to demonstrate phenotype-specific cell capture from a mixed cell population. By using spotting of protein drops, sub-100 µm patterns of avidin on a fluorinated mold surface could be achieved. Addition of 10% DMSO to the spotting

buffer increased the spot homogeneity by reducing evaporation of deposited droplets. This also enabled spotting on superhydrophobic nanostructured Ni surfaces. Furthermore, transfer of avidin spots to polymer replicas by injection molding was achieved, with retained biotin recognition. Biotinylated anti-CD14 bound to transferred avidin demonstrated an increased monocyte adhesion on untreated COC polymer, although not to the same level as biotinylated anti-CD14 bound to avidin deposited by passive adsorption. In addition, monocyte adhesion was only slightly higher compared to an isotype control, showing that the level of unspecific binding to antibodies was high.

Highly efficient transfer of antibodies passively adsorbed on a surface functionalized mold inlay surface to a COC replica by injection molding was demonstrated. Insignificant amounts of protein residuals remained on the mold surface after transfer, as verified by AFM and XPS, thus making multiple subsequent protein transfers using the same mold possible. The antigen-binding affinity of transferred capture antibodies was similar to that of antibodies adsorbed by passive adsorption directly on polymer surfaces, as verified by sandwich ELISA. In addition, 10 min incubation time of antibody solution on the mold surface prior to transfer resulted in fully satisfactory antigen response curves on replicas with transferred antibody. Also, it was possible to re-use the same mold for at least six consecutive protein transfers, while retaining antigen-binding affinity. Finally, antibodies transferred during injection molding retained their functionality after 3 weeks of dry storage followed by 9 days of immersion in standard serum-containing cell culture medium. Thus, direct immobilization of antibodies at a polymer surface during injection molding is a promising approach for high-volume production of functionalized disposable polymer biochips for immunoassay or cell capture applications.

The last objective of this thesis was to fabricate disposable polymer chips for the generation of a large number of mature DCs in a closed microfluidic perfusion culture. Chips were fabricated by ultrasonic welding of a flat microscope slide to a chamber-containing slide injection molded against a micro-milled aluminum mold. A chamber height of 290 µm with a variation less than 7% CV over an area of 10 cm^2 was achieved. Through numerical modeling of oxygen levels over time in an impermeable microfluidic chamber containing metabolic active cells, it was found that an exchange frequency of one chamber volume every 30 min by pulsating flow was optimal. Furthermore, it was found that using PEEK tubings with low gas permeability allowed a constant pH and bubble-free culture medium for 7 days, when the medium reservoir and culture chip was kept outside a CO_2 cell incubator. Maturation of $CD83^+$ mature DCs generated from $CD14^+$ monocytes was demonstrated inside the disposable culture chip, with a yield almost comparable to standard culture procedures in an open Petri dish, thus indicating that closed chip-culture systems may increase automation and reduce cost of currently used procedures for cancer immunotherapy.

This thesis has contributed to new knowledge on polymer micro- and nanofabrication of polymers, with respect to large-area replication of DUV-defined nanotopography, protein micropatterning and physical integration of capture antibodies, as well as DC culture in a polymer microfluidic system. Still, there are various obstacles remaining before the results presented here can be directly integrated into cancer immunotherapy. While DC maturation on chip was demonstrated, the perfusion system was not fully optimized, especially with regards to seeding of cell suspension inside the chip and the optimal medium exchange rate during the 7 day culture. Integration of end-point sensors for oxygen or pH could provide a non-invasive method to monitor cellular response to various perfusion parameters, and

therefore assist in finding the optimal culture conditions. Upscaling from the microscope slide to the microtiter plate format, in order to increase the number of cells in culture closer to the clinically relevant range, can readily be achieved with the existing equipment and methods, although maintaining a constant chamber height over a larger area will likely require incorporation of support structures during welding. Ultimately, the goal is to integrate the remaining steps involved in cancer immunotherapy, i.e. transfection of mature DCs with tumor antigen and potentially also the activation of T-cells, on a single chip. Alternatively, multiple chip components may be connected further downstream, such as the continuous microfluidic electroporation system of DCs previously demonstrated by our group [240].

One of the remaining challenges that need to be solved is the low harvest efficiency of DCs achieved without using excessive shear forces that might be detrimental to cell viability. While some indications were found that nanotopography on injection molded polymers might reduce monocyte adhesion, these surfaces need to be integrated into the DC culture chip and tested for the entire length of a 7 day culture. Although close to complete replication of nanostructures on mold inlays were achieved by cycling of the mold temperature, it would greatly reduce the cost of fabrication by reducing the process cycle time with constant mold temperatures. HSQ demonstrated a reduced cooling rate of the polymer melt, although further effort to achieve thicker films with reduced thermally-induced stress will likely improve the replication even further.

Finally, although physical integration of polyclonal IgG with retained antigen-capture ability on injection molded replicas was demonstrated, transfer of monoclonal IgG such as anti-CD14 antibody and testing the ability to capture monocytes would be a highly relevant topic for further studies. Furthermore, the capture specificity, i.e. the adhesion of lymphocytes to these antibodies needs to be verified, as it would be advantageous to achieve both a high purity and a high yield after sorting. Eventually, by using ink-jet printing to deposit patches of multiple antibodies on mold inlays, such as anti-CD3 and anti-CD14, polymer replicas with injection molded proteins for cell panning of lymphocytes and monocytes could potentially be produced.

References

[1] J. N. Blattman and P. D. Greenberg, “Cancer immunotherapy: a treatment for the masses.,” *Science*, vol. 305, no. 5681, pp. 200–5, Jul. 2004.

[2] V. Groh, J. Wu, C. Yee, and T. Spies, “Tumour-derived soluble MIC ligands impair expression of NKG2D and T-cell activation,” vol. 419, no. OCTOBER, pp. 2–6, 2002.

[3] D. Gabrilovich, H. Chen, and K. Girgis, “Production of vascular endothelial growth factor by human tumors inhibits the functional maturation of dendritic cells,” *Nat. Med.*, vol. 2, no. 10, pp. 1096–1103, 1996.

[4] T. Wang, G. Niu, M. Kortylewski, L. Burdelya, K. Shain, S. Zhang, R. Bhattacharya, D. Gabrilovich, R. Heller, D. Coppola, W. Dalton, R. Jove, D. Pardoll, and H. Yu, “Regulation of the innate and adaptive immune responses by Stat-3 signaling in tumor cells.,” *Nat. Med.*, vol. 10, no. 1, pp. 48–54, Jan. 2004.

[5] T. J. Kindt, R. A. Goldsby, B. A. Osborne, and J. Kuby, *Immunology*, 6th ed. New York: W.H. Freeman and Company, 2004.

[6] I. Mellman and R. M. Steinman, “Dendritic Cells : Specialized and Regulated Antigen Minireview,” *Cell*, vol. 106, pp. 255–258, 2001.

[7] J. Banchereau and A. K. Palucka, “Dendritic cells as therapeutic vaccines against cancer.,” *Nat. Rev. Immunol.*, vol. 5, no. 4, pp. 296–306, Apr. 2005.

[8] G. Jego, A. K. Palucka, J. Blanck, C. Chalouni, V. Pascual, and J. Banchereau, “Plasma Cell Differentiation through Type I Interferon and Interleukin 6,” *Immunity*, vol. 19, pp. 225–234, 2003.

[9] A. E. Pedersen, M. Thorn, M. Gad, M. R. Walter, H. E. Johnsen, E. Gaarsdal, K. Nikolajsen, S. Buus, M. H. Claesson, and I. M. Svane, “Phenotypic and functional characterization of clinical grade dendritic cells generated from patients with advanced breast cancer for therapeutic vaccination.,” *Scand. J. Immunol.*, vol. 61, no. 2, pp. 147–56, Feb. 2005.

[10] R. Trepiakas, A. E. Pedersen, O. Met, M. H. Hansen, A. Berntsen, and I. M. Svane, “Comparison of alpha-Type-1 polarizing and standard dendritic cell cytokine cocktail for maturation of therapeutic monocyte-derived dendritic cell preparations from cancer patients.,” *Vaccine*, vol. 26, no. 23, pp. 2824–32, Jun. 2008.

[11] M. Hansen, G. M. Hjortø, M. Donia, Ö. Met, N. B. Larsen, M. H. Andersen, P. thor Straten, and I. M. Svane, “Comparison of clinical grade type 1 polarized and standard matured dendritic cells for cancer immunotherapy.,” *Vaccine*, vol. 31, no. 4, pp. 639–46, Jan. 2013.

[12] F. Sallusto and A. Lanzavecchia, “Efficient Presentation of Soluble Antigen by Cultured Human Dendritic Cells Is Maintained by Granulocyte/Macrophage Colony-stimulating Factor Plus Interleukin 4 and Downregulated by Tumor Necrosis Factor alpha,” *J. Exp. Med.*, vol. 179, no. April, pp. 1109–1118, 1994.

[13] H. Jonuleit, U. Kühn, G. Müller, K. Steinbrink, L. Paragnik, E. Schmitt, J. Knop, and A. H. Enk, “Pro-inflammatory cytokines and prostaglandins induce maturation of potent immunostimulatory dendritic cells under fetal calf serum-free conditions.,” *Eur. J. Immunol.*, vol. 27, no. 12, pp. 3135–42, Dec. 1997.

[14] S. Beglery, “Exclusive: Questionable data propped up cancer drug Provenge,” *Reuters*, 2012. [Online]. Available: http://www.reuters.com/article/2012/10/11/us-drugs-dendreon-provenge-idUSBRE89A15420121011. [Accessed: 17-Jun-2014].

[15] M. L. Huber, L. Haynes, C. Parker, and P. Iversen, “Interdisciplinary critique of sipuleucel-T as immunotherapy in castration-resistant prostate cancer.,” *J. Natl. Cancer Inst.*, vol. 104, no. 4, pp. 273–9, Feb. 2012.

[16] E. W. K. Young and D. J. Beebe, “Fundamentals of microfluidic cell culture in controlled microenvironments.,” *Chem. Soc. Rev.*, vol. 39, no. 3, pp. 1036–48, Mar. 2010.

[17] J. El-Ali, P. K. Sorger, and K. F. Jensen, “Cells on chips.,” *Nature*, vol. 442, no. 7101, pp. 403–11, Jul. 2006.

[18] L. Kim, Y.-C. Toh, J. Voldman, and H. Yu, “A practical guide to microfluidic perfusion culture of adherent mammalian cells.,” *Lab Chip*, vol. 7, no. 6, pp. 681–94, Jun. 2007.

[19] A. Manz, N. Graber, and H. M. Widmer, “Miniaturized total chemical analysis systems: A novel concept for chemical sensing,” *Sensors Actuators B Chem.*, vol. 1, no. 1–6, pp. 244–248, Jan. 1990.

[20] S. P. Forry and L. E. Locascio, “On-chip CO2 control for microfluidic cell culture,” *Lab Chip*, 2011.

[21] E. Berthier, E. W. K. Young, and D. Beebe, “Engineers are from PDMS-land, Biologists are from Polystyrenia.,” *Lab Chip*, vol. 12, no. 7, pp. 1224–37, Feb. 2012.

[22] H. Becker and C. Gärtner, “Polymer microfabrication technologies for microfluidic systems.,” *Anal. Bioanal. Chem.*, vol. 390, no. 1, pp. 89–111, 2008.

[23] K. J. Regehr, M. Domenech, J. T. Koepsel, K. C. Carver, S. J. Ellison-Zelski, W. L. Murphy, L. A. Schuler, E. T. Alarid, and D. J. Beebe, “Biological implications of polydimethylsiloxane-based microfluidic cell culture.,” *Lab Chip*, vol. 9, no. 15, pp. 2132–9, Aug. 2009.

[24] L. Belov, O. De Vega, C. G. Remedios, S. P. Mulligan, and R. I. Christopherson, “Immunophenotyping of Leukemias Using a Cluster of Differentiation Antibody Microarray Immunophenotyping of Leukemias Using a Cluster of Differentiation,” *Cancer Res.*, vol. 61, pp. 4483–4489, 2001.

[25] L. Belov, P. Huang, J. S. Chrisp, S. P. Mulligan, and R. I. Christopherson, “Screening microarrays of novel monoclonal antibodies for binding to T-, B- and myeloid leukaemia cells.,” *J. Immunol. Methods*, vol. 305, no. 1, pp. 10–9, Oct. 2005.

[26] L. Belov, S. P. Mulligan, N. Barber, A. Woolfson, M. Scott, K. Stoner, J. S. Chrisp, W. A. Sewell, K. F. Bradstock, L. Bendall, D. S. Pascovici, M. Thomas, W. Erber, P. Huang, M. Sartor, G. A. R. Young, J. S. Wiley, S. Juneja, W. G. Wierda, A. R. Green, M. J. Keating, and R. I. Christopherson, “Analysis of human leukaemias and lymphomas using extensive immunophenotypes from an antibody microarray.,” *Br. J. Haematol.*, vol. 135, no. 2, pp. 184–97, Oct. 2006.

[27] K. Sekine, A. Revzin, R. G. Tompkins, and M. Toner, “Panning of multiple subsets of leukocytes on antibody-decorated poly(ethylene) glycol-coated glass slides.,” *J. Immunol. Methods*, vol. 313, pp. 96–109, Jun. 2006.

[28] B. Passlick, D. Flieger, and H. Löms Ziegler-Heitbrock, “Identification and characterization of a novel monocyte subpopulation in human peripheral blood,” *Blood*, vol. 74, no. 7, pp. 2527–2534, 1989.

[29] J. LaBaer and N. Ramachandran, “Protein microarrays as tools for functional proteomics.,” *Curr. Opin. Chem. Biol.*, vol. 9, no. 1, pp. 14–9, Feb. 2005.

[30] L. A. Liotta, V. Espina, A. I. Mehta, V. Calvert, K. Rosenblatt, D. Geho, P. J. Munson, L. Young, J. Wulfkuhle, E. F. Petricoin, and E. F. Petricoin III, “Protein microarrays: meeting analytical challenges for clinical applications.,” *Cancer Cell*, vol. 3, no. 4, pp. 317–325, Apr. 2003.

[31] J. Petrik, “Diagnostic applications of microarrays,” *Transfus. Med.*, vol. 16, no. 4, pp. 233–47, Aug. 2006.

[32] S. A. Soper, A. C. Henry, B. Vaidya, M. Galloway, M. Wabuyele, and R. L. McCarley, “Surface modification of polymer-based microfluidic devices,” *Anal. Chim. Acta*, vol. 470, pp. 87–99, Jan. 2002.

[33] S. B. N. Biancardo, H. J. Pranov, and N. B. Larsen, “Protein In-Mold Patterning,” *Adv. Mater.*, vol. 20, no. 10, pp. 1825–1829, May 2008.

[34] E. Martínez, E. Engel, J. A. Planell, and J. Samitier, “Effects of artificial micro- and nano-structured surfaces on cell behaviour.,” *Ann. Anat.*, vol. 191, no. 1, pp. 126–35, Jan. 2009.

[35] M. J. Dalby, N. Gadegaard, R. Tare, A. Andar, M. O. Riehle, P. Herzyk, C. D. W. Wilkinson, and R. O. C. Oreffo, “The control of human mesenchymal cell differentiation using nanoscale symmetry and disorder,” *Nat. Mater.*, vol. 6, no. 12, pp. 997–1003, Dec. 2007.

[36] R. J. McMurray, N. Gadegaard, P. M. Tsimbouri, K. V Burgess, L. E. McNamara, R. Tare, K. Murawski, E. Kingham, R. O. C. Oreffo, and M. J. Dalby, "Nanoscale surfaces for the long-term maintenance of mesenchymal stem cell phenotype and multipotency," *Nat. Mater.*, vol. 10, no. 8, pp. 637–644, Jul. 2011.

[37] P. Tsimbouri, N. Gadegaard, K. Burgess, K. White, P. Reynolds, P. Herzyk, R. Oreffo, and M. J. Dalby, "Nanotopographical effects on mesenchymal stem cell morphology and phenotype," *J. Cell. Biochem.*, vol. 115, no. 2, pp. 380–90, Feb. 2014.

[38] C. J. Bettinger, R. Langer, and J. T. Borenstein, "Engineering substrate topography at the micro- and nanoscale to control cell function.," *Angew. Chem. Int. Ed. Engl.*, vol. 48, no. 30, pp. 5406–15, Jan. 2009.

[39] I. Patla, T. Volberg, N. Elad, V. Hirschfeld-Warneken, C. Grashoff, R. Fässler, J. P. Spatz, B. Geiger, and O. Medalia, "Dissecting the molecular architecture of integrin adhesion sites by cryo-electron tomography.," *Nat. Cell Biol.*, vol. 12, no. 9, pp. 909–15, Sep. 2010.

[40] C. Selhuber-Unkel, T. Erdmann, M. López-García, H. Kessler, U. S. Schwarz, and J. P. Spatz, "Cell adhesion strength is controlled by intermolecular spacing of adhesion receptors.," *Biophys. J.*, vol. 98, no. 4, pp. 543–51, Mar. 2010.

[41] S. Bennett and S. N. Breit, "Variables in the isolation and culture of human monocytes that are of particular relevance to studies of HIV.," *J. Leukoc. Biol.*, vol. 56, no. 3, pp. 236–40, Sep. 1994.

[42] H. Nielsen, "Isolation and functional activity of human blood monocytes after adherence to plastic surfaces: comparison of different detachment methods," *Acta Pathol. Microbiol. Immunol. Scand. A.*, vol. 95, no. 2, pp. 81–84, 1987.

[43] T. G. Berger, B. Feuerstein, E. Strasser, U. Hirsch, D. Schreiner, G. Schuler, and B. Schuler-Thurner, "Large-scale generation of mature monocyte-derived dendritic cells for clinical application in cell factories.," *J. Immunol. Methods*, vol. 268, no. 2, pp. 131–40, Oct. 2002.

[44] V. R. Manfrinato, L. Zhang, D. Su, H. Duan, R. G. Hobbs, E. a Stach, and K. K. Berggren, "Resolution limits of electron-beam lithography toward the atomic scale.," *Nano Lett.*, vol. 13, no. 4, pp. 1555–8, Apr. 2013.

[45] S. Franssila, "Advanced Lithography," in *Introduction to Microfabrication*, John Wiley & Sons, Ltd, 2010, pp. 115–126.

[46] K. Grassie, E. Teuckhoff, G. Wegner, J. Hausselt, and H. Hanselka, "Silicon Moulds for Micro-Injection Moulding Techniques," *Funct. Mater.*, vol. 13, pp. 473–476, 2006.

[47] D. Macintyre and S. Thoms, "The fabrication of high resolution features by mould injection," *Microelectron. Eng.*, vol. 41/42, pp. 211–214, 1998.

[48] M. T. Gale, "Replication techniques for diffractive optical elements," *Microelectron. Eng.*, vol. 34, pp. 321–339, 1997.

[49] J. C. Viana, "Development of the skin layer in injection moulding: phenomenological model," *Polymer (Guildf).*, vol. 45, no. 3, pp. 993–1005, Feb. 2004.

[50] M. Loboda and G. Toskey, "Understanding hydrogen silsesquioxane-based dielectric film processing," *Solid State Technol.*, vol. 41, no. 5, p. 99, 1998.

[51] J. K. W. Yang, B. Cord, H. Duan, K. K. Berggren, J. Klingfus, S.-W. Nam, K.-B. Kim, and M. J. Rooks, "Understanding of hydrogen silsesquioxane electron resist for sub-5-nm-half-pitch lithography," *J. Vac. Sci. Technol. B*, vol. 27, no. 6, pp. 2622–2627, 2009.

[52] N. Gadegaard and D. McCloy, "Direct stamp fabrication for NIL and hot embossing using HSQ," *Microelectron. Eng.*, vol. 84, no. 12, pp. 2785–2789, Dec. 2007.

[53] M. R. Saleem, P. A. Stenberg, M. B. Khan, Z. M. Khan, S. Honkanen, and J. Turunen, "Hydrogen silsesquioxane resist stamp for replication of nanophotonic components in polymers," *J. Micro/Nanolith. MEMS MOEMS*, vol. 11, no. 1, p. 013007, Mar. 2012.

[54] J. Cech, H. Pranov, G. Kofod, M. Matschuk, S. Murthy, and R. Taboryski, "Surface roughness reduction using spray-coated hydrogen silsesquioxane reflow," *Appl. Surf. Sci.*, vol. 280, pp. 424–430, Sep. 2013.

[55] M. Beck, M. Graczyk, I. Maximov, E.-L. Sarwe, T. G. I. Ling, M. Keil, and L. Montelius, "Improving stamps for 10 nm level wafer scale nanoimprint lithography," *Microelectron. Eng.*, vol. 61–62, pp. 441–448, Jul. 2002.

[56] S. Park, H. Schift, C. Padeste, B. Schnyder, R. Kötz, and J. Gobrecht, "Anti-adhesive layers on nickel stamps for nanoimprint lithography," *Microelectron. Eng.*, vol. 73–74, pp. 196–201, Jun. 2004.

[57] R. Maboudian, W. R. Ashurst, and C. Carraro, "Self-assembled monolayers as anti-stiction coatings for MEMS: characteristics and recent developments," *Sensors And Actuators*, vol. 82, pp. 219–223, 2000.

[58] C.-W. Wu, Y.-K. Shen, S.-Y. Chuang, and C. S. Wei, "Anti-adhesive effects of diverse self-assembled monolayers in nanoimprint lithography," *Sensors Actuators A*, vol. 139, no. 1–2, pp. 145–151, Sep. 2007.

[59] W. Zhou, J. Zhang, Y. Liu, X. Li, X. Niu, Z. Song, G. Min, Y. Wan, L. Shi, and S. Feng, "Characterization of anti-adhesive self-assembled monolayer for nanoimprint lithography," *Appl. Surf. Sci.*, vol. 255, no. 5, pp. 2885–2889, Dec. 2008.

[60] S. Garidel, M. Zelsmann, N. Chaix, P. Voisin, J. Boussey, A. Beaurain, and B. Pelissier, "Improved release strategy for UV nanoimprint lithography," *J. Vac. Sci. Technol. B*, vol. 25, no. 6, p. 2430, 2007.

[61] J. Cech and R. Taboryski, "Stability of FDTS monolayer coating on aluminum injection molding tools," *Appl. Surf. Sci.*, vol. 259, pp. 538–541, Oct. 2012.

[62] M. Matschuk, H. Bruus, and N. B. Larsen, "Nanostructures for all-polymer microfluidic systems," *Microelectron. Eng.*, vol. 87, no. 5–8, pp. 1379–1382, May 2010.

[63] M. Matschuk and N. B. Larsen, "Injection molding of high aspect ratio sub-100 nm nanostructures," *J. Micromech. Microeng.*, vol. 23, no. 2, p. 025003, Feb. 2013.

[64] A. B. Christiansen, J. S. Clausen, N. A. Mortensen, and A. Kristensen, "Injection moulding antireflective nanostructures," *Microelectron. Eng.*, vol. 121, pp. 47–50, Jun. 2014.

[65] Gelest, "Hydrophobicity, Hydrophilicity and Silane Surface Modification," 2006. [Online]. Available: http://www.gelest.com/goods/pdf/hydrophobicity.pdf. [Accessed: 12-Aug-2014].

[66] S. M. George, "Atomic layer deposition: an overview.," *Chem. Rev.*, vol. 110, no. 1, pp. 111–31, Jan. 2010.

[67] D. Nečas and P. Klapetek, "Gwyddion: an open-source software for SPM data analysis," *Cent. Eur. J. Phys.*, vol. 10, no. 1, pp. 181–188, Nov. 2011.

[68] D. K. . Owens and R. C. Wendt, "Estimation of the surface free energy of polymers," *J. Appl. Polym. Sci.*, vol. 13, no. 8, pp. 1741–1747, Oct. 1969.

[69] F. M. Fowkes, "Attractive forces at interfaces," *Ind. Eng. Chem.*, vol. 56, no. 12, pp. 40–52, 1964.

[70] M. Feigl, M. Nofz, R. Sojref, and A. Kohl, "Improved wetting of bare and pre-coated steels by aqueous alumina sols for optimum coating success," *J. Sol-Gel Sci. Technol.*, vol. 55, no. 2, pp. 191–198, May 2010.

[71] W. Jerome, "Digital Image Capture for Confocal Microscopy," in *Basic Confocal Microscopy*, R. L. Price and W. G. (Jay) Jerome, Eds. Springer New York, 2011, pp. 133–155.

[72] JSR Micro NV, "Technical data KRF M230Y," 2003. [Online]. Available: http://labadviser.danchip.dtu.dk/images/9/9c/M230Y_PSM_annular_130C_PEB.pdf. [Accessed: 12-Aug-2014].

[73] S. Franssila, "Thin-Film Materials and Processes," in *Introduction to Microfabrication*, John Wiley & Sons, Ltd, 2010, pp. 47–67.

[74] H.-C. Liou and J. Pretzer, "Effect of curing temperature on the mechanical properties of hydrogen silsesquioxane thin films," *Thin Solid Films*, vol. 335, pp. 186–191, 1998.

[75] I. D. Johnston, D. K. McCluskey, C. K. L. Tan, and M. C. Tracey, "Mechanical characterization of bulk Sylgard 184 for microfluidics and microengineering," *J. Micromech. Microeng.*, vol. 24, no. 3, p. 035017, Mar. 2014.

[76] M. Keil, M. Beck, G. Frennesson, E. Theander, E. Bolmsjö, L. Montelius, and B. Heidari, "Process development and characterization of antisticking layers on nickel-based stamps designed for nanoimprint lithography," *J. Vac. Sci. Technol. B Microelectron. Nanom. Struct.*, vol. 22, no. 6, p. 3283, 2004.

[77] B. Arkles, Y. Pan, Y. M. Kim, E. Eisenbraun, C. Miller, and A. E. Kalyeros, "Hydridosilane Modification of Metals: An Exploratory Study," *J. Adhes. Sci. Technol.*, vol. 26, no. 1–3, pp. 41–54, 2012.

[78] J. Giboz, T. Copponnex, and P. Mélé, "Microinjection molding of thermoplastic polymers: a review," *J. Micromech. Microeng.*, vol. 17, no. 6, pp. R96–R109, Jun. 2007.

[79] C. Yang, X.-H. Yin, and G.-M. Cheng, "Microinjection molding of microsystem components: new aspects in improving performance," *J. Micromech. Microeng.*, vol. 23, no. 9, p. 093001, Sep. 2013.

[80] U. M. Attia, S. Marson, and J. R. Alcock, "Micro-injection moulding of polymer microfluidic devices," *Microfluid. Nanofluid.*, vol. 7, no. 1, pp. 1–28, Feb. 2009.

[81] E. Puukilainen, T. Rasilainen, M. Suvanto, and T. A. Pakkanen, "Superhydrophobic polyolefin surfaces: controlled micro- and nanostructures," *Langmuir*, vol. 23, no. 13, pp. 7263–7268, Jun. 2007.

[82] E. Huovinen, J. Hirvi, M. Suvanto, and T. A. Pakkanen, "Micro-micro hierarchy replacing micro-nano hierarchy: a precisely controlled way to produce wear-resistant superhydrophobic polymer surfaces," *Langmuir*, vol. 28, no. 41, pp. 14747–14755, Oct. 2012.

[83] E. Huovinen, L. Takkunen, T. Korpela, M. Suvanto, T. T. Pakkanen, and T. A. Pakkanen, "Mechanically robust superhydrophobic polymer surfaces based on protective micropillars," *Langmuir*, vol. 30, no. 5, pp. 1435–1443, Feb. 2014.

[84] K. J. Cha, M.-H. Na, H. W. Kim, and D. S. Kim, "Nano Petri dishes: a new polystyrene platform for studying cell-nanoengineered surface interactions," *J. Micromech. Microeng.*, vol. 24, no. 5, p. 055002, May 2014.

[85] H. Schift, C. David, M. Gabriel, J. Gobrecht, L. Heyderman, W. Kaiser, S. Koppel, and L. Scandella, "Nanoreplication in polymers using hot embossing and injection molding," *Microelectron. Eng.*, vol. 53, no. 1–4, pp. 171–174, 2000.

[86] H. Schift, C. David, J. Gobrecht, A. D' Amore, D. Simoneta, W. Kaiser, and M. Gabriel, "Quantitative analysis of the molding of nanostructures," *J. Vac. Sci. Technol. B*, vol. 18, no. 6, pp. 3564–3568, 2000.

[87] N. Gadegaard, S. Mosler, and N. B. Larsen, "Biomimetic polymer nanostructures by injection molding," *Macromol. Mater. Eng.*, vol. 288, no. 1, pp. 76–83, Jan. 2003.

[88] A.-C. Liou and R.-H. Chen, "Injection molding of polymer micro- and sub-micron structures with high-aspect ratios," *Int. J. Adv. Manuf. Technol.*, vol. 28, no. 11–12, pp. 1097–1103, Sep. 2006.

[89] K. Mönkkönen, J. Hietala, P. Pääkkönen, E. J. Pääkkönen, T. Kaikuranta, T. T. Pakkanen, and T. Jääskeläinen, "Replication of sub-micron features using amorphous thermoplastics," *Polym. Eng. Sci.*, vol. 42, no. 7, pp. 1600–1608, Jul. 2002.

[90] C. Gornik, "Injection moulding of parts with microstructured surfaces for medical applications," *Macromol. Symp.*, vol. 217, no. 1, pp. 365–374, Oct. 2004.

[91] S.-C. Tseng, Y.-C. Chen, C.-L. Kuo, and B.-Y. Shew, "A study of integration of LIGA and M-EDM technology on the microinjection molding of ink-jet printers' nozzle plates," *Microsyst. Technol.*, vol. 12, no. 1–2, pp. 116–119, Aug. 2005.

[92] Y. Kim, Y. Choi, and S. Kang, "Replication of high density optical disc using injection mold with MEMS heater," *Microsyst. Technol.*, vol. 11, no. 7, pp. 464–469, Jul. 2005.

[93] C.-L. Xiao and H.-X. Huang, "Multiobjective optimization design of heating system in electric heating rapid thermal cycling mold for yielding high gloss parts," *J. Appl. Polym. Sci.*, vol. 131, no. 6, p. 39976, Mar. 2014.

[94] G. Wang, G. Zhao, and Y. Guan, “Thermal response of an electric heating rapid heat cycle molding mold and its effect on surface appearance and tensile strength of the molded part,” *J. Appl. Polym. Sci.*, vol. 128, no. 3, pp. 1339–1352, Jul. 2013.

[95] K. Park and S.-I. Lee, “Localized mold heating with the aid of selective induction for injection molding of high aspect ratio micro-features,” *J. Micromech. Microeng.*, vol. 20, no. 3, p. 035002, Mar. 2010.

[96] J. Bekesi, J. J. J. Kaakkunen, W. Michaeli, F. Klaiber, M. Schoengart, J. Ihlemann, and P. Simon, “Fast fabrication of super-hydrophobic surfaces on polypropylene by replication of short-pulse laser structured molds,” *Appl. Phys. A*, vol. 99, no. 4, pp. 691–695, May 2010.

[97] P.-C. Chang and S.-J. Hwang, “Experimental investigation of infrared rapid surface heating for injection molding,” *J. Appl. Polym. Sci.*, vol. 102, no. 4, pp. 3704–3713, Nov. 2006.

[98] H.-Y. Lin, C.-H. Chang, and W.-B. Young, “Experimental study on the filling of nano structures with infrared mold surface heating,” *Int. Polym. Process.*, vol. 26, no. 1, pp. 73–81, 2011.

[99] J. Liu, G. Zhao, G. Wang, and Y. Guan, “Fully coupled transient heat transfer and melt filling simulations in rapid heat cycle molding with steam heating,” *Polym. Plast. Technol. Eng.*, vol. 50, no. 4, pp. 423–437, Feb. 2011.

[100] W. Michaeli and F. Klaiber, “Development of a system for laser-assisted molding of micro- and nanostructures,” *J. Vac. Sci. Technol. B*, vol. 27, no. 3, pp. 1323–1326, 2009.

[101] J.-S. Lee, K.-W. Park, S.-W. Lee, J.-H. Kim, and S. Kim, “Substrates for ultra small optical disks,” in *Optical Data Storage*, 2003, pp. 228–230.

[102] K. Inoue, K. Hayashi, Y. Kawasaki, and E. Ohno, “Study on 40 Gbits/inch2 density molding using heat insulated mold,” *Jpn. J. Appl. Phys.*, vol. 42, no. Part 1, No. 2B, pp. 774–775, Feb. 2003.

[103] H. Schift, P. Urwyler, and P. M. Kristiansen, “Surface-patterned micromechanical elements by polymer injection molding with hybrid molds,” *J. Vac. Sci. Technol. B*, vol. 31, no. 6, p. 06FD01, 2013.

[104] S. H. Park, W. I. Lee, S. N. Moon, Y. E. Yoo, and Y. H. Cho, “Injection molding micro patterns with high aspect ratio using a polymeric flexible stamper,” *Express Polym. Lett.*, vol. 5, no. 11, pp. 950–958, Aug. 2011.

[105] J. M. Stormonth-Darling and N. Gadegaard, “Injection moulding difficult nanopatterns with hybrid polymer inlays,” *Macromol. Mater. Eng.*, vol. 297, no. 11, pp. 1075–1080, Nov. 2012.

[106] W. M. Haynes and D. R. Lide, *CRC Handbook of Chemistry & Physics: A Ready-Reference Book of Chemical and Physical Data*, 95th ed. Boca Raton, FL: CRC, 2014.

[107] T. R. Tofteberg and E. Andreassen, “Multiscale simulation of injection molding of parts with low aspect ratio microfeatures,” *Int. Polym. Process.*, vol. 25, no. 1, pp. 63–74, 2010.

[108] N. Zhang, J. S. Chu, C. J. Byrne, D. J. Browne, and M. D. Gilchrist, “Replication of micro/nano-scale features by micro injection molding with a bulk metallic glass mold insert,” *J. Micromech. Microeng.*, vol. 22, no. 6, p. 065019, Jun. 2012.

[109] S. Kim, S. Choi, K. Lee, D. Kim, and Y. Yoo, “Observation of instabilities in flow front during micro injection molding process,” *Polym. Eng. Sci.*, vol. 50, no. 7, pp. 1377–1381, 2010.

[110] G. Fu, S. B. Tor, D. E. Hardt, and N. H. Loh, “Effects of processing parameters on the micro-channels replication in microfluidic devices fabricated by micro injection molding,” *Microsyst. Technol.*, vol. 17, no. 12, pp. 1791–1798, Oct. 2011.

[111] R. K. Jena, X. Chen, C. Y. Yue, and Y. C. Lam, “Viscosity of COC polymer (TOPAS) near the glass transition temperature: Experimental and modeling,” *Polym. Test.*, vol. 29, no. 8, pp. 933–938, Dec. 2010.

[112] H. Pranov, H. K. Rasmussen, N. B. Larsen, and N. Gadegaard, “On the injection molding of nanostructured polymer surfaces,” *Polym. Eng. Sci.*, vol. 46, no. 2, pp. 160–171, Feb. 2006.

[113] A. Bendada, A. Derdouri, M. Lamontagne, and Y. Simard, “Analysis of thermal contact resistance between polymer and mold in injection molding,” *Appl. Therm. Eng.*, vol. 24, no. 14–15, pp. 2029–2040, Oct. 2004.

[114] W. Bennett and Z. Cohn, “The isolation and selected properties of blood monocytes,” *J. Exp. Med.*, vol. 123, no. 1, pp. 145–160, 1966.

[115] W. J. Jr, B. Mei, and Z. Cohn, “The separation, long-term cultivation, and maturation of the human monocyte,” *J. Exp. Med.*, vol. 146, pp. 1613–1626, 1977.

[116] T. G. Berger, E. Strasser, R. Smith, C. Carste, B. Schuler-Thurner, E. Kaempgen, and G. Schuler, “Efficient elutriation of monocytes within a closed system (Elutra) for clinical-scale generation of dendritic cells.,” *J. Immunol. Methods*, vol. 298, no. 1–2, pp. 61–72, Mar. 2005.

[117] J. T. Delaney, P. J. Smith, and U. S. Schubert, “Inkjet printing of proteins,” *Soft Matter*, vol. 5, no. 24, p. 4866, 2009.

[118] R. D. Deegan, “Pattern formation in drying drops,” *Phys. Rev. E. Stat. Phys. Plasmas. Fluids. Relat. Interdiscip. Topics*, vol. 61, no. 1, pp. 475–85, Jan. 2000.

[119] A. Ressine, D. Finnskog, J. Malm, C. Becker, H. Lilja, G. Marko Varga, and T. Laurell, “Macro/Nano-Structured Silicon as Solid Support for Antibody Arrays,” *NanoBiotechnology*, vol. 1, no. 1, 2005.

[120] L. Mugherli, O. N. Burchak, L. A. Balakireva, A. Thomas, F. Chatelain, and M. Y. Balakirev, “In situ assembly and screening of enzyme inhibitors with surface-tension microarrays.,” *Angew. Chem. Int. Ed. Engl.*, vol. 48, no. 41, pp. 7639–44, Jan. 2009.

[121] A. Ressine, G. Marko-Varga, and T. Laurell, “Porous silicon protein microarray technology and ultra-/superhydrophobic states for improved bioanalytical readout.,” *Biotechnol. Annu. Rev.*, vol. 13, no. 07, pp. 149–200, Jan. 2007.

[122] Sensirion, “Dew-point calculation.” [Online]. Available: http://irtfweb.ifa.hawaii.edu/~tcs3/tcs3/Misc/Dewpoint_Calculation_Humidity_Sensor_E.pdf. [Accessed: 08-Jul-2014].

[123] H. Asgari and J. Fuglø, “Cell Capture Microarrays,” 2008.

[124] V. Dugas, J. Broutin, and E. Souteyrand, “Droplet evaporation study applied to DNA chip manufacturing.,” *Langmuir*, vol. 21, no. 20, pp. 9130–6, Sep. 2005.

[125] C.-H. Choi and C.-J. C. J. Kim, “Droplet evaporation of pure water and protein solution on nanostructured superhydrophobic surfaces of varying heights.,” *Langmuir*, vol. 25, no. 13, pp. 7561–7, Jul. 2009.

[126] L. Technologies, “Fetal Bovine Serum.” [Online]. Available: http://tools.lifetechnologies.com/content/sfs/productnotes/F_FBS Qualified RD-MKT-TL-HL0506021.pdf. [Accessed: 16-Jul-2014].

[127] X. Qian, B. Han, Y. Liu, H. Yan, and R. Liu, “Vapor pressure of dimethyl sulfoxide and water binary system,” *J. Solution Chem.*, vol. 24, no. 11, pp. 1183–1189, Nov. 1995.

[128] A. Buck, “New equations for computing vapor pressure and enhancement factor,” *J. Appl. Meteorol.*, vol. 20, pp. 1527–1532, 1981.

[129] R. Wenzel, “Resistance of solid surfaces to wetting by water,” *Ind. Eng. Chem.*, pp. 988–994, 1936.

[130] A. Cassie and S. Baxter, “Wettability of porous surfaces,” *Trans. Faraday Soc.*, no. 5, pp. 546–551, 1944.

[131] A. Lafuma and D. Quéré, “Superhydrophobic states.,” *Nat. Mater.*, vol. 2, no. 7, pp. 457–60, Jul. 2003.

[132] Y. C. Jung and B. Bhushan, “Wetting transition of water droplets on superhydrophobic patterned surfaces,” *Scr. Mater.*, vol. 57, no. 12, pp. 1057–1060, Dec. 2007.

[133] J. Catalán, C. Díaz, and F. García-Blanco, “Characterization of binary solvent mixtures of DMSO with water and other cosolvents.,” *J. Org. Chem.*, vol. 66, no. 17, pp. 5846–52, Aug. 2001.

[134] S. B. Nyrup, “Patterning Biomolecules on Polymer Surfaces for Applications in Life Sciences,” 2005.

[135] A. S. Curtis, J. V Forrester, C. McInnes, and F. Lawrie, “Adhesion of cells to polystyrene surfaces.,” *J. Cell Biol.*, vol. 97, no. 5 Pt 1, pp. 1500–6, Nov. 1983.

[136] A. S. Curtis and J. V Forrester, “The competitive effects of serum proteins on cell adhesion.,” *J. Cell Sci.*, vol. 71, pp. 17–35, Oct. 1984.

[137] G. E. Davis, “The Mac-1 and p150,95 beta 2 integrins bind denatured proteins to mediate leukocyte cell-substrate adhesion.,” *Exp. Cell Res.*, vol. 200, no. 2, pp. 242–52, Jun. 1992.

[138] P. Antal-Szalmas, J. A. G. Van Strijp, A. J. L. Weersink, J. Verhoef, and K. P. M. Van Kessel, “Quantitation of surface CD14 on human monocytes and neutrophils.,” *J. Leukoc. Biol.*, vol. 61, no. June, pp. 721–728, 1997.

[139] H. Zhu, G. Stybayeva, M. Macal, E. Ramanculov, M. D. George, S. Dandekar, and A. Revzin, “A microdevice for multiplexed detection of T-cell-secreted cytokines.,” *Lab Chip*, vol. 8, no. 12, pp. 2197–205, Dec. 2008.

[140] H. Zhu, M. Macal, C. N. Jones, M. D. George, S. Dandekar, and A. Revzin, “A miniature cytometry platform for capture and characterization of T-lymphocytes from human blood.,” *Anal. Chim. Acta*, vol. 608, no. 2, pp. 186–96, Feb. 2008.

[141] X. Cheng, A. Gupta, C. Chen, R. G. Tompkins, W. Rodriguez, and M. Toner, “Enhancing the performance of a point-of-care CD4+ T-cell counting microchip through monocyte depletion for HIV/AIDS diagnostics.,” *Lab Chip*, vol. 9, no. 10, pp. 1357–64, May 2009.

[142] J. B. Recknor, J. C. Recknor, D. S. Sakaguchi, and S. K. Mallapragada, “Oriented astroglial cell growth on micropatterned polystyrene substrates.,” *Biomaterials*, vol. 25, no. 14, pp. 2753–67, Jun. 2004.

[143] S. Y. Hwang, K. W. Kwon, K.-J. Jang, M. C. Park, J. S. Lee, and K. Y. Suh, “Adhesion assays of endothelial cells on nanopatterned surfaces within a microfluidic channel.,” *Anal. Chem.*, vol. 82, no. 7, pp. 3016–22, Apr. 2010.

[144] L. Hanson, Z. C. Lin, C. Xie, Y. Cui, and B. Cui, “Characterization of the cell-nanopillar interface by transmission electron microscopy.,” *Nano Lett.*, vol. 12, no. 11, pp. 5815–20, Nov. 2012.

[145] M. J. P. Biggs, R. G. Richards, N. Gadegaard, C. D. W. Wilkinson, and M. J. Dalby, “The effects of nanoscale pits on primary human osteoblast adhesion formation and cellular spreading.,” *J. Mater. Sci. Mater. Med.*, vol. 18, no. 2, pp. 399–404, Feb. 2007.

[146] K. J. Cha, J. M. Hong, D.-W. Cho, and D. S. Kim, “Enhanced osteogenic fate and function of MC3T3-E1 cells on nanoengineered polystyrene surfaces with nanopillar and nanopore arrays.,” *Biofabrication*, vol. 5, no. 2, p. 025007, Jun. 2013.

[147] A. S. G. Curtis, N. Gadegaard, M. J. Dalby, M. O. Riehle, C. D. W. Wilkinson, and G. Aitchison, “Cells react to nanoscale order and symmetry in their surroundings.,” *IEEE Trans. Nanobioscience*, vol. 3, no. 1, pp. 61–5, Mar. 2004.

[148] M. J. Dalby, N. Gadegaard, M. O. Riehle, C. D. W. Wilkinson, and A. S. G. Curtis, “Investigating filopodia sensing using arrays of defined nano-pits down to 35 nm diameter in size.,” *Int. J. Biochem. Cell Biol.*, vol. 36, no. 10, pp. 2005–15, Oct. 2004.

[149] J. O. Gallagher, K. F. McGhee, C. D. W. Wilkinson, and M. O. Riehle, “Interaction of animal cells with ordered nanotopography.,” *IEEE Trans. Nanobioscience*, vol. 1, no. 1, pp. 24–8, Mar. 2002.

[150] E. Engvall and P. Perlmann, “Enzyme-linked immunosorbent assay (ELISA). Quantitative assay of immunoglobulin G,” *Immunochemistry*, vol. 8, no. 9, pp. 874–879, Sep. 1971.

[151] F. Rusmini, Z. Zhong, and J. Feijen, “Protein immobilization strategies for protein biochips.,” *Biomacromolecules*, vol. 8, pp. 1775–89, Jun. 2007.

[152] P. Jonkheijm, D. Weinrich, H. Schröder, C. M. Niemeyer, and H. Waldmann, “Chemical strategies for generating protein biochips.,” *Angew. Chemie Int. Ed.*, vol. 47, no. 50, pp. 9618–47, Jan. 2008.

[153] M. Hansen, G. M. Hjortø, O. Met, M. H. Jakobsen, I. M. Svane, and N. B. Larsen, “Cell culture plastics with immobilized interleukin-4 for monocyte differentiation.,” *J. Biomed. Mater. Res. A*, vol. 96, no. 2, pp. 372–83, Feb. 2011.

[154] U. Bora, L. Chugh, and P. Nahar, “Covalent immobilization of proteins onto photoactivated polystyrene microtiter plates for enzyme-linked immunosorbent assay procedures.,” *J. Immunol. Methods*, vol. 268, no. 2, pp. 171–7, Oct. 2002.

[155] P. Nahar, N. M. Wali, and R. P. Gandhi, “Light-induced activation of an inert surface for covalent immobilization of a protein ligand.,” *Anal. Biochem.*, vol. 294, no. 2, pp. 148–53, Jul. 2001.

[156] D. Sung, S. Park, and S. Jon, “Facile immobilization of biomolecules onto various surfaces using epoxide-containing antibiofouling polymers.,” *Langmuir*, vol. 28, no. 9, pp. 4507–14, Mar. 2012.

[157] D. Sung, D. H. Shin, and S. Jon, “Toward immunoassay chips: Facile immobilization of antibodies on cyclic olefin copolymer substrates through pre-activated polymer adlayers.,” *Biosens. Bioelectron.*, vol. 26, no. 9, pp. 3967–3972, Mar. 2011.

[158] E. K. U. Larsen, M. B. L. Mikkelsen, and N. B. Larsen, “Facile Photoimmobilization of Proteins onto Low-Binding PEG-Coated Polymer Surfaces.,” *Biomacromolecules*, vol. 15, no. 3, pp. 894–9, Mar. 2014.

[159] H. J. Pranov, “Processes For Nanostructuring Of Plastic Parts For Biological And Optical Applications,” Technical University of Denmark, 2006.

[160] B. L. Welch, “The Generalization of ‘Student’s’ Problem when Several Different Population Variances are Involved,” *Biometrika*, vol. 34, no. 1/2, pp. 28–35, 1947.

[161] A. Hill, “The possible effects of the aggregation of the molecules of haemoglobin on its dissociation curves,” *J. Physiol.*, vol. 40, pp. iv–vii, Jan. 1910.

[162] D. MacDougall and W. B. Crummett, “Guidelines for data acquisition and data quality evaluation in environmental chemistry,” *Anal. Chem.*, vol. 52, no. 14, pp. 2242–2249, Dec. 1980.

[163] J. L. Tan, J. Tien, and C. S. Chen, “Microcontact Printing of Proteins on Mixed Self-Assembled Monolayers,” *Langmuir*, vol. 18, no. 2, pp. 519–523, 2002.

[164] D. C. Pease, “The Significance of the Contact Angle in Relation to the Solid Surface,” *J. Phys. Chem.*, vol. 49, no. 2, pp. 107–110, 1945.

[165] H. Stadler, M. Mondon, and C. Ziegler, “Protein adsorption on surfaces: dynamic contact-angle (DCA) and quartz-crystal microbalance (QCM) measurements.,” *Anal. Bioanal. Chem.*, vol. 375, no. 1, pp. 53–61, Jan. 2003.

[166] M. E. Wiseman and C. W. Frank, “Antibody adsorption and orientation on hydrophobic surfaces.,” *Langmuir*, vol. 28, no. 3, pp. 1765–74, Jan. 2012.

[167] M. Rabe, D. Verdes, and S. Seeger, “Understanding protein adsorption phenomena at solid surfaces.,” *Adv. Colloid Interface Sci.*, vol. 162, no. 1–2, pp. 87–106, Feb. 2011.

[168] A. W. P. Vermeer and W. Norde, “The thermal stability of immunoglobulin: unfolding and aggregation of a multi-domain protein.,” *Biophys. J.*, vol. 78, no. 1, pp. 394–404, Jan. 2000.

[169] U. Mayor, N. R. Guydosh, C. M. Johnson, J. G. Grossmann, S. Sato, G. S. Jas, S. M. V. Freund, D. O. V. Alonso, V. Daggett, and A. R. Fersht, “The complete folding pathway of a protein from nanoseconds to microseconds,” *Nature*, vol. 421, no. 6925, pp. 863–867, 2003.

[170] J. Kubelka, J. Hofrichter, and W. A. Eaton, “The protein folding ‘speed limit’.,” *Curr. Opin. Struct. Biol.*, vol. 14, no. 1, pp. 76–88, Feb. 2004.

[171] B. C. Steel, D. R. McKenzie, M. M. M. Bilek, N. J. Nosworthy, and C. G. dos Remedios, “Nanosecond responses of proteins to ultra-high temperature pulses.,” *Biophys. J.*, vol. 91, no. 6, pp. L66–L68, Sep. 2006.

[172] L. Kim, M. D. Vahey, H.-Y. Lee, and J. Voldman, “Microfluidic arrays for logarithmically perfused embryonic stem cell culture.,” *Lab Chip*, vol. 6, no. 3, pp. 394–406, Mar. 2006.

[173] T. Hassell, S. Gleave, and M. Butler, “Growth inhibition in animal cell culture,” *Appl. Biochem. Biotechnol.*, vol. 30, no. 1, pp. 29–41, 1991.

[174] S. S. Ozturk, “Engineering challenges in high density cell culture systems.,” *Cytotechnology*, vol. 22, no. 1–3, pp. 3–16, Jan. 1996.

[175] A. W. Tilles, H. Baskaran, P. Roy, M. L. Yarmush, and M. Toner, “Effects of oxygenation and flow on the viability and function of rat hepatocytes cocultured in a microchannel flat-plate bioreactor.,” *Biotechnol. Bioeng.*, vol. 73, no. 5, pp. 379–89, Jun. 2001.

[176] T. Ezashi, P. Das, and R. M. Roberts, “Low O2 tensions and the prevention of differentiation of hES cells.,” *Proc. Natl. Acad. Sci. U. S. A.*, vol. 102, no. 13, pp. 4783–8, Mar. 2005.

[177] J. W. Allen and S. N. Bhatia, “Formation of steady-state oxygen gradients in vitro: application to liver zonation.,” *Biotechnol. Bioeng.*, vol. 82, no. 3, pp. 253–62, May 2003.

[178] M. Holm Olsen, G. M. Hjortø, M. Hansen, Ö. Met, I. M. Svane, and N. B. Larsen, “In-chip fabrication of free-form 3D constructs for directed cell migration analysis,” *Lab Chip*, no. 207890, 2013.

[179] L. M. Przybyla and J. Voldman, “Attenuation of extrinsic signaling reveals the importance of matrix remodeling on maintenance of embryonic stem cell self-renewal.,” *Proc. Natl. Acad. Sci. U. S. A.*, vol. 109, no. 3, pp. 835–40, Jan. 2012.

[180] N. Korin, A. Bransky, U. Dinnar, and S. Levenberg, “Periodic ‘flow-stop’ perfusion microchannel bioreactors for mammalian and human embryonic stem cell long-term culture,” *Biomed. Microdevices*, vol. 11, no. 1, pp. 87–94, 2009.

[181] S. Giulitti, E. Magrofuoco, L. Prevedello, and N. Elvassore, “Optimal periodic perfusion strategy for robust long-term microfluidic cell culture.,” *Lab Chip*, Sep. 2013.

[182] R. I. Freshney, *Culture of Animal Cells - A Manual of Basic Technique*. New York: Wiley-Liss, Inc., 2000.

[183] K. Schumacher, R. Strehl, V. U. De, and W. W. Minuth, “Advanced technique for long term culture of epithelia in a continuous luminal-basal medium gradient.,” *Biomaterials*, vol. 23, no. 3, pp. 805–15, Feb. 2002.

[184] N. Good, G. Winget, W. Winter, T. Connolly, S. Izawa, and R. Singh, “Hydrogen ion buffers for biological research,” *Biochemistry*, no. 2, 1966.

[185] A. Itagaki and G. Kimura, “TES and HEPES buffers in mammalian cell cultures and viral studies: problem of carbon dioxide requirement,” *Exp. Cell Res.*, vol. 40, 1974.

[186] Sigma-Aldrich, “HEPES solution 1 M, pH 7.0-7.6, sterile-filtered, BioReagent, suitable for cell culture.” [Online]. Available: http://www.sigmaaldrich.com/catalog/product/sigma/h0887?lang=en&region=DK. [Accessed: 20-Jun-2014].

[187] A. Grzelak, B. Rychlik, and G. Bartosz, “Light-dependent generation of reactive oxygen species in cell culture media,” *Free Radic. Biol. Med.*, vol. 30, no. 12, pp. 1418–1425, 2001.

[188] L. W. McKeen, *Permeability Properties of Plastics and Elastomers*. Elsevier, 2012, pp. 1–20.

[189] G. Mehta, K. Mehta, D. Sud, J. W. Song, T. Bersano-Begey, N. Futai, Y. S. Heo, M.-A. Mycek, J. J. Linderman, and S. Takayama, “Quantitative measurement and control of oxygen levels in microfluidic poly(dimethylsiloxane) bioreactors during cell culture.,” *Biomed. Microdevices*, vol. 9, no. 2, pp. 123–34, Apr. 2007.

[190] C.-C. Hu, K.-R. Lee, R.-C. Ruaan, Y. C. Jean, and J.-Y. Lai, “Gas separation properties in cyclic olefin copolymer membrane studied by positron annihilation, sorption, and gas permeation,” *J. Memb. Sci.*, vol. 274, no. 1–2, pp. 192–199, Apr. 2006.

[191] Y. S. Heo, L. M. Cabrera, J. W. Song, N. Futai, Y.-C. Tung, G. D. Smith, and S. Takayama, “Characterization and resolution of evaporation-mediated osmolality shifts that constrain microfluidic cell culture in poly(dimethylsiloxane) devices.,” *Anal. Chem.*, vol. 79, no. 3, pp. 1126–34, Feb. 2007.

[192] Y. Zhang, M. Ishida, Y. Kazoe, Y. Sato, and N. Miki, “Water-vapor permeability control of PDMS by the dispersion of collagen powder,” *IEEJ Trans. Electr. Electron. Eng.*, vol. 4, no. 3, pp. 442–449, May 2009.

[193] T. Gervais, J. El-Ali, A. Günther, and K. F. Jensen, “Flow-induced deformation of shallow microfluidic channels.,” *Lab Chip*, vol. 6, no. 4, pp. 500–7, Apr. 2006.

[194] A. L. Paguirigan and D. J. Beebe, “From the cellular perspective: exploring differences in the cellular baseline in macroscale and microfluidic cultures.,” *Integr. Biol. (Camb).*, vol. 1, no. 2, pp. 182–95, Mar. 2009.

[195] D. Bodas and C. Khan-Malek, “Hydrophilization and hydrophobic recovery of PDMS by oxygen plasma and chemical treatment—An SEM investigation,” *Sensors Actuators B*, vol. 123, no. 1, pp. 368–373, Apr. 2007.

[196] X. Su, E. W. K. Young, H. a S. Underkofler, T. J. Kamp, C. T. January, and D. J. Beebe, “Microfluidic cell culture and its application in high-throughput drug screening: cardiotoxicity assay for hERG channels.,” *J. Biomol. Screen.*, vol. 16, no. 1, pp. 101–11, Jan. 2011.

[197] Topas Advanced Polymers, “Cyclic Olefin Copolymer (COC),” 2014. [Online]. Available: http://www.topas.com/sites/default/files/files/TOPAS_Brochure_E_2014_06.pdf. [Accessed: 12-Aug-2014].

[198] E. K. U. Larsen and N. B. Larsen, “One-step polymer surface modification for minimizing drug, protein, and DNA adsorption in microanalytical systems.,” *Lab Chip*, vol. 13, no. 4, pp. 669–75, Mar. 2013.

[199] E. A. Campo, *The Complete Part Design Handbook For Injection Molding of Thermoplastics*. Hanser, 2006.

[200] J. Kim, B. Jeong, M. Chiao, and L. Lin, “Ultrasonic Bonding for MEMS Sealing and Packaging,” *IEEE Trans. Adv. Packag.*, vol. 32, no. 2, pp. 461–467, May 2009.

[201] Z. Zhang, Y. Luo, X. Wang, S. He, F. Meng, and L. Wang, “Bonding of planar poly (methyl methacrylate) (PMMA) nanofluidic channels using thermal assisted ultrasonic bonding method,” *Microsyst. Technol.*, vol. 16, no. 12, pp. 2043–2048, Sep. 2010.

[202] Z. Zhang, Y. Luo, X. Wang, Y. Zheng, Y. Zhang, and L. Wang, “Thermal assisted ultrasonic bonding of multilayer polymer microfluidic devices,” *J. Micromech. Microeng.*, vol. 20, no. 1, p. 015036, Jan. 2010.

[203] Z. Zhang, Y. Luo, X. Wang, Y. Zheng, Y. Zhang, and L. Wang, “A low temperature ultrasonic bonding method for PMMA microfluidic chips,” *Microsyst. Technol.*, vol. 16, no. 4, pp. 533–541, Jan. 2010.

[204] Y. Sun, Y. Luo, and X. Wang, “Micro energy director array in ultrasonic precise bonding for thermoplastic micro assembly,” *J. Mater. Process. Technol.*, vol. 212, no. 6, pp. 1331–1337, Jun. 2012.

[205] M. Bu, I. R. Perch-Nielsen, K. S. Sørensen, J. Skov, Y. Sun, D. Duong Bang, M. E. Pedersen, M. F. Hansen, and A. Wolff, “A temperature control method for shortening thermal cycling time to achieve rapid polymerase chain reaction (PCR) in a disposable polymer microfluidic device,” *J. Micromech. Microeng.*, vol. 23, no. 7, p. 074002, Jul. 2013.

[206] S. W. Li, J. H. Xu, Y. J. Wang, Y. C. Lu, and G. S. Luo, “Low-temperature bonding of poly-(methyl methacrylate) microfluidic devices under an ultrasonic field,” *J. Micromech. Microeng.*, vol. 19, no. 1, p. 015035, Jan. 2009.

[207] Z. Zhang, Y. Luo, X. Wang, Z. Zhang, L. Wang, T. Precision, N. Machining, N. Technology, and L. N. Province, “Ultrasonic Bonding of Polymer Microfluidic Chips 1,” vol. 0, no. 3, pp. 8–12, 2008.

[208] T. Visser, J. Oud, and G. Brakenhoff, “Refractive index and axial distance measurements in 3-D microscopy,” *Optik (Stuttg).*, vol. 90, no. 1, pp. 17–19, 1992.

[209] S. Marson, U. M. Attia, G. Lucchetta, A. Wilson, J. R. Alcock, and D. M. Allen, “Flatness optimization of micro-injection moulded parts: the case of a PMMA microfluidic component,” *J. Micromech. Microeng.*, vol. 21, no. 11, p. 115024, Nov. 2011.

[210] C.-W. Tsao and D. L. DeVoe, “Bonding of thermoplastic polymer microfluidics,” *Microfluidics and Nanofluidics*, vol. 6, no. 1. pp. 1–16, 2009.

[211] E. Haberstroh and R. Lützeler, “Influence of Carbon Black Pigmentation on the Laser Beam Welding of Plastics Micro Parts,” *J. Polym. Eng.*, vol. 21, pp. 119–129, 2001.

[212] C.-A. Peng and B. O. Palsson, “Determination of specific oxygen uptake rates in human hematopoietic cultures and implications for bioreactor design.,” *Ann. Biomed. Eng.*, vol. 24, no. 3, pp. 373–81, 1996.

[213] L. Bai, M. Feuerer, P. Beckhove, V. Umansky, and V. Schirrmacher, “Generation of dendritic cells from human bone marrow mononuclear cells: Advantages for clinical application in comparison to peripheral blood monocyte derived cells,” *Int. J. Oncol.*, vol. 20, no. 2, pp. 247–253, 2002.

[214] A. Carreau, B. El Hafny-Rahbi, A. Matejuk, C. Grillon, and C. Kieda, “Why is the partial oxygen pressure of human tissues a crucial parameter? Small molecules and hypoxia.,” *J. Cell. Mol. Med.*, vol. 15, no. 6, pp. 1239–53, Jun. 2011.

[215] M. J. P. Leiner and P. Hartmann, “Theory and practice in optical pH sensing,” *Sensors Actuators B Chem.*, vol. 11, no. 1–3, pp. 281–289, Mar. 1993.

[216] Saint-Gobain, “Permeability Coefficients for Peristaltic Pump Tubings.” [Online]. Available: http://www.processsystems.saint-gobain.com/uploadedFiles/SGPPL-PS/Documents/Peri_Pump/PS-PeriPumps-Permeability(1).pdf. [Accessed: 25-Jun-2014].

[217] Saint-Gobain, “PharMed BPT Biocompatible Tubing.” [Online]. Available: http://www.processsystems.saint-gobain.com/uploadedFiles/SGPPL-PS/Documents/Flexible_Tubing/FT-PharMed-BPT.pdf. [Accessed: 25-Jun-2014].

[218] Saint-Gobain, “Tygon E-3603.” [Online]. Available: http://www.biopharm.saint-gobain.com/en/Products/PDFs/TYGON_E-3603.pdf. [Accessed: 25-Jun-2014].

[219] M. Erdmann, J. Dörrie, N. Schaft, E. Strasser, M. Hendelmeier, E. Kämpgen, G. Schuler, and B. Schuler-Thurner, “Effective clinical-scale production of dendritic cell vaccines by monocyte elutriation directly in medium, subsequent culture in bags and final antigen loading using peptides or RNA transfection.,” *J. Immunother.*, vol. 30, no. 6, pp. 663–74, Sep. 2007.

[220] L. Zhou and T. Tedder, “CD14+ blood monocytes can differentiate into functionally mature CD83+ dendritic cells,” *Proc. Natl. Acad. Sci.*, vol. 93, no. March, pp. 2588–2592, 1996.

[221] R. P. Lauener, S. M. Goyert, R. S. Geha, and D. Vercelli, “Interleukin 4 down-regulates the expression of CD14 in normal human monocytes.,” *Eur. J. Immunol.*, vol. 20, no. 11, pp. 2375–81, Nov. 1990.

[222] T. J. Dennes and J. Schwartz, “A nanoscale adhesion layer to promote cell attachment on PEEK.,” *J. Am. Chem. Soc.*, vol. 131, no. 10, pp. 3456–7, Mar. 2009.

[223] R. Mallone, S. I. Mannering, B. M. Brooks-Worrell, I. Durinovic-Belló, C. M. Cilio, F. S. Wong, and N. C. Schloot, “Isolation and preservation of peripheral blood mononuclear cells for analysis of islet antigen-reactive T cell responses: position statement of the T-Cell Workshop Committee of the Immunology of Diabetes Society.,” *Clin. Exp. Immunol.*, vol. 163, no. 1, pp. 33–49, Jan. 2011.

[224] J. Babatz, C. Röllig, U. Oelschlägel, S. Zhao, G. Ehninger, M. Schmitz, and M. Bornhäuser, “Large-scale immunomagnetic selection of CD14+ monocytes to generate dendritic cells for cancer immunotherapy: a phase I study,” *J. Hematother. Stem Cell Res.*, vol. 12, pp. 515–523, 2003.

[225] A. M. Dohnal, S. Graffi, V. Witt, C. Eichstill, D. Wagner, S. Ul-Haq, D. Wimmer, and T. Felzmann, “Comparative evaluation of techniques for the manufacturing of dendritic cell-based cancer vaccines.,” *J. Cell. Mol. Med.*, vol. 13, no. 1, pp. 125–35, Jan. 2009.

[226] A. Lenshof and T. Laurell, “Continuous separation of cells and particles in microfluidic systems.,” *Chem. Soc. Rev.*, vol. 39, no. 3, pp. 1203–17, Mar. 2010.

[227] D. W. Inglis, J. A. Davis, R. H. Austin, and J. C. Sturm, “Critical particle size for fractionation by deterministic lateral displacement.,” *Lab Chip*, vol. 6, no. 5, pp. 655–8, May 2006.

[228] J. a Davis, D. W. Inglis, K. J. Morton, D. a Lawrence, L. R. Huang, S. Y. Chou, J. C. Sturm, and R. H. Austin, “Deterministic hydrodynamics: taking blood apart.,” *Proc. Natl. Acad. Sci. U. S. A.*, vol. 103, no. 40, pp. 14779–84, Oct. 2006.

[229] D. W. Inglis, J. A. Davis, T. J. Zieziulewicz, D. A. Lawrence, R. H. Austin, and J. C. Sturm, “Determining blood cell size using microfluidic hydrodynamics.,” *J. Immunol. Methods*, vol. 329, no. 1–2, pp. 151–6, Jan. 2008.

[230] J. Yang, Y. Huang, X. B. Wang, F. F. Becker, and P. R. Gascoyne, “Differential analysis of human leukocytes by dielectrophoretic field-flow-fractionation.,” *Biophys. J.*, vol. 78, no. 5, pp. 2680–9, May 2000.

[231] K. Inaba, M. Inaba, N. Romani, H. Aya, M. Deguchi, S. Ikehara, S. Muramatsu, and R. M. Steinman, “Generation of large numbers of dendritic cells from mouse bone marrow cultures supplemented with granulocyte/macrophage colony-stimulating factor.,” *J. Exp. Med.*, vol. 176, no. 6, pp. 1693–702, Dec. 1992.

[232] S. Haskill, C. Johnson, D. Eierman, S. Becker, and K. Warren, “Adherence induces selective mRNA expression of monocyte mediators and proto-oncogenes.,” *J. Immunol.*, vol. 140, no. 5, pp. 1690–4, Mar. 1988.

[233] A. Leen, M. Ratnayake, and A. Foster, “Contact-activated monocytes: efficient antigen presenting cells for the stimulation of antigen-specific T cells,” *J. Immunother.*, vol. 30, no. 1, pp. 96–107, 2007.

[234] S. Burns, S. J. Hardy, J. Buddle, K. L. Yong, G. E. Jones, and A. J. Thrasher, “Maturation of DC is associated with changes in motile characteristics and adherence.,” *Cell Motil. Cytoskeleton*, vol. 57, no. 2, pp. 118–32, Feb. 2004.

[235] T. Nagel, N. Resnick, W. J. Atkinson, C. F. Dewey, and M. A. Gimbrone, “Shear Stress Selectively Upregulates Intercellular Adhesion Molecule-1 Expression in Cultured Human Vascular Endothelial Cells,” *J. Clin. Invest.*, vol. 94, no. August, pp. 885–891, 1994.

[236] L. Macke, H. S. P. Garritsen, W. Meyring, H. Hannig, U. Pägelow, B. Wörmann, C. Piechaczek, R. Geffers, M. Rohde, W. Lindenmaier, and K. E. J. Dittmar, “Evaluating maturation and genetic modification of human dendritic cells in a new polyolefin cell culture bag system.,” *Transfusion*, vol. 50, no. 4, pp. 843–55, Apr. 2010.

[237] M. Elias, J. van Zanten, G. A. P. Hospers, A. Setroikromo, M. A. de Jong, L. F. M. H. de Leij, and N. H. Mulder, “Closed system generation of dendritic cells from a single blood volume for clinical application in immunotherapy.,” *J. Clin. Apher.*, vol. 20, no. 4, pp. 197–207, Dec. 2005.

[238] R. Rouas, H. Akl, H. Fayyad-Kazan, N. El Zein, B. Badran, B. Nowak, H. Duvillier, P. Martiat, and P. Lewalle, “Dendritic cells generated in clinical grade bags strongly differ in immune functionality when compared with classical DCs generated in plates.,” *J. Immunother.*, vol. 33, no. 4, pp. 352–63, May 2010.

[239] S. Tuyaerts, S. M. Noppe, J. Corthals, K. Breckpot, C. Heirman, C. De Greef, I. Van Riet, and K. Thielemans, “Generation of large numbers of dendritic cells in a closed system using Cell Factories.,” *J. Immunol. Methods*, vol. 264, no. 1–2, pp. 135–51, Jun. 2002.

[240] D. Selmeczi, T. S. Hansen, O. Met, I. M. Svane, and N. B. Larsen, “Efficient large volume electroporation of dendritic cells through micrometer scale manipulation of flow in a disposable polymer chip.,” *Biomed. Microdevices*, vol. 13, no. 2, pp. 383–92, Apr. 2011.

[241] P. C. Hiemenz and R. Rajagopalan, *Principles of Colloid and Surface Chemistry, revised and expanded*, vol. 14. CRC Press, 1997.

[242] R. J. Good and L. A. Girifalco, “A Theory for Estimation of Surface and Interfacial Energies. III. Estimation of Surface Energies of Solids from Contact Angle Data,” *J. Phys. Chem.*, vol. 64, no. 5, pp. 561–565, 1960.

[243] C. Rulison, “Two-Component Surface Energy Characterization As a Predictor of Wettability and Dispersability, Application note 213,” 2000.

[244] G. Beamson and D. Briggs, *High Resolution XPS of Organic Polymers - The Scienta ESCA300 Database*. Chichester: John Wiley & Sons, 1992.

Appendix A:

A.1 External dissemination

Papers in peer reviewed journals

- *One-step Immobilization of Functionally Active Antibodies in Thermoplastics by Injection Molding*
  T.C. Hobæk, H. Pranov, N.B. Larsen
  Submitted to Analytical Chemistry, July 31, 2014
- *Hydrogen silsesquioxane (HSQ) mold coatings for improved replication of nanopatterns by injection molding*
  T.C. Hobæk, M. Matschuk, J. Kafka, H. Pranov, N.B. Larsen
  Submitted to Journal of Micromechanics and Microengineering, August 1, 2014

First author conference contributions

- *Polymer Micro- and Nanotechnology for On-Chip Cell Selection (Poster);*
  T.C. Hobæk, H. Pranov, I.M. Svane, N.B.Larsen
  Nano Update 2012, Helsingborg, Sweden, March 2012
- *Polymer Micro- and Nanotechnology for On-Chip Cell Selection (Oral talk and poster);*
  T.C. Hobæk, H. Pranov, I.M. Svane, N.B.Larsen
  7th ProteinDTU Workshop, Copenhagen, Denmark, May 2012
- *Polymer Micro- and Nanotechnology for On-Chip Cell Selection (Poster);*
  T.C. Hobæk, H. Pranov, I.M. Svane, N.B.Larsen
  38th International Conference on Micro and Nano Engineering (MNE), Toulouse, France, September 2012
- *Replication on large-area nanostructures by injection molding (Oral talk);*
  T.C.Hobæk, M. Matschuk, J. Kafka, H. Pranov, K. Haugshøj, L. Thamdrup, J. Nørregaard, N. B. Larsen;
  Polymer Replication on Nanoscale (PRN), Copenhagen, Denmark, May 2014
- *Direct Immobilization of Capture Antibodies on Injection Molded Plastics (Poster);*
  T.C.Hobæk, H. Pranov, N. B. Larsen;
  Fourth International Workshop on Analytical Miniaturization and NANOtechnologies (WAM-NANO 2014), Copenhagen, Denmark, June 2014

A.2 Content related to the various chapters

A.2.1 Chapter 2

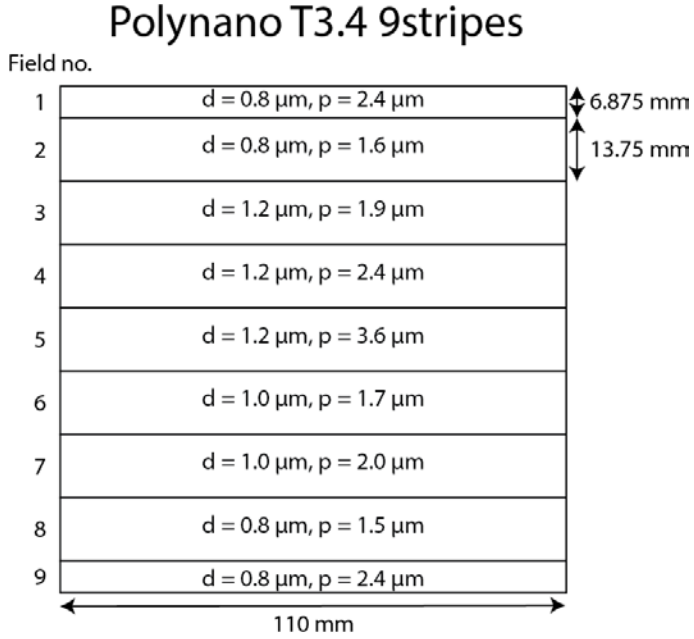

Figure A-1. Layout of the "9stripes" first-generation reticle used for DUV-stepping. Each field is filled with different patterns of squares with a width *d* in a square array with pitch *p*.

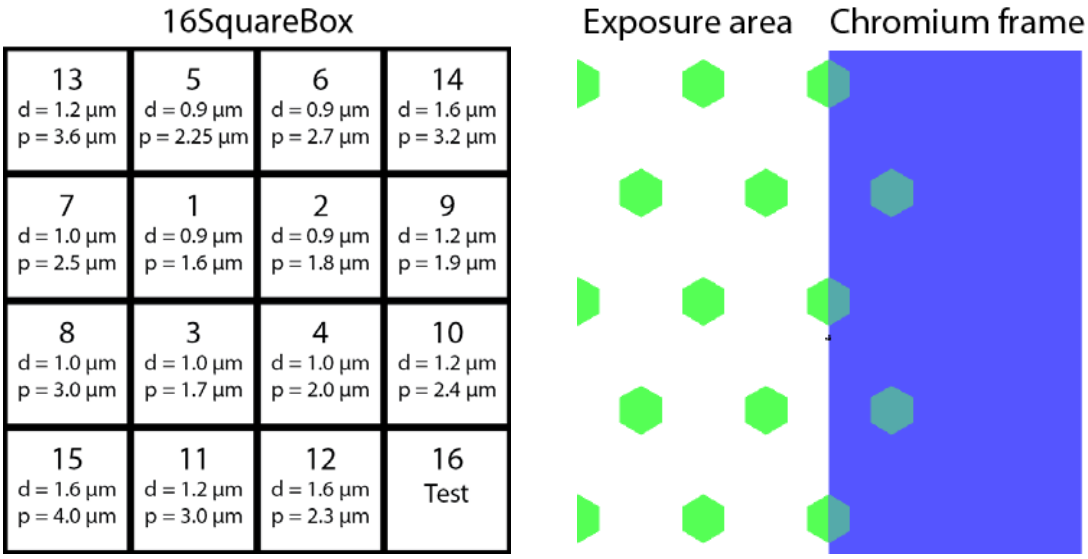

Figure A-2. Layout of the "16Box" second-generation reticle used for DUV-stepping. **Left:** Each 26.25 x 26.25 mm^2 field is filled with different patterns of hexagons with flat-to-flat distance *d* in a hexoganal array with pitch *p*. A 1 mm chromium frame separates the different fields from each other, which enables individual exposure of each structure. Field 16 is split in four parts, containing "test" structures as well as horizontal and vertical gratings with a nominal width of 1.5 µm and a pitch of 3.0 µm. **Right:**The pitch was matched so that the stitching inaccuracy between neighbouring chips was minimized.

0-5 (DCHimm 18-04)

Step no.	dt [min]	dI [A]
1	15	0.5
2	15	1.0
3	30	0.0
4	10	4.0
5	180	0.0
6	17	3.4
7	360	0

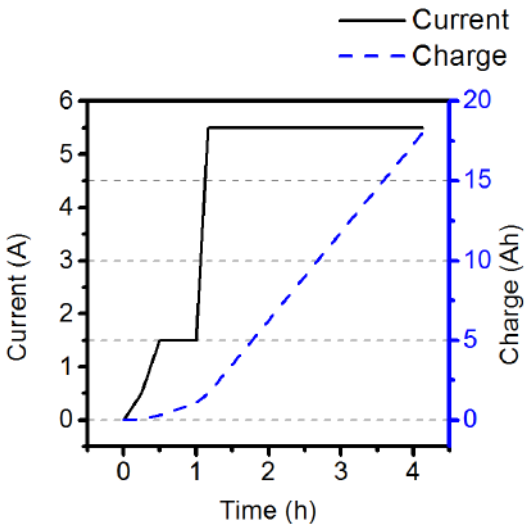

Figure A-3. The electroplating parameters and a plot of the current and charge over time, for the program used to produce Ni shims from 4" wafers (0-9 – DCHimm 18-04). The charge setpoint was 18.0 Ah, which resulted in a thickness of around 320 µm. Initially, the current was ramped up slowly (2.0 A/h), before the ramping rate was increased until reaching a maximum value of 5.5 A. The total duration of the program was about 4h and 8 min.

0-9 (DCH_40.5Ah_7h)

Step no.	dt [min]	dI [A]
1	30	0.1
2	12	0.4
3	15	1.0
4	15	2.0
5	30	0.0
6	17	3.4
7	360	0

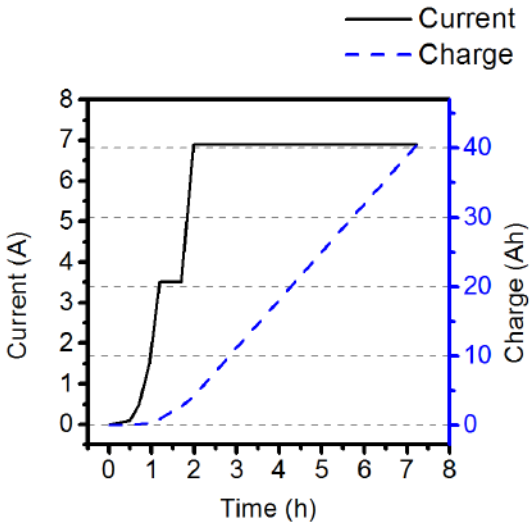

Figure A-4. The electroplating parameters and a plot of the current and charge over time, for the program used to produce Ni shims from 6" wafers (0-9 - DCH6_40.5Ah_7h). The charge setpoint was 40.5 Ah, which resulted in a thickness of around 320 µm. Initially, the current was ramped up slowly (0.2 A/h), before the ramping rate was increased until reaching a maxium value of 6.9 A. The total duration of the program was about 7h and 15 min.

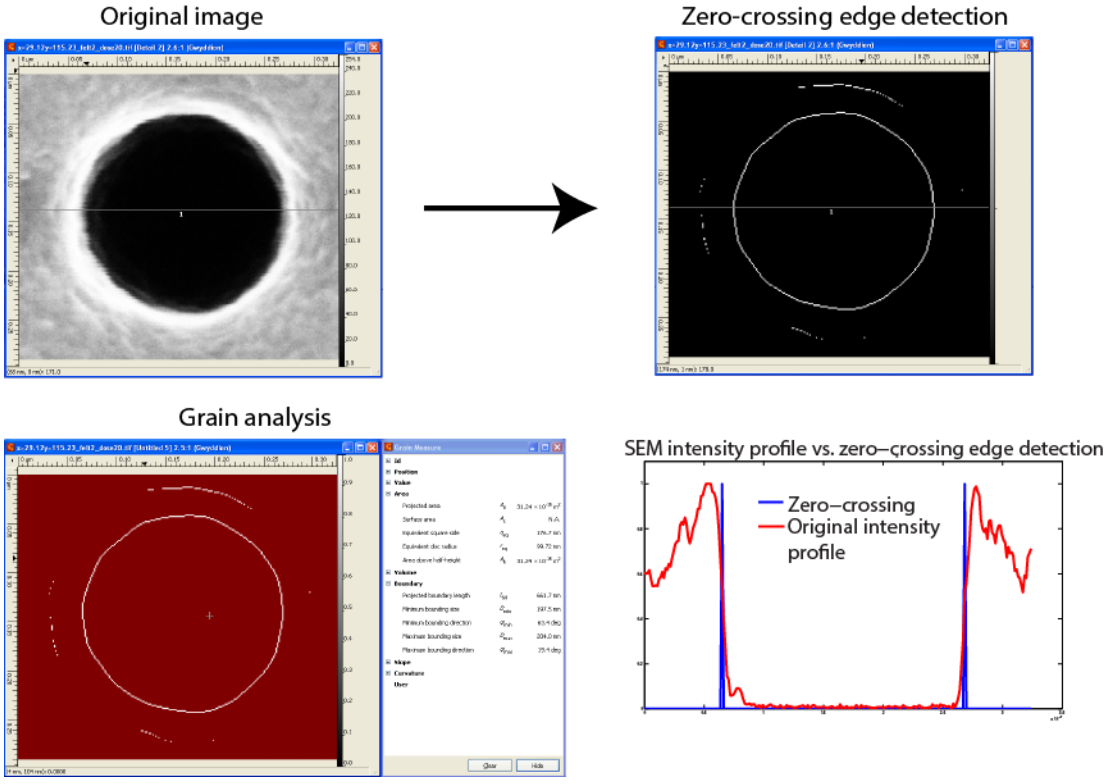

Figure A-5. Holes in the resist from SEM micrographs were analyzed by the Gwyddion SPM data analysis software. A zero-crossing step detection was applied to the original image, before grains were defined by the threshold method and the diameter measured. An overlay of the intensity profiles along the horizontal line shows the placement of the detected step.

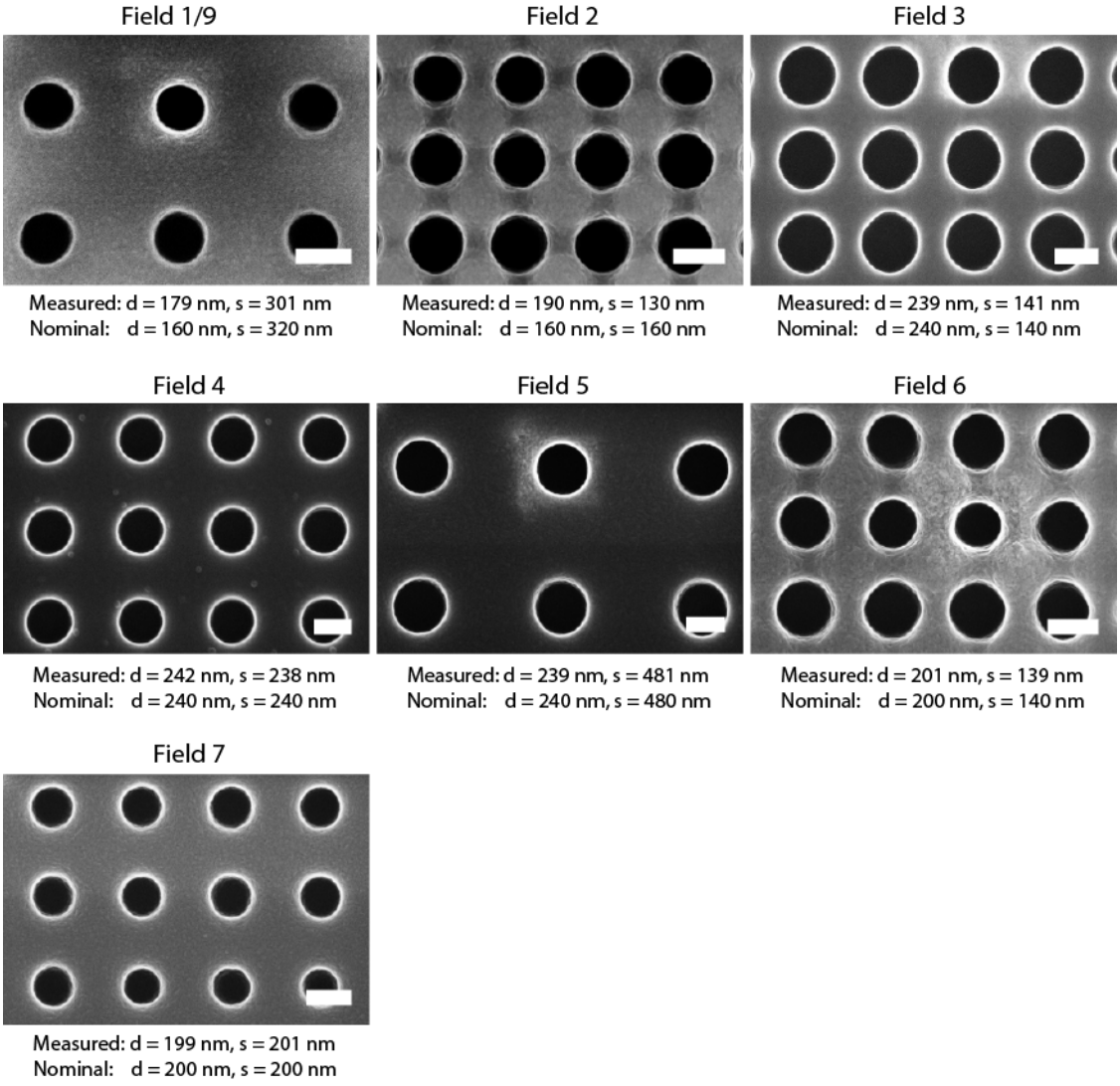

Figure A-6. SEM micrographs of resist exposed by the DUV stepper from different fields of the reticle "*9stripes*" (**Figure A-1**), using optimal doses (**Table 2-2**). The measured and nominal dimensions are notated for each structure.

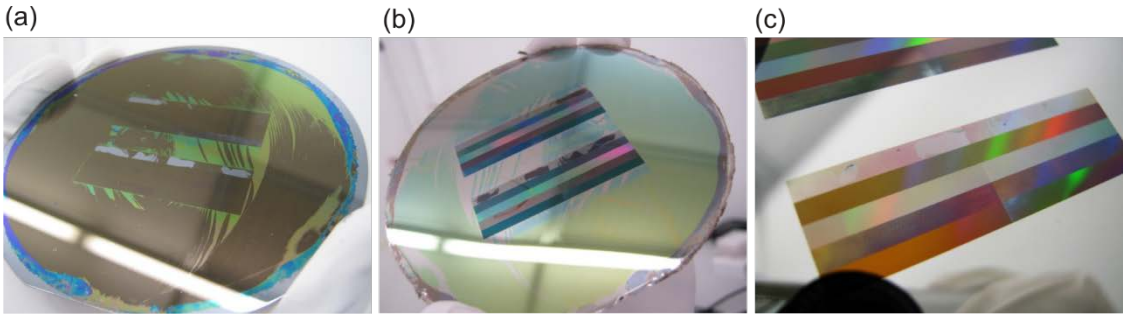

Figure A-7. A photograph of separated Si wafer (**a**) and Ni shim plated on metallized resist (**b**), shows that some of the resist on the Si is transferred to the shim, exposing the underlying BARC layer (brown film). After rinsing with ethanol and plasma ashing, the resist was stripped, although some inhomogeneities could be observed in the patterend region (**c**).

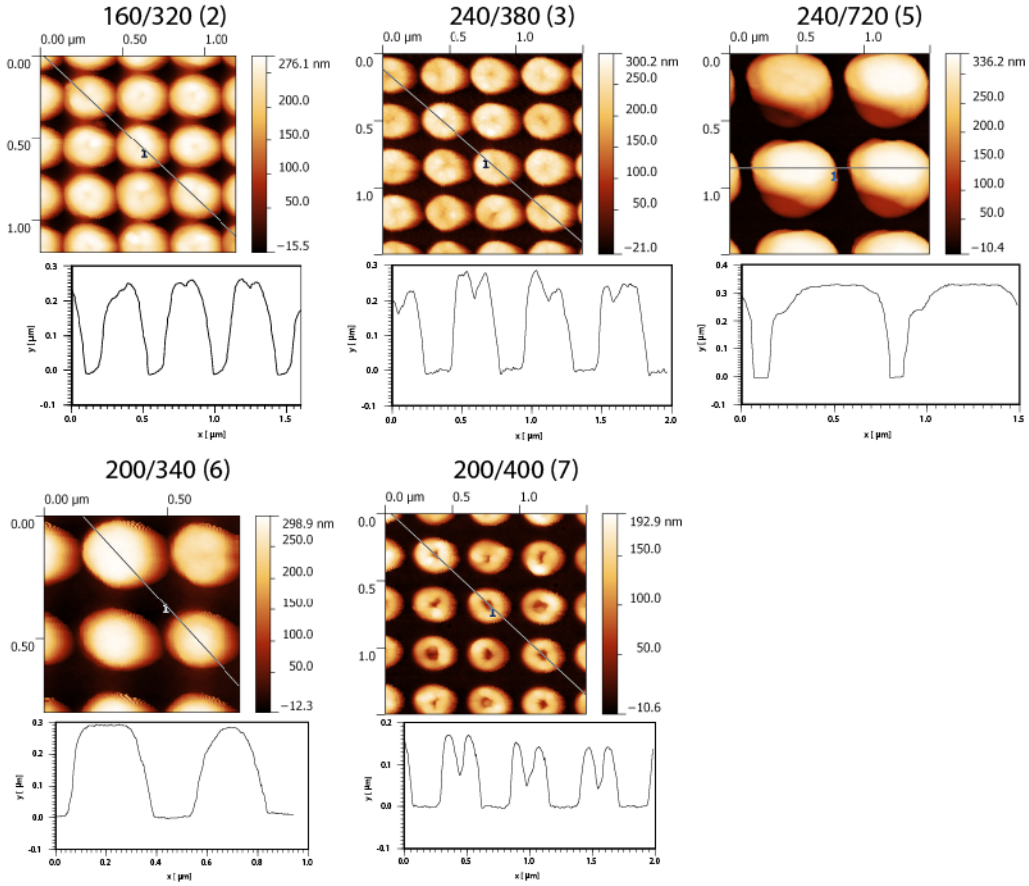

Figure A-8. AFM topography micrographs and corresponding line profiles for different nanostructures electroplated from a NiV seed layer sputter coated on developed DUV resist. The average height of protruding pillars are 274 nm, 289 nm, 327 nm, 273 nm and 197 nm for field 2, 3, 5, 6, and 7 respectively.

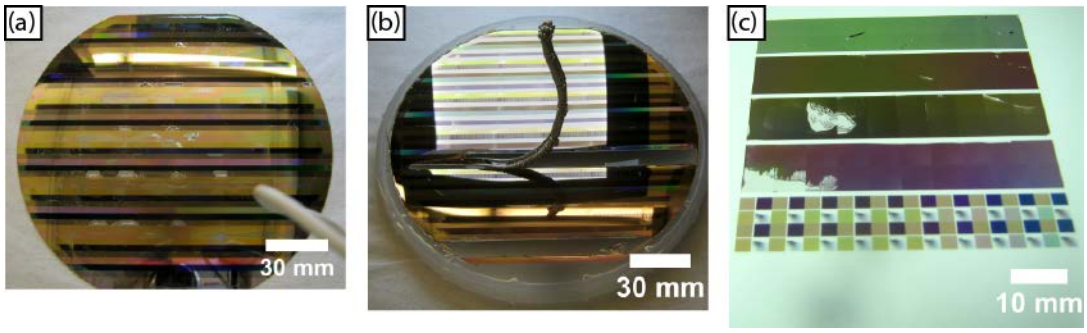

Figure A-9. Photographs of unsuccessful electroplating of nanostructured Ni shims, using NiV as the seed layer. Some of the Ni shims plated from metallized DUV resist had mm-sized holes through the inlay, while some of the shims plated from metallized etched Si displayed delamination of large patches of nanopatterned areas. Images provided by NIL Technology.

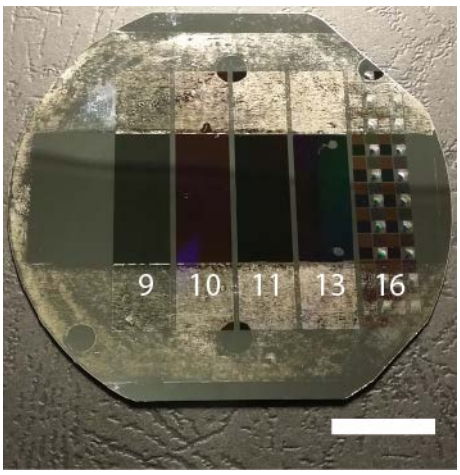

Figure A-10. Photograph of Ni shim for molding polymer replicas in microscope slide format. The nanostructures are numbered according to the different areas on the reticle in **Figure A-2**. The indicated scale bar is 20 mm.

Table A-1. Process parameters for conditioning of MVD chamber "COLDPRP2" and FDTS-coating "STAMP2" of shims. The FDTS and water sources were heated to 55 °C and 50 °C respectively. The chamber temperature was 35 °C.

COLDPRP2					
Step	**Cycles**	**Source**	**Parameters**		
1	1	O_2	Flow	200	sccm
			Power	250	W
			Time	300	s
2	4	FDTS	Pressure	0.4	Torr
			Time	10	s
3	1	O_2	Flow	200	sccm
			Power	250	W
			Time	300	s
4	5	N_2			

STAMP2						
Step	**Cycles**	**Source**	**Vapor order**	**Parameters**		
1	1	O_2	1	Flow	200	sccm
				Power	250	W
				Time	300	s
2	4	FDTS	1	Pressure	0.5	Torr
				Time	900	s
		H_2O	2	Pressure	6	Torr
				Time	900	s
3	5	N_2				

A.2.1.1 Surface energy calculations by Owens-Wendt method

The Owens-Wendt theory is a two component model for calculating the surface energy of a solid [68]. It describes the surface energy of a solid as having two components; a dispersive component and a polar component. It is based on the fundamental Young's equation which relates the interfacial energy between the solid-gas (γ_{SG}), the solid-liquid (γ_{SL}) and the liquid-gas (γ_{LG}) phase.

$$\gamma_{LG}\cos(\theta) = \gamma_{SG} - \gamma_{SL}$$

This form is valid for low-energy surfaces, such as most solid organic compounds, where the adsorption of vapor onto the solid surface has a negligible effect on the interfacial energies [241]. Good and Girifalco [242], proposed an equation for the interfacial energy between two phases a or b which may be liquid or solid, as a balance between the cohesive energy in the bulk a and b, and the energy of attraction due to dispersion forces between unlike pairs of molecules at the interface, expressed as the geometric mean of the energy of attraction between pairs of like molecules:

$$\gamma_{AB} = \gamma_A + \gamma_B - 2(\gamma_A\gamma_B)^{\frac{1}{2}}$$

Furthermore, Fowkes [69] postulated that the total free energy of a liquid or solid could be written as the sum of polar (γ^P) and dispersive (γ^D) contributions at the surface:

$$\gamma = \gamma^P + \gamma^D$$

Combining equation 2 and 3 gives the interfacial energy between a solid-liquid interface written as

$$\gamma_{SL} = \gamma_{SG} + \gamma_{LG} - 2(\gamma_{SG}^D\gamma_{LG}^D)^{\frac{1}{2}} - 2(\gamma_{SG}^P\gamma_{LG}^P)^{\frac{1}{2}}$$

Inserting into equation 1 and rearranging gives the Owens-Wendt equation [68]

$$\frac{\gamma_{LG}(\cos\theta + 1)}{2(\gamma_{LG}^D)^{\frac{1}{2}}} = (\gamma_{SG}^P)^{\frac{1}{2}}\left(\frac{\gamma_{LG}^P}{\gamma_{LG}^D}\right)^{\frac{1}{2}} + (\gamma_{SG}^D)^{\frac{1}{2}}$$

The polar and dispersive contributions of a solid surface can then be found by linear regression ($y = ax + b$) using

$$y = \frac{\gamma_{LG}(\cos\theta + 1)}{2(\gamma_{LG}^D)^{\frac{1}{2}}}$$

$$x = \left(\frac{\gamma_{LG}^P}{\gamma_{LG}^D}\right)^{\frac{1}{2}}$$

and measuring contact angles using the sessile drop technique with two or more probe liquids having well-defined polar and dispersive components [243]

$$\gamma_{SG}^P = a^2$$
$$\gamma_{SG}^D = b^2$$

An example of such a linear fit using contact angles measured on Si-FDTS with water, diiodomethane, and benzyl alcohol, is shown in **Figure A-11**.

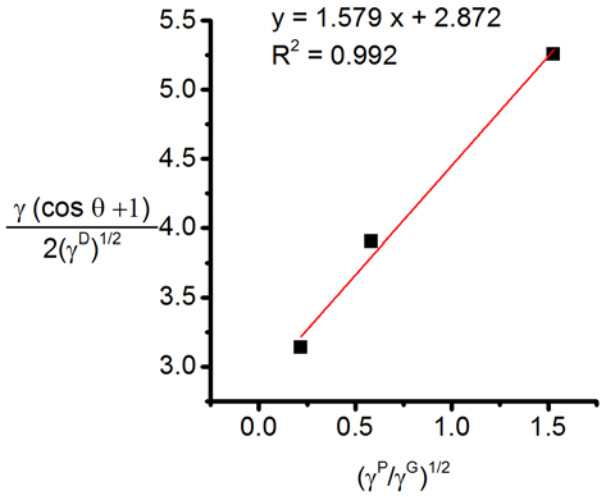

Figure A-11. Calculation of the surface energy components by the Owens-Wendt method, using linear fit.

A.2.2 Chapter 4

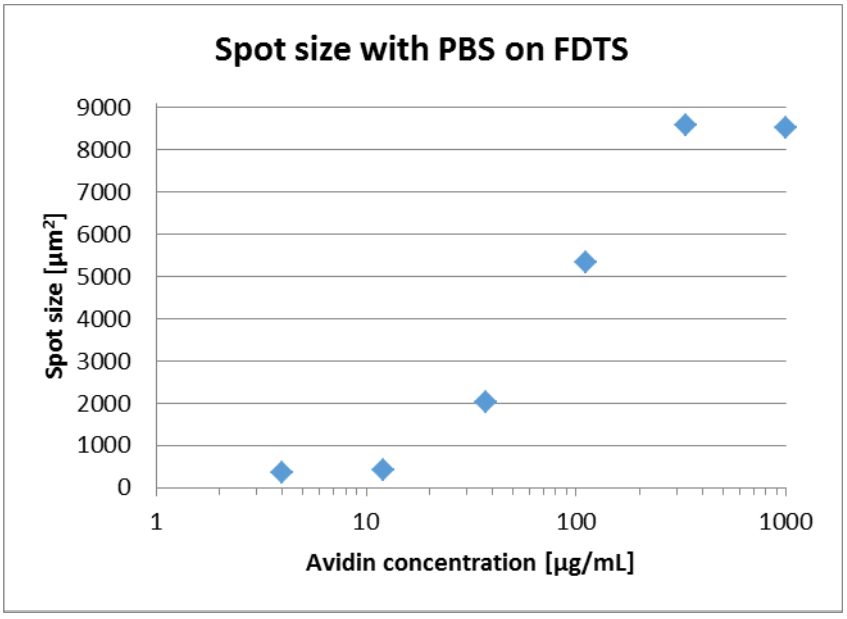

Figure A-12. Spot size of avidin in PBS from single droplets on FDTS as a function of protein concentration.

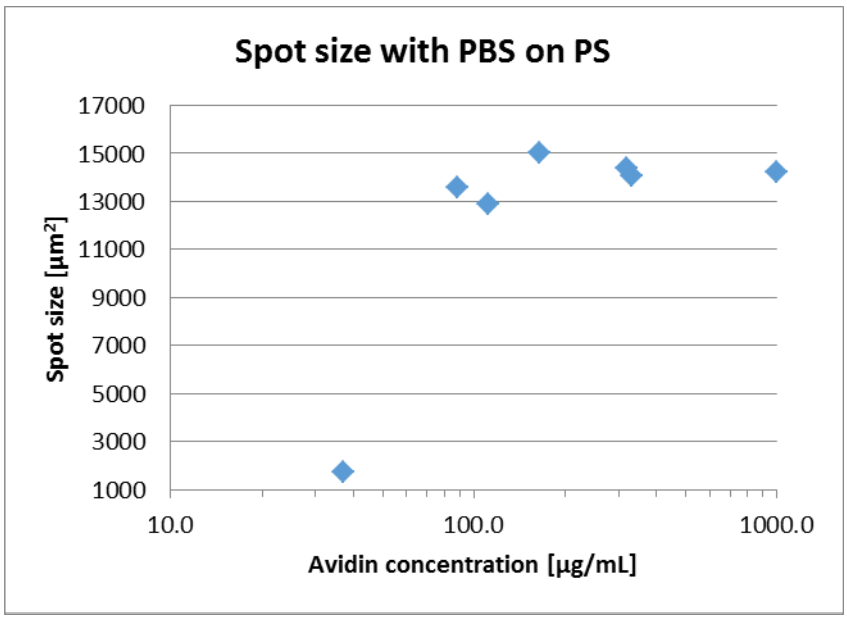

Figure A-13. Spot size of avidin in PBS from single droplets on polystyrene (PS) as a function of protein concentration.

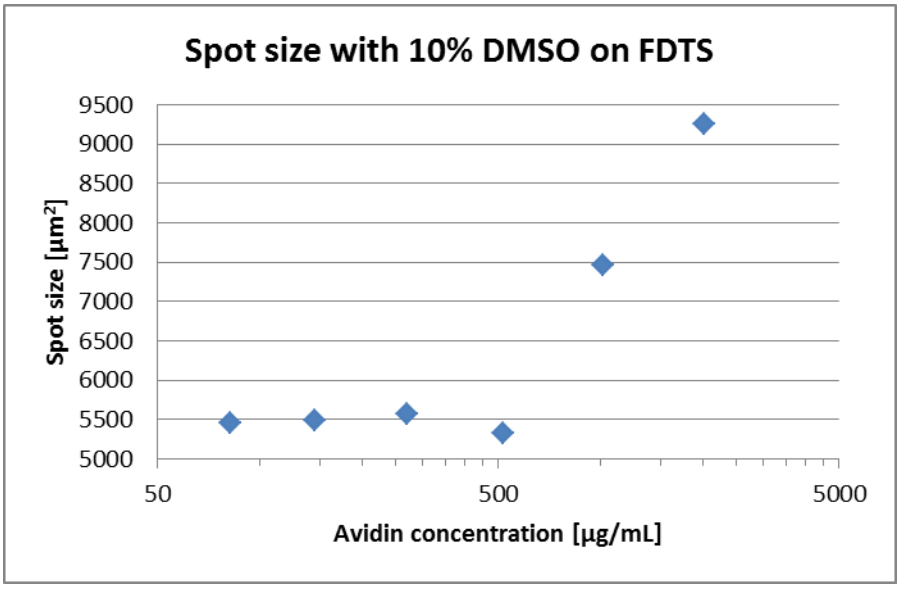

Figure A-14. Spot size of avidin in 10% DMSO + 90% PBS from single droplets on FDTS as a function of protein concentration.

A.2.3 Chapter 5

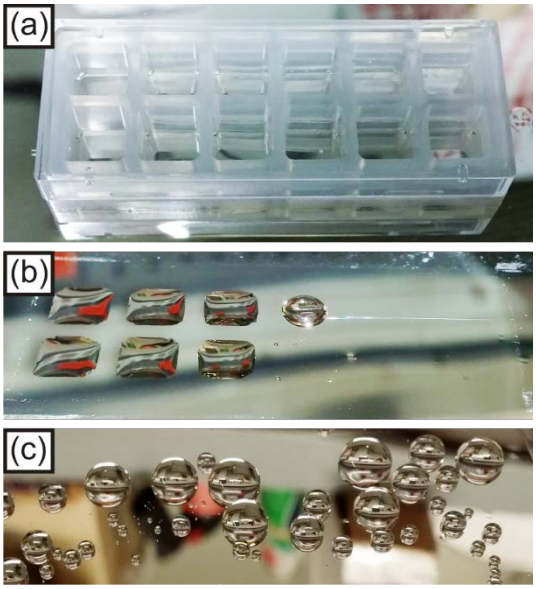

Figure A-15. Deposition of antigen concentration series at mold inlay surface. (a) The 12-well chamber was mounted on the shim and protein was titrated in PBS. (b) After 10 min incubation, the wells were removed and the shim was washed with MilliQ water. Due to adsorption, water droplets sticked to areas incubated with more than 10 µg/mL protein. (c) After InMold transfer, the mold inlay was again hydrophobic.

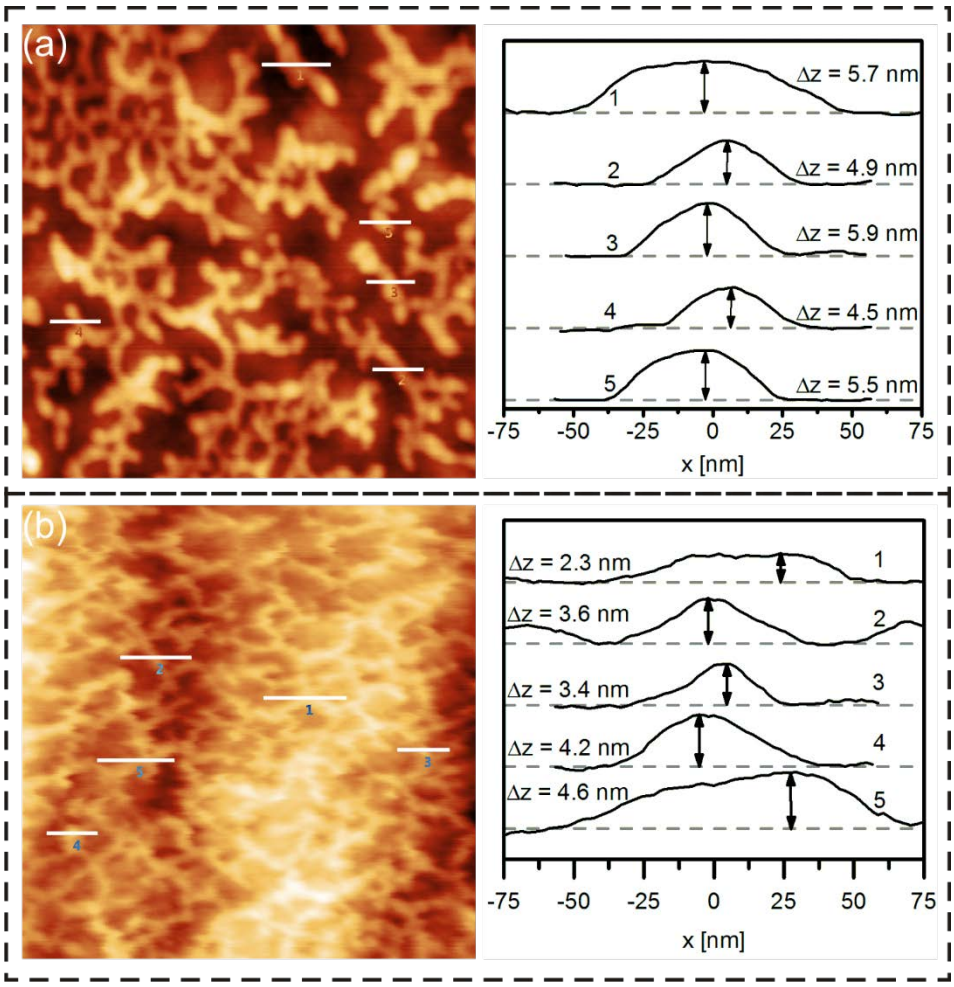

Figure A-16. Line profiles across IgG adsorbed on mold inlay (a) and on polymer replica after transfer (b) suggest a partial embedding of the protein in the polymer surface. The average peak height of five line scans was 5.3 nm and 3.6 nm for the two samples respectively.

A.2.4 Chapter 6

Figure A-17. Chip with 12 integrated Luer-lock connectors and mold inlay. Each connector were integrated with energy directors at the bottom side for welding.

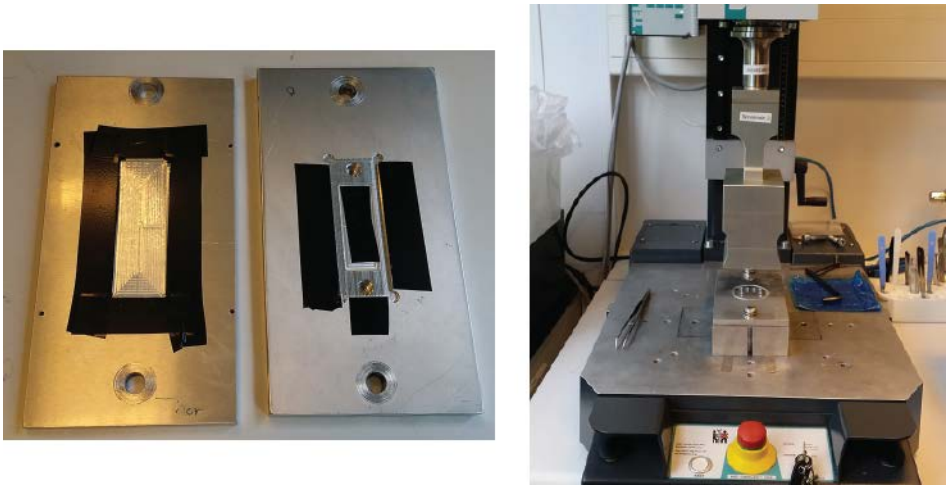

Figure A-18: Aluminum holders for bonding of the microfluidic chamber (left) and the Luer-Lock connectors to the assembly (right). To the right is the Telsonic Ultrasonics UPS-3000 welder.

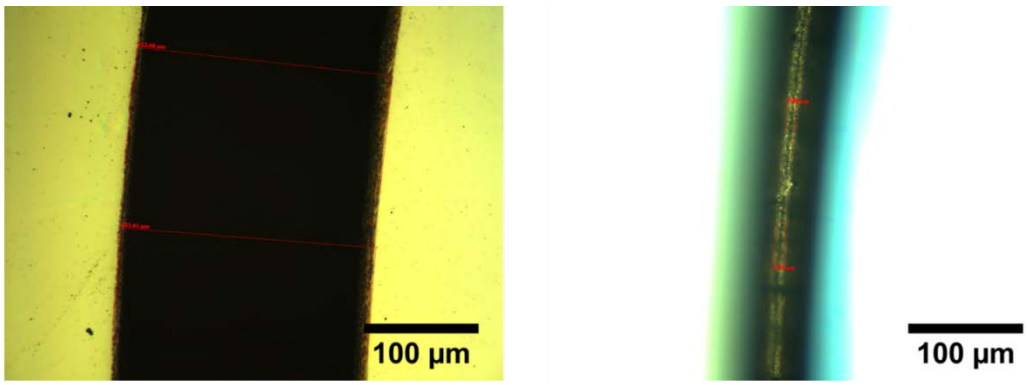

Figure A-19. Energy directors milled in a Ni mold by a microSTRUCT vario (3D-Micromac AG), using a 355 nm laser at 1.72 W. The top of the ED was 223 µm wide, while the bottom was 8 µm.

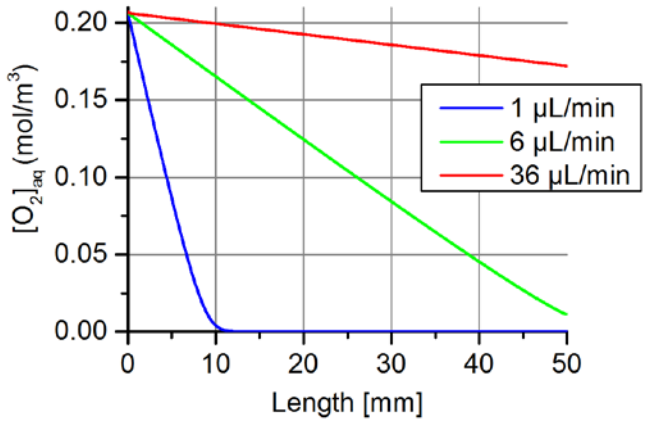

Figure A-20. Surface concentration of dissolved oxygen along the length of a microfluidic channel with different flow rates.

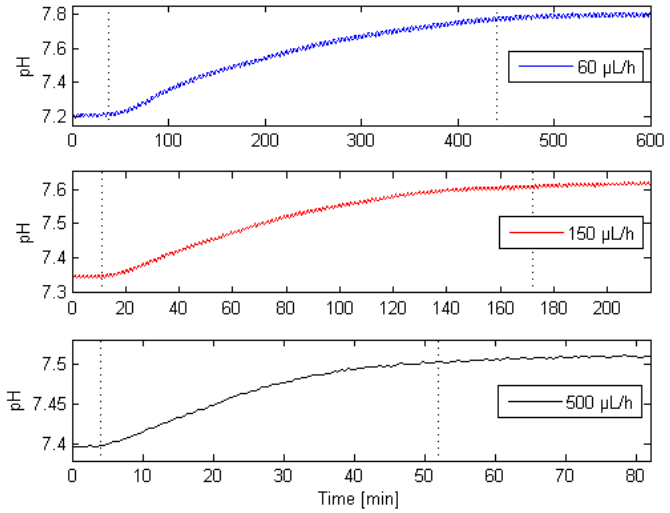

Figure A-21. Continous pH measurements of medium after flowing through Pharmed BPT peristaltic tubing at three different rates, determined by the absorbance of phenol red in cell medium. The inner diameter of the tubing was 0.8 mm and the length between medium reservoir and optical cell was 80 cm. The vertical dashed lines show the medium residence time before entering the optical cell.

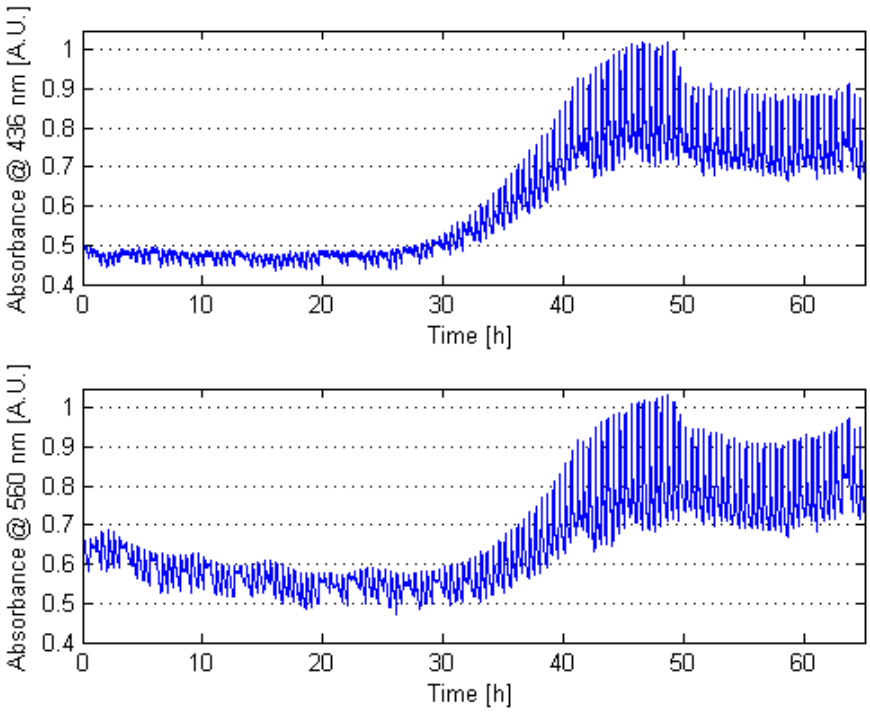

Figure A-22. Absolute absorbance values of X-VIVO 15 culture medium at 436 nm and 560 nm measured over time by photospectroscopy.

A.2.5 Chapter 7

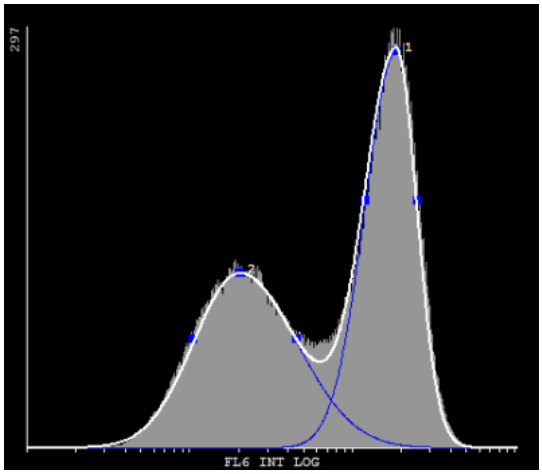

Figure A-23. Gaussian peak fit of the bimodal CD83-APC histogram for harvested DCs (donor 1).

A.3 Deconvolution of peaks in the C1s spectra

First, peaks for "Mold before IM" (**Figure A-24**) were added at 285.6 eV (A), 286.3 eV (B), 291.9 eV (C) and 294.2 eV (D), which are believe to originate from the primary and secondary carbon at the Si-end of the FDTS molecular chain, -CF_2 groups and -CF_3 groups respectively. A constraint of separation by 0.7 eV was added between (A) and (B), based on the fact that the binding energy of –CH_2 groups in poly(vinylidene fluoride) (neighbouring –CF_2 groups) and poly(vinyl fluoride) (neighbouring –CF groups) differs by the same amount [244]. With these conditions, the peaks were fitted to the XPS data. Then, the peak separation of (A), (B) and (D) was locked to have a constant separation relative to (C) of -6.25 eV, -5.55 eV and +2.31 eV respectively. Furthermore, the area under each peak component was locked to be C/6.6, C/6.49 and C/6.51 of (A), (B) and (D) respectively, and the FWHM of all peaks was locked.

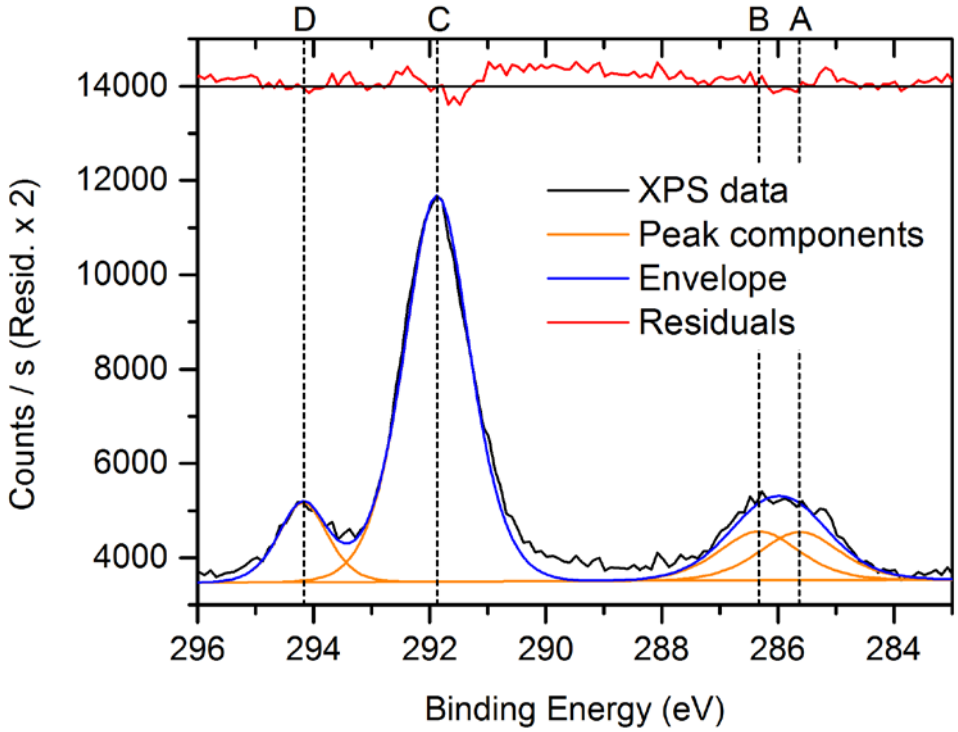

Figure A-24. Deconvolution of peaks in the C1s spectra of the mold surface before protein adsorption.

The peak fit parameters with all constraints were then imported to the data for the sample with "Mold with IgG" (**Figure A-25**). Three new peaks were added at 285.2 eV (E), 286.5 eV (F) and 288.4 eV (G), which were believe to originate from carbonyl carbons in the backbone and carboxyl carbons in the side-chains of the amino acids (C=O and COOH), the amine-bound α-carbon (C-N) and carbon single bonds (C-C) respectively. The peaks were fitted and the peaks of (E), (F) and (G) were locked at a separation of -6.63 eV, -5.34 eV and -3.46 eV respectively. The peak area of (F) and (G) were locked at E/1.56 and E/1.73 respectively. The FWHM of all peaks were locked and the data was fitted again. After assigning the parameters of all 7 peak components, the parameters were imported to "Mold before IM" and "Mold after IM"

and the data was fitted with the new constraints.

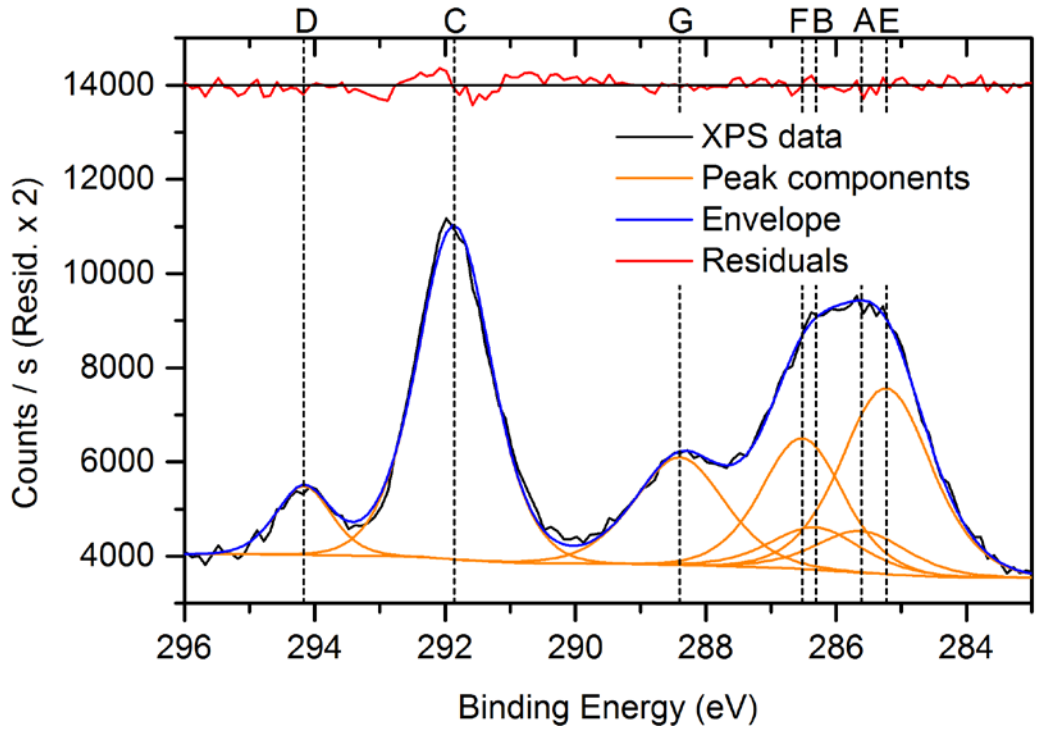

Figure A-25. Deconvolution of peaks in the C1s spectra of the mold surface after protein adsorption.

A.4 Protocol for DC generation in dish

Protocol: **Production of human dendritic cells (DCs) from peripheral blood mononuclear cells (PBMCs) in Ø50 mm culture dish**	Revision date: 28-11-2013
Author: Thor Christian Hobæk	Version no: 3

Apparatus:
Ø50 mm Nunclon Delta culture dish
15 mL centrifuge tubes
50 mL centrifuge tubes
Sterile pasteur pipettes
Laboratory pipettes and sterile pipette tips
FACS tubes
Cell scraper
Sterile flow bench
Incubator 37C
Water bath at 37C
Laboratory centrifuge
Flow cytometer

Reagents:
Frozen PBMCs from Herlev Hospital stored at -140 C (10^7 cells/vial)
X-VIVO 15 medium, Cambrex PN BE04-418Q
Glutamin 100x stock concentration
Human AB serum
GM-CSF, CellGenix (35 µL per vial, corresponds to 35 mL medium)
TNF-α, CellGenix (35 µL per vial, corresponds to 35 mL medium)
IL-1β, CellGenix (35 µL per vial, corresponds to 35 mL medium)
IL-4, CellGenix (35 µL per vial, corresponds to 35 mL medium)
IL-6, CellGenix (35 µL per vial, corresponds to 35 mL medium)
PGE-2 (175 µL per vial, corresponds to 17.5 mL medium)
1x PBS
FBS
Mouse Anti-Human CD3 – FICT
Mouse Anti-Human CD14 – PE
Mouse Anti-Human CD83 – APC
IgG2a – PE isotype control
IgG1 – APC isotype control
IgG2a – FITC isotype control
7AAD

Thawing and washing medium (WM):
100% X-VIVO 15 with phenol red and gentamicin

Culture medium (CM):
97% X-VIVO 15 with phenol red and gentamicin
2% Human AB serum
1% Glutamin

Culture medium with cytokines 1 (CM1)
97% X-VIVO 15 with phenol red and gentamicin
2% Human AB serum
1% Glutamin
1000 U/mL GM-CSF
250 U/mL IL-4

Culture medium with cytokines 2 (CM2)
97% X-VIVO 15 with phenol red and gentamicin
2% Human AB serum
1% Glutamin
1000 U/mL GM-CSF

250 U/mL IL-4
1000 U/mL IL-1β
1000 U/mL IL-6
1000 U/mL TNF-α
1 µg/mL PGE-2

Flow cytometry staining buffer:
99% 1x PBS
10% FBS
0.1% NaN_3

Flow cytometry wash buffer:
99.9% 1x PBS
0.1% NaN_3

Day 0 (day for start of culture):

Cell thawing and washing
Needed: $4*10^7$ PBMCs from the same donor (-140 C freezer, $3*10^7$ cells/vial)
2x50 mL centrifuge tubes
2x15 mL centrifuge tubes
30 mL WM at 37C
10 mL CM at 37C
45 mL PBS+0.1% NaN_3
2 mL PBS+10% FBS
600 µL PCR tubes

1. Two 50 mL centrifuge tube are numbered, and each are filled with 15 mL X-VIVO 15. Place the tubes in a 37C water bath.
2. Prepare 10 mL CM in a 15 mL centrifuge tube and place in a 37C water bath.
3. Thaw one 50 mL tube of frozen PBS+0.1% NaN_3 in the water bath
4. Make sure there is cold PBS+10%FBS+0.1% NaN_3 in the fridge
5. At least $4*10^7$ frozen PBMCs are taken from the -140C freezer and thawed for the shortest time possible in the water bath.
6. Just before the last lump of ice disappears, add warm X-VIVO 15 dropwise from tube 1 to the cryotube, mix and transfer the contents repeatedly back and forth, and transfer the entire contents back to tube 1.
7. Centrifuge the tube at 400g for 10 min at room temperature.
8. The supernatant is aspirated using a long Pasteur pipette.
9. The cell pellet is dispersed by pulling across the bench table perforation.
10. 15 mL are transferred carefully from tube 2. The cells are dispersed by carefully dispensing and sucking using a pipette.
11. Take out 10 µL of the cell suspension and add to a 600 µL PCR tube. Add 30 µL PBS, mix and add 15 µL to a hemocytometer.
12. Count all of the 4, 4x4 square arrays and average the number. The total number of cells are: Average cell count x 4 (dilution) x 15 mL x 10^4 cells/mL = Average cell count x $4*10^5$ cells.
13. Centrifuge the tube at 400g for 10 min at room temperature.
14. The supernatant is aspirated using a long Pasteur pipette.
15. The cell pellet is dispersed by pulling across the bench table perforation.
16. Resuspend the cells to about $7*10^6$ cells/mL or to minimum 5 mL of CM. Disperse the cells carefully using a pipette.
17. Pipette out $3*10^6$ cells and aliquot equally to three blue FACS tubes. Suspend the cells with PBS+10% FBS to a total volume of 100 µL in each tube.
18. Label the three FACS tubes with “Blank - before”, “Ab - before” and “Isotype - before” and store them in the fridge.

Cell seeding and sorting

Needed: 5 mL WM at 37C
5 mL CM1 at 37C
600 µL PCR tubes
Hemocytometer
3x FACS tubes

1. Add 5 mL of the PBMCs dispersed in culture medium to a Ø50 mm Nunclon culture dish.
2. Incubate the dish at 37C for 1h in the primary cell incubator
3. Prepare 5 mL CM1 with cytokines by taking one vial each of GM-CSF and IL-4 from the -140C freezer. 5 µL of each cytokine solution is added to the 5 mL of remaining CM and vortex. Store the vials with the remaining cytokines at 4C for up to 1 week.
4. Label an empty 15 mL centrifuge tube with "Non-adherent cells".
5. After incubating for 1 h, remove the non-adherent cells by slowly rotating the dish 25 times counter-clockwise, then 25 times clock-wise
6. Tilt the dish and aspirate the supernatant carefully using a pipette. Transfer the contents to the empty centrifuge tube.
7. Wash the dish by carefully adding 5 mL warm X-VIVO. Repeat step 5 and 6.
8. Immediately add 5 mL of CM1 with GM-CSF and IL-4 cytokines to the petri dish, and store in the primary cell incubator.
9. Vortex the tube with the non-adherent cells and transfer 10 µL of the cell suspension to a 600 µL PCR tube.
10. Spin down the non-adherent cells to a pellet by centrifugation at 400g for 10 min.
11. Add 10 µL PBS to the PCR tube, vortex and add 15 µL to a hemocytometer.
12. Count all of the 4, 4x4 square arrays and average the number. The total number of cells are: Average cell count x 2 x 10 x 10^4 = Average cell count x $2*10^5$.
13. After the non-adherent cells have been spun down, aspirate the supernatant using a long Pasteur pipette.
14. The cell pellet is dispersed by pulling the tube across the bench table perforation.
15. Resuspend the cells to 300 µL with PBS+10% FBS and aliquot to three FACS tubes labeled "Blank – non-adherent", "Ab - non-adherent" and "Isotype - non-adherent".

Flow cytometry

1. Add to the FACS tubes, vortex and incubate for 30 min in the fridge:
    1. "Blank – before" and "Blank – non-adherent":
        i. Nothing (blank control)
    2. "Ab - before" and "Ab - non-adherent":
        i. 20 µL of PE Anti-CD14
        ii. 20 µL of FITC Anti-CD3
    3. "Isotype - before" and "Isotype - non-adherent":
        i. 20 µL PE IgG2a control
        ii. 20 µL of FITC IgG2a control
2. After incubating with antibodies, wash the cells by adding 3 mL of PBS+0.1% NaN_3 and spin down to pellets at 400g for 5 min.
3. Remove supernatant, re-suspend the pellets by vortexing and repeat step 2.
4. Remove supernatant, re-suspend the pellets by vortexing and add 5 µL 7AAD to all tubes except the two blank tubes. Vortex.
5. Incubate tubes for 10 min in the fridge.
6. Add 300 µL of PBS+0.1% NaN_3 to the tubes and analyze with flow cytometry.

Day 1-4:

1. Look after the cells every 2-3 days and monitor the color of the culture medium. If it turns orange or yellow, exchange with 5 mL freshly prepared CM1.

Day 5:

Needed: 5 mL CM2 at 37C

1. Prepare 5 mL CM and put in waterbath at 37C.
2. Add cytokines to the CM and mix thoroughly: 5 µL of GM-CSF, IL-4, IL-1β, TNF-α and IL-6, and 50 µL PGE-2.
3. Tilt the petri dish and discard the supernatant carefully using a pipette.
4. Add 5 mL of CM2 and place petri dish in the primary cell incubator.

Day 7:

Needed:
1x50 mL centrifuge tube
15 mL cold 0.2% Na-EDTA in PBS
20 mL flow cytometry staining buffer
Mouse Anti-Human CD3 FITC
Mouse Anti-Human CD14 PE
Mouse Anti-Human CD83 APC
7AAD
Mouse IgG2a – PE isotype control
Mouse IgG1γ – APC isotype control
Mouse IgG2a – FITC isotype control
3 FACS tubes

1. Culture medium and cells are aspirated from the culture dish and transferred to a 50 mL centrifuge tube labeled "Harvested cells".
2. The dish is washed with 5 mL cold Na-EDTA in PBS, and the contents are transferred to the centrifuge tube.
3. Add 5 mL cold Na-EDTA in PBS and incubate for 30 min at 4C.
4. The cells are harvested carefully by using a cell scraper. Transfer the contents to the centrifuge tube.
5. Wash again with 5 mL cold Na-EDTA in PBS and transfer the cells to the tube.
6. Centrifuge the tube at 400 g for 10 min at 4C.
7. The supernatant is aspirated using a long Pasteur pipette.
8. The supernatant is aspirated using a long Pasteur pipette.
9. The cell pellet is dispersed by pulling across the bench table perforation.
10. Resuspend the cells to about 10 mL in PBS+10%FBS.
11. Take 30 µL of cell suspension for cell counting. Add 15 µL to a hemocytometer.
12. Count all of the 4, 4x4 square arrays and average the number. The total number of cells are: Average cell count x 2 x 10 x 10^4 = Average cell count x $2*10^5$. Dilute and count again if the concentration is too high.
13. Centrifuge the tube at 400 g for 10 min at 4C.
14. Aspirate the supernatant using a long Pasteur pipette.
15. The cell pellet is dispersed by pulling the tube across the bench table perforation.
16. Resuspend the cells to 300 µL with PBS+10% FBS and aliquot to three FACS tubes labeled "Blank – DC", "Ab - DC" and "Isotype - DC". Add 100 µL of cell suspension to each.
17. Add:
    a. "Blank - DC":
        i. Nothing
    b. "Ab-DC":
        i. 20 µL of FITC Anti-CD3
        ii. 5 µL of APC-CD83
    c. "Isotype control":
        i. 20 µL FITC IgG2a control
        ii. 20 µL APC-IgG1γ control
18. Incubate the cells for 30 min in the fridge.
19. After incubating with antibodies, wash the cells by adding 3 mL of PBS+0.1% NaN_3 and spin down to pellets at 400g for 5 min.
20. Remove supernatant, re-suspend the pellets by vortexing and repeat step 2.
21. Remove supernatant, re-suspend the pellets by vortexing and add 5 µL 7AAD to all tubes except the two blank tubes. Vortex.
22. Incubate tubes for 10 min in the fridge.
23. Add 300 µL of PBS+0.1% NaN_3 to the tubes and analyze with flow cytometry.

A.5 Protocol for DC generation on chip

Protocol: **Production of human dendritic cells (DCs) from peripheral blood mononuclear cells (PBMCs) in a microscope slide chamber**	Revision date: 19-05-2014
Author: Thor Christian Hobæk	Version no: 10

Apparatus:
2 microscope slide chips with female Luer connectors
50 mL centrifuge tubes
2x40 mL culture flasks
Masterflex L/S peristaltic pump
Masterflex PharMed BPT Tubing, L/S #13 (ID = 0.8 mm)
PEEK tubing, ID = 0.5 mm, OD = 1.6 mm (idex)
BD Connecta T-junction with extension tubing (#394982)
1 mL syringes
Centrifuge bottle cap with 3x Ø=1.5mm drilled holes.

Reagents:
Frozen PBMCs from Herlev Hospital stored at -140 °C
X-VIVO 15 medium with phenol red and gentamicin, Cambrex PN BE04-418Q
Glutamin 100x stock concentration (200 mM)
Human AB serum, Herlev Hospital
GM-CSF, CellGenix (35 µL per vial, corresponds to 35 mL medium)
TNF-α, CellGenix (35 µL per vial, corresponds to 35 mL medium)
IL-1β, CellGenix (35 µL per vial, corresponds to 35 mL medium)
IL-4, CellGenix (35 µL per vial, corresponds to 35 mL medium)
IL-6, CellGenix (35 µL per vial, corresponds to 35 mL medium)
PGE-2 (175 µL per vial, corresponds to 17.5 mL medium)
Di-sodium EDTA, Na-EDTA
1x Dulbecco's Phosphate Buffered Saline (dPBS)
Fetal Bovine Serum (FBS)
FITC Mouse Anti-Human CD3, BD Pharmingen 561802
FITC Mouse IgG2a, k Isotype Control, BD Pharmingen 555573
PE Mouse Anti-Human CD14, BD Biosciences 555398
PE Mouse IgG2a, k Isotype Control, BD Pharmingen 555574
APC Mouse Anti-Human CD83, HB15e, BD Pharmingen 551073
APC Mouse IgG1, k Isotype Control, MOPC-21, BD Pharmingen 555751
7AAD, BD Pharmingen 559925

Wash medium (WM):
100% X-VIVO 15 with phenol red and gentamicin

Culture medium (CM):
97% X-VIVO 15 with phenol red and gentamicin
2% Human AB serum
1% Glutamin (200 µM)

Culture medium with cytokines 1 (CM1)
97% X-VIVO 15 with phenol red and gentamicin
2% Human AB serum
1% Glutamin (200 µM)
1000 U/mL GM-CSF
250 U/mL IL-4

Culture medium with cytokines 2 (CM2)
97% X-VIVO 15 with phenol red and gentamicin
2% Human AB serum
1% Glutamin (200 µM)
1000 U/mL GM-CSF
250 U/mL IL-4

1000 U/mL IL-1β
1000 U/mL IL-6
1000 U/mL TNF-α
1 µg/mL PGE-2

FACS buffer:
90% 1x dPBS without Ca^{2+} and Mg^{2+}
10% FBS
0.1% NaN_3

Cell harvesting buffer:
99,4% 1x dPBS without Ca^{2+} and Mg^{2+}
0,6% Di-sodium EDTA (15mM)

Overview:

Day -1 (1h): Sterilize medium reservoir and tubings
Prepare WM and CM and allow it to equilibrate with 5% CO_2 at 37 °C overnight to avoid bubbles
Prepare waterbath for medium reservoir and microscope incubator downstairs
Day 0 (6h): Assemble tubings and prime tubings with WM
Seed peripheral blood mononuclear cells (PBMCs) into chip
Wash out non-adherent cells
Start periodic perfusion culture
Analyse cells before seeding and non-adherent cells with flow cytometer
Day 1-4: Refill waterbath and cell incubator with DI water and monitor the CO2-level and look out for bubbles in chip.
Prepare CM2 and allow it to equilibrate with 5% CO_2 at 37 °C overnight to avoid bubbles
Day 5 (0.5h): Change from CM1 to CM2 and continue periodic perfusion culture
Day 7 (3h): Harvest dendritic cells (DCs) by flushing with EDTA in PBS and analyze cells with flow cytometer.

Day -1 (1 day prior to start of culture, requires 1h)

Sterilization of equipment

Needed:
50 mL centrifuge tube with 3xØ1.5 mm holes drilled in the cap
1x silicone tubing (ID=0.5mm, OD=2.1mm) inserted through the Ø1.5mm hole
4 segments of PEEK tubing (ID=0.5mm, OD=1.6mm)
1 segment of Masterflex PharMed BPT Tubing, L/S #13 (ID = 0.8 mm)
5x blue ferrules (Tefzel ETFE for OD=1.6 mm tubing)
5x blue nuts (Delrin Acetal for OD=1.6 mm tubing)
3x 1/4"-28 flat bottom female thread to male luer lock adapter (Tefzel Polyprop)
2x 1/4"-28 flat bottom female thread to female luer lock adapter (Tefzel Polyprop)
2x barbed male luer lock connectors for ID=0.8mm tubings
Autoclavable 0.22 µm Ø=15mm sterile filter

1. Flush all used tubings with at least 5 mL virkon, followed by at least 5 mL MilliQ, using the peristaltic pump or a syringe connected to the 3-way stopcock valve.
2. Label a 50 mL centrifuge tube with "WM", remove the cap and put the old cap with througholes on.
3. The end of the outlet tubing are placed inside the 50 mL centrifuge tubes through one of the holes, and an autoclavable sterile filter is connected to the silicone tubing on the inside of the cap, through the male luer lock connector.
4. Throw out the old 3-way stopcock valve, and separate the flexible peristaltic pump tubing from the barbed luer-lock adapters (otherwise the inside of the peristaltic tube end will be expanded during autoclaving and will fit poorly afterwards).
5. The equipment to be autoclaved should be disassembled as they appear on the pictures below before autoclaving.
6. After autoclaving, the equipment is dried in an oven at 50 °C.

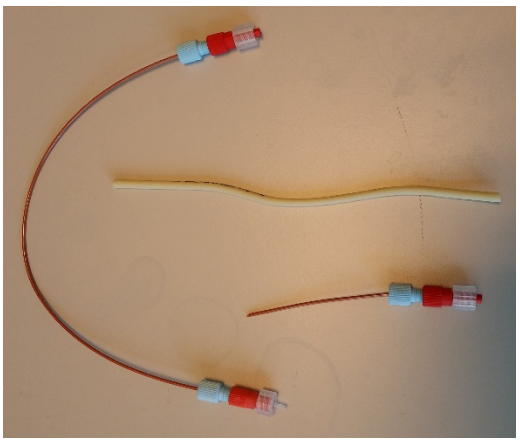

Short segments of the outlet tubes

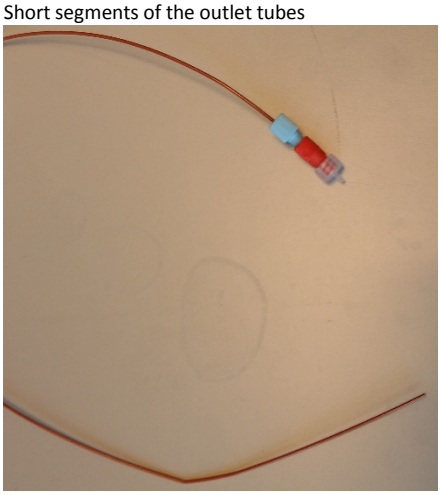

Outlet tube

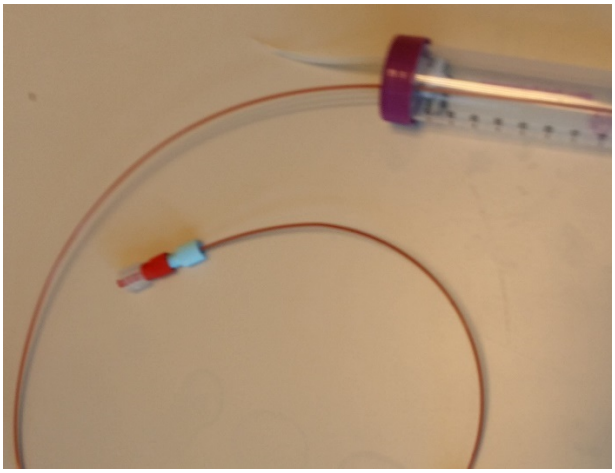

Inlet tube with end fitted through holes in the bottle cap. A sterile filter is fitted inside the centrifuge tube

Preparation of culture medium (15 ml in total; cytokines not added here)

Needed: X-vivo 15 with phenol red and gentamicin (cell lab fridge)
Human AB serum (cell lab freezer, bottom rack)
Glutamin (cell lab freezer, bottom rack)
Tissue culture flask, 40 ml, blue cap

1. Prepare 15 ml of CM and transfer to a sterile tissue culture flask. Label "CM". The flask is placed in the incubator (37˚C, 5% CO_2) overnight to equilibrate.

Preparation of wash medium (25 mL in total)

Needed: X-vivo 15 with phenol red and gentamicin (cell lab fridge)
Tissue culture flask, 40 ml, blue cap

1. Fill the flask with 25 mL WM.
2. The flask is placed in the incubator (37˚C, 5% CO_2) overnight to equilibrate.

Preparation of incubator and waterbath

Needed: DI water

1. Fill the waterbath up to the rim with DI water. Add a sanitizing pill and set temperature to 40 °C and turn on heating.
2. Turn on incubator heating (setpoint = 44 °C). Add more water to the tank and humidifying column.
3. Adjust gas mixer control unit so that the air pressure is 0.95 bar and the CO_2 pressure is 0.05 bar, by adjusting the screws.
4. If point 3 cannot be done, check that the air valve mounted on the wall is opened, and that the pressure regulator is set to 2 bars. Check that the valve on the CO_2 flask is open.

Day 0 (day for start of culture; requires 6h):

Mounting tubings and reservoir

Needed: DI water
50 mL sterilized centrifuge tube with 3xØ1.5 mm holes drilled in the cap
Sterilized tubings
Tissue culture flask with equilibrated wash medium
5 mL PBS+10% FBS+0.1% NaN_3
70% ethanol
Parafilm
Scalpel

1. Refill the two waterbaths with DI water.
2. Two 50 mL centrifuge tubes are numbered; tube 1 and 2 is filled with 15 mL WM and placed in a 37 °C water bath.
3. Prepare 5 mL PBS+10% FBS+0.1% NaN_3 if there is not already some available.
4. Bring the autoclaved tubings into the sterile bench.
5. Attach the two luer lock adaptors with barbed end firmly into the peristaltic pump tubing
6. Make sure all luer adaptors (blue and red) are fitted tightly
7. Cut off the extension tube of the T-junction (BD connecta) with a scalpel, but leave around 10 mm of tubing close to the valve (1→2 in the pictures below).
8. Take the shortest PEEK tubing and press the sharp end inside the remaining extension tube, until it is firmly attached. Attach the outlet tubing to the luer connector on the other side of the valve (3).
9. Wipe a piece of parafilm tape with 70% ethanol and wrap around the bottle cap.
10. Wrap the luer-lock connector ends of the inlet and outlet tubings with sterilized parafilm tape.
11. Take out the tissue culture flask with WM from the incubator and place in the flow bench. Transfer the contents to the sterilized centrifuge tube.
12. Bring the WM and the tubings down to the basement
13. Place the WM tube in the waterbath. Insert the silicone tubing into the hole of the humidifying chamber (above the water meniscus).
14. Attach the outlet tubing to the peristaltic pump, by fixing the flexible part of the tubing to the pump head.
15. Label a 50 mL centrifuge tube with “Non-adherent cells” and place in the rack.
16. Place the inlet tube end (without luer lock adapter) inside the non-adherent centrifuge tube and seal with a parafilm around the opening.
17. Attach both Luer connectors at the inlet and outlet end to the chip and make sure it’s tight.

1

2

3

Cell thawing and washing

Needed: At least $6*10^7$ PBMCs per chip (-140 C freezer)
15 mL WM at 37˚C

1 mL culture medium at 37˚C

19. The vials of frozen PBMCs are taken from the -140C freezer and thawed for the shortest time possible in the water bath.
20. Add warm WM dropwise to the cryotube from centrifuge tube 1, and transfer the entire content to the centrifuge tube 1.
21. When all cells has been thawed, centrifuge the tube at 400g for 10 min at room temperature.
22. Prepare a hemocytometer for cell counting.
23. Add 30 µL PBS to a 600 µL PCR tube
24. After the cells has been spinned down, the supernatant is aspirated using a long Pasteur pipette.
25. The cell pellet is dispersed by pulling across the bench table perforation.
26. 15 mL are transferred carefully from CM2. The cells are dispersed by dispensing and sucking using a pipette, with the pipette tip close to the bottom of the centrifuge tube.
27. Pipette out 10 µL of the cell suspension and add to the 600 µL PCR tube. Vortex and add 15 µL to a hemocytometer.
28. Centrifuge the tube at 400g for 10 min at room temperature.
29. Count all of the 4, 4x4 square arrays and average the number. The total number of cells are: Average cell count x 4 (dilution) x 15 mL x 10^4 cells/mL = Average cell count x $6*10^5$ cells.
30. The supernatant is aspirated using a long Pasteur pipette.
31. The cell pellet is dispersed by pulling across the bench table perforation.
32. Resuspend the cells to about $7*10^6$ cells/mL or to minimum 0.5 mL of CM per chip. Disperse the cells using a pipette and transfer to an Eppendorf tube.
33. Pipette out $3*10^6$ cells and aliquot equally to three blue FACS tubes. Suspend the cells with FACS buffer to a total volume of 100 µL in each tube.
34. Label the three FACS tubes with “1”, “2” and “3” and store them in the fridge

Cell seeding and Flow cytometer analysis

Needed:
25 mL WM at 37C
15 mL culture medium with cytokines (CM1) at 37C
15 µL GM-CSF
15 µL IL-4
FITC Mouse Anti-Human CD3
PE Mouse Anti-Human CD14
FITC Mouse IgG2a, k Isotype Control
PE Mouse IgG2a, k Isotype Control
7AAD
2x15 mL centrifuge tubes
1 mL syringe
Water bath at 40C
40 mL FACS buffer (PBS + 10% FBS + 0,1% NaN_3)

16. Bring the Eppendorf tube with cells down to the basement.
17. Prime the outlet tubing by pumping WM through (clockwise ↻) until the medium reaches past the T-junction, when the pump is stopped.
18. Transfer at least 500 µL cell suspension to a 1 mL syringe fitted with an 18G needle without bevel. Suck until air is drawn into the syringe. Remove any bubbles in the syringe by knocking with your finger and remove the needle. Slowly inject until cell suspension is coming out.
19. Attach the syringe to the T-junction valve
20. While tilting the chip so that the inlet end is lifted higher than the outlet, slowly inject the cells without introducing bubbles. It might be necessary to pull the liquid back into the syringe to achieve this. Close off the injection port with the valve after injection.
21. Remove the syringe. Dried up any spilled medium and wipe the outside of the chips with 70% EtOH.
22. Place the chips on top of the glass slide and use the clamps to fix it to the incubator.
23. Incubate the chips at 37 °C for 60 min.
24. While incubating, add the stage positions to take images for the timelapse study.
25. Capture one image of all positions.
26. Get one vial each of GM-CSF (15 µL or 35 µL) and IL-4 (35 µL) from the -140C freezer in the waterbath. 15 µL of each cytokine solution is added to the flask with culture medium and mixed thoroughly. Store the vials with the remaining cytokines at 4 °C for up to 1 week.
27. Transfer the culture medium to a 50 mL centrifuge tube and bring down to the basement and place in the waterbath.

28. Inspect the chip and the T-junction for bubbles
29. Remove the non-adherent cells in the chip by pumping at 2 mL/min for 10 min (clockwise: ↻)
30. After sorting, remove the WM flask, and replace with the CM flask, keeping the same cap. Avoid touching the tubings and tighten the cap firmly.
31. Change the flow direction to counterclockwise (↺) pump briefly in that direction to remove bubbles in outlet tube end.
32. Change the flow direction again to clockwise direction (↻) and replace the WM inside the tubings by pumping CM at 1 mL/min for 3 min. Watch out for bubbles.
33. Remove the inlet tube from the non-adherent centrifuge tube and wipe off the tube end with 70% ethanol. Insert the tube end into the open hole in the reservoir with CM1.
34. Briefly run the pump in the clockwise direction (↻) to remove any bubbles in the inlet tube end.
35. Change the flow direction to counterclockwise (↺).
36. Set the peristaltic pump to time disp. mode. The pump rate should be 80 µL/min. The ON time should be 5 min and the OFF time should be 25 min. Start pumping.
37. Start the microscope timelapse series.
38. Bring the tube with the non-adherent cells upstairs to the cell lab.
39. Vortex the tube with the non-adherent cells and transfer 15 µL of the cell suspension to a hemocytometer.
40. Spin down the non-adherent cells to a pellet by centrifugation at 400g for 10 min.
41. Count all of the 4, 4x4 square arrays and average the number. The total number of cells are: Average cell count x 23 mL x 10^4 cells/mL = Average cell count x $2.3*10^5$ cells
42. After the non-adherent cells have been spun down, aspirate the supernatant using a long Pasteur pipette.
43. The cell pellet is dispersed by pulling the tube across the bench table perforation.
44. Resuspend in 300 µL FACS buffer and aliquout 100 µL into three FACS tubes labelled “4”, “5” and”6”.

Flow cytometry

7. Add to the FACS tubes, vortex and incubate for 30 min in the fridge:
    1. “1” and “4”:
        i. Nothing (blank control)
    2. “2” and “5”:
        i. 20 µL of PE Anti-CD14
        ii. 20 µL of FITC Anti-CD3
    3. “3” and “6”:
        i. 20 µL PE IgG2a control
        ii. 20 µL of FITC IgG2a control
8. After incubating with antibodies, wash the cells by adding 3 mL of PBS and spin down to pellets at 400g for 5 min.
9. Remove supernatant, re-suspend the pellets by vortexing and repeat step 2.
10. Remove supernatant, re-suspend the pellets by vortexing and add 5 µL 7AAD to all tubes except the two blank tubes(“1” and “4”). Vortex and make sure the pellets are dispersed.
11. Incubate tubes for 10 min in the fridge.
12. Add 300 µL of PBS to the tubes and analyze with flow cytometry using the panel called “PBMCs”.

Day 4 (requires 15 min):

1. Prepare 15 ml of culture medium and transfer to a culture flask. Label “CM2”. The flask is placed in the incubator (37˚C, 5% CO_2) overnight (cap should not be completely sealed to allow gas exchange).

Day 5 (requires 30 min):

Needed: 15 mL of culture medium (CM) equilibrated in the cell incubator

5. Prepare 15 mL of culture medium 2 , by adding to the culture flask:
    a. 15 µL GM-CSF (1000 U/mL)
    b. 15 µL IL-4 (250 U/mL)
    c. 15 µL IL-1β (1000 U/mL)
    d. 15 µL TNF-α (1000 U/mL)
    e. 15 µL IL-6 (1000 U/mL)
    f. 150 µL PGE-2 (1 µg/mL).
6. Transfer the contents to a 50 mL centrifuge tube
7. Transfer the bottle down to the basement
8. Pause the pump.
9. Change the CM1 bottle to CM2 bottle, keeping the same cap, without touching the tubings hanging from the bottle cap.

10. Remove the outlet tube end from the reservoir and place in a 50 mL waste reservoir. Seal the opening with parafilm.
11. Briefly run the pump in the clockwise direction (↻) to remove any bubbles in the inlet tube end.
12. Change the flow direction to counterclockwise (↺). Change the flowrate to 300 µL/min and pump for 10 min.
13. Wipe the outlet tube end with ethanol and place back in the medium reservoir through the open hole.
14. Change flowrate back to 80 µL/min and start pumping in time disp. Mode. The ON time should be 5 min and the OFF time should be 25 min.

Day 7 (requires 3h):

Needed:
- 50 mL centrifuge tubes
- 45 mL cold 0.6% Na-EDTA in PBS
- 20 mL FACS buffer
- FITC Mouse Anti-Human CD3
- PE Mouse Anti-Human CD14
- APC Mouse Anti-Human CD83
- 7AAD
- FITC IgG2a isotype control
- PE IgG2a isotype control
- APC IgG1γ isotype control
- dPBS
- 3 FACS tubes

24. Turn off the chip incubators.
25. Place a 50 mL centrifuge tube filled with 45 mL frozen 0.6% Na-EDTA in PBS in the waterbath in the basement.
26. Transfer the outlet tube end into the EDTA-buffer solution.
27. Transfer the end of the inlet tube into a clean 50 mL centrifuge tube. Seal off with parafilm.
28. Briefly run the pump in the counterclockwise direction (↻) to remove any bubbles in the outlet tube end.
29. Start the pump in the clockwise direction (↻) at 1 mL/min for 3 min.
30. Incubate for 30 min with EDTA-buffer inside the chips.
31. Pump at 12.5 mL/min for 3 min and take snapshot at all positions.
32. Remove the waste tube and centrifuge the tube with harvested cells at 400g for 10 min at 4 °C.
33. The supernatant is aspirated using a long Pasteur pipette.
34. 200 µL of cold FACS staining buffer is added to the pellet from the centrifuge tube, and the cells are dispersed by pulling across the bench table perforation.
35. Resuspend the cells to about 5 mL in FACS buffer.
36. Take out 30 µL of the cell suspension and add to the 600 µL PCR tube. Vortex and add 15 µL to a hemocytometer.
37. Count all of the 4, 4x4 square arrays and average the number. The total number of cells are: Average cell count x 1 (dilution) x 5 mL x 10^4 cells/mL = Average cell count x $5*10^4$ cells.
38. If the count is too high, dilute and count again.
39. Centrifuge at 400g for 10 min at 4 °C.
40. Resuspend in 300 µL FACS buffer and aliquout 100 µL into three FACS tubes
41. Add:
    a. Blank (unstained)
    b. Antibodies
        i. 20 µL FITC Mouse Anti-Human CD14
        ii. 20 µL APC Mouse Anti-Human CD83
    c. Isotype control
        i. 20 µL PE Mouse IgG2a, k Isotype Control
        ii. 20 µL APC Mouse IgG1, k Isotype Control
42. After incubating with antibodies for 30 min, wash the cells 2x by adding 3 mL of PBS and spin down to pellets at 400g for 5 min.
43. Remove supernatant, re-suspend the pellets by vortexing and add 5 µL 7AAD to tube 2 and 3. Vortex.
44. Incubate tubes for 10 min in the fridge.
45. Add 300 µL of PBS to the tubes and analyze with flow cytometry. Use the panel called “DCs”

Appendix B:

Paper I

One-Step Immobilization of Functionally Active Antibodies in Thermoplastics by Injection Molding

Thor Christian Hobæk, Henrik J. Pranov, Niels B. Larsen
Submitted to Analytical Chemistry, July 31, 2014

One-step immobilization of functionally active antibodies in thermoplastics by injection molding

Journal:	*Analytical Chemistry*
Manuscript ID:	ac-2014-02866w
Manuscript Type:	Article
Date Submitted by the Author:	31-Jul-2014
Complete List of Authors:	Hobæk, Thor; DTU-Nanotech, Pranov, Henrik; InMold Biosystems, Larsen, Niels; DTU-Nanotech,

One-step Immobilization of Functionally Active Antibodies in Thermoplastics by Injection Molding

Thor Christian Hobæk[†], *Henrik J. Pranov*[‡], *Niels B. Larsen**[†]

[†] Department of Micro- and Nanotechnology, Technical University of Denmark, Ørsteds Plads 345E, 2800 Kgs. Lyngby, Denmark

[‡] InMold Biosystems, Diplomvej 381, 2800 Kgs. Lyngby, Denmark

We demonstrate the transfer of functional antibodies from a mold surface to thermoplastic replicas using injection molding in a process compatible with mass production of single-use devices for molecular analysis and cell culture. The transfer process is highly efficient, as verified by atomic force microscopy (AFM) and x-ray photoelectron spectroscopy (XPS) of the mold and replica surfaces. Injection molded rabbit anti-mouse IgG showed similar affinity for mouse IgG in sandwich enzyme-linked immunosorbent assay (ELISA) as capture antibodies deposited by passive adsorption to bare thermoplastic replica. Short antibody deposition times of 10 min are shown to be sufficient for producing highly sensitive ELISA assay. The transferred proteins are stable during incubation in serum-containing cell medium for >1 week. Injection molding, being the industrially preferred method for polymer shaping, may now simultaneously shape and integrate antibodies on the polymer surface simultaneously, making this a highly promising method for mass-fabrication of point-of-care or cell-capture lab-on-a-chip devices.

Introduction

Immobilization of proteins to solid substrates is of great importance for various applications, such as protein microarrays for proteomics[1], development of personalized drugs[2] and point-of-care diagnostics[3], immunoassays such as the enzyme-linked immunosorbent assay (ELISA)[4], and sorting of cells through surface antigen-recognition[5,6]. Most biochips employing covalent protein immobilization are made from materials such as glass or silicon[7,8]. However, there is an increasing interest in using industrially moldable polymers for the production of miniaturized lab-on-a-chip devices, not only due to lower raw material costs but also due to lower production time and cost[9]. This is especially important for clinical applications that require disposable devices to eliminate the risk of sample contamination[10]. Injection molding has been the most industrially relevant fabrication method of polymers for decades, and has also gained attention as a production technology for microfluidic devices during the last years[11]. It is a rapid replication technique with cycle times from 1-30 s, which involves heating of a thermoplastic polymer to >250 °C followed by injection of the polymer melt into a closed mold maintained below the polymer glass transition temperature (T_g) where the polymer subsequently solidifies in its final shape. Popular thermoplastic materials for life science applications include polystyrene (PS), polypropylene (PP), polycarbonate (PC), poly(methyl methacrylate) (PMMA), and cyclic olefin copolymers (COC). All these polymers are fairly chemically inert in their native form thus calling for chemical activation steps prior to covalent binding of proteins[12]. This can be done by introducing functional groups on the surface like epoxy or amines by photoactivation[13–15], by forming functionalized polymer adlayers[16,17] prior to protein linkage, or by direct photoimmobilization of proteins using a photoinitiator[18]. However, these methods inevitably add extra steps to a production line, increasing both time and cost.

An untraditional approach for antibody immobilization is the direct entrapment of the protein on a polymer surface during molding, where pre-adsorbed proteins on a mold surface are transferred to the polymer replica during shaping. This has previously been demonstrated with poly(dimethylsiloxane) (PDMS)[19,20], which in liquid form is cast on an antibody-coated poly(tetrafluoroethylene) (PTFE) mold followed by thermal curing and separation of the replica. PDMS is the preferred prototyping material for lab-on-a-chip devices[21] based on a facile molding process. However, it has numerous limitations compared to thermoplastics, such as high bulk absorption of hydrophobic compounds from solution[22], leaching of uncrosslinked polymer chains into solution[23], hydrophobic recovery[24], and very long curing times of hours to days at elevated temperatures. We have previously reported on a similar approach based on fast injection molding of PMMA and PP to achieve simultaneous topography replication and pattern transfer of horseradish peroxidase (HRP), fibronectin and avidin with some retained biochemical activity[25]. With this method, no prior functionalization of the polymer replicas is required, allowing for complete process cycle times down to 30 s in a fully automated setup.

Here, we demonstrate the transfer of functionally active antibodies, specifically anti-mouse IgG, from the mold surface to a COC replica by injection molding, using the same approach. We demonstrate a highly efficient transfer procedure mediated by an anti-stiction coating on the mold surface, as well as retained antigen-binding affinity of the transferred antibody at a level equal to that of antibodies deposited on the polymer surface by conventional passive adsorption.

Materials and Methods

Materials

Dulbecco's Phosphate Buffered Saline (dPBS, D8537), Dulbecco's Modified Eagle's Medium (DMEM, D5030), IgG from mouse serum (I5381), anti-mouse IgG (whole molecule) antibody produced in rabbit (M7023), bovine serum albumin essentially IgG free (BSA; ≤25 ng IgG/mg BSA, A9085), fetal bovine serum (FBS, F2442), penicillin/streptomycin (P/S, P4333), and 3,3',5,5'-tetramethylbenzidine (TMB) liquid substrate system for ELISA (T0440) were purchased from Sigma Aldrich (St. Louis, MO). Rabbit anti-mouse IgG antibody conjugated with horseradish peroxidase (HRP) (P0260) was purchased from Dako (Glostrup, Denmark). All water used was purified with a Millipore MilliQ system (Boston, MA). The blocking buffer consisted of 0.05 % v/v Tween 20 (Merck-Schuchardt, Hohenbrunn, Germany) and 0.1% w/v BSA in 1x dPBS. The wash buffer consisted of 0.05% v/v Tween 20 in 1x dPBS. The colorimetric reaction was stopped by addition of 0.5 M H_2SO_4 in MilliQ water. Protein stability tests used an incubation buffer of 10% v/v FBS and 100 U/mL (P/S) in DMEM. All incubation steps were done at room temperature (25 °C) unless otherwise stated. 12-well removable silicone chambers (81201) and 8-well sticky-slide chambers (80828) was purchased from ibidi (Martinsried, Germany). Nunc 96-well polystyrene plates (260860) were acquired from Fischer Scientific (Roskilde, Denmark). For injection molding, TOPAS ® 8007-S04 (COC) was purchased from Topas Advanced Polymers (Frankfurt-Höchst, Germany) and shims of electroplated nickel (300 µm thickness) were obtained from DVD Norden (Sakskøbing, Denmark).

Surface Modification of Nickel Mold Inlays

Mold inlays in the format of electroplated nickel shims were used as mold substrates for the protein transfer. To improve protein transfer, a tri-layered "anti-stiction" coating was applied on the surface of the inlays by initial atomic layer deposition (ALD, PICOSUN R-150, Picosun Oy, Espoo, Finland) of 5 nm Al_2O_3 and 5 nm SiO_2, followed by molecular vapor deposition (MVD, MVD 100, Applied Microsystems Inc., San Jose, USA) of a monolayer of heptadecafluoro-1,1,2,2-tetrahydrodecyltrichlorosilane (FDTS) using a previously described process[26]. The mold inlay surfaces were cleaned between each protein transfer cycle by plasma treatment (200 sccm O_2, 250 W, 300 s; MVD 100, Applied Microsystems Inc., San Jose, USA) and subsequent reapplication of the FDTS-coating using MVD, unless otherwise stated.

InMold Transfer of Capture Antibodies

Rabbit anti-mouse IgG was deposited by passive adsorption on the FDTS-coated mold inlays by dispensing a solution of 10 µg/mL protein in dPBS for 10 or 60 min as specified. Excess protein and salt from the buffer were removed by immersing the molds in 30 mL MilliQ water for 1 min, before the inlay surfaces were dried with a pressurized air gun. The protein-coated mold inlays were immediately installed in a commercial injection molding machine (VC 80/45, Engel, Schwertberg, Austria). Polymer replicas in the microscope slide format were made by injecting COC at a melt temperature of 250 °C and a volumetric injection speed of 43 cm^3/s into the mold cavity that was maintained at a constant temperature of 20 °C. The replicas with transferred protein were kept in a sealed zip-lock bag in a refrigerator at 4 °C until analysis by ELISA.

Characterization of Transfer Efficiency by Surface Analysis

The mold inlay surface before protein deposition, after protein deposition, and after protein transfer by injection molding, as well as the surface of the polymer replicas with and without

transferred proteins were characterized by atomic force microscopy (AFM, XE-100, Park Systems, Korea) using BudgetSensor-300 cantilevers operated in intermittent contact mode. The recorded micrographs were adjusted with a plane fit at an average zero height. X-ray photoelectron spectroscopy (XPS) was performed with a K-Alpha spectrometer (Thermo Scientific, U.K.) using a 400 μm wide monochromatized Al K_α X-ray beam spot and analyzer pass energies of 50 and 200 eV for high resolution and survey spectra, respectively. Elemental composition analysis and deconvolution of C1s spectra were performed using the instrument manufacturer's Avantage software package. Contact angles of water, diiodomethane and benzyl alcohol on the mold inlay and COC replica surfaces were measured optically using an OCA 20 system (dataphysics, Germany). The surface energy with dispersive and polar components was calculated using the Owens-Wendt method[27].The advancing and receding contact angles were determined by the dynamic sessile drop method, through adding/removing liquid at 0.1 μL/s and calculating the average angle while the length of the contact line increased/decreased. At least 5 drops on different positions on each sample were measured.

ELISA with InMold Transferred Capture Antibody

A sandwich ELISA using the injection molded anti-mouse IgG antibody as capture antibody was used to assess the functionality of the immobilized protein. A 12-well silicone chamber was mounted on the polymer replica slides with transferred antibody, before adding 300 μL of blocking buffer to each well and incubating for 1 h. The excess solution was tapped out and 100 μL mouse IgG (antigen) in blocking buffer was added and incubated for 16 h at 4 °C. Each well was washed 6 x 3 min with washing buffer, and 100 μL 0.5 μg/mL rabbit anti-mouse IgG-HRP (detection antibody) in blocking buffer was added and incubated for 1 h. Afterwards, the same washing procedure was repeated followed by adding 100 μL TMB substrate and incubating for

10 min on a shaking table. 100 µL 0.5 M aqueous H_2SO_4 was added to stop the enzymatic reaction, and 100 µL supernatant was transferred from each well on the polymer replicas to a transparent 96 well PS plate. The absorbance was read at 450 nm using a Victor3 plate reader (Perkin Elmer, Santa Clara, USA). For comparison, capture antibody was deposited on uncoated polymer replica slides by passive adsorption from solution, using the same coating procedure and concentrations as for the mold inlays, before washing with MilliQ water, drying and mounting the silicone well chambers.

For the protein stability tests, a bottomless 8-well slide was attached to the polymer replicas by adhesive tape and 500 µL of DMEM with 10% v/v FBS and 100 U/mL P/S was added. The slides were incubated in a sealed bag for 9 days in the refrigerator at 4 °C, to minimize the risk of infection, before performing a sandwich ELISA as described. It should be noted that the slides with transferred proteins were stored in the dry state for 3 weeks at 4 °C before the stability tests were initiated.

Data Analysis and Curve Fitting

Quantitative data are reported as mean ± standard error of the mean (SEM) unless otherwise stated. Statistical significance was evaluated using Welch's t-test for two samples having possibly unequal variances[28].

The antigen standard curves were quantified using a Four Parameter Logistic (4PL) curve fit, $A = A_0 + (A_{max} - A_0)/\left(1 + \left(\frac{c}{EC_{50}}\right)^{\alpha}\right)$, where A is the measured absorbance, A_0 the absorbance at zero analyte concentration, A_{max} the saturation absorbance from the analyte, c the analyte concentration, EC_{50} the half maximum effective concentration, and α is the Hill curve steepness[29]. A limit of detection (LoD) for each assay was defined as the mean + 3× the standard deviation of the zero antigen well [30].

Results and Discussion

IgG is Transferred with High Efficiency from the Mold Inlay to the Polymer Replica

Efficient transfer of antibodies during the injection molding process is essential to produce replicas with biofunctionally active surfaces and to establish an automatable process sequence. Initial experiments compared IgG transfer from mold inlays of native hydrophilic nickel to inlays of nickel with a hydrophobic anti-stiction coating presenting a molecular layer of fluorocarbonsilane (FDTS) at the surface. Native nickel inlays resulted in markedly poorer transfer efficiency (data not shown). Thus, only FDTS-coated mold inlays were considered in the further work. Experiments proceeded by initial protein coating of the mold inlay from solution, insertion of the inlay in the mold cavity, and injection molding to produce the polymer replica. The transfer efficiency was evaluated qualitatively by atomic force microscopy (AFM) and contact angle analysis, and quantitatively by x-ray photoelectron spectroscopy (XPS) on both the mold inlay and replica surfaces.

Figure 1 (a + b) compare the topography of the mold inlay surface before and after protein transfer. Proteins on the inlay surface (**Figure 1**a) appear as surface protrusions (bright dots and lines) of an apparent width <50 nm, while the inlay surface after transfer (**Figure 1**b) shows a lower surface roughness and on a longer lateral length scale, indicating that most of the proteins were removed during transfer. **Figure 1** (c + d) compare the topography of polymer replicas molded against inlays with or without adsorbed protein. The surface roughness is clearly higher for the replica surface molded against an IgG-coated inlay (**Figure 1**d) than the replica from an uncoated inlay (**Figure 1**c). The topography of the replica with molded protein (**Figure 1**d) is similar in appearance to proteins adsorbed on the mold surface (**Figure 1**a), although the peak-

to-valley heights on the line profiles are slight smaller on the replica. The apparent height reduction of the transferred proteins is likely caused by partial embedding into the polymer support during molding.

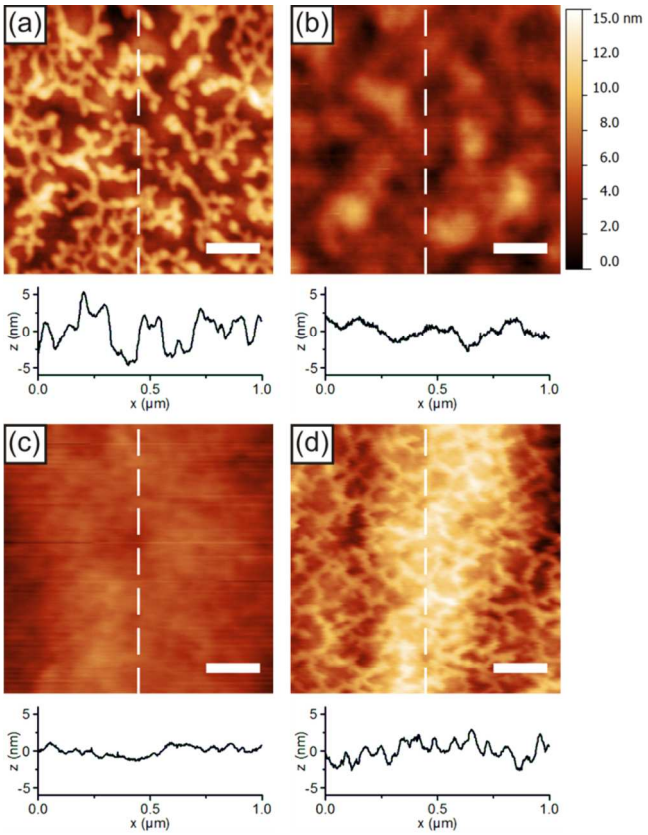

Figure 1. Adsorbed protein molecules are efficiently transferred to polymer replicas during injection molding, as visualized by AFM topography micrographs of the mold inlay surface and polymer replica surface with or without protein (IgG) coating. The height profiles are extracted along the stipulated lines in the micrographs. (a) IgG coated mold inlay surface prior to injection molding, and (b) after injection molding. (c) Polymer replica injection molded on an inlay without IgG coating or (d) with IgG coating. The height scale of all topography images is 15 nm. Scale bars are 200 nm.

XPS was employed to obtain quantitative information on the amount of proteins transferred, through analysis of the elemental composition of the mold surface before and after deposition of IgG, and after injection molding as well as of the polymer replicas with and without InMold transferred IgG (**Table 1**). The analysis showed an increase in carbon (21.4 vs. 11.4 atom%) and nitrogen (2.8 vs. <0.3 atom%) surface concentrations after IgG adsorption on the mold, as expected from the polyamide backbone of the proteins. After injection molding, the chemical composition is close to the initial values, with no detectable nitrogen (<0.3 atom%), a minor increase in the surface concentrations of carbon and fluorine, and a small decrease in the amount of oxygen. The signals from oxygen, fluorine, and silicon presumably originate from the FDTS monolayer and the underlying SiO_2 adhesion promoting layer on the mold inlay surface. Correspondingly, nitrogen and oxygen signals were detected on a COC polymer replica molded against an IgG-coated inlay but not on a COC (hydrocarbon) replica against an uncoated replica. The amount of adsorbed or transferred protein can be semi-quantitated by the nitrogen surface concentration. Similar concentrations were detected on the IgG-coated mold inlay (2.8 atom%) and on the polymer replica (3.6 atom%) in support of highly efficient protein transfer from the FDTS-coated inlay.

Table 1. Elemental composition, as determined by XPS, of mold and replica surfaces with or without protein (IgG) coating before or after injection molding. The values are the average of two measurement points on each sample. The detection limit is estimated to be 0.3 atom%.

	Elemental composition (atom%)				
	C	N	O	F	Si
Mold inlay surface (FDTS on SiO_2)	11.4	-	39.5	24.4	24.8
IgG-coated mold inlay	21.4	2.8	34.2	21.2	21.0
IgG-coated mold inlay after injection molding	11.9	-	38.6	24.7	24.8
Polymer replica from uncoated mold inlay	100	-	-	-	-
Polymer replica from IgG-coated mold inlay	90.7	3.6	5.3	-	-

High resolution XPS analysis of the carbon signals from the mold inlay surfaces supported the results of the elemental analysis (**Figure 2**). Peak contributions from the mold inlay surface components and from the adsorbed protein were extracted by curve fitting, and subsequently fitted in combination to C_{1s} spectra from the mold inlay in different process stages. Details of the peak fitting procedure are presented in the supporting information (**Figures S1** and **S2**). In brief, mold inlay peak contributions to the carbon spectra are from the fluorocarbon part of the FDTS monolayer at 294.2 eV (C^*F_3-) and 291.9 eV (-C^*F_2-) and from the two methylene units closest to the SiO_2 layer at 286.3 eV (-CH_2-C^*H_2-CF_2-) and 285.6 eV (-Si-C^*H_2-CH_2-), respectively. Adsorbed proteins are assigned to peaks at 288.4 eV, 286.6 eV, and 285.2 eV originating from the amide carbon (-NH-CR-C*(=O)-) in the protein backbone, the nitrogen-bound α-carbon (-NH-C*R-C(=O)-) in the backbone as well as oxygen- and nitrogen-bonded carbon in the side groups, and carbon-carbon bonds in the side groups, respectively. A strong increase in the

protein-associated peaks is evident after protein deposition, while contributions from these peaks are hardly detectable for the mold inlay surface after protein transfer.

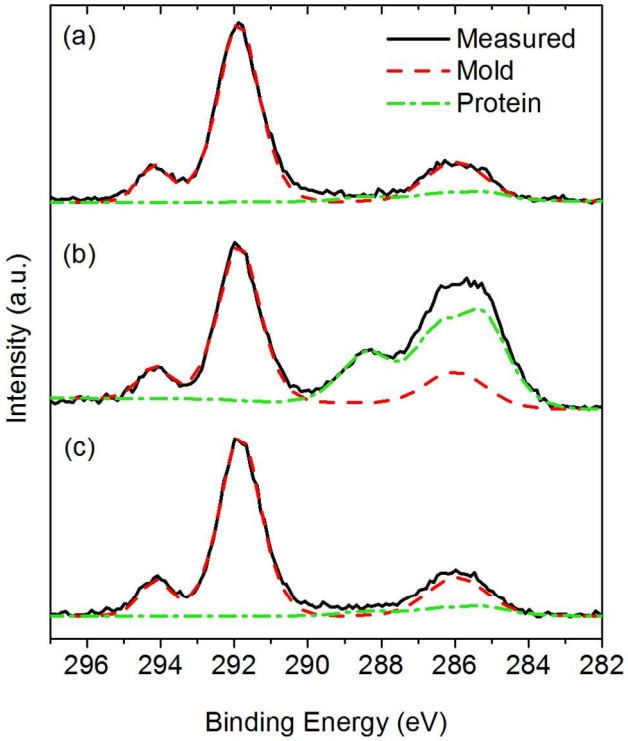

Figure 2. C1s high-resolution XPS spectra supports complete transfer of protein from the mold inlay during injection molding. (a) Mold inlay surface (FDTS on SiO_2) without proteins, (b) after protein deposition, and (c) after protein transfer to the polymer replica by injection molding. The photoelectron contributions from the mold inlay FDTS layer and the protein coating are fitted by the dashed and dash-dotted curves, respectively.

The transfer efficiency was additionally evaluated by contact angle measurements of water droplets on the mold inlays (**Figure 3**). The bare surface, i.e. FDTS-coated SiO_2, exhibited mean advancing and receding contact angles of 110.8 ± 0.6° and 96.2 ± 1.0° respectively. Additional contact angle analysis using diiodomethane and benzyl alcohol were performed (data not shown) to estimate the polar and dispersive components of the surface energy. The total

surface energy was 10.1 ± 0.1 mJ/m^2, with a polar component of 0.9 ± 0.1 mJ/m^2 and a dispersive component of 9.2 ± 0.2 mJ/m^2. Protein adsorption or transfer to a replica did not give rise to a significant change in the advancing water contact angle on the mold inlay, while the receding contact angle was significantly reduced ($p < 0.002$). After plasma treatment and re-coating of the inlay surface with FDTS, both the advancing and receding contact angles returned to their original values.

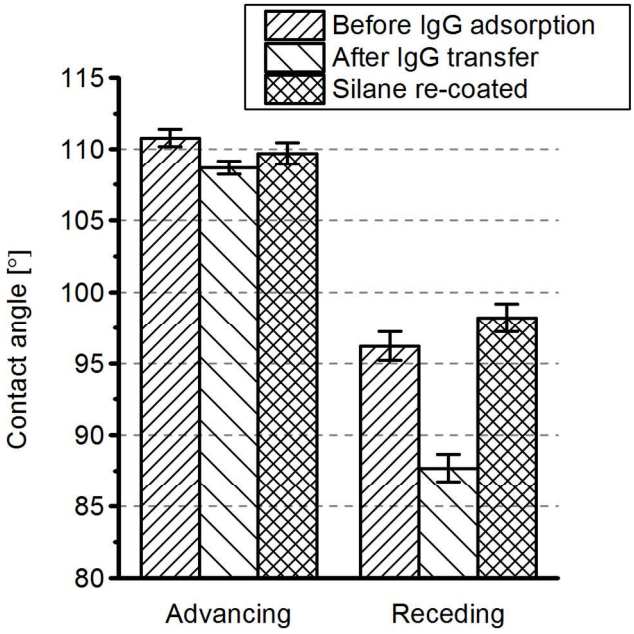

Figure 3. Advancing and receding water contact angles on mold inlay surfaces (FDTS-coated SiO_2) before adsorption of IgG, after IgG transfer to a polymer replica during injection molding, and after a new FDTS-coating is applied. Error bars show the SEM (n=3).

AFM and XPS revealed changes in topography and elemental composition associated with the presence of proteins on the surface of the InMold polymer replica. but there was no detectable difference between the mold inlay before and after transfer using either analysis method. However, we observed a small, significant decrease in the receding contact angle and a corresponding increase in the contact angle hysteresis on the mold after protein transfer (**Figure**

3). Heterogeneity in either topography or surface energy is well known to cause hysteresis, where the hydrophilic groups on a surface dictates the receding angle[31]. Introduction of hydrophilic groups by adsorbed proteins could therefore explain the apparent increase in contact angle hysteresis[32]. However, the lower receding contact angle could also be related to other types of surface in homogeneities, such as residual COC-polymer on the mold surface. In either case, the surface properties could be completely restored by plasma oxidation and subsequent vapor phase deposition of FDTS, suggesting that the molds inlays can be re-used after multiple subsequent protein transfers.

The results document a highly efficient transfer process that may be mediated by stronger interfacial interaction forces with the polymer than the mold surface and by partial or full embedding of the protein in the polymer melt leading to mechanical anchoring. FDTS is a highly non-polar molecule that has routinely been used as an anti-stiction coating on moving parts in microelectromechanical systems (MEMS)[33], as well as for improved separation of polymer replica and their molding surface in the format of stamps for nanoimprint lithography[34–38] or nickel inlays for injection molding[26,39–41]. Adsorbed proteins on the fluorinated surface are thus expected to interact mainly by weak van der Waals forces with their support. The olefinic COC polymer is also hydrophobic in its native form. However the measured the contact angle of water was 95.7° and the total surface energy was calculated to be 40.8 mJ/cm^2, with the dispersive component contributing to 99.5% of the total. Prior work on the transfer of proteins using microcontact-printing (μCP) concluded that successful pattern transfer depends on a lower water wettability of the printing surface than on the printed substrate[42]. Although the difference in water contact angle is small between the mold and the polymer, compared to what is usually reported between stamp and substrate for μCP, the transfer of antibodies might be facilitated by

the almost four times lower surface energy of the FDTS-coated mold. Another explanation for the efficient transfer could be partial embedding of the proteins into the polymer during injection molding, as suggested by the lower measured height variations on the replica with transferred protein than on the protein-coated mold inlay (**Figure 1**). Partial embedding would increase the protein-polymer interfacial area and therefore also the total interaction energy and additionally support partially mechanical anchoring of the protein in the polymer matrix, thus facilitating transfer of proteins from the low-binding mold inlay surface.

IgG Immobilized During Injection Molding Retains its Antigen-Binding Affinity

Antibodies are efficiently transferred from the mold surface to the polymer replica. However, for applications relying on biomolecular recognition such as immunoassays and cell panning, it is equally important to know how well the antibody retains its antigen-binding affinity after the injection molding process. We employed ELISA using an antibody as antigen to evaluate the biofunctional activity of the transferred IgG: sandwich ELISA analysis was performed on polymer replica slides with molded antibodies and compared to replica slides with antibodies deposited by passive adsorption from PBS. The antigen response curves, fitted with Four Parameter Logistic (4PL) curves in **Figure 4**, show no significant difference between the two methods of capture antibody immobilization for antigen concentrations below 100 ng/mL. The linear range was from 10-75 ng/mL, and the LoD was 0.30 ng/mL antigen for both immobilization methods. The EC_{50} values obtained from the curve fits were 27 and 21 ng/mL antigen for passive adsorption and transfer from mold inlay, respectively.

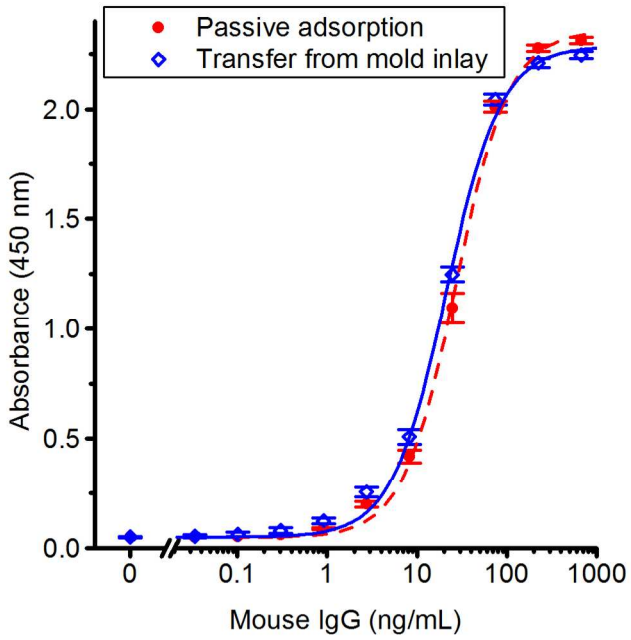

Figure 4. ELISA assays using antibodies immobilized during injection molding or by passive adsorption show equal sensitivity and response range. Standard curves for mouse IgG as antigen, comparing the antigen-binding capacity of capture antibodies adsorbed passively to a blank polymer replica surface to antibodies transferred from a mold inlay. The data points are fitted to a Four Parameter Logistic (4PL) curve. Error bars show the SEM (n=3 for passive adsorption; n=4 for transfer from mold inlay).

These results suggest that there is no apparent reduction of the antigen-affinity of the transferred capture antibodies related to the injection molding process. This might seem surprising as the proteins on the mold inlay are brought in contact with a polymer melt initially at 250 °C. Earlier differential scanning calorimetry (DSC) studies showed irreversible denaturation of the F_{ab}-domain of IgG above 61 °C at a heating rate of 0.5 °C/min, while a higher heating rate of 5 °C/min increased the denaturation temperature to 65 °C [43]. Thus, denaturation kinetics are clearly limiting the extent of irreversible function loss. The cooling rates of the polymer melt in

the immediate vicinity of the mold inlay metal surfaces has been suggested to exceed 10^4 °C/s [44] due to the high thermal conductivity of nickel, thereby only exposing the adsorbed protein to high temperatures for extremely short time periods. Indeed, modelling has predicted that the first nanometers of polymer melt at 270 °C brought in thermal contact with a metal mold surface maintained at 30 °C is cooled to 50 °C within 100 ns [25]. Molecular dynamics simulations predicted that the unfolding of a 61-residue α-helical protein at 225°C is on the order of tens of nanoseconds[45], although generally the protein folding speed limit increases with increasing number of residues in the polypeptide chain[46]. Similarly, prior experimental work demonstrated that peak temperatures of 290 °C are required to decrease the activity of horseradish peroxidase by 50% using multiple nanosecond laser pulses [47]. Antibodies transferred from the mold inlay during injection molding may therefore avoid irreversible loss of function due to the heating by the polymer melt and subsequent cooling by the cold mold being on a sufficiently short timescale to avoid permanent denaturation.

Short and Industrially Relevant Production Cycle Times Are Possible

Robot replacement of a number of insertable mold parts during production is a standard process technology, but long mold inlay incubation times would be a major challenge for viable automation and industrial application of the proposed technology as the required number of inlays would be large to sustain low process cycle times. We targeted an injection molding cycle time of 30 s using 20 replaceable mold inlays, thus calling for an individual inlay incubation time of 10 min in comparison to 60 min incubation used for the results presented in **Figure 4**. Antigen response curves using transferred antibodies with the two incubation times prior to injection molding are displayed in **Figure 5**. Replicas only showed significant differences in the response

curves between the two incubation times for antigen concentrations ≥75 ng/mL ($p = 0.04$). Since the amount of adsorbed capture antibody is likely lower at the shorter incubation time, the binding of antigens to the immobilized capture antibodies is expected saturate at lower antigen concentrations, resulting in a reduced absorbance at high antigen concentrations. Additionally, the uncertainty in the antigen-response is higher for the shorter incubation time, most notably seen most in the upper part of the sigmoidal curve, suggesting that the density of capture antibodies is less homogeneous. However, for applications where a lower detection range is targeted, the shorter incubation time does not affect the assay performance.

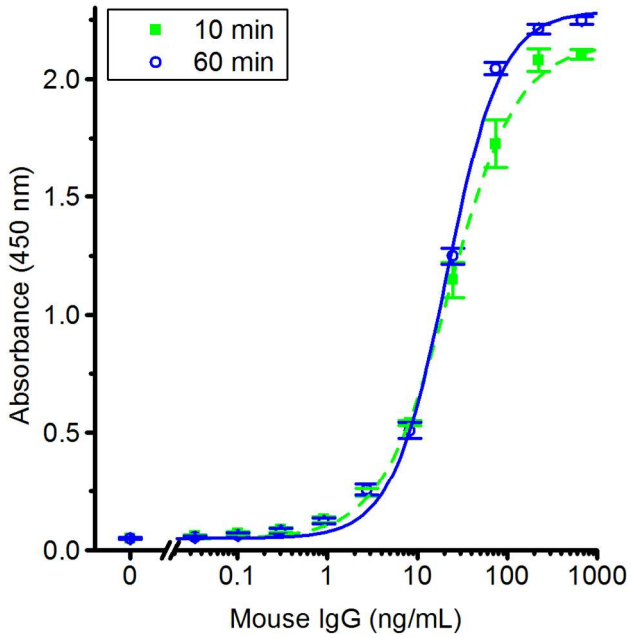

Figure 5. Highly sensitive ELSA assays can be produced by short incubation times prior to injection molding. Standard curves for mouse IgG comparing the effect of incubating the capture antibody on the mold inlay surface for 10 min and 60 min prior to transfer by injection molding. The data points are fitted by 4PL curves. Error bars shows the SEM (n=5 for 10 min; n=4 for 60 min).

Immobilized IgG is Stable in Cell Culture Medium for Weeks

We investigated the stability of the transferred antibodies over time by incubating the wells in DMEM with 10% v/v FBS and 1% P/S for 9 days at 4 °C. The reduced temperature was chosen to minimize the risk of bacterial growth. Subsequently, we washed the wells and performed a sandwich ELISA as described in the Materials and Methods Section. **Figure 6** shows that capture IgG transferred from mold inlays has a similar response as passively adsorbed capture IgG at antigen concentrations below 10 ng/mL and with equal limits of detection of 0.9 ng/mL. At higher antigen concentrations the response is significantly lower in magnitude ($p < 0.05$) while 4PL curve fitting yields similar EC_{50} values for both modes of capture antibody deposition (39 and 27 ng/mL for antibodies transferred during molding and passively adsorbed antibodies, respectively). It should be noted that the polymer slides with transferred capture IgG were stored in a dried state at 4 °C for 3 weeks before addition of medium, while slides with passively adsorbed capture IgG were analyzed immediately after protein deposition. The extended storage time of the transferred IgG may have reduced the protein activity.

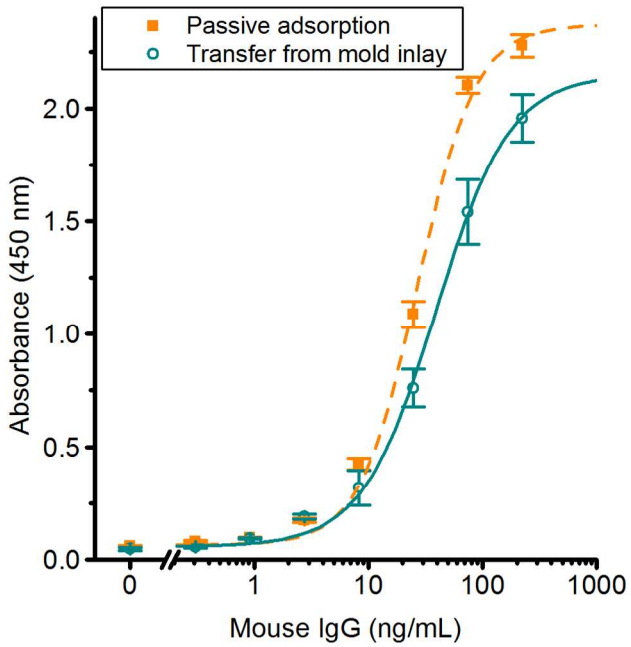

Figure 6. Antibodies transferred during injection molding retain their function in cell culture medium for >1 week. Standard curves for mouse IgG bound to capture antibody immobilized by passive adsorption or molded in the plastic, and stored for 9 days in DMEM + 10% v/v FBS + 1% P/S at 4 °C. Error bars show the SEM (n=3).

Conclusion

Antibodies passively adsorbed on a surface functionalized mold inlay surface can be transferred with a high efficiency to a COC replica slide by injection molding. Insignificant amounts of protein residuals remain on the mold surface after transfer, as verified by AFM and XPS, thus making multiple subsequent protein transfers using the same mold possible. The antigen-binding affinity of the transferred capture antibody is similar to that of antibodies adsorbed by passive adsorption directly on polymer surfaces, as verified by sandwich ELISA. In addition, short incubation times (10 min) of antibody solution on the mold surface prior to transfer results in fully satisfactory antigen response curves on replicas with transferred antibody.

Finally, antibodies transferred during injection molding retain their functionality after 3 weeks of dry storage followed by 9 days of immersion in standard serum-containing cell culture medium. Thus, direct immobilization of antibodies at polymer surface during injection molding is a promising approach for high-volume production of protein functionalized disposable polymer biochips for immunoassay or cell capture applications.

ASSOCIATED CONTENT

Supporting Information. Detailed description of the deconvolution of the XPS C1s spectra and survey spectra. This material is available free of charge via the Internet at http://pubs.acs.org.

AUTHOR INFORMATION

Corresponding Author

*E-mail: niels.b.larsen@nanotech.dtu.dk

Notes

Two of the authors (H.J.P and N.B.L) are co-inventors on a patent issued on the general technique of transferring heat-sensitive compounds from a molding surface to a polymer replica.

ACKNOWLEDGMENTS

The authors would like to thank Kenneth Brian Haugshøj from the Danish Technological Institute (DTI) for coating the nickel molds with ALD. This work was supported by the Danish Council for Strategic Research through the Strategic Research Center PolyNano (grant no 10-092322/DSF).

REFERENCES

(1) LaBaer, J.; Ramachandran, N. *Curr. Opin. Chem. Biol.* **2005**, *9*, 14–19.

(2) Liotta, L. A; Espina, V.; Mehta, A. I.; Calvert, V.; Rosenblatt, K.; Geho, D.; Munson, P. J.; Young, L.; Wulfkuhle, J.; Petricoin, E. F. *Cancer Cell* **2003**, *3*, 317–325.

(3) Petrik, J. *Transfus. Med.* **2006**, *16*, 233–247.

(4) Engvall, E.; Perlmann, P. *Immunochemistry* **1971**, *8*, 871–874.

(5) Belov, L.; Vega, O. De; Remedios, C. G.; Mulligan, S. P.; Christopherson, R. I. *Cancer Res.* **2001**, *61*, 4483–4489.

(6) Sekine, K.; Revzin, A.; Tompkins, R. G.; Toner, M. *J. Immunol. Methods* **2006**, *313*, 96–109.

(7) Rusmini, F.; Zhong, Z.; Feijen, J. *Biomacromolecules* **2007**, *8*, 1775–1789.

(8) Jonkheijm, P.; Weinrich, D.; Schröder, H.; Niemeyer, C. M.; Waldmann, H. *Angew. Chem. Int. Ed. Engl.* **2008**, *47*, 9618–9647.

(9) Becker, H.; Gärtner, C. *Anal. Bioanal. Chem.* **2008**, *390*, 89–111.

(10) Kuo, J. S.; Chiu, D. T. *Lab Chip* **2011**, 2656–2665.

(11) Attia, U. M.; Marson, S.; Alcock, J. R. *Microfluid. Nanofluidics* **2009**, *7*, 1–28.

(12) Soper, S. A.; Henry, A. C.; Vaidya, B.; Galloway, M.; Wabuyele, M.; McCarley, R. L. *Anal. Chim. Acta* **2002**, *470*, 87–99.

(13) Hansen, M.; Hjortø, G. M.; Met, O.; Jakobsen, M. H.; Svane, I. M.; Larsen, N. B. *J. Biomed. Mater. Res. A* **2011**, *96*, 372–383.

(14) Bora, U.; Chugh, L.; Nahar, P. *J. Immunol. Methods* **2002**, *268*, 171–177.

(15) Nahar, P.; Wali, N. M.; Gandhi, R. P. *Anal. Biochem.* **2001**, *294*, 148–153.

(16) Sung, D.; Park, S.; Jon, S. *Langmuir* **2012**, *28*, 4507–4514.

(17) Sung, D.; Shin, D. H.; Jon, S. *Biosens. Bioelectron.* **2011**, *26*, 3967–3972.

(18) Larsen, E. K. U.; Mikkelsen, M. B. L.; Larsen, N. B. *Biomacromolecules* **2014**, *15*, 894–899.

(19) Heyries, K. A.; Marquette, C. A.; Blum, L. J. *Langmuir* **2007**, *23*, 4523–4527.

(20) Heyries, K. A.; Mandon, C. A.; Ceriotti, L.; Ponti, J.; Colpo, P.; Blum, L. J.; Marquette, C. A. *Biosens. Bioelectron.* **2009**, *24*, 1146–1152.

(21) Berthier, E.; Young, E. W. K.; Beebe, D. *Lab Chip* **2012**, *12*, 1224–1237.

(22) Toepke, M. W.; Beebe, D. J. *Lab Chip* **2006**, *6*, 1484–1486.

(23) Regehr, K. J.; Domenech, M.; Koepsel, J. T.; Carver, K. C.; Ellison-Zelski, S. J.; Murphy, W. L.; Schuler, L. A.; Alarid, E. T.; Beebe, D. J. *Lab Chip* **2009**, *9*, 2132–2139.

(24) Bodas, D.; Khan-Malek, C. *Sens. Actuators B* **2007**, *123*, 368–373.

(25) Biancardo, S. B. N.; Pranov, H. J.; Larsen, N. B. *Adv. Mater.* **2008**, *20*, 1825–1829.

(26) Cech, J.; Taboryski, R. *Appl. Surf. Sci.* **2012**, *259*, 538–541.

(27) Owens, D. K.; Wendt, R. C. *J. Appl. Polym. Sci.* **1969**, *13*, 1741–1747.

(28) Welch, B. L. *Biometrika* **1947**, *34*, 28–35.

(29) Hill, A. *J. Physiol.* **1910**, *40*, iv–vii.

(30) MacDougall, D.; Crummett, W. B. *Anal. Chem.* **1980**, *52*, 2242–2249.

(31) Pease, D. C. *J. Colloid Interface Sci.* **1944**, *168*, 40–46.

(32) Stadler, H.; Mondon, M.; Ziegler, C. *Anal. Bioanal. Chem.* **2003**, *375*, 53–61.

(33) Maboudian, R.; Ashurst, W. R.; Carraro, C. *Sens. Actuators* **2000**, *82*, 219–223.

(34) Wu, C.-W.; Shen, Y.-K.; Chuang, S.-Y.; Wei, C. S. *Sens. Actuators A* **2007**, *139*, 145–151.

(35) Zhou, W.; Zhang, J.; Liu, Y.; Li, X.; Niu, X.; Song, Z.; Min, G.; Wan, Y.; Shi, L.; Feng, S. *Appl. Surf. Sci.* **2008**, *255*, 2885–2889.

(36) Garidel, S.; Zelsmann, M.; Chaix, N.; Voisin, P.; Boussey, J.; Beaurain, A.; Pelissier, B. *J. Vac. Sci. Technol. B Microelectron. Nanom. Struct.* **2007**, *25*, 2430.

(37) Beck, M.; Graczyk, M.; Maximov, I.; Sarwe, E.-L.; Ling, T. G. I.; Keil, M.; Montelius, L. *Microelectron. Eng.* **2002**, *61-62*, 441–448.

(38) Park, S.; Schift, H.; Padeste, C.; Schnyder, B.; Kötz, R.; Gobrecht, J. *Microelectron. Eng.* **2004**, *73-74*, 196–201.

(39) Matschuk, M.; Larsen, N. B. *J. Micromech. Microeng.* **2013**, *23*, 025003.

(40) Matschuk, M.; Bruus, H.; Larsen, N. B. *Microelectron. Eng.* **2010**, *87*, 1379–1382.

(41) Christiansen, A. B.; Clausen, J. S.; Mortensen, N. A.; Kristensen, A. *Microelectron. Eng.* **2014**, *121*, 47–50.

(42) Tan, J. L.; Tien, J.; Chen, C. S. *Langmuir* **2002**, *18*, 519–523.

(43) Vermeer, A. W. .; Norde, W. *Biophys. J.* **2000**, *78*, 394–404.

(44) Tofteberg, T. R.; Andreassen, E. *Int. Polym. Process.* **2010**, *25*, 63–74.

(45) Mayor, U.; Guydosh, N. R.; Johnson, C. M.; Grossmann, J. G.; Sato, S.; Jas, G. S.; Freund, S. M. V.; Alonso, D. O. V.; Daggett, V.; Fersht, A. R. *Nature* **2003**, *421*, 863–867.

(46) Kubelka, J.; Hofrichter, J.; Eaton, W. A. *Curr. Opin. Struct. Biol.* **2004**, *14*, 76–88.

(47) Steel, B. C.; McKenzie, D. R.; Bilek, M. M. M.; Nosworthy, N. J.; dos Remediosy, C. G. *Biophys. J.* **2006**, *91*, L66–L68.

For table of contents only:

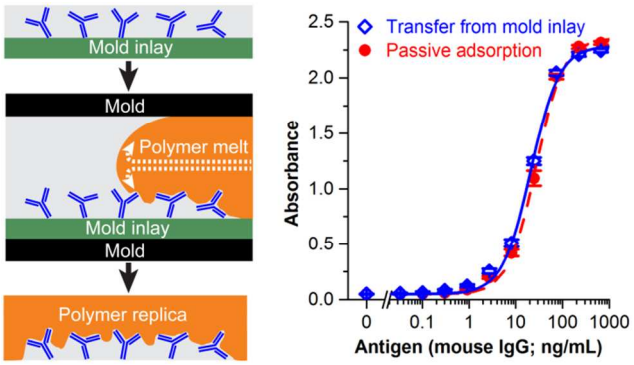

Appendix C:

Paper II

Hydrogen silsesquioxane (HSQ) mold coatings for improved replication of nanopatterns by injection molding

T.C. Hobæk, M. Matschuk, J. Kafka, H. Pranov, N.B. Larsen
Submitted to Journal of Micromechanics and Microengineering, August 1, 2014

Hydrogen silsesquioxane (HSQ) mold coatings for improved replication of nanopatterns by injection molding

Journal:	*Journal of Micromechanics and Microengineering*
Manuscript ID:	Draft
Manuscript Type:	Paper
Date Submitted by the Author:	n/a
Complete List of Authors:	Hobæk, Thor; Technical University of Denmark, Department of Micro and Nanotechnology Matschuk, Maria; InMold Biosystems, Kafka, Jan; InMold Biosystems, Pranov, Henrik; InMold Biosystems, Larsen, Niels; Technical University of Denmark, Department of Micro and Nanotechnology
Article Keywords:	HSQ, injection molding, nanostructures, hydrogen silsesquioxane, cyclic olefin copolymer
Abstract:	We demonstrate the replication of nanosized pillars in polymer (cyclic olefin copolymer) by injection molding using nanostructured ceramic hydrogen silsesquioxane (HSQ) coatings on stainless steel mold inserts. At isothermal mold conditions, the average pillar height increases by up to 100% and a more uniform height distribution is observed compared to a traditional metal mold insert. Thermal heat transfer simulations predict that the HSQ film retards the cooling of the polymer melt during the initial stages of replication, thus allowing more time to fill the nanoscale cavities compared to standard metal molds. A monolayer of a fluorinated silane (FDTS) deposited on the mold surface reduces the mold/polymer interfacial energy to support demolding of the polymer replica. The mechanical stability of thermally cured HSQ makes it a promising material for nanopattern replication on an industrial scale without the need for slow and energy intensive variotherm processes.

Hydrogen silsesquioxane (HSQ) mold coatings for improved replication of nanopatterns by injection molding

Thor Christian Hobæk[1], Maria Matschuk[2], Jan Kafka[2], Henrik J. Pranov[2] and Niels B. Larsen[1]

[1] Department of Micro- and Nanotechnology, Technical University of Denmark, Ørsteds Plads 345E, 2800 Kgs. Lyngby, Denmark

[2] InMold Biosystems, Diplomvej 381, 2800 Kgs. Lyngby, Denmark

E-mail: niels.b.larsen@nanotech.dtu.dk

Abstract

We demonstrate the replication of nanosized pillars in polymer (cyclic olefin copolymer) by injection molding using nanostructured ceramic hydrogen silsesquioxane (HSQ) coatings on stainless steel mold inserts. At isothermal mold conditions, the average pillar height increases by up to 100% and a more uniform height distribution is observed compared to a traditional metal mold insert. Thermal heat transfer simulations predict that the HSQ film retards the cooling of the polymer melt during the initial stages of replication, thus allowing more time to fill the nanoscale cavities compared to standard metal molds. A monolayer of a fluorinated silane (FDTS) deposited on the mold surface reduces the mold/polymer interfacial energy to support demolding of the polymer replica. The mechanical stability of thermally cured HSQ makes it a promising material for nanopattern replication on an industrial scale without the need for slow and energy intensive variotherm processes.

1 Introduction

Injection molding has been the preferred industrial process for polymer shaping for decades due to low cycle times and the multitude of technologies established for full process automation [1,2]. Considerable know-how and experience is established on replication on the macroscopic scale using this technique. During the last two decades this knowledge base has been extended to replication of micro- and nanoscale features. A wide range of applications has been explored including microfluidic devices [3,4], diffractive optical elements [5], anti-reflective surfaces [6,7], superhydrophobic surfaces [8–10], and functional cell culture substrates [11–14]. Commercial injection molding is routinely used to replicate features with details down to 150 nm in the case of Blu-Ray discs, while replication demonstrating lateral resolution as low as 5 nm has been demonstrated in research [15–20]. This suggests that the lower limit of replication is determined by the structural detail of the mold surface.

Replication of nanoscale features is more challenging when targeting height-to-width aspect ratio above 1. A limiting factor in the replication of higher aspect ratio structures is the rapid formation of a solidified skin layer after the hot polymer melt contacts the cold mold surface [21] resulting in a significant increase in the flow resistance inside micro- and nano-scale cavities due to the high viscosity. A general strategy for improving replication of high aspect-ratio features is to increase the melt and mold temperature as well as the injection speed, which reduces the thickness of the skin layer formed prior to filling of the cavity. Additionally, high injection pressures also help to force the melt into cavities even after skin formation [19,20,22,23].

The most important factor for achieving good replication appears to be the mold temperature, $T_{m,}$ [16,19,22] that often needs to be above the glass-transition temperature, T_g, of the polymer for replicating high aspect ratio structures [24,25]. This calls for the use of a “variotherm” process, i.e. active heating and cooling of the mold for each replication cycle. The main disadvantage is longer process cycle times: While conventional injection molding uses cycle times from 1-30 s, variotherm processes may require 100-300 s for each replication [24]. The repeated thermal cycling can also lead to lower mold lifetime due to thermal stresses [25], as well as higher energy consumption, which both contribute to overall higher production costs.

Several authors have reported on methods to reduce the thermal cycling time for variotherm processes. These involves heating of the stamper material itself by electrical (Joule heating) [26–28] or induction heating [29,30]. Other methods involve external heating of the stamper surface, such as infrared heating [31,32] or steam heating [33]. Laser-heating of the mold has been used to achieve extremely rapid mold heating (300 °C/s) [34], although the heated area is rather small and inhomogeneous. Although several of these methods have demonstrated cycle times comparable to conventional injection molding, they add complexity to the mold and the machine, making it more expensive to set up and maintain a production line.

A simpler alternative to variotherm processes involves the use of heat retardant materials to impede the heat transfer from the polymer melt to the cold mold. Nickel shims formed by electroplating from a metallized silicon master have become the standard insert material for micro-

and nano-replication, due to its ease of replication and good durability [3,5]. Nickel has a high thermal conductivity, like most other metals, which leads to fast heat dissipation from the polymer melt during mold filling and rapid formation of a solidified polymer skin layer. Adding a heat-insulating plate on the backside of a nickel shim has been shown to slow the heat transfer resulting in increased replication quality [35,36]. Likewise, a polymer foil covering one of the mold halves allowed fabrication of high-aspect ratio microcantilevers through an isothermal process [37]. Furthermore, polymeric stampers with imprinted micro- [38] and nano-structures [39] showed improved filling at low mold temperatures compared to a nickel stamper. Although these examples demonstrated impressive replication without the need for a variotherm process, they are likely not suitable for high-volume production as the mold materials used lack the mechanical durability that is required in an industrial setting.

Here, we demonstrate the improved filling of nanostructures using a hybrid mold consisting of a film of hydrogen silsesquioxane (HSQ) with imprinted nanostructures on a stainless steel mold. HSQ is a soluble organosilicon compound that forms hard cross-linked molecular networks upon heating. HSQ thin films are established in commercial integrated circuit production as a precursor for interlayer dielectrics [40] and as an electron-beam resist with lateral resolution down to 5 nm [41]. For polymer shaping, structured HSQ films on silicon have previously been used as stamps for nanoscale features by hot embossing [42,43]. Heat treated HSQ forms a silica-like material that easily reacts with silane-based chemistry employed for applying anti-stiction coatings to the stamp for improved release of polymer replicas [7,19,20,44]. In addition, planar HSQ films have been used as a surface coating on steel molds to lower the surface roughness [45] with a demonstrated injection molding lifetime of at least 10 000 cycles without measurable wear. Here, we show an improved filling of nanoscale holes using heat treated nanopatterned HSQ films under isothermal mold conditions compared to an electroplated nickel shim with an outer chromium/gold coating. Simulation of the heat transfer between polymer melt and mold shows that the HSQ-layer significantly retards the cooling after thermal contact between the materials is established, thus enabling improved nanoscale replication.

2 Methods

2.1 Mold insert fabrication

2.1.1 Silicon master fabrication

The pattern was defined in a silicon (Si) master by deep-UV (DUV) stepper lithography. This technique is capable of exposing areas at full wafer-scale in less than a minute with a lateral resolution better than 250 nm. First, a 60 nm thick bottom anti-reflective coating (DUV42P-6, Brewer Science, MO) was spin-coated to minimize interference effects and to promote adhesion. A 350 nm thick positive photoresist (JSR-M230Y, JSR Corporation, Japan) was spin-coated and baked at 130 °C for 90 s. The resist was exposed with a FPA-3000 EX4 stepper system (Canon, Japan) using a 248 nm KrF illumination source producing a square grid of exposed areas with a pitch of 700 nm. A post-

exposure bake was employed at 130 °C for 60 s before development of the photoresist. Openings in the resist were transferred into the underlying silicon by reactive-ion etching (Pegasus, SPTS, UK) using continuous etching (38 sccm SF_6) and deposition of a passivation layer (75 sccm C_4F_8) at a pressure of 4 mTorr, a coil/platen power of 800 W/40 W, a temperature of -20 °C, and a total process time of 180 s.

2.1.2 Metal mold insert fabrication

Pure metal mold inserts resulted from electroplating on the reactive-ion etched Si master. A metallic seeding layer of 15 nm Cr and 45 nm Au was deposited on the master structures by sputter-coating (CMS 18, Kurt J. Lesker Company, UK). Nickel electroplating proceeded in a nickel sulfamate bath operated at 56 °C and at pH 3.6-3.8 (Microform 200, Technotrans, Germany). The resulting Ni shim had a thickness of 330 µm. The Ni shim could not easily be separated from the master, so the Si wafer was fully dissolved in 28% w/v aqueous KOH at 90 °C. The electroplated shim was cut out with a mechanical punching tool defining a circular perimeter with two flats for aligning the shim in the mold.

2.1.3 HSQ/steel mold insert fabrication

Stainless steel substrates with a thickness of 1 mm were cut out by milling to include alignment flats. The substrates were wet polished with a series of sandpaper with grit size P500, P800 and P1200 (Norton Abrasives, UK), followed by Al_2O_3 paper with 5 µm and 0.3 µm mean particle size (Laser Components, Germany). The substrates were cleaned with 1 %v/v Triton X-100 in MilliQ water (Millipore, MA) at 60 °C for 1 h, followed by a 10 min air plasma (0.5 mbar, 50 W) treatment to reduce hydrocarbon contamination. HSQ (FOx-16, Dow Corning, MI) was deposited by spin-coating at 2000 rpm. The HSQ was subsequently imprinted with a nanostructured elastomer stamp originating from the same Si master pattern. Afterwards, the stamp was released and the HSQ/steel mold was thermally cured, first at 80 °C for 24 h to remove solvent and subsequently at 450 °C for 2 h to cross-link the HSQ.

2.1.4 Surface coating of mold inserts

Both the metal and HSQ/steel mold inserts were coated with a monolayer of heptadecafluoro-1,1,2,2-tetrahydrodecyltrichlorosilane (FDTS) by molecular vapor deposition (MVD 100, Applied Microstructures, CA) using a previously described process [44].

2.2 Injection molding

Polymer replicas were injection molded on a Victory 80/45 Tech injection molder (Engel, Austria), using TOPAS 8007-S04 (TOPAS Advanced Polymers, Germany) cyclic olefin copolymer (COC) with $T_g \sim 78$ °C. The molded polymer replicas were 50 mm circular discs with a thickness of 2.0 mm. The metal mold inserts were installed in the mold with a 1.0 mm aluminum back plate, while the HSQ/steel inserts were installed with a 330 µm Ni back plate. Thus, both assemblies had a total

thickness of 1.33 mm. The parameters used for injection molding are summarized in table 1. The mold temperature was varied from 40 to 70 °C in random sequential order to avoid systematic errors from the thermal history of the mold. After each parameter change, at least 40 replicas were injection molded to achieve stable molding conditions before collecting replicas for structural analysis.

Table 1. Injection molding conditions.

T_{mold} (°C)	T_{melt} (°C)	V_{inject} (cm^3/s)	P_{inject} (bar)	P_{hold} (bar)	t_{hold} (s)	t_{cool} (s)	t_{cycle} (s)
40 – 70	250	45	1300	800	10	29	60.2

2.3 Mold insert and replica characterization

Scanning electron micrographs (SEM) of uncoated metal and HSQ/steel mold inserts were acquired on a Supra 40 VP microscope (Carl Zeiss, Germany) using 5 kV acceleration potential. The HSQ film thickness was measured by optical reflectance at incidence angles of 0° and 70° using a FilmTek 4000 reflectometer (Scientific Computing International, CA).

Surface topography micrographs of the polymer replicas were acquired by atomic force microscopy (AFM) using BudgetSensor-300 cantilevers on an XE-150 AFM (Park Systems, Korea) operating in intermittent contact mode. For each set of molding temperature, three individual samples were each scanned at three different positions, separated by at least 1 mm. The image scan size was 5 x 5 μm^2 (256 x 256 pixels) at a line rate of 0.5 Hz. The scans were analyzed using the SPIP 6.2.8 software package (Image Metrology, Denmark).

Each pillar was analyzed as grains using height threshold detection. At least 300 pillars for each parameter set were included in the analysis. The background level, defined as the base area surrounding the pillars, was corrected with a 2^{nd} degree polynomial plane fit. Each of the 256 line profiles was then fitted individually with a linear curve (excluding the data above the threshold level). This method was the most reliable to produce a zero-level flat background. The maximum height value of each grain was recorded and used to quantify the degree of replication. The same method was applied to quantify the depth of the structures in the mold, only measuring the negative grain height instead.

2.4 Initial contact temperature calculation and finite element modeling of heat transfer

Finite element modeling of the polymer melt cooling was performed with the COMSOL Multiphysics 4.4 software package (COMSOL, Sweden) by numerically solving the one-dimensional heat equation:

$$\frac{\partial T}{\partial t} - \alpha \frac{\partial^2 T}{\partial x^2} = 0 \quad (1)$$

$$\alpha = \frac{k}{\rho c_p} \quad (2)$$

where T is the temperature, α the thermal diffusivity, k the thermal conductivity, ρ the mass density, and c_p the specific heat capacity at constant pressure. The initial contact temperature, T, between two semi-infinite bodies at temperature T_1 and T_2, respectively, can be calculated analytically from their thermal effusivities e:

$$\boldsymbol{T = T_1 + (T_2 - T_1)\frac{e_2}{e_2+e_1}} \quad (3)$$

$$\boldsymbol{e = \left(k \cdot \rho \cdot c_p\right)^{\frac{1}{2}}} \quad (4)$$

The material constants used for Cr, Au, Ni, HSQ, stainless steel, and COC [46] are shown in table 2, together with the calculated thermal diffusivities and thermal effusivities. Any temperature-dependence is neglected. The outer layer of the pure metal mold used for injection molding consists of ~15 nm Cr and ~45 nm Au on top of the bulk electroplated Ni. In the numerical simulations, the othermost two layers were approximated by a single 100 nm thick Au layer, as the chromium layer is extremely thin and has similar thermal transport properties as gold (table 2). A boundary probe for the temporal development of the temperature was defined at a location inside the polymer melt at a distance of 50 nm from the mold/melt interface. Perfect thermal contact between the mold and the polymer melt was assumed, with T_{mold} = 70 °C and T_{melt} = 250 °C as initial temperatures. The initial mold temperature of 70 °C was maintained within the mold at a distance of 500 µm from the mold/melt interface, and a symmetry plane was defined within the polymer melt at a distance of 500 µm from the mold/melt interface. No movement of material was included in the simulations, thus heat dissipation by viscous effects was not considered.

Table 2. Material constants used for heat transfer analysis

	Thermal conductivity, k ($W \cdot m^{-1} \cdot K^{-1}$)	Heat capacity, c_p ($J \cdot kg^{-1} K^{-1}$)	Density, ρ ($kg \cdot m^{-3}$)	Thermal diffusivity, α ($m^2 \cdot s^{-1}$)	Thermal effusivity, e ($W \cdot s^{1/2} \cdot m^{-2} \cdot K^{-1}$)
Cr	93.7	448	7150	$2.92 \cdot 10^{-5}$	$1.73 \cdot 10^{4}$
Au	317	129	19300	$1.27 \cdot 10^{-4}$	$2.81 \cdot 10^{4}$
Ni	90.7	445	8900	$2.29 \cdot 10^{-5}$	$1.90 \cdot 10^{4}$
HSQ	0.15	730	1400	$1.46 \cdot 10^{-7}$	$3.92 \cdot 10^{2}$
Stainless steel	16.2	500	8000	$4.05 \cdot 10^{-6}$	$8.05 \cdot 10^{3}$
COC	0.21	2200	1003	$9.51 \cdot 10^{-8}$	$6.81 \cdot 10^{2}$

3 Results

3.1 HSQ significantly improves replication compared to pure metal at isothermal mold conditions

The lower heat conductivity of HSQ was expected to retard the heat dissipation between the polymer melt and the mold during the initial phase of the cavity filling, and thus delay the formation of a solidified skin layer. Figure 1 shows SEM micrographs of (a) the pure metal mold insert fabricated by electroplating and (b) the HSQ/steel mold insert fabricated by imprinting the HSQ layer with a surface structured elastomer stamp. The structures in HSQ appear to have more rounded edges due to the different fabrication processes between the two molds. However, this was not expected to affect the replication quality significantly. Charging effects were observed during SEM imaging of the HSQ film due to its low electrical conductivity leading to reduced image contrast. The average HSQ film thickness in the patterned area was ~500 nm as measured by optical reflectometry.

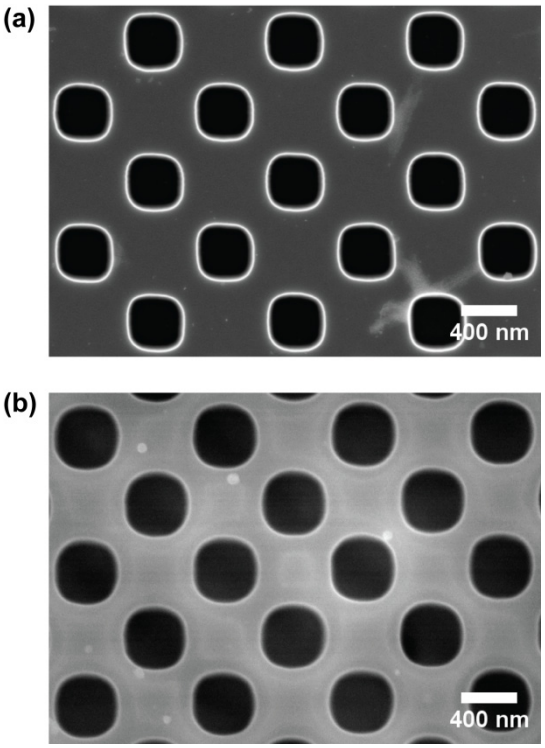

Figure 1. SEM micrographs of hole arrays in (a) the metal mold and (b) the HSQ/steel mold insert.

Figure 2 shows AFM micrographs of polymer replicas injection molded against the structured mold inserts at different mold temperatures. The micrographs show that the mean pillar height increases monotonically with increasing mold temperature and is generally higher for HSQ than for a pure metal mold surface. The replicated structures appear to be wider for HSQ molds, although this is likely an artefact caused by AFM tip convolution. Injection molding with a metal insert at mold temperatures ≤60 °C leads to a spatially inhomogeneous distribution of pillar heights over the scan area and with some features not being replicated at all. Replicas from the HSQ/steel mold insert also shows some pillar height variations but to a much smaller extent and only at lower mold temperatures.

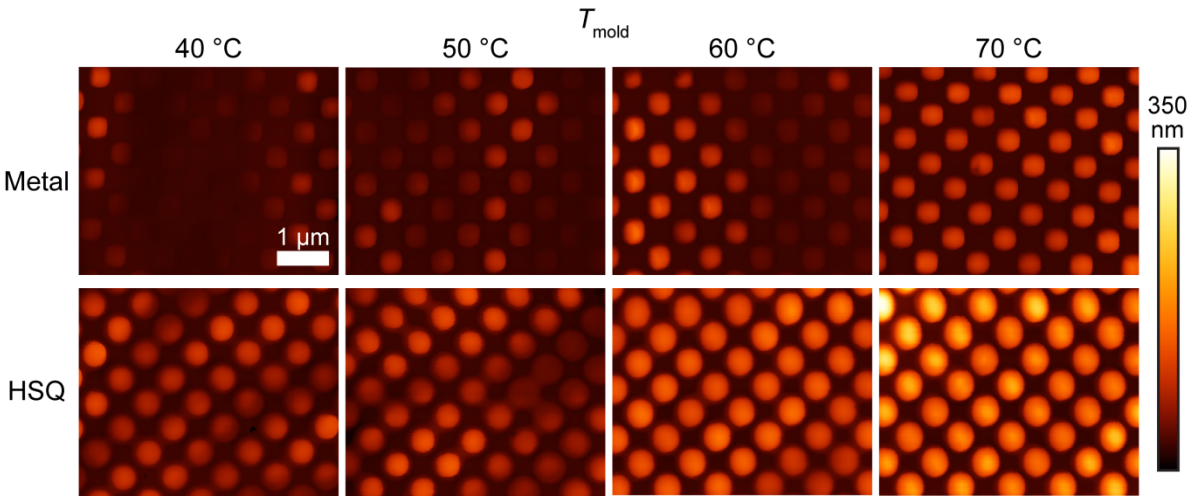

Figure 2. AFM micrographs of polymer replicas injection molded on a pure metal mold insert (upper row) or a HSQ/steel mold insert (lower row) at different mold temperatures. The displayed scan areas are 5×4 µm^2 and the height scale is 350 nm.

The replication was quantified and is plotted in figure 3 for pure metal and HSQ/steel mold inserts based on height measurements of at least 300 replicated pillars from 3 individual samples, at each mold temperature. These measurements confirm that structured HSQ molds results in better replication than metal molds at all mold temperatures, as visually apparent in figure 2. At mold temperatures of 40 °C and 50 °C, i.e. ~40 °C and ~30 °C lower than the polymer T_g, the mean replicated pillar height is increased by 100% compared to the metal mold, while the improvement at 70 °C, close to T_g, is 50%. Full replication is still not achieved at this temperature as the HSQ hole structures (figure 1b) have a mean depth of 326 nm as determined by AFM (data not shown).

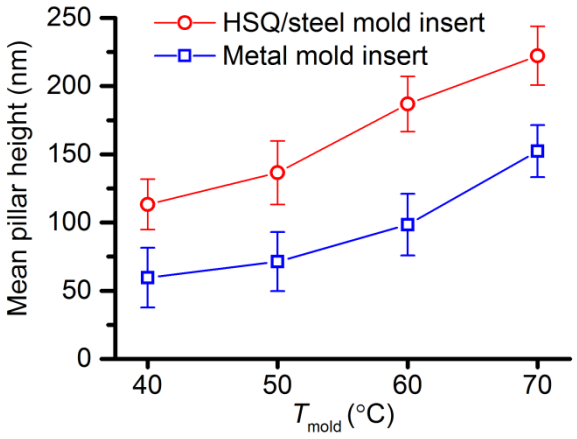

Figure 3. Mean pillar height of polymer replicas from structured metal and HSQ/steel mold inserts at various mold temperatures. The mean depth of the mold structures are 398 nm and 326 nm for the metal mold insert and the HSQ/steel mold insert, respectively. Error bars show the standard error of the mean (n=3).

Table 3 shows the calculated coefficient of variation (CV) of the pillar height defined as the ratio of the standard deviation to the mean. These data confirm a more homogeneous pillar replication with the HSQ/steel mold insert than with the metal mold insert at all mold temperatures and especially at the lower temperatures investigated.

A total cycle time (t_{cycle}) of 60.2 s was the shortest achievable at T_{mold} = 70 °C. With shorter cooling times, the sprue part of the replicas were still too soft for the replica to be reliably picked up by the robot arm in automatic machine mode. However, at T_{mold} = 40 °C the cooling time could be significantly reduced resulting in a minimum cycle time of 31.6 s. Despite this possibility to shorten the production time, the total cycle time was kept constant at 60 s in this study to allow a direct comparison between the different mold temperatures. The HSQ/steel mold inserts were used during 900 injection molding cycles in this study, after which no damage to the surface could be observed by SEM analysis (data not shown).

Table 3. Coefficient of variation (%) of the replicated pillars

	T_{mold}			
	40 °C	50 °C	60 °C	70 °C
Metal mold insert	64%	53%	40%	22%
HSQ/steel mold insert	28%	30%	19%	17%

3.2 Heat transfer simulations confirm heat retardation by HSQ

The initial contact temperature between the COC polymer melt and the mold surface can be calculated using equation 3. The results for initial temperatures T_{mold} = 70 °C and T_{melt} = 250 °C are 77 °C for COC/Cr and 184 °C for COC/HSQ, which gives a first indication that HSQ may support sustained polymer flow after initial contact. The simulated cooling of a polymer melt at a position 50 nm from the polymer/mold interface is shown in figure 4 for a metal mold insert and a stainless steel mold insert with a 500 nm thick HSQ layer. The metal mold insert is modeled as consisting of a 100 nm thick Au layer on a nickel support, thus disregarding the minute influences expected from having a Cr/Au layer instead of pure gold on the actual metal mold used for injection molding. Upon thermal contact with the metal mold insert, the polymer melt cools rapidly from an initial temperature of 250 °C and reaches T_g after only 10 µs. In contrast, the polymer melt remains at temperatures above T_g for >100 ms when contacting the HSQ/steel mold surface, i.e. 4 orders of magnitude longer.

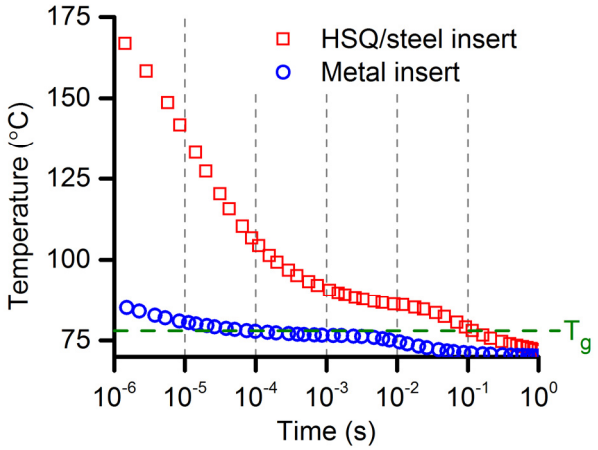

Figure 4. Finite element modeling of polymer melt cooling at a position 50 nm from the polymer melt/mold interface after the polymer melt at 250 °C is brought in thermal contact with a metal mold insert or a HSQ/steel mold insert at 70 °C.

Figure 5 shows the results of modeling the time-dependent spatial temperature distribution across the polymer/mold interface. The pure metal insert (figure 5a) gives rise to a sharp transition in temperature across the polymer/mold interface with the melt temperature reaching 100 °C (T_g + 20 °C) after 10 µs at a distance of 200 nm from the mold surface, i.e. half the nanopillar diameter in figure 2. The temperature at the mold surface barely increases from 70 °C to 76 °C during this time period. In contrast, the HSQ/steel mold insert (figure 5b) causes much slower cooling of the polymer melt with a polymer/HSQ interface temperature of 184 °C at 100 ns after initial contact and reaching 160 °C (T_g + 80 °C) after 10 µs at a distance of 200 nm from the mold surface. A temperature gradient arises across the HSQ film after 10 µs, with the outer surface being at 139 °C and the inner surface (towards stainless steel) still being at 70 °C. After 1 ms, the steel surface reaches a temperature of 83 °C.

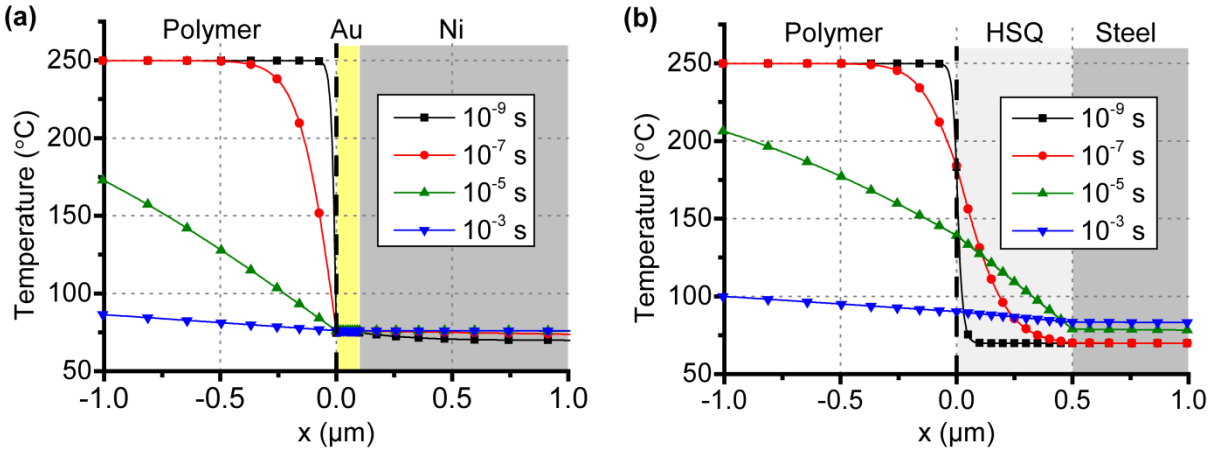

Figure 5. Finite element modeling of the spatial temperature distribution across the polymer/mold interface (x = 0) at different time points for (a) metal mold inserts and (b) HSQ/steel mold inserts. In (a), x < 0 µm: COC, 0 µm < x < 0.1 µm: Au, 0.1 µm < x: Ni. In (b), x < 0 µm: COC, 0 µm < x < 0.5 µm: HSQ, 0.5 µm < x: stainless steel.

4 Discussion

An imprinted HSQ film on a stainless steel mold insert significantly increases the replication quality of nanoscale features compared to a nickel mold insert fabricated by electroplating (figure 2 and 3). The replicated pillars are taller at all mold temperatures and with the difference being largest for T_{mold} = 40 °C or 50 °C, i.e. well below T_g of the polymer. Due to the lower thermal diffusivity of the HSQ film (table 2), heat dissipation across the polymer/mold surface is retarded. The melt is allowed to stay in a flowable state for a longer time and can therefore penetrate longer into the nanostructured holes before it solidifies. This is exemplied by the modeling results presented in figure 5 where a difference in melt temperature of T_g + 20 °C vs T_g + 80 °C on the metal mold vs HSQ/steel mold after 10 µs corresponds to a reduction in melt flow viscosity by several orders of magnitude [47].

These findings agree well with previous literature on other heat-retarding mold materials. For instance, by using a nano-imprinted layer of SU-8 on a 740 µm polyimide (PI) sheet as a mold inlay, full replication of 100 nm holes in polycarbonate (PC) with an aspect ratio of 1 was achieved at T_{mold} = 60 °C [39]. Injection molding using a Ni mold with the same surface pattern resulted in replicated pillars with only about 30% of the nominal height. Another study demonstrated replication of 1 µm wide polymer gratings with an aspect ratio of 9 using a patterned polyurethane acrylate (PUA) layer on a 40 µm thick polyethylene terephthalate (PET) film, although the replication quality was not uniform [38].

The non-uniform replication at low mold temperatures with a pure metal mold (figure 2 and table 3) may be explained by thermally induced flow instabilities that have previously been observed at low injection velocities and large differences between T_{melt} and T_{mold} (high cooling rates) [48]. With the onset of flow instability, the polymer solidifies before the cavity is completely filled, causing surface waviness with a periodicity of several micrometers. Flow instability is not observed to the same degree when using the HSQ-coated mold, and the surface topography is more uniformly replicated.

Numerical simulation of the heat transfer showed that the polymer melt close to the mold surface stays above T_g significantly longer for HSQ/stainless steel compared to a metal mold insert, due to the much lower thermal diffusivity. The initial temperatures for the Ni/COC and the HSQ/COC as predicted by the simulations fit perfectly with the analytical solution in equation 3. The effect of viscous heat dissipation is not included in these simulations, although for replication of microstructures they have previously been assumed to be negligible [46]. Also, we have assumed a perfect thermal contact between the melt and the mold surface, which is a good approximation during the initial filling phase when the viscosity is low [49]. The polymer contracts during cooling, which is compensated by the holding pressure as long as polymer melt is allowed to move through the gate. After the gate is frozen, the cavity pressure drops and the polymer may separate from the mold due to continuous shrinking. Thus, a thermal contact resistance arises. However, as the replication of nanoscale features happens at a much shorter timescale, this is likely of less relevance for our study.

To our knowledge, the materials used to demonstrate heat retardation in an injection molding process have so far only been polymer-based. These materials may be suitable for prototyping or small-volume productions. However, for high-volume productions that could involve more than 100 000 cycles, they lack the wear-resistance offered by those materials typically used in industry, such as tool steel. Thermally cured HSQ has previously demonstrated a lifetime of at least 10 000 cycles in an injection molding process [45] and has also shown to be mechanically stable during hot embossing [42]. Above 400 °C, the Si-H bonds in the monomer dissociates and a cross-linked silica network is formed resulting in an increase in hardness to 2-15 GPa depending on the curing conditions [50]. This ceramic-like coating is highly scratch resistant and is a robust candidate for mold coatings.

Another advantage of using HSQ as a heat-retardant mold coating is its ability to reduce surface roughness of the mold due to its high flowability, an important factor for the production of optically smooth polymer replica [45]. In addition, HSQ was shown to be fully compatible with silane surface chemistry. Thus, an anti-stiction coating like FDTS can be applied without any intermediate process steps. This is an important finding as a strong adhesion between polymer and mold can lead to incomplete replication or in worst case damage to the mold surface [19,42].

5 Conclusion

We have demonstrated that replication is improved with a HSQ-coated steel mold compared to a pure metal mold formed by sputtering and electroplating, both in terms of a larger mean height and more uniformly distributed height of pillars in the polymer. In contrast to the rapid formation of skin layers caused by the high cooling rates during isothermal molding, the HSQ film acts as an insulating layer that allows more time for the melt to flow before solidifying. Furthermore, a dense anti-sticking monolayer can be applied directly to the thermally cured HSQ by an vapor deposition process to improve release of the polymer replica. In addition, the coated films have demonstrated sufficient durability for high-volume fabrication processes. Thus, HSQ-coatings have the potential to improve nanoscale replication in an industrially relevant setting, by reducing the need for variotherm mold cycling.

Acknowledgements

This work was supported by the Danish Council for Strategic Research through the Strategic Research Center PolyNano (grant no 10-092322/DSF). We would like to thank Matthias Keil and Elena Khomtchenko at DTU Danchip for performing the DUV lithographic patterning of the silicon masters.

References

[1] Giboz J, Copponnex T and Mélé P 2007 Microinjection molding of thermoplastic polymers: a review *J. Micromech. Microeng.* **17** R96–R109

[2] Yang C, Yin X-H and Cheng G-M 2013 Microinjection molding of microsystem components: new aspects in improving performance *J. Micromech. Microeng.* **23** 093001

[3] Becker H and Gärtner C 2008 Polymer microfabrication technologies for microfluidic systems. *Anal. Bioanal. Chem.* **390** 89–111

[4] Attia U M, Marson S and Alcock J R 2009 Micro-injection moulding of polymer microfluidic devices *Microfluid. Nanofluid.* **7** 1–28

[5] Gale M T 1997 Replication techniques for diffractive optical elements *Microelectron. Eng.* **34** 321–39

[6] Ting C-J, Chang F-Y, Chen C-F and Chou C P 2008 Fabrication of an antireflective polymer optical film with subwavelength structures using a roll-to-roll micro-replication process *J. Micromech. Microeng.* **18** 075001

[7] Christiansen A B, Clausen J S, Mortensen N A and Kristensen A 2014 Injection moulding antireflective nanostructures *Microelectron. Eng.* **121** 47–50

[8] Puukilainen E, Rasilainen T, Suvanto M and Pakkanen T A 2007 Superhydrophobic polyolefin surfaces: controlled micro- and nanostructures *Langmuir* **23** 7263–8

[9] Huovinen E, Hirvi J, Suvanto M and Pakkanen T A 2012 Micro-micro hierarchy replacing micro-nano hierarchy: a precisely controlled way to produce wear-resistant superhydrophobic polymer surfaces *Langmuir* **28** 14747–55

[10] Huovinen E, Takkunen L, Korpela T, Suvanto M, Pakkanen T T and Pakkanen T A 2014 Mechanically robust superhydrophobic polymer surfaces based on protective micropillars *Langmuir* **30** 1435–43

[11] Dalby M J, Gadegaard N, Tare R, Andar A, Riehle M O, Herzyk P, Wilkinson C D W and Oreffo R O C 2007 The control of human mesenchymal cell differentiation using nanoscale symmetry and disorder *Nat. Mater.* **6** 997–1003

[12] McMurray R J, Gadegaard N, Tsimbouri P M, Burgess K V, McNamara L E, Tare R, Murawski K, Kingham E, Oreffo R O C and Dalby M J 2011 Nanoscale surfaces for the long-term maintenance of mesenchymal stem cell phenotype and multipotency *Nat. Mater.* **10** 637–44

[13] Tsimbouri P, Gadegaard N, Burgess K, White K, Reynolds P, Herzyk P, Oreffo R and Dalby M J 2014 Nanotopographical effects on mesenchymal stem cell morphology and phenotype *J. Cell. Biochem.* **115** 380–90

[14] Cha K J, Na M-H, Kim H W and Kim D S 2014 Nano Petri dishes: a new polystyrene platform for studying cell-nanoengineered surface interactions *J. Micromech. Microeng.* **24** 055002

[15] Macintyre D and Thoms S 1998 The fabrication of high resolution features by mould injection *Microelectron. Eng.* **41/42** 211–4

[16] Schift H, David C, Gobrecht J, D' Amore A, Simoneta D, Kaiser W and Gabriel M 2000 Quantitative analysis of the molding of nanostructures *J. Vac. Sci. Technol. B* **18** 3564–8

[17] Schift H, David C, Gabriel M, Gobrecht J, Heyderman L, Kaiser W, Koppel S and Scandella L 2000 Nanoreplication in polymers using hot embossing and injection molding *Microelectron. Eng.* **53** 171–4

[18] Gadegaard N, Mosler S and Larsen N B 2003 Biomimetic polymer nanostructures by injection molding *Macromol. Mater. Eng.* **288** 76–83

[19] Matschuk M and Larsen N B 2013 Injection molding of high aspect ratio sub-100 nm nanostructures *J. Micromech. Microeng.* **23** 025003

[20] Matschuk M, Bruus H and Larsen N B 2010 Nanostructures for all-polymer microfluidic systems *Microelectron. Eng.* **87** 1379–82

[21] Viana J C 2004 Development of the skin layer in injection moulding: phenomenological model *Polymer* **45** 993–1005

[22] Liou A-C and Chen R-H 2006 Injection molding of polymer micro- and sub-micron structures with high-aspect ratios *Int. J. Adv. Manuf. Technol.* **28** 1097–103

[23] Mönkkönen K, Hietala J, Pääkkönen P, Pääkkönen E J, Kaikuranta T, Pakkanen T T and Jääskeläinen T 2002 Replication of sub-micron features using amorphous thermoplastics *Polym. Eng. Sci.* **42** 1600–8

[24] Gornik C 2004 Injection moulding of parts with microstructured surfaces for medical applications *Macromol. Symp.* **217** 365–74

[25] Tseng S-C, Chen Y-C, Kuo C-L and Shew B-Y 2005 A study of integration of LIGA and M-EDM technology on the microinjection molding of ink-jet printers' nozzle plates *Microsyst. Technol.* **12** 116–9

[26] Kim Y, Choi Y and Kang S 2005 Replication of high density optical disc using injection mold with MEMS heater *Microsyst. Technol.* **11** 464–9

[27] Xiao C-L and Huang H-X 2014 Multiobjective optimization design of heating system in electric heating rapid thermal cycling mold for yielding high gloss parts *J. Appl. Polym. Sci.* **131** 39976

[28] Wang G, Zhao G and Guan Y 2013 Thermal response of an electric heating rapid heat cycle molding mold and its effect on surface appearance and tensile strength of the molded part *J. Appl. Polym. Sci.* **128** 1339–52

[29] Park K and Lee S-I 2010 Localized mold heating with the aid of selective induction for injection molding of high aspect ratio micro-features *J. Micromech. Microeng.* **20** 035002

[30] Bekesi J, Kaakkunen J J J, Michaeli W, Klaiber F, Schoengart M, Ihlemann J and Simon P 2010 Fast fabrication of super-hydrophobic surfaces on polypropylene by replication of short-pulse laser structured molds *Appl. Phys. A* **99** 691–5

[31] Chang P-C and Hwang S-J 2006 Experimental investigation of infrared rapid surface heating for injection molding *J. Appl. Polym. Sci.* **102** 3704–13

[32] Lin H-Y, Chang C-H and Young W-B 2011 Experimental study on the filling of nano structures with infrared mold surface heating *Int. Polym. Process.* **26** 73–81

[33] Liu J, Zhao G, Wang G and Guan Y 2011 Fully coupled transient heat transfer and melt filling simulations in rapid heat cycle molding with steam heating *Polym. Plast. Technol. Eng.* **50** 423–37

[34] Michaeli W and Klaiber F 2009 Development of a system for laser-assisted molding of micro- and nanostructures *J. Vac. Sci. Technol. B* **27** 1323–6

[35] Lee J-S, Park K-W, Lee S-W, Kim J-H and Kim S 2003 Substrates for ultra small optical disks *Optical Data Storage* pp 228–30

[36] Inoue K, Hayashi K, Kawasaki Y and Ohno E 2003 Study on 40 Gbits/inch^2 density molding using heat insulated mold *Jpn. J. Appl. Phys.* **42** 774–5

[37] Schift H, Urwyler P and Kristiansen P M 2013 Surface-patterned micromechanical elements by polymer injection molding with hybrid molds *J. Vac. Sci. Technol. B* **31** 06FD01

[38] Park S H, Lee W I, Moon S N, Yoo Y E and Cho Y H 2011 Injection molding micro patterns with high aspect ratio using a polymeric flexible stamper *Express Polym. Lett.* **5** 950–8

[39] Stormonth-Darling J M and Gadegaard N 2012 Injection moulding difficult nanopatterns with hybrid polymer inlays *Macromol. Mater. Eng.* **297** 1075–80

[40] Loboda M and Toskey G 1998 Understanding hydrogen silsesquioxane-based dielectric film processing *Solid State Technol.* **41** 99

[41] Yang J K W, Cord B, Duan H, Berggren K K, Klingfus J, Nam S-W, Kim K-B and Rooks M J 2009 Understanding of hydrogen silsesquioxane electron resist for sub-5-nm-half-pitch lithography *J. Vac. Sci. Technol. B* **27** 2622–7

[42] Gadegaard N and McCloy D 2007 Direct stamp fabrication for NIL and hot embossing using HSQ *Microelectron. Eng.* **84** 2785–9

[43] Saleem M R, Stenberg P A, Khan M B, Khan Z M, Honkanen S and Turunen J 2012 Hydrogen silsesquioxane resist stamp for replication of nanophotonic components in polymers *J. Micro/Nanolithogr., MEMS, MOEMS* **11** 013007

[44] Cech J and Taboryski R 2012 Stability of FDTS monolayer coating on aluminum injection molding tools *Appl. Surf. Sci.* **259** 538–41

[45] Cech J, Pranov H, Kofod G, Matschuk M, Murthy S and Taboryski R 2013 Surface roughness reduction using spray-coated hydrogen silsesquioxane reflow *Appl. Surf. Sci.* **280** 424–30

[46] Tofteberg T R and Andreassen E 2010 Multiscale simulation of injection molding of parts with low aspect ratio microfeatures *Int. Polym. Process.* **25** 63–74

[47] Jena R K, Chen X, Yue C Y and Lam Y C 2010 Viscosity of COC polymer (TOPAS) near the glass transition temperature: Experimental and modeling *Polym. Test.* **29** 933–8

[48] Pranov H, Rasmussen H K, Larsen N B and Gadegaard N 2006 On the injection molding of nanostructured polymer surfaces *Polym. Eng. Sci.* **46** 160–71

[49] Bendada A, Derdouri A, Lamontagne M and Simard Y 2004 Analysis of thermal contact resistance between polymer and mold in injection molding *Appl. Therm. Eng.* **24** 2029–40

[50] Liou H-C and Pretzer J 1998 Effect of curing temperature on the mechanical properties of hydrogen silsesquioxane thin films *Thin Solid Films* **335** 186–91